TECHNISCHE UNIVERSITÄT MÜNCHEN

TUM School of Natural Sciences

Synthesis of patterned metal oxide thin films via amphiphilic block copolymer templates and their applications in perovskite solar cells

Shanshan Yin

Vollständiger Abdruck der von der TUM School of Natural Sciences der Technischen Universität München zur Erlangung des akademischen Grades einer

Doktorin der Naturwissenschaften (Dr. rer. nat.)

genehmigten Dissertation.

Vorsitz: Prof. Dr. Martin Zacharias
Prüfer der Dissertation:
1. Prof. Dr. Peter Müller-Buschbaum
2. Prof. Dr. Aliaksandr Bandarenka

Die Dissertation wurde am 15.11.2022 bei der Technischen Universität München eingereicht und durch die TUM School of Natural Sciences am 12.12.2022 angenommen.

Abstract

In this thesis, a serie of nano-patterned metal oxide films were prepared with the assistance of different block copolymer templates and precursors. By adjusting the type of block copolymer, the solvent category, the content of poor solvent, the ratio of copolymer to precursor, and post-processing condition, the morphology of the samples were systematically regulated. By calcination, metal oxide thin films with spherical, cylindrical, cystic pores are acquired. Different block copolymers possess different separation strengths; the solvent category and the content of poor solvent in the solution determines the preferential affinity of solvents to the polymer chains; the weight ratios between the block copolymer templates and the precursor affect the stretching of the molecular chains, and the further thermol post-treatment impart high mobility to the ploymer chains. These factors together affect the phase separation behavior of the block copolymers in the solution, which in turn affects the phase separated structures in the thin film. Moreover, the structural changes of PS-b-P4VP and PS-b-P4VP/$FeCl_3$ films during the printing process as well as the self-assembly of polymer chains in the solution are also investigated in detail. Regarding the applications in solar cells, the $\alpha - Fe_2O_3$ films prepared before and after thermal annealing are used as the electron transport modification layer of perovskite solar cells and the corresponding photoelectrochemical properties are systematically investigated.

Zusammenfassung

In dieser Arbeit wurde eine Reihe von nano-strukturierten Metalloxidfilmen mit Hilfe verschiedener Blockcopolymer-Template und Vorstufen hergestellt. Durch Einstellen des Typs des Blockcopolymers, der Lösungsmittelkategorie, des Gehalts an schlechtem Lösungsmittel, des Verhältnisses von Copolycdmer zu Vorläufer und der Nachbearbeitungsbedingungen wurde die Morphologie der Proben systematisch reguliert. Durch Kalzinierung werden dünne Metalloxidfilme mit kugelförmigen, zylindrischen, zystischen Poren erhalten. Unterschiedliche Blockcopolymere besitzen unterschiedliche Trennfestigkeiten; die Lösungsmittelkategorie und der Gehalt an schlechtem Lösungsmittel in der Lösung bestimmen die bevorzugte Affinität von Lösungsmitteln zu den Polymerketten; die Gewichtsverhältnisse zwischen den Blockcopolymermatrizen und dem Vorläufer beeinflussen die Streckung der Molekülketten, und die weitere Thermol-Nachbehandlung verleiht den Polymerketten eine hohe Mobilität. Diese Faktoren beeinflussen zusammen das Phasentrennungsverhalten der Blockcopolymere in der Lösung, was wiederum

die phasengetrennten Strukturen in dem dünnen Film beeinflusst. Darüber hinaus werden die Strukturänderungen von PS-b-P4VP- und PS-b-P4VP/$FeCl_3$-Filmen während des Druckprozesses sowie die Selbstorganisation von Polymerketten in der Lösung detailliert untersucht. Im Hinblick auf die Anwendungen in Solarzellen werden die vor und nach dem thermischen Tempern hergestellten $\alpha - Fe_2O_3$ Filme als Elektronentransport-Modifikationsschicht von Perowskit-Solarzellen verwendet und die entsprechenden photoelektrochemischen Eigenschaften systematisch untersucht.

Contents

List of abbreviations

DWBA:	distorted wave Born approximation
FF:	fill factor
FTIR:	Fourier transformed infrared spectroscopy
FTO:	fluorine doped tin oxide
FWHM:	full width at half maximum
GISAXS:	grazing incidence small angle X-ray scattering
GIWAXS:	grazing incidence wide angle X-ray scattering
I/V:	current-voltage characteristics
J_{SC}:	short circuit current
V_{OC}:	open circuit voltage
LMA:	local monodisperse approximation
M_n:	number average molecular weight
M_w:	weight average molecular weight
PCE:	power conversion efficiency
PSD:	power spectral density
PS-b-PEO:	poly(styrene-block-ethylene oxide)
CMC:	critical micelle concentration
SDD:	sample detector distance
SLD:	scattering length density
spiro-OMeTAD:	2,2',7,7'-tetrakis(N,N di-p-methoxyphenyl-amine)9,9'-spiro-bifluorene
XRD:	X-ray diffraction
EBL:	electron blocking layer
HBL:	hole blocking layer

1 Introduction

Due to the tremendous application potential in the field of photocatalysis, [1] photovoltaics, [2] gas sensing, [3] and Li-ion batteries, [4] investigations on the synthesis of nanostructured metal oxide thin films have been widely reported in the past decades. In photovoltaic devices, the morphology of the metal oxide thin films directly influenced the interfacial charge carrier extraction efficiency. Whereas the specific surface area of the thin films determines the active-site density available for surface reactions in photocatalysis, gas sensing, and Li-ion battery applications.

The commonly used metal oxide thin film preparation methods involve spray pyrolysis, [5] thermal oxidation, [6] atomic layer deposition (ALD), [7] and electrochemical deposition, [8] thermal decompositions, [9] sol-gel methods. [10] Among these methods, the block copolymer templated sol-gel method shows great potential and flexibility for the preparation of various nanostructured thin films as it is compatible with the industrial large scale thin film deposition facilities. By tuning the phase separation behavior of the block polymer in the solution, spherical, cylindrical, lamellar, granular, and capsular structures can be easily obtained. [11–13] Multiple approaches can be adopted to tune the final structure of the thin film based on the solution processability of this method. Literature reported factors that influence the final thin film structures involve the component content in the solution, the duration of the sol-gel reaction, the post-treatment conditions, and the deposition methods, the surface conditions of the substrate, the operational environment, and the way of removing the polymer template, and so on. [14–23] However, no systematic investigation about the influence of the poor solvent content and the solvent categories on the film morphology has been reported so far. This two factors are crucial for the selectivity of the solvent to the polymer segments in the solution, which in turn determines the phase separation behavior of polymers in the solution to a large extent.

Concerning the emphasis of the investigations in the present thesis lies in the applications of the porous metal oxide films in perovskite solar cell devices, systematic structural regulation for three kinds of commonly used electron transport materials, TiO_2, SnO_2 and α-Fe_2O_3, are implemented based on a laboratory-scale spin coating method. In addition, an in-situ GISAXS technique was used for observing the structural evolution of

the pure PS-b-P4VP and PS-b-P4VP/$FeCl_3$ thin films. α-Fe_2O_3 thin films with different morphologies are prepared and used as an electron transport modification layer for checking their influence on the photovoltaic performance of the devices. Figure 1.1 shows an overview of the five different research topics covered in the present thesis.

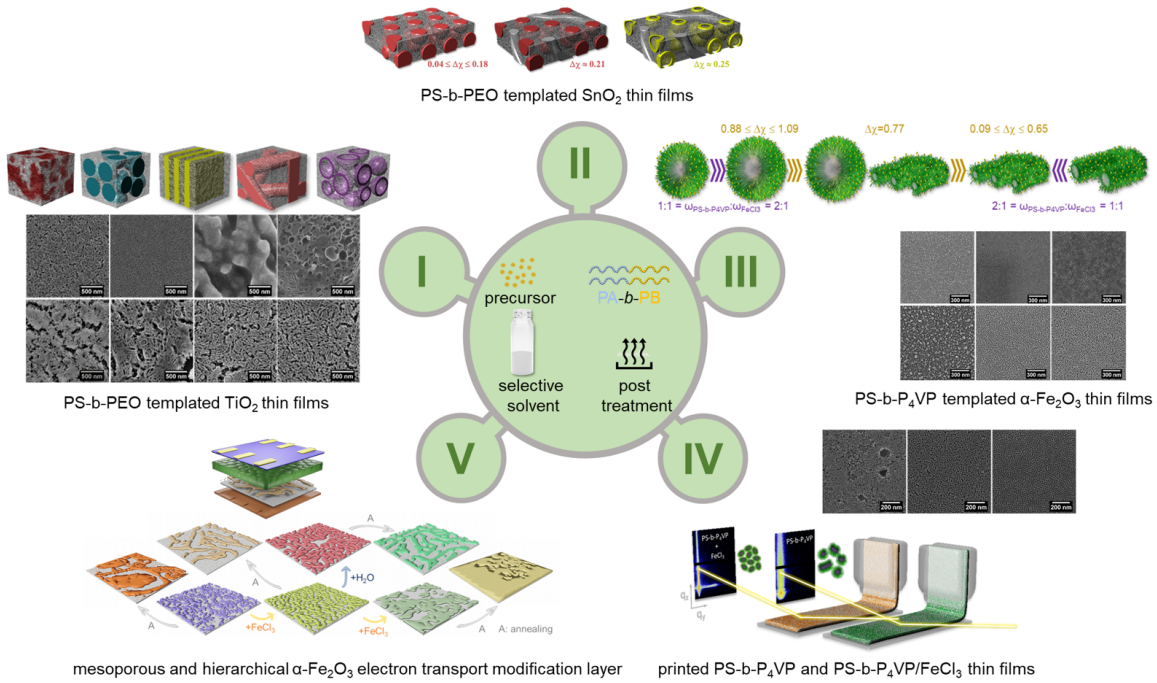

Figure 1.1: *A schematic illustration of the different research projects of the present thesis. (a) to (c) Morphology tailoring of mesoporous TiO_2, SnO_2, and α-Fe_2O_3 thin films. (d) In situ observation of the slot-die printed PS-b-P4VP and PS-b-P4VP/$FeCl_3$ films. (e) application of the different patterned α-Fe_2O_3 thin films on the perovskite solar cells.*

In the first result chapter, the morphology control for the most conventional electron transport material, TiO_2, is discussed. Three kinds of solvent, THF, 1,4-dioxane, toluene/1-butanol mixture, and five HCl concentration gradients are used for tunning the preferential affinity of the cosolvent to the polymer segments. As a consequence, a series of TiO_2 thin films with proper thickness in combination with spherical, lamellar, cylindrical, and vesicle nanostructures are obtained.

Compared with TiO_2, SnO_2 shows more depth conduction-band minimum and optimal energy level alignment, higher bulk electron mobility and conductivity, larger bandgap and higher optical transparency, more outstanding stability under light, heat, and moisture, and less photoactivity. Therefore, in the second result chapter, systematic morphology control for the SnO_2 thin films is carried out by using two kinds of solvent and four HCl

concentration gradients. Series of SnO_2 thin films with proper thickness in combination with spherical, cylindrical, and vesicle nanostructures are acquired.

Hematite (α-Fe_2O_3) is another attractive electron transport material because of its wide abundant, low cost, non-toxic nature and suitable bandgap (2.2 eV). [24] In the third result chapter, the morphology control for the α-Fe_2O_3 thin films is realized by tunning the polymer to $FeCl_3$ precursor ratio and the solvent category. Serious single layer α-Fe_2O_3 thin films with large-area uniform nanoclusters, honeycomb-like structures, and worm-like structures are obtained. Moreover, a series of DMF/1,4-dioxane mixtures with different compositions are confected for tuning the preferential affinity of the cosolvent for tracking the continuous evolution of the nanostructures.

The structure formation mechanism for the above-mentioned metal oxide thin films is discussed based on the preferential affinity theory in detail. Apart from this, the complexation effect between utilized solvent and the inorganic precursors is also taken in to account for the morphology analysis. In addition, the compositional and crystallinity information of the calcined thin films are also examined.

Compared to the lab-scale spin coating, slot-die coating, as an industrial thin film deposition technique, possess more advantages in terms of a precise control of the microstructure and large-scale homogeneity of the deposited thin films. In the fourth result chapter, an in situ observing for the structural evolution of the PS-b-P4VP and PS-b-P4VP/$FeCl_3$ thin films are implemented. Through a careful regulation of the printing parameters and the printing temperature, PS-b-P4VP and PS-b-P4VP/$FeCl_3$ thin films with different homogeneity and domain sizes are obtained. Particularly, the morphology and size of micelles in the solution is detected with DLS measurements. Therefore, an in-depth knowledge between the microstructure of polymer chains in the solution and the final morphology of the deposited thin films is gained. Apart from the in situ observation of the structure evolution, the large area homogeneity of the thin films is also examined via in-situ GISAXS.

In the last result chapter, the influence of the α-Fe_2O_3 morphology on the photovoltaic performance of the perovskite solar cells is verified. Through a facile thermal annealing post treatment, quasi-isoporous and hierarchical α-Fe_2O_3 electron transport modification layer can be obtained, which allows for the association between the optoelectronic property of the devices and the morphology of the electron transport modification layer.

Based on all scientific research mentioned above, a brief conclusion and outlook is summarized at the end of this thesis.

2 Theoretical Background

In this chapter, the theoretical background for all materials, characterizations and devices is discussed. The basic knowledge of polymer physics is given in section 2.1. An overview about perovskite solar cells, Lithium ion battery and photocatalyst are detialed from section 2.5 to section 2.7. Lastly, the basic principles of different x-ray scattering techniques, which were used in the present thesis to probe thin films, are discussed in section 2.8 .

2.1 Polymer

Polymers, also referred as macromolecules, are made up of a large number of one or more types of repeating subunits. The subunit is called monomer, which are connected to each other by covalent bonds. The number of monomeric units is defined as the degree of polymerization. If the molecular mass of the monomers is known, the molecular weight of the polymer M can be calculated. Polymers have a $M > 10$ kg/mol. The molecules with M between 1 kg/mol and 10 kg/mol are called oligomers, whereas micromolecules are referred to the molecules which have a M less than 1 kg/mol.

Rather than a unique degree of polymerization, polymers usually have various chain lengths and thereby various molar masses. Therefore, statistical mean values are required for a full characterization.The number average molar mass M_n, is the ordinary arithmetic average of the molecular masses of the individual polymers.

$$M_n = \frac{\sum_i n_i M_i}{\sum_i n_i} \tag{2.1}$$

where M_i and n_i are the molar mass and chain number of component i, respectively. Instead of using M_n, the average molecular weight M_w is also used to describe the molar mass distribution in terms of weight fractions. M_w is described by

$$M_w = \frac{\sum_i n_i M_i^2}{\sum_i n_i M_i}. \tag{2.2}$$

Normally, M_w is larger than M_n. The ratio of M_w to M_n is called the polydispersity index PDI. PDI is given by

$$PDI = \frac{M_w}{M_n} \tag{2.3}$$

When the PDI value is 1, the polymer shows a uniform molar mass distribution, also known as perfect mododisperse. Molar mass distributions greatly depend on the methods used in the polymerization synthesis, and most of them can be categorized into two classes. The first class of synthesis methods is called step polymerization, where monomers and polymer fragments can be coupled with each other randomly. This way, the molar mass distribution is very broad, which is often described by the Schulz-Zimm distribution. In the second class, known as chain polymerizations, triggers for polymerization can only react with monomers, called reactive centers. Each time a new monomer is linked to reactive centers, the active site is regenerated, thus the polymer grows only at one end. In this way, a much sharper distribution can be obtained, which is in a good agreement with the Poisson-distribution.

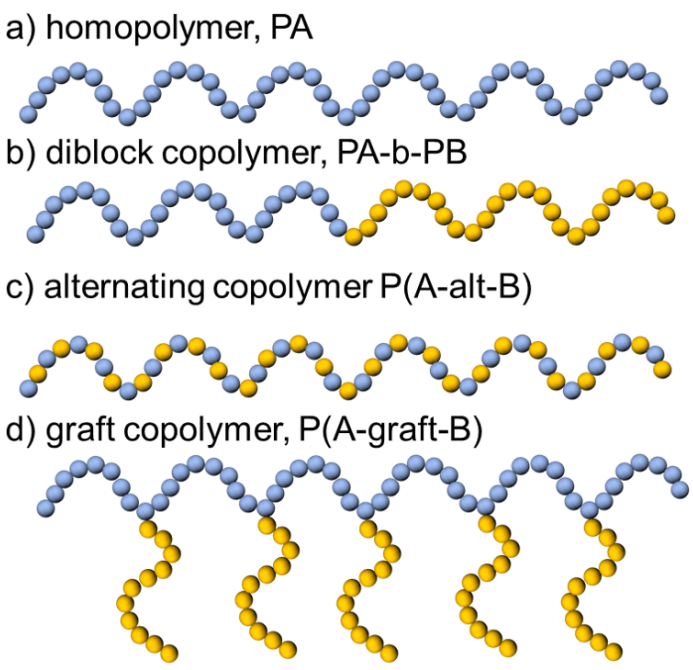

Figure 2.1: *a) Homopolymer, b) diblock copolymer, c) alternating copolymer and d) graft copolymer.*

Various polymer structures can be formed depending on the sequence and the type of monomers. With respect to polymer shapes, the most simple one is the chain-like

structure. By substituting the hydrogen atoms with additional side groups, more complex polymer structures can be obtained, such as ring-like structures, brush-like geometries, or star-shaped polymers. Moreover, different types of monomers can be linked together to form a polymer. If the polymer consists of only one type of monomer, it is called homopolymer (figure 2.1a). If more than one type of monomers are involved in the polymer formation, the obtained polymer is named as copolymer. It can be divided into several subspecies based on the arrangement of the different monomers, as shown in figure 2.1. A diblock copolymer PA-b-PB can be formed if a homopolymer subunit PA and the other homopolymer subunit PB are linked by covalent bonds. (figure 2.1b). If the polymer consists of alternating monomers A and B, it is called alternating copolymer (figure 2.1c). The so-called graft copolymer describes a special branched copolymer where some small side groups are replaced by long side chains. Additionally, the side chains are structurally different from the back bone. Figure 2.1d shows a schematic sketch of a graft copolymer.

2.2 Diblock copolymer

As shown in figure 2.1b, the diblock copolymer consists of two different homopolymer blocks which are linked together with a covalent bond. The polymer is termed as polyA-block-polyB, short as PA-b-PB. Typically, PA and PB in the diblock copolymer have different degrees of polymerization N_A and N_B, from which the so-called block ratios f_A and f_B can be calculated:

$$f_A = \frac{N_A}{N_A + N_B} \tag{2.4}$$

$$f_B = \frac{N_B}{N_A + N_B} = 1 - f_A \tag{2.5}$$

Recently, block copolymers have received great attention because a microphase separation can occur between two blocks to form periodic nanostructures when PA and PB are incompatible. To minimize the system energy, each homopolymer block of the copolymers tends to aggregate together and thereby domains are formed. Because PA and PB are covalently linked to each other, they cannot demix macroscopically as in polymer blends. The size of the domains is determined by the chain length y of each block.

The interaction parameter χ also known as the Flory-Huggins interaction parameter is an important parameter for diblock copolymers, which describes the interaction between two homopolymers PA and PB [25].

$$\chi = \chi_S + \frac{\chi_H}{T} \tag{2.6}$$

where χ_S and χ_H are the entropic and enthalpic contribution, respectively. Normally, an intermixed phase of the two blocks can be formed when the value of χ is sufficient small. Some polymers, for example, can be dissolved in solvents at elevated temperatures rather than room temperature. The reason is that the χ_H decreases with increasing temperature. The degree of microphase separation in a diblock copolymer greatly depends on the factor χN. For instance, in case of a symmetric diblock copolymer the critical value of χN is about 10.5. When χN is smaller than the critical value, an intermixed phase is built. Upon increasing the χN value, compatibility between the two blocks decreases, which leads to a composition fluctuation in the homogeneous melt. When χN reaches the critical value, a so-called weak segregation limit (WSL) is observed. With continuously increasing the χN value, the repulsion between the two blocks enhances and a strong segregation limit (SSL) is reached in the system. Upon this point, a sharp interface between the blocks can be observed.

For a symmetric diblock copolymer ($f_A = 0.5$), microphase separation typically gives periodic lamellar nanostructures. Moreover, various ordered nanostructures can be obtained by varying the value of f_A. In figure 2.2 the possible morphologies for a diblock copolymer PA-b-PB are depicted in a phase diagram. By changing f_A and χN, the structures which form during the phase separation can be tuned. The white region in figure 2.2 indicates the disordered state, in which the diblock copolymer is a homogeneous melt without ordered nanostructures. However, typically asymmetric phase diagrams are reported in literature due to the chemical differences between two blocks A and B [27,28]. Moreover, other factors have an influence such as different conformation of polymer blocks or some specific features of the blocks like crystallization. In addition, confinement effects have a strong impact on the phase behavior. For example, in case of a thin film of a diblock copolymer, interfacial interactions might result in different morphologies than those defined in figure 2.2.

2.3 Flory–Huggins solution theory

Flory–Huggins solution theory is a lattice model of the thermodynamics of polymer solutions which takes account of the great dissimilarity in molecular sizes in adapting the usual expression for the entropy of mixing. The result is an equation for the Gibbs free energy change for mixing a polymer with a solvent.

The thermodynamic equation for the Gibbs energy change accompanying mixing at constant temperature and pressure is

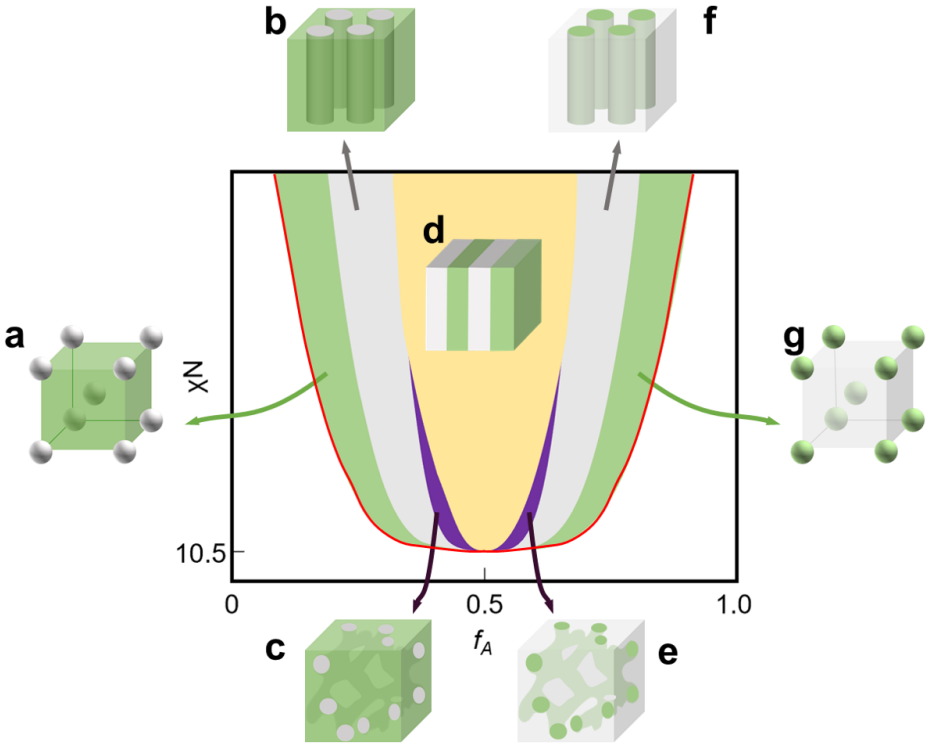

Figure 2.2: *Typical phase diagram of a diblock copolymer PA-b-PB. With increasing block ratio f_A, the A domains inside the B matrices undergoes a morphological transition from (1) spheres via (2) hexagonal cylinders to (3) gyroid. When $f_A = 0.5$, (4) a lamellar nanostructure is achieved. For $f_A > 0.5$, the structure inverts to the scheme that B domains are incorporated in the A matrices and undergoes the same transition with: (5) gyroid, (6) hexagonal cylinders and (7) spheres. The red line indicates the order-disorder transition (ODT) below which the diblock copolymer is a homogeneous melt without ordered nanostructures. [26]*

$$\Delta G_m = \Delta H_m - T\Delta S_m \tag{2.7}$$

Δ is the value of a variable for a solution or mixture minus the values for the pure components considered separately. The objective is to find explicit formulas for ΔH_m and ΔS_m, the enthalpy and entropy increments associated with the mixing process.

The Gibbs energy change obtained by Flory and Huggins is

$$\Delta G_m = RT[\, n_1 \ln \phi_1 + n_2 \ln \phi_2 + n_1 \phi_2 \chi_{12} \,] \tag{2.8}$$

The right-hand side is a function of the number of moles n_1 and volume fraction ϕ_1 of solvent (component 1), the number of moles n_2 and volume fraction ϕ_2 of polymer (component 2), with the introduction of a parameter χ to take account of the energy of interdispersing polymer and solvent molecules. R is the gas constant and T is the absolute temperature. The volume fraction is analogous to the mole fraction, but is weighted to take account of the relative sizes of the molecules. For a small solute, the mole fractions would appear instead, and this modification is the innovation due to Flory and Huggins. In the most general case the mixing parameter, χ, is a free energy parameter, thus including an entropic component. The value of the interaction parameter can be estimated from the Hildebrand solubility parameters δ_a and δ_b

$$\chi_{12} = V_{seg}(\delta_a - \delta_b)^2/RT \tag{2.9}$$

where V_{seg} is the actual volume of a polymer segment.

Polymers can separate out from the solvent, and do so in a characteristic way. The Flory-Huggins free energy per unit volume, for a polymer with N monomers, can be written in a simple dimensionless form

$$f = \frac{\phi}{N}\ln\phi + (1-\phi)\ln(1-\phi) + \chi\phi(1-\phi) \tag{2.10}$$

ϕ is the volume fraction of monomers, and $N \gg 1$. The osmotic pressure is

$$\Pi = \phi/N - \ln(1-\phi) - \phi - \chi\phi^2 \tag{2.11}$$

The polymer solution is stable with respect to small fluctuations when the second derivative of this free energy is positive. This second derivative is

$$f'' = \frac{1}{N\phi} + \frac{1}{1-\phi} - 2\chi \tag{2.12}$$

and the solution first becomes unstable when this and the third derivative

$$f''' = -1/(N\phi^2) + 1/(1-\phi)^2 \tag{2.13}$$

are both equal to zero. A little algebra then shows that the polymer solution first becomes unstable at a critical point at

$\chi_{CP} \simeq 1/2 + N^{-1/2} + \cdots$

This means that for all values of $0 < \chi \lesssim 1/2$ the monomer-solvent effective interaction is weakly repulsive, but this is too weak to cause liquid/liquid separation. However, when $\chi > 1/2$, there is separation into two coexisting phases, one richer in polymer but poorer in solvent, than the other.

2.4 Synthesis of mesoporous metal oxide thin films with block copolymer

Nanostructured metal oxide thin films show great potential in multiple applications. Such as in photovoltaics, lithium ion batteries and photocatalysis, and so on. In these applicatiions, a high surface to volume ratio as well as the morphology of the metal oxide thin films is of great essential to ensure their functionality. Therefore, in this thesis, the synthesis of various mesoporous metal oxide, such as TiO_2, SnO_2 and α-Fe_2O_3 thin films is realized via a so-called block-copolymer-assisted sol-gel method.

Figure 2.3 shows the basic princeple of the mesoporous metal oxide thin film synthesis. Typically, the functional metal oxide precursor can be specifically incorporated in one domain of the phase seperated block copolymer thin film via hydrogen-bond interaction. By means of the strong self-assembly capability of the block copolymer, various patterns made of spherical, cylindrical and saccate micellar structures can be formed in the block copolymer thin films. The crystallization process of the metal oxide as well as the removal of the polymer template occurs in the high temperature calcination process.

2.5 Perovskite solar cell

In a typical perovskite solar device configuration, the active layer is sandwiched between EBL and HBL, with the front transparent electrode at the back and electrode at the top. Figure 2.4a refer to the four main steps involve in the PSCs mechanism. 1) charge generation and diffusion, 2) charge transport, 3) charge extraction, and 4) charge recombination. [29]

One of the most outstanding properties of perovskite material is its high extinction coefficient, which allows a great absorption of incident light. When the perovskite active layer is exposed to the light, it is excited by the photon which has a higher energy. As a concequence, the generation of the so called electron–hole pair is induced. Once the electrons and holes are photo-generated, they are separated by the built-in electric field

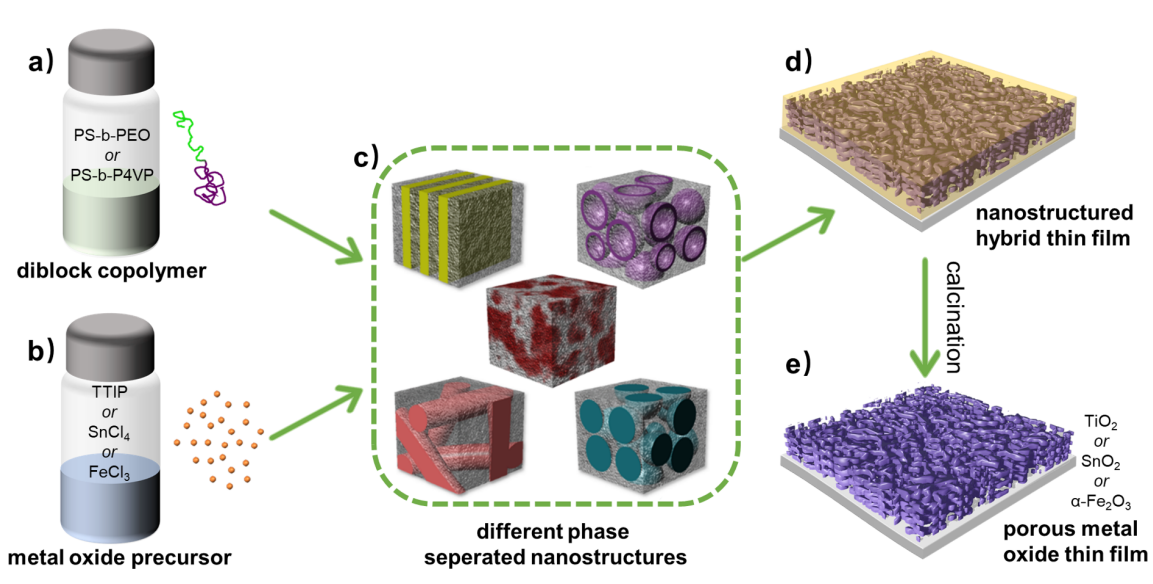

Figure 2.3: *Schematic illustration of the block copolymer templated sol-gel synthesis of various mesoporous metal oxide thin films*

and convey to the contacts electrodes. [30] The transport of the charge carrier in the perovskite active layer is mostly determined by the diffusion length (L)

$$L = \sqrt{\frac{\mu q}{k_b T}\tau} \tag{2.14}$$

where μ is the mobility, q the elementary charge, k_B the Boltz-mann constant, and T the temperature and τ is the time. The charge carriers' transport in PSCs can be facilitated by the excellent charge carrier mobility as well as the long charge carrier diffusion lengths.

The extraction of the charges from the transporting layer to electrodes determines the device photovoltaic parameters. Successful charge carriers' extraction at the interface could minimize the loss of voltage, current, and fill factor (FF). [31] However, many studies revealed the existence of another mechanism, so-called recombination, which induce the charge loss and hinders the device performance (Figure 2.4b). The recombination process is generally classified into radiative recombination and nonradiative recombination (Auger recombination, Shockley-Read-Hall recombination generated by the defects in the bulk perovskite, surface and interface recombination). [32] The nonradiative recombination is the most encountered in PSCs devices recombination process and is easily understood through ideality factors measured from the dark current versus voltage characteristics following the equation:

$$J_{dark}(V) = J_R(V) = J_0 e^{\left(\frac{qV}{n_{ID} k_B T}\right)} \tag{2.15}$$

Where q is the elementary charge, V is the externall applied voltage, k_B is the Boltzmann constant, and T is the temperature. Passivation for perovskite layer and also the charge transport layers is recommended by several researchers as an effective strategy to overcome these recombination issues. [30]

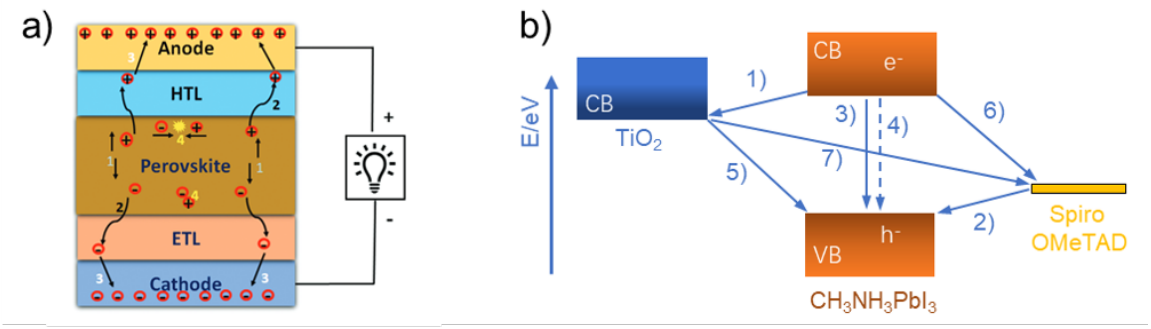

Figure 2.4: *a) Working princeple of the perovskite solar cell:1) Charge generation and diffusion, 2) charge transport, 3) charge extraction and 4) charge recombination. b) Schematic representation of possible recombination and charge transfer mechanism: 1) Electron injection in to the TiO_2, 2) hole injection in to the Spiro-OMeTAD, 3) radiative and 4) non-radiative charge recombination within the peroskite layer. Interfacial recobination with 5)TiO_2 and 6) spiro-OMeTAD. 7) Shunt paths recombination.*

For the architecture of perovskite solar cells, if the light goes through the ETL, then it is known as n-i-p structure. The opposite one should be p-i-n structure. The upper row in Figure 2.5 refer to the energy band diagram of typical n-i-p and p-i-n structured PSCs. Mesoscopic and planar are two basic structures; typically mesoscopic structure has an n–i–p configuration: compact ETL/mesoporous ETL/perovskite/HTL/electrode. The planar type PSCs are further divided into two band configurations: n-i-p planar and p-i-n planar. (the lower row in Figure 2.5) The n-i-p structure usually involves depositing the perovskite material onto transparent substrates covered with a compact TiO_2 layer and an optional mesoporous TiO_2 or Al_2O_3 scaffold layer. The p–i–n structure, which involves depositing the perovskite material onto transparent substrates which are covered with an HTL, such as the poly(3,4-ethylene dioxythiophene):polystyrene sulfonic acid (PEDOT:PSS). So far, PSCs based on both mesoporous and planar structure exhibit high performance and stability. However, the comparison of the advantages of two different strucutres in stability is still under debate.

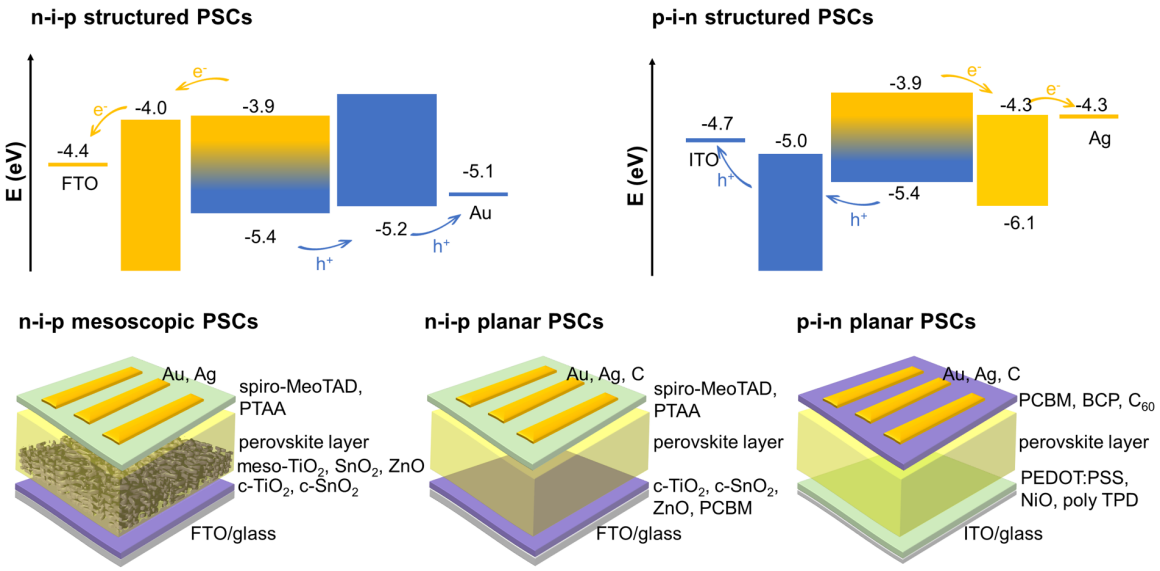

Figure 2.5: *Top: energy band diagram of typical n–i–p and p–i–n structured PSCs; Lower: device structures of n–i–p mesoscopic, n–i–p planar, and p–i–n planar PSCs.*

2.6 Lithium ion battery

Li-ion batteries are electrochemical reversible devices widely acknowledged for their power density, no need of maintenance, reliability and long lifetime. The energy of Li-ion batteries is stored in the electrode materials. The central electrolyte ensures the transfer of ions, while the separator electrically isolates the electrodes and the electrolyte. The electrons are transferred from an electrode to the other through an external electric circuit. [33] While discharging, the lithium ions travel from the anode to the cathode through the electrolyte. While charging the device, lithium ions are released by the cathode and then go back to the anode. Figure 2.6 shows the basic working principle of a Li-ion battery.

The open circuit voltage (OCV) of a Li-ion battery is usually close to 4.2 V. The voltage of a Li-ion battery mainly depends on both the load current and the state of charge (SOC). The voltage range of the cell depends on the chemical reactants used but is commonly from 4.2 V to 3 or 2.5 V. As the reactants are stored in the electrodes, the voltage response strongly depends on the electrochemical reaction kinetics.

2.7 Photocatalyst

Photocatalysis processes involve charge excitation, migration, recombination, separation, and the subsequent photochemical reactions on the surfaces of semiconductors. [34] The

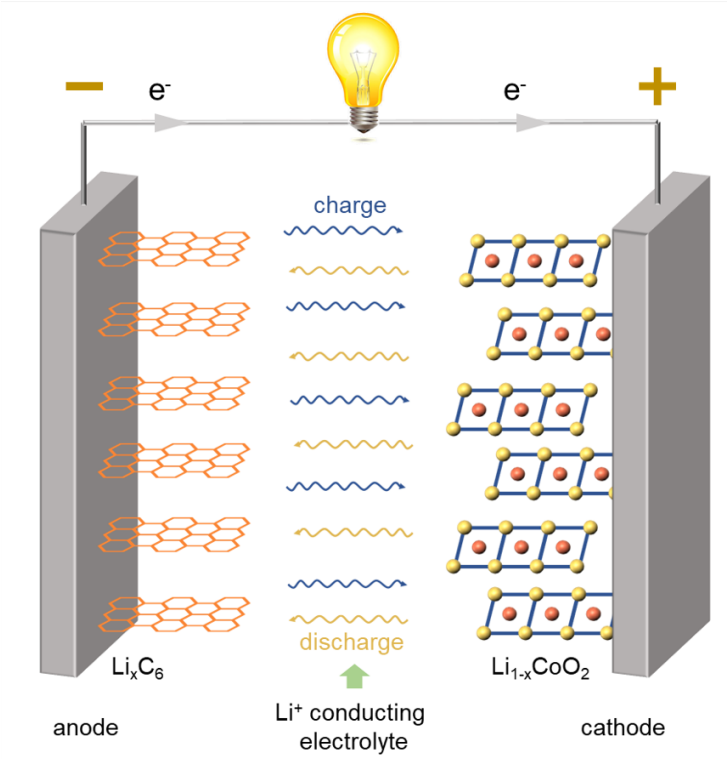

Figure 2.6: *Sketch of a lithium-ion(Li-ion) battery*

above mentioned processes can be summarized in the following (Figure 2.7). Firstly, the photons with sufficient energy are absorbed by a semiconductor, then electron–hole pairs are generated; Secondly, the generated electron–hole pairs are separated into reductive electrons and oxidizing holes; Thirdly, the separated electrons and holes consequently participate in the redox reactions.

It is well known that efficient charge separation and surface catalytic reactions related to charge energy are the key factors for determining the photocatalytic activities of the devices. Typically, the thermodynamic energy of photogenerated electrons is the decisive factor for the ultimate photocatalytic activity. Photocatalytic pollutant degradation is a promising technique for eliminating the low-concentration, but highly toxic, organic pollutants in water. [35]

Therefore, the photogenerated electrons must possess sufficient thermodynamic energy to activate O_2 for an efficient pollutant degradation. However, the O_2 molecule has a triplet ground state with two spin-parallel electrons, indicating that one of the two electrons would be spin-reversed during the O_2 reduction half-reaction, which is a spin-forbidden and kinetically unfavorable process. [36] Therefore, the activation of O_2 by the photogenerated electrons is the rate-determining step during pollutant degradation.

Moreover, photocatalytic H_2 production and CO_2 reduction are important applications of photocatalysis. In these reactions, the separated photogenerated electrons reduce H_2O and CO_2 to produce H_2, CO, CH_4. The thermodynamic energy and reduction capability of photogenerated electrons has a considerable effect on the activities of photocatalytic H_2 production and CO_2 reduction. [37] In order to effectively initiate the photocatalytic reaction of H_2 production and CO_2 reduction, photogenerated electrons should have sufficient reductive energy close to the thermodynamic reduction potential. Photocatalysts with more negative CB levels can produce photogenerated electrons with strong reduction abilities. Above all, it is obvious that sufficient thermodynamic energy of electrons is the essential condition for efficient photocatalytic reactions. Hence, it is meaningful to tune the thermodynamically electronic energy for improve the activities of photocatalytic pollutant degradation, H_2 production, and CO_2 reduction.

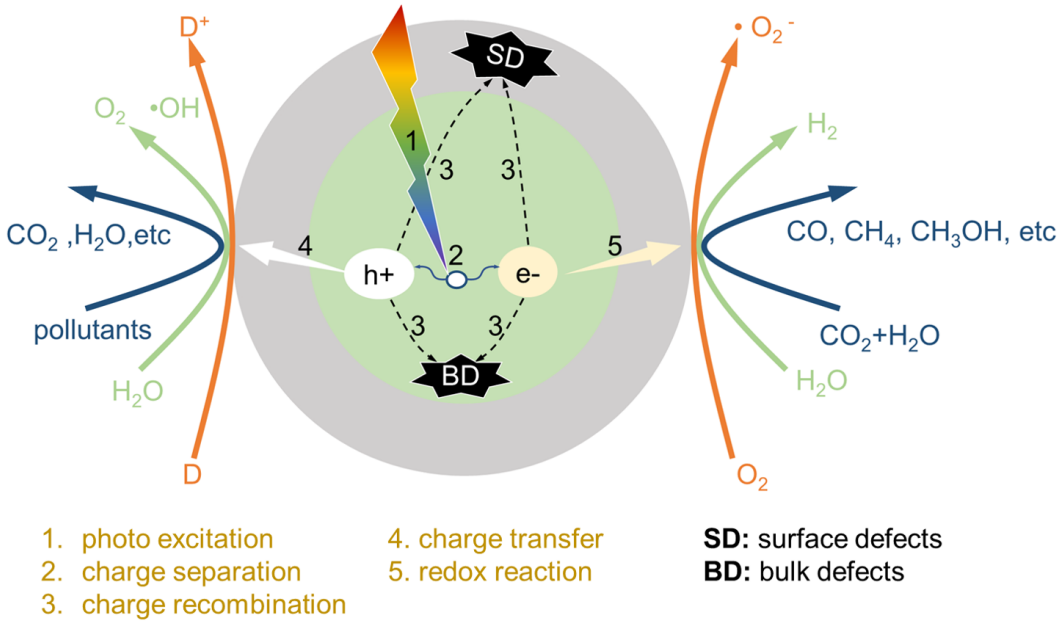

Figure 2.7: *Schematic of the main processes in a photocatalytic reaction.*

2.8 Scattering methods

Some real space measurements can only provide alone structure information on the nanoscale. In contrast to these techniques, scattering methods using x-rays are able to probe the film volume over a macroscopic sample area and structural information about the inner film morphology can be obtained with a high statistical relevance. The basic principles of scattering techniques are discussed in section 2.8.1, followed by a description

about x-ray diffraction in section 2.8.2 and grazing incidence small angle x-ray scattering (GISAXS) in section 2.8.3. For probing crystalline order of thin films, grazing incidence wide angle x-ray scattering (GIWAXS) is used, which is discussed in section 2.8.4.

2.8.1 Principles

X-ray scattering techniques are based on the interaction of an electromagnetic wave with electrons in the sample. The electric field vector $\vec{E}(\vec{r})$ as a function of the position vector $\vec{r}$ with r = (x,y,z) is given by

$$\vec{E}(\vec{r}) = \vec{E_0} exp\left(i\vec{k_i} \cdot \vec{r}\right) \tag{2.16}$$

where $\vec{E_0}$ reflects the polarization dependent amplitude and $\vec{k_i}$ is the wave vector. The modulus of the wave vector $\left|\vec{k_i}\right|$ is known as the wave number k, which is described by the wavelength λ as

$$\left|\vec{k_i}\right| = k = 2\pi/\lambda \tag{2.17}$$

When electromagnetic wave travels through a medium with a refractive index of $n(\vec{r})$, the propagation follows the Helmholtz equation [38].

$$\nabla^2 \vec{E}(\vec{r}) + k^2 n^2(\vec{r}) E(\vec{r}) = 0 \tag{2.18}$$

where $\vec{r}$ is the position of the electromagnetic wave and $k = 2\pi/\lambda$ is the modulus of the wave vector $\vec{k}$. The refractive index for x-rays in the investigated material can be described by

$$n(\vec{r}) = 1 - \delta(\vec{r}) + i\beta(\vec{r}) \tag{2.19}$$

based on the dispersion part δ and the absorption part β. Both δ and β can be written as a function of the wavelength λ of x-rays

$$\delta = \rho\frac{\lambda^2}{2\pi} = \rho_e r_e \frac{\lambda^2}{2\pi} \tag{2.20}$$

$$\beta = \mu\frac{\lambda}{4\pi} \tag{2.21}$$

where ρ is the scattering length density (SLD) of the homogeneous medium, which relies on the classical electron radius r_e (2.814×10^{-5} Å) and the electron density of the probed sample ρ_e. μ describes the linear absorption coefficient. Typically, δ ranges from 10^{-5} to 10^{-6} and β is of the order of 10^{-7} for x-rays. Therefore, the refractive index of x-rays is slightly smaller than 1. Different materials usually have different SLDs, which leads to the scattering contrast between different materials.

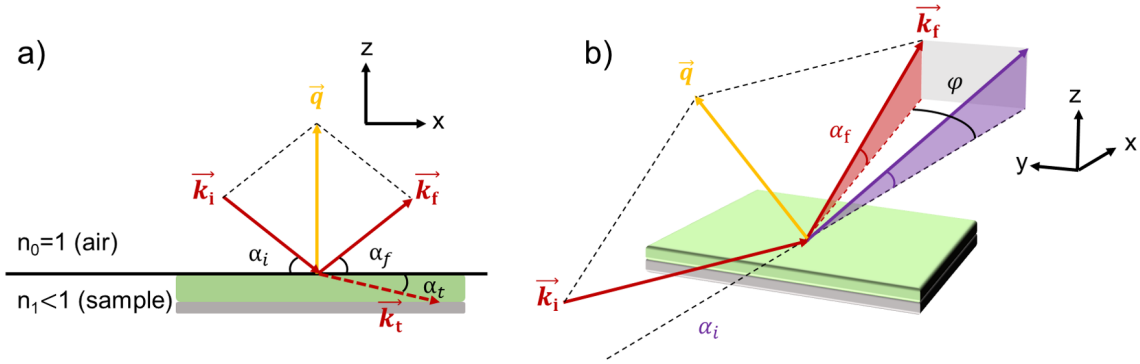

Figure 2.8: *Schematic geometry of a) specular scattering and b) diffuse scattering with basic definitions of directions and angles.*

For increasing the scattering signal, a grazing incidence geometry is used. Specular and diffuse scattering are schematically illustrated in figure 2.8a and 2.8b. For specular scattering, the incident and specular vector are represented with ($\vec{k_i}$) and ($\vec{k_f}$) and the incident angle α_i is equal to the exit angle α_f. (figure 2.8a). The scattering vector $\vec{q}$ is determined by the momentum transfer from the incident beam to the exi t beam:

$$\vec{q} = \vec{k_f} - \vec{k_i} \tag{2.22}$$

Under diffuse conditions, the scattered beam is presented in the xy-plane with an scattering angle of ψ (figure 2.8b).

At the interface between air and a medium with a refractive index of n, the diffraction of the x-rays beam follows Snell's law,

$$n_0 \cos(\alpha_i) = n \cos(\alpha_t) \tag{2.23}$$

where n_0 is 1 for air and α_t is the exit angle of the transmitted beam $\vec{k_t}$. When the α_t is equal to 0, the incident angle is called the critical angle of the material.

If the incident angle is smaller than the criticle angle of the material, total external reflection occurs. However, in this case, the X-ray can penetrate the sample to a certain depth, and their intensity decreases exponentially with the penetrating distance. The depth where the intensity of the X-ray is decreases to 1/e of its original intensity is called the scattering depth. When the incident angle is lager than the criticle angle of the material, the x-ray are able to penetrate the whole thin films and informations about the whole volume of the sample can be detected.

2.8.2 X-ray diffraction

X-ray diffraction can be used for characterizing the crystal structure of the samples. During the XRD measurement, the ordered arrangment of the atoms in the crystals acts as periodic gratings for x-rays and the electrons around the atoms are the scatterers for x-rays. The electrons can produce spherical waves after the interaction with x-rays. Each crystal structure has its own lattice parameters, which therefore corresponds to a unique scattering pattern.

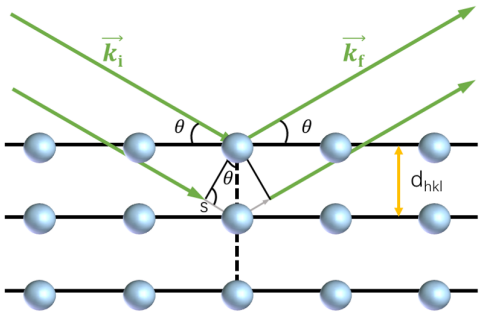

Figure 2.9: *Schematic illustration of the Bragg equation. The incoming beams (black lines) interact with the scatterers (blue circles) which are located in regular lattice planes. The distance between these planes is described by the lattice spacing d. The x-ray travels a longer distance when it interacts with the lower lattice plane. The increased path lengths are marked by grey lines.*

Figure 2.9 shows the diffraction of the x-ray between two neighboring lattice planes. The interference of the scattered x-ray gives rise to different intensities. When the path difference is an integer multiple of the x-ray wavelength λ, constructive interference will occur. In this situation, the Bragg equation is satisfied.

$$2d_{hkl}\sin(\theta) = n\lambda \tag{2.24}$$

where d_{hkl} is the lattice spacing of a crystal and θ is the incident angle. When the wavelength of the X-ray is a fixed value, the term $\sin(\theta)$ in the Bragg equation is inverse proportional to the lattice spacing. Typically, the angle between the incoming and the scattered x-ray beam 2θ, is used as Bragg reflex. Based on the relative position of the resulting reflexes, the crystal structure of the material can be determined. The crystallite size D_{hkl} along $<hkl>$ crystal direction can be estimated from the width of the Bragg reflex:

$$D_{hkl} = \frac{K\lambda}{\Delta(2\theta)\cos(\theta_0)} \tag{2.25}$$

where K is the Scherrer form factor, which typically has a value of 0.9. $\Delta(2\theta)$ is the full width half maximum (FWHM) of the Bragg peak at 2θ. The position of the Bragg reflexes can be converted to $\vec{q}$, then the Scherrer equation is writen as:

$$D_{hkl} = \frac{2\pi K}{\Delta q_{hkl}} \tag{2.26}$$

where Δq_{hkl} is the integral line width, which can be calculated by the FWHM of the Bragg peak.

2.8.3 Grazing incidence small angle x-ray scattering

Due to the very shallow incidence angle used in the measurment, both the surface and inner morphologies of the thin films can be probed via grazing incidence small angle x-ray scattering (GISAXS) . Typically, the incident angle is far less than 1° and the probed sample structure are ranging from nanometer to micrometer. Based on the beam size and the incident angle, the length of the footprint can be calculated:

$$l = \frac{h}{tan\,(\alpha_i)} \tag{2.27}$$

where h is the size of the incident beam along with the sample normal. α_i is the incident beam. In the present thesis, only the elastic scattering phenomena is considered. Under this condition, the scattering vector $\vec{q}$ can be writte as the following equation: [39]

$$\vec{q} = \frac{2\pi}{\lambda}\begin{pmatrix} q_x \\ q_y \\ q_z \end{pmatrix} = \frac{2\pi}{\lambda}\begin{pmatrix} \cos(\alpha_f)\cos(\psi) - \cos(\alpha_i) \\ \cos(\alpha_f)\sin(\psi) \\ \sin(\alpha_f) + \sin(\alpha_i) \end{pmatrix}. \tag{2.28}$$

The lateral structure of the film can be deterrmined by the lateral component (q_x, q_y). q_x can be neglected as the very small α_i and α_f. In grazing incidence mode, both the reflection and the refraction occur at the sample and substrate interface. In this situation, the DWBA method is widely used to describe the diffuse scattering. Four different scattering events used to be considered for the scattering object on the substrate, which are schematically displayed in figure 2.10. [40] The first event is where the X-ray beam is directly scattered by the object. The second event occurs when the beam is firsly reflected on the substrate and then scattered by the object. For the third event, the beam is firstly scattered by the object and then reflected on the substrate. The last event describes a reflected-scattered-reflected beam. In the DWBA, the differential cross-section of the scatterring can be denoted as the following equation:

$$\frac{d\sigma}{d\Omega} = \frac{S\pi^2}{\lambda^4}(1-n^2)^2 \mid T_i \mid^2 \mid T_f \mid^2 P_{diff}(\vec{q}) \propto P_{diff}(\vec{q}) \tag{2.29}$$

with S as the illuminated area and $P_{diff}(\vec{q})$ as the diffuse scattering factor, T_i and T_f are the Fresnel transmission functions of the incident and scattered beams, respectively,

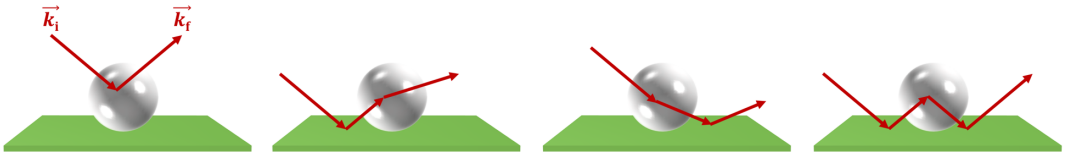

Figure 2.10: *Schematic of four different scattering events in the framework of DWBA. The X-ray beam is (a) scattered directly without reflection, (b) reflected first before scattering,(c) scattered first before reflection and (d) reflected before and after scattering.*

The Fresnel transmission functions have a maximum at the critical angle of the probed material, which lead to a pronounced scattering intensity. This peak is called Yoneda peak. [41] Since the critical angle depends on the scattering length density (SLD), the Yodeda peak is a material-sensitive scattering signal.

GISAXS measurements only record the intensities of the diffuse scattering. In order to extract structural information on the probed material, the intensity signal needs to be modeled. For a system with N identical objects in a geometrical arrangement, the diffuse scattering factor $P_{diff}(\vec{q})$ (recorded intensity) can be determined as

$$P_{diff}(\vec{q}) \propto N|F(\vec{q})|^2 S(\vec{q}) \tag{2.30}$$

where $F(\vec{q})$ describes the scattering objects with a certain shape and size, and $S(\vec{q})$ is the structure factor, which is related to the spatial arrangement of the scattering objects.

For the quantified analysis, effective interface approximation (EIA) and local monodisperse approximation (LMA) is applied in the present thesis. [40] For the effective interface approximation, the scattered pattern is only analyzed as a horizontal line cut at a constant q_z value. The LMA is based on the assumption that in local domains, which have the size of the coherence length of the X-ray beam, only objects of one type are found. The spherical or cylindrical form factors with a Gaussian size distribution are assumed for the data modeling.

2.8.4 Grazing incidence wide angle x-ray scattering

Grazing incidence wide angle x-ray scattering (GIWAXS) can be used for probing atomic and molecular distances in the crystals. It is noteworthy that, the setup of GIWAXS measurements is simultaneous to GISAXS, and only change from GISAXS to GIWAXS is realized by decreasing the sample-detector distance from several meters to several centimeters.

This change allows for recording the scattered x-ray beams under larger exit angles, which is able to provide structural information in the sub-nanometer scale. In this situation, the single atoms are the scatterers for the x-ray. When $\{hkl\}$ lattice planes fulfill Bragg's law at a certain angle, the surface of the Ewald sphere intersects with certain reciprocal lattice points and constructive interference occurs. Figure 2.11 shows the illustration of the Ewald sphere in the reciprocal space.

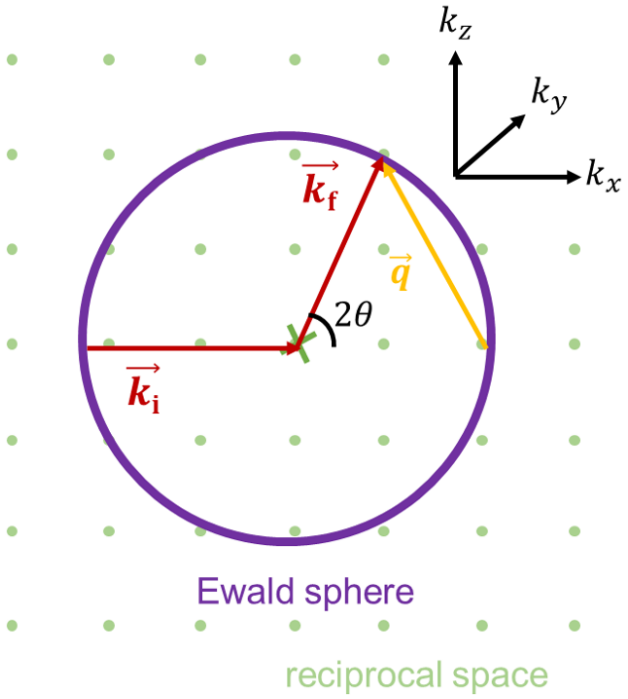

Figure 2.11: *Illustration of the Ewald sphere in reciprocal space. The Bragg's law is fulfilled when a reciprocal lattice point (green circles) touches the Ewald sphere (purple).*

Due to the short sample to deteter distance, the q_x contribution cannot be neglected in the 2D GIWAXS data and the contribution of q_x increases with α_f. To extract structure information, the raw 2D GIWAXS data is supposed to be reconstructed into the natural reciprocal space coordinates [42]. Then, q_x and q_y cannot be decoupled, the x axis in the GIWAXS data is q_r:

$$q_r = \sqrt{{q_x}^2 + {q_y}^2} \tag{2.31}$$

The transformation of the 2D GIWAXS data results in a missing wedge as $q_r = 0$ is not accessible. Typically, the GIWAXS data can be represented by plotting q_z versus q_r or by plotting $q = |\vec{q}|$ versus the azimuthal angle χ. For the crystal orientation analysis, we can perform azimuthal cuts, also called tube cuts, along the q position of the specific (hkl) plane, or sector integrals in the vertical direction (e.g. $-15° \leq \chi \leq 15°$) and the horizontal direction (e.g. $75° \leq \chi \leq 85°$).

From the 2D GIWAXS data, information on the preferred orientation of the crystals can be extracted. Figure 2.12 depict four basic correlation between the crystal orientation and scattering signals in the GIWAXS pattern.

For the ideal face-on lamellar stacking, the Bragg peaks with a distance of $2\pi/d$ will appear along the q_z axis (figure 2.12a). If there are only face-on and edge-on lamellar stacking within the thin film, scattering signal along the q_z and the q_r axis will be observed (figure 2.12b). Slight distortion of the face-on lamellar stacking will lead to a broadening of the Bragg peaks (figure 2.12c). For the full rotational disordered stacking, Debye-Scherrer rings are observed in the GIWAXS pattern (figure 2.12d).

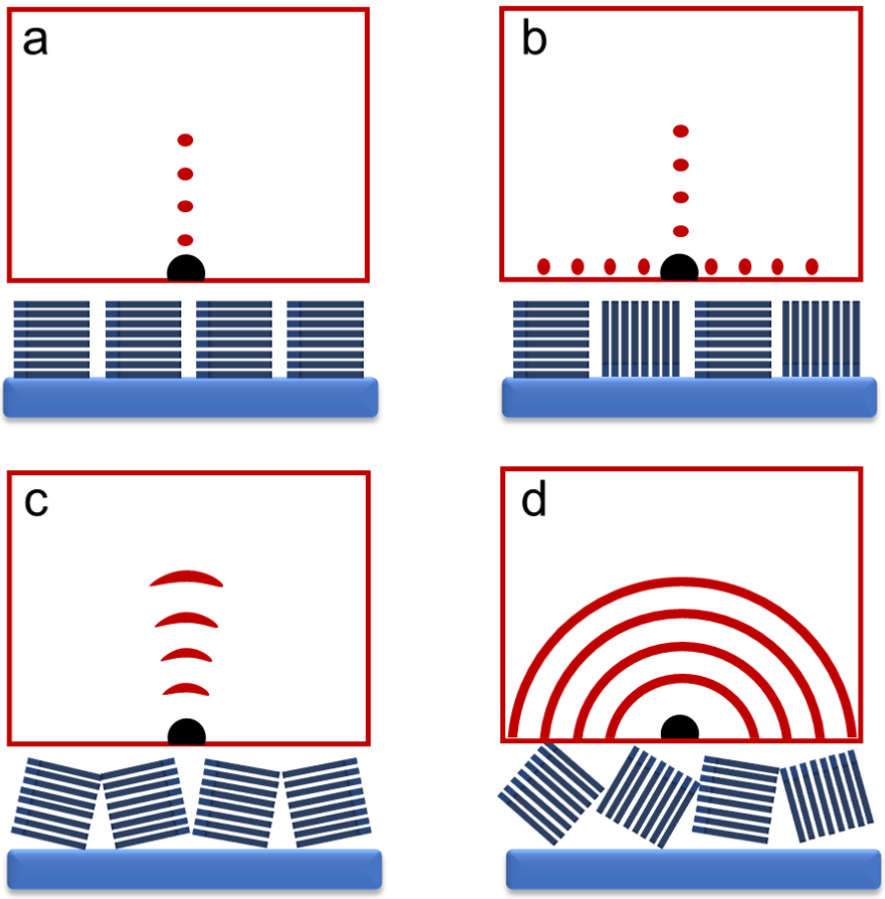

Figure 2.12: *Sketch of film crystallinity and corresponding 2D GIWAXS data in case of (a) vertical lamellar stacking, (b) vertical and horizontal lamellar stacking, (c) textured lamellar stacking parallel to the substrate, (d) disordered lamellar stacking Figure inspired by the phD thesis of Lin Song, E13, physics department, TUM.*

3 Characterization methods

In the present chapter, various techniques utilized for characterizing the mesoporous metal oxide thin films, uncalcined hybrid thin films and solar cells are presented. Different real- and reciprocal-space imaging methods are used to investigate the film form and structure. Various spectroscopic and electronic characterizations are applied to probe the sample functionality. All the characterization methods are introduced in terms of the instrument specifications as well as the corresponding working principles.

3.1 Height profilometry

Profilometry is a widely used method to measure height differences on samples. In the present thesis, a DektakXT®stylus profiler (Bruker corp.) is used for measuring the thickness of the thin films. The working principle of the profilometry is schematically illustrated in figure3.1. The sample is placed on a movable sample stage. Then the diamond-tipped stylus is brought down and in contact with the sample surface by applying a constant force over the sample. The stylus scans the sample surface by moving the stage back and forth. The height changes on the sample surface are measured by the variation in the vertical displacement, which is converted to a digital signal by a linear variable differential transformer. The procedure is carried out several times over multiple scratches to exclude possible local differences in film thickness. Data acquisition and analysis are performed with the software Vision64 by Bruker. All the measurements are carried out using a contact force of 1 mN, a scan speed of 40 μm s^{-}1, and a scan distance of 3 mm.

3.2 Dynamic light scattering

Dynamic light scattering is a well-established, technique for particle size analysis in the nanometer range. DLS provides information on the mean particle size as well as on particle size distribution. It covers a broad size range from the lower nanometer range up to several micrometers. Only low sample volumes are required and the sample can be re-used after

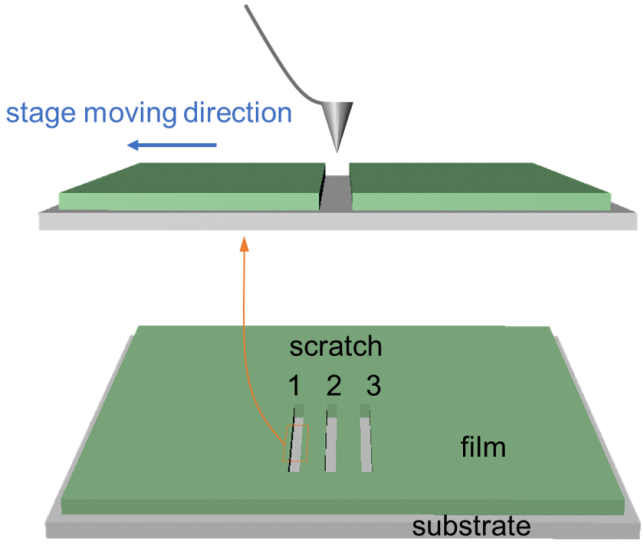

Figure 3.1: *Sketch of the height profilometer measuring a sample. The sample is loaded on on a movable stage. The stylus contacts to the sample surface with a certain force. The scan on sample surface is achieved by a movable sample stage.*

the measurement. Small particles in suspension undergo random thermal motion known as Brownian motion. This random motion is modeled by the Stokes-Einstein equation 3.2

$$D_h = \frac{k_B T}{3\pi\eta D_t} \tag{3.1}$$

D_h is the translational diffusion coefficient

D_t is the hydrodynamic diameter

k_B is Boltzmann constant

T is thermodynamic temperature

η is dynamic viscosity

The calculations are handled by instrument software and the particle size determined by dynamic light scattering is the hydrodynamic size. For the polymers in the solution, the hydrodynamic radius is not the same as the radius of gyration. Hydrodynamic sizes are more easily measured than radii of gyration and can be measured over a wider range of sizes. The conversion from hydrodynamic radius to radius of gyration is a function of chain architecture (including questions of random coil vs. hard sphere, globular, dendrimer, chain stiffness, and degree of branching). A top view of the optical setup for DLS is shown in figure 3.2

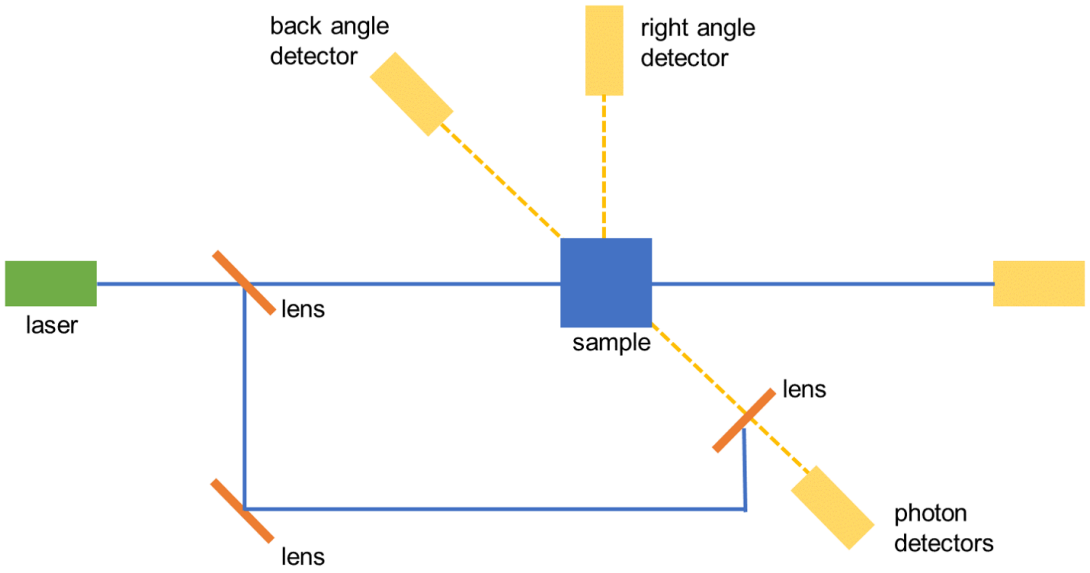

Figure 3.2: *A top view of the optical setup for dynamic light scattering*

3.3 Scanning electron microscopy

Scanning electron microscopy (SEM) is used to probe the surface morphology of titania and titania/polymer films on the nanometer scale. Compared to optical microscopy, SEM uses electrons as the illumination source. As the wavelength of electrons is much shorter than that of visible light, SEM possesses a very high resolution which allows sample being probed in the nanometer range. The wavelength of an electron follows the de Broglie relation:

$$\lambda_e = \frac{h}{p_e\,(U_b)} \tag{3.2}$$

where λ_e is the wavelength of the electron, h is the Planck's constant and $p_e(U_B)$ is the momentum of the electron depending on the acceleration voltage U_B. All SEM measurements in the present thesis are performed with a FESEM Gemini NVision 40 instrument (Carl Zeiss), which is controlled by the software SmartSEM. The working princeple of the SEM instrument is shown in figure 3.3. The electrons are generated from a field emission gun using a tungsten filament. Subsequently, the electrons are guided to form an electron beam through magnetic and electrostatic lenses, which focus the electron beam. Then the electron beam is accelerated by a voltage on the order of several kV. The resulting beam scans the sample surface in a line-wise manner and it causes three main types of emission: Secondary electrons with small escape depth due to low energy, backscattered electrons with large escape depth due to high energy and characteristic X-rays with the highest escape depth. Position of detector in combination with a de-acceleration bias voltage then

allows to detect electrons of a certain energy. The image acquisition in the present thesis is performed through the detection of the secondary, low-energy electrons. The intensity of detected secondary electrons is plotted against the scanning position. Thereby, a grey scale image can be reconstructed. Among other parameters, the brightness value depends on the specific material, height and geometry of the scanned area. Edges typically appear especially bright. As these influences on brightness cannot easily be decoupled, SEM only gives a qualitative impression of the topography. The intensity of the secondary electrons is mainly correlated to the surface morphology, beam size and the incident angle between beam and sample surface. During scanning, the beam size and incident angle are fixed, thus the obtained grey scaled image with different brightness values is a picture of the sample surface. It is important to note that the intensity of secondary electrons strongly depends on the surface morphology. Therefore, it's unreasonable to use SEM measurement to parametrize height information. For example, two nano-objects with different shapes will give different intensity of secondary electrons even if they are at the same height.

A system vacuum of 2×10^{-6} mbar is necessary for the measurements. The acceleration voltage of the electron beam is set in 5 kV, the working distance (distance between the gun and the sample surface) is adjusted to 3.5 mm. The aperture size of the primary electron gun is 10 μm. Different measuring parameters are aiming to obtain clear images with high resolution. It is worthwhile to note that a lower acceleration voltage is used to measure the organic/inorganic thin films with poor electrical conductivity. The original SEM images are post-treated with the software ImageJ v1.43u to obtain a better image quality.

In order to do cross sectional measurements, a line-scratch is firstly made on the backside of the sample with a diamond cutter. During the measurement, the sample stage is tilted by 45° with respect to the horizon.

3.4 X-ray diffraction

X-ray diffraction (XRD) is a tool used for identifying the crystalline phase, crystal size and the degree of crystallinity. In the present thesis, XRD measurements are performed on a Bruker D8 ADVANCE X-ray diffractometer. In the instrument, a copper anode is used as the source to generate the x-ray beam. The copper anode is operated at 40 kV and 40 mA. The resulting Cu K_α radiation, which has a wavelength of 0.1541 nm, is used for the measurements. The x-ray beam impinges on the sample at an angle θ. Due to the large footprint of the x-ray beam on the sample surface, the size of the sample should

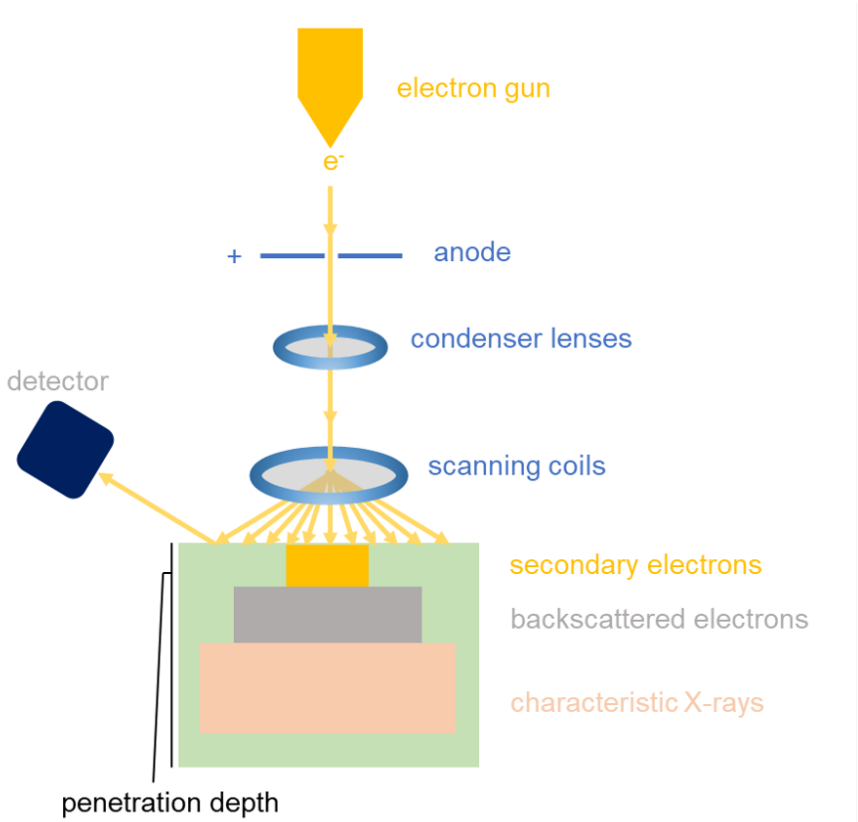

Figure 3.3: *Illustration of the basic principle of SEM, Electrons are emitted from the electron gun and accelerated towards the anode. Electromagnetic condenser lenses and scanning coils are used to shape and focus the electron beam on the sample. Detectable secondary electrons are typically emitted from surface-near regions, while backscattered electrons and characteristic X-ray radiation come from the increased penetration depth.(image inspired by a graph from [43])*

be sufficient large (at least 2.5 × 2.5 cm^2) to ensure the experimental accuracy. The specular x-ray beam is detected by a point detector at the same angle. During the entire measuring process, the angle between the incident and the reflected beam is kept at 2θ as the coupled $\theta/2\theta$ mode is applied. A typical 2θ scan ranging from 20° to 60° is used with a step size of 0.04° for scanning all samples. Each step takes 30 s. Thus, about 8 h is required for the measurement of each sample. The probed samples are deposited on the silicon substrates. To get a good quality of the XRD spectra, slits of 0.6 mm are used to collimate the x-rays after the beam source and before the detector. The instrument is controlled by the software Diffrac.commander, where the measurement protocols are submitted to.

The obtained XRD data is analyzed with software Jade. The extracted full width at half

maximum (FWHM) values are used to calculate crystal sizes via the Scherrer equation. The obtained XRD peaks of the samples are identified by making a comparison with the reference data taken from the International Centre for Diffraction Data (ICDD).

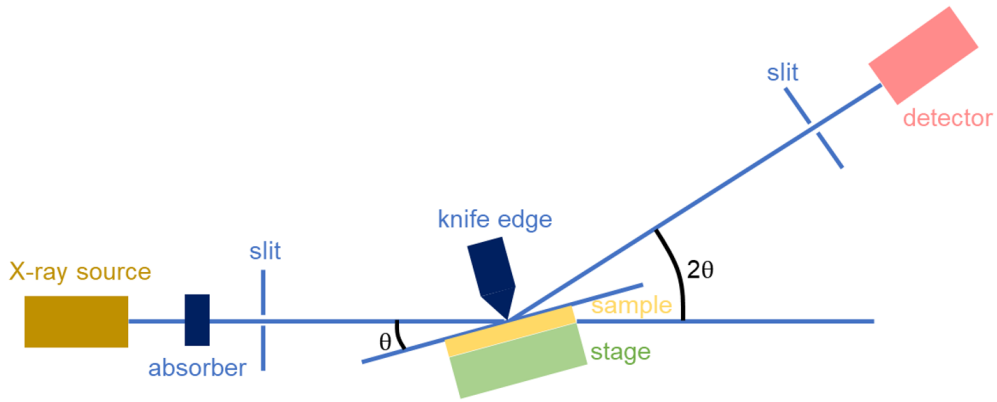

Figure 3.4: *Schematic overview of a typical setup used for X-ray diffraction measurements. The Xray beam is guided through an absorber and slits before impinging at an angle θ on approximately 2 x 2 cm^2-sized samples. The angle-dependent diffraction pattern in a coupled θ-2θ configuration is measured via a point detector.*

3.5 Grazing incidence scattering

In order to probe the inner morphology, grazing incidence scattering (GIS) methods are used. A reflection geometry is employed in GIS measurements instead of transmission geometry, which is schematically shown in figure 3.5. Benifit from the reflection geometry, a large footpint of the X-ray beam on the sample surface is ensured. Therefore, with the aid of the this technique, the structures either on the surface or in the bulk of the thin film can be detected with high statistical relevance. Due to the limited size of the detector, the sample-detector distance (SDD) determines the accessible scattering angles. Hence, various feature sizes of the sample can be detected by varying the SDD. For example, very small distance below 1 nm can be probed by setting a short SDD ($\approx$ 10 cm). This measuring technique is named as grazing incidence wide angle x-ray scattering (GIWAXS). A longer SDD ($\approx$ 2-4 m) usually allows for accessing structural distances ranging from approximately 1 nm up to 1 μm, which is called grazing incidence small angle x-ray scattering (GISAXS). For both measurements, a proper incident angle of the x-ray beam determines the measurements are surface or volume sensitive. To probe the structural information either on the surface or in the volume of the thin films prepared

in the present thesis, all the incident angles for the GIS measurement are higher than the critical angles of the probed materials.

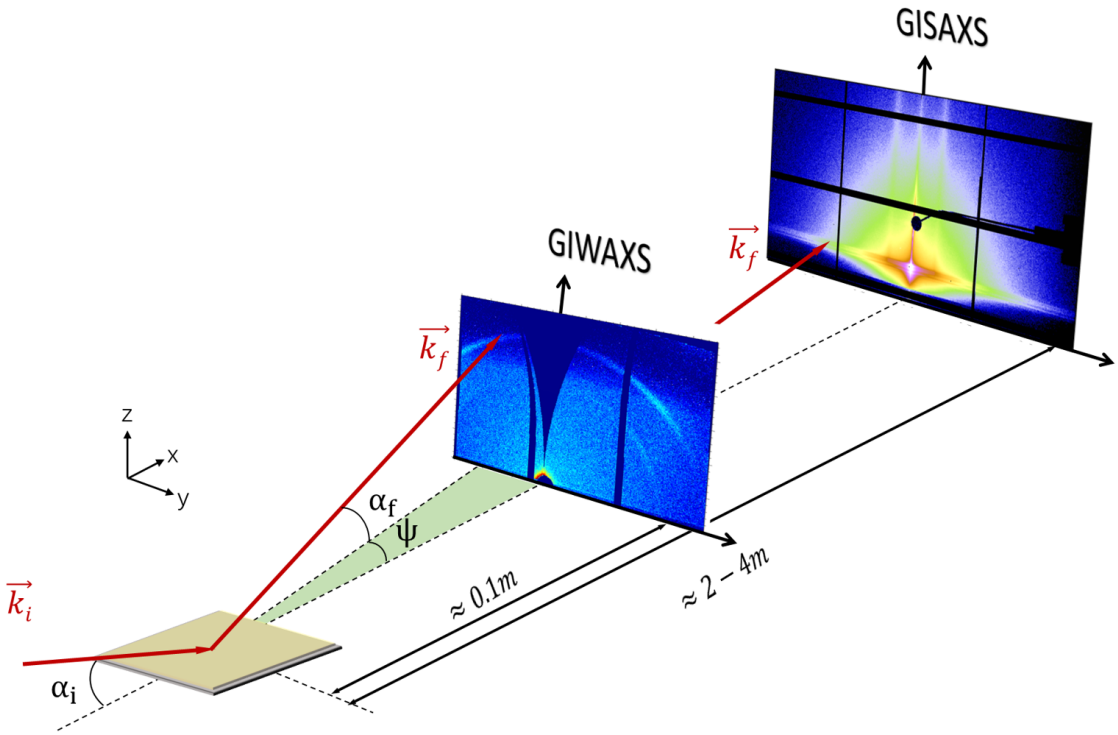

Figure 3.5: *Schematic of grazing incidence X-ray scattering (image inspired by a graph from [44]). The incident beam (red) impinges onto the sample surface under a small angle. The diffusely scattered beam leaves the sample under an exit angle given by a component in vertical (red area) and lateral (green area) direction. The scattering signal is collected by a 2D detector mounted at different SDD. For GISAXS the SDD is usually in the range of meters, whereas GIWAXS is performed at a much shorter SDD in the range of some tens of centimeters*

The GIS measurements were conducted either at Technical University of Munich or at the PETRA III storage ring at DESY (Hamburg, Germany). Due to the long distance between the sample and the detector, a vacuum flight tube is necessary in the x-ray pathway to minimize scattering from air. The SDD value at Technical University of Munich is around 1 m and the SDD values at the P03 beamline is usually located in the range from 3 m to 4 m. Different SDD values meet the demand for different resolvable structural length scales. For the GISAXS measurement excuted at Technical University of Munich, a Pilatus 300K (Dectris) detector with a pixel size of (172 × 172) μm^2 is used to record the scattering signal. For the GISAXS measurement at DESY, a Pilatus 1M (Dectris) detec-

tor with a pixel size of (172 × 172) μm^2 is used to record the scattering signal. Moreover, the Pilatus 1M detector has a readout time of 3.6 ms, which allows kinetic measurements with high temporal resolution. To protect the detector from oversaturation, the direct and specular beams are blocked with beamstops.

For the quantitative analysis, line cuts are made either in the vertical direction or in the horizontal direction of the 2D GISAXS data. The vertical line cuts offer the structure information perpendicular to the substrate, whereas horizontal line cuts reflect the structural information parallel to the substrate. Both vertical and horizontal line cuts are performed on the 2D GISAXS data with the aid of the software DPDAK (Gunthard Benecke, DESY Hamburg&MPIKG Potsdam). Afterwards, the line cuts are fitted with a custom-made program, which models the data in the framework of the distorted wave Born approximation (DWBA) using the local monodisperse approximation (LMA). Within this model, the scattering objects are assumed to have a cylindrical structures with a Gaussian size distribution. The distance between two neighboring objects are modeled with an one-dimensional paracrystal approach [45]. From fitting, the lateral structure sizes and their corresponding center-to-center distances can be obtained. Figure 3.6a shows a 2D GISAXS data. In the 2D scattering image, the positions for performing the vertical and horizontal line cuts are marked with red cuboid. In the vertial line cuts (Figure 3.6b), an enhanced scattering is observed between the sample horizon and the specular beam, which is called the Yoneda peak. (Figure 3.6c shows a horizontal line cut which is performed at the critical angle of the material under investigation, the as obtained line cut is modeled with a model based on the EIA of the DWBA (red line).

The setup of the GIWAXS measurements is similar to that of the GISAXS measurements, but the SDD values for the GIWAXS mmeasurement is much shorter. When the SDD value is less than 10 cm, information about the molecular stacking, crystal orientation and crystal size can be acquired.

The GIWAXS measurements are conducted at DESY (Hamburg, Germany). The beam source, detector and experimental environment are the same as for GISAXS measurements except the absence of a flight tube. Due to the very short SDD, the scattering from air is negligible. Before analyzing the 2D GIWAXS data, solid angle correction, q-reshaping and conversion, efficiency correction (air path and pixel sensitivity under tilt angles) and polarization correction on the raw 2D GIWAXS data are required in order to retrieve the corrected reciprocal space patterns [46]. figure 3.7a shows the corrected 2D GIWAXS data. All corrections are done with the aid of the software Grazingincidence x-ray Scattering Graphical User Interface (GIXSGUI), which is developed by the Advanced Photon Source, Argonne National Laboratory, USA [42]. Afterwards, the radial integrals are taken from 0° to 90°. The obtained curves are fitted with Gaussian functions. From the fit, the

lattice constants can be obtained (figure 3.7b). Based on the full-width-at-half-maximum (FWHM) values, the crystal sizes can be estimated. Moreover, information about crystal orientations can be extracted from the tube cuts figure 3.7c.

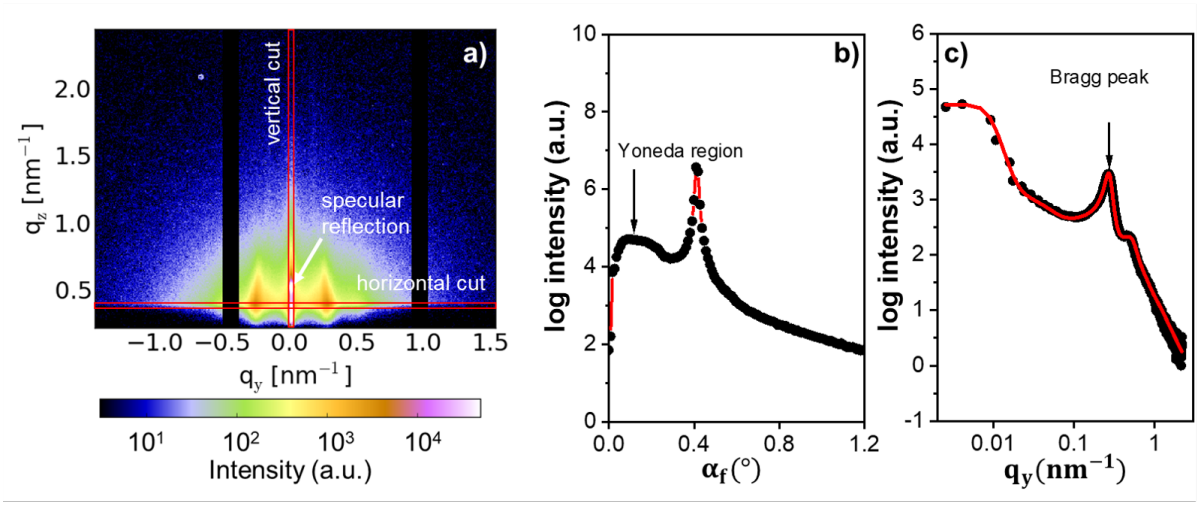

Figure 3.6: *2D GISAXS data and its corresponding line cuts are shown. (a) In the 2D scattering image, the positions for performing the vertical and horizontal line cuts are marked with red cuboid. (b) In the vertial line cuts, an enhanced scattering is observed between the sample horizon and the specular beam, which is called the Yoneda peak. (marked with a black arrow) (c) A horizontal line cut is performed at the critical angle of the material under investigation and modeled with a model based on the EIA of the DWBA (red line).*

3.6 FT-IR spectroscopy

Fourier transform infrared spectroscopy (FT-IR) is a technique to identify the organic functional groups in the polymeric samples. In the section of "Multi-Dimensional Morphology Control for PS-b-P4VP Templated Mesoporous Iron (III) Oxide Thin Films", FT-IR spectroscopy is used for certifying the complexation effect between the P4VP groups and the Fe^{3+}. A VERTEX 70 FT-IR spectrometer is used to measure the samples. It provides a spectral range from 6000 cm^{-1} to 130 cm^{-1} in a one step measurement, which covers a complete far and mid IR spectrum. Moreover, it has a spectral resolution of better than 0.4 cm^{-1}, which is adequate for most measurements. A schematic overview of the light path inside a FTIR spectrometer is given in Figure 3.9. The spectrum of interest is generated by a light source. IR light is generated and guided to a Michelson interferometer. The beam is split into reflected beam R1 and transmitted beam T1 via a beamsplitter. The transmitted beam T1 is reflected at a moving mirror. Thereby, the

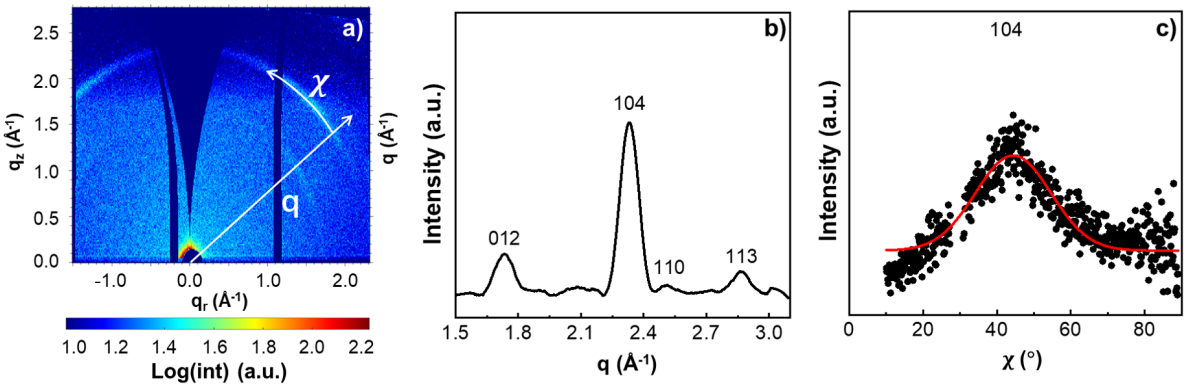

Figure 3.7: *Reshaped 2D GISWXS data and its corresponding line cuts. (a) In the reshaped 2D GIWAXS data, the positions for performing the q cut and χ cut are marked with wite arrows. The exemplary q cut and χ cut are shwon in b) and c) The fit result for the χ cut is represented with a red line.*

optical path difference between reflected beam and transmitted beam can be changed. The combined beam C1 then passes through the sample and the intensity is measured as a function of the mirror position x (so called interferogram). The difference of the optical path goes along with the occurrence of constructive and destructive interference. At zero optical path difference, a maximum can be found. Since the IR source generates non-monochromatic light, the intensity of the interference pattern decreases with increasing optical path difference. The obtained interferogram is then translated into a single beam spectrum (intensity vs. wavenumber) through Fourier transformation. Absorbance peaks arise due to excitation of vibrational modes (bending or stretching) of a molecule. The detector tells the energy difference as a function of time for all wavelengths simultaneously. It is noticeable that the relationship between energy and time is reciprocal. Therefore, a Fourier transform function converts the spectrum of intensity *vs* time spectrum into the spectrum of intensity versus frequency. In the present thesis, the FT-IR spectra are recorded with an Equinox 55 by Bruker and the instrument is operated with the software Opus v6.0. The standard procedure consists of the measurement of a background spectrum I_0 with the bare substrate, followed by the sample spectrum I with the actual sample installed in the spectrometer. The final absorbance A is calculated via the following equation:

$$A = log\left(\frac{I_0}{I}\right) \tag{3.3}$$

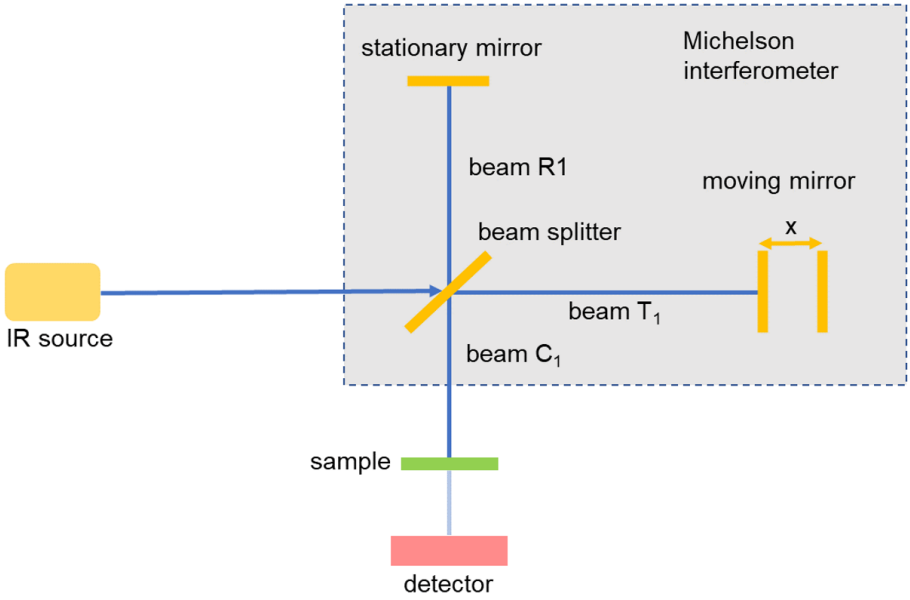

Figure 3.8: *Schematic overview of the light path inside a Fourier transform infrared spectrometer. An IR source is used to generate polychromatic light, which is split into reflected beam R1 and transmitted beam T1. A moving mirror serves to change the optical path difference between reflected and transmitted beam. The combined beam C1 is then guided through the sample, where vibrational states can be excited. An IR detector is used to record the resulting interferogram.*

3.7 X-ray photoelectron spectroscopy

X-ray photoelectron spectroscopy (XPS) is a technique to investigate the elemental composition on the surface of the thin film. A schematic construction of a XPS setup is shown in figure 3.9. X-rays with a photon energy $\hbar\omega$ are generated typically as Al Kα or Mg Kα radiation with photon energies of 1486.6 eV and 1253.5 eV, respectively. The photon energy $\hbar\omega$ can get completely absorbed by electrons inside the investigated sample. In order to be able to escape the surface of the sample, the electron requires a transferred energy larger than the sum of binding energy EB and workfunction Ω_ω. All additional energy is used to excite the electron to states of higher kinetic energy E_{kin} (movement). The relationship between $\hbar\omega$, Ω_ω, E_B, and E_{kin} can be written as the following equation:

$$E_{kin} = \hbar\omega - E_B - \Omega_\omega \tag{3.4}$$

The number of electrons with a kinetic energy E_{kin} are measured through a hemispherical analyzer with an electron detector. In a typical XPS spectrum, E_B is plotted against the number of photoelectrons with this specific energy. As each chemical element has

distinct core-level binding energy, the recorded spectrum can be used to reconstruct the elemental composition at the sample surface. Limitation to surface-near regions (around 10 nm) is caused by the typical strong interaction of electrons and solid matter [47].

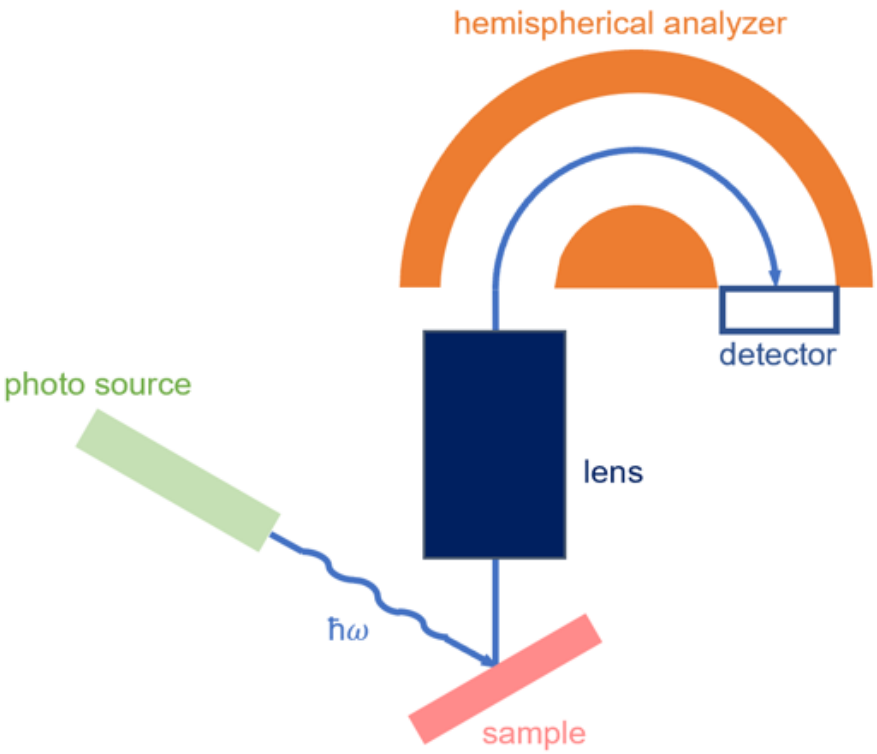

Figure 3.9: *Schematic overview of an X-ray photo electron spectrometer used to determine the elemental composition of the thin films. Generated photons are used to emit core-level electrons from the surface of the respective sample. Electrons and their respective kinetic energy are detected via a hemispherical analyzer with an electron detector.*

3.8 Optical microscopy

In the present thesis, the optical microscopy (OM) is applied to measure and count the surfacce area of the fabricated perovskite solar cells. The used OM is an Axiolab A microscope (Carl Zeiss) combined with a PixeLink USB Capture BE 2.6 charge coupled device (CCD) camera. A halogen Hal 100 lamp is used as the light source. The available magnifications of the objectives include 1.25, 2.5, 10, 50, and 100. The obtained the images are recored with a digital camera(1280 $\times$ 1024 pixels). The resolution of each

pixel are 6.26 μm/pixel, 3.11μm/pixel, 0.82 μm/pixel, 0.17 μm/pixel, 0.082 μm/pixel under the magnification of 1.25, 2.5, 10, 50, 100, respectively. The reselution can be used to calculate the real–space distance. In this thesis, the obtained images are processed and analyzed by ImageJ.

3.9 Raman spectroscopy

In the third result part of the present thesis, the compositional information of the α-Fe_2O_3 thin films is checked with the Raman spectroscopy. For enhancing the intensity of the spectroscopy, the samples used for this measurement is prepared with drop casting. Raman spectra were acquired with an "inVia Reflex Raman System", which consisted of a research-grade optical microscope (Leica DM2700M, Magnification 5x, 20x, 50x) and a high-performance Raman spectrometer (Renishaw).

3.10 I-V characterization

The *I-V* curve is measured to probe the photovoltaic performance of the perovskite solar cells. *I-V* sweeps are recorded with a Keithley 2400 sourcemeter by applying an external bias to the probed solar cells under simulated solar illumination. The irradiation is provided by a solar simulator Solar Constant 1200 (K.H. Steuernagel Lichttechnik GmbH) equipped with a rare earth Xenon lamp. Before *I-V* measurements, the light intensity is calibrated to be 1000 W/m^2 by a silicon-based calibration solar cell (WPVS Reference Solar Cell Typ RS-ID-3 by Fraunhofer ISE).

An exemplary *I-V* curve of a solid-state dye-sensitized solar cell is shown in figure 3.10. From the curve, the related photovoltaic parameters can be extracted. The open-circuit voltage (V_{oc}) and short-circuit current density (J_{sc}) are the values of x- and y-intercepts, respectively, as indicated in figure 3.10. In general, V_{oc} is determined by the n- and p-type semiconductors in the active layer, whereas J_{sc} is related to many factors, such as charge carrier generation, transportation, and extraction. Along the curve, a point, where the power density of $P = J\ V$ is maximum, is defined as maximum power point (MPP) as indicated in figure 3.10. The fill factor (FF) is the ratio between the power at the MPP (indicated by the light grey rectangle) and the theoretical maximum possible power of $P_{max} = V_{oc}\ J_{sc}$ (indicated by light green rectangle):

$$FF = \frac{P_{MPP}}{P_{max}} = \frac{V_{MPP} J_{MPP}}{V_{oc} J_{sc}} \tag{3.5}$$

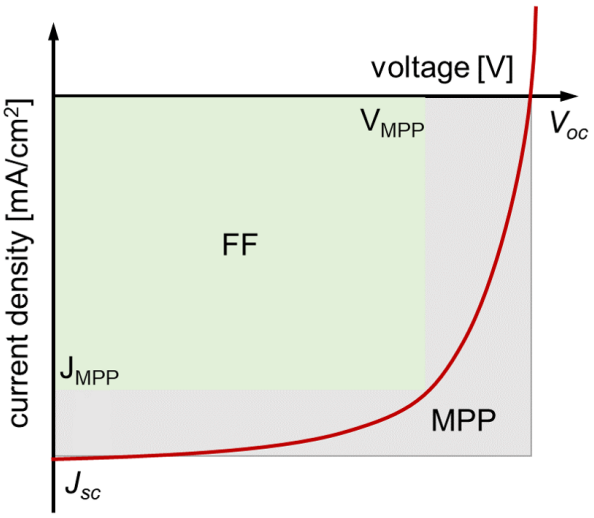

Figure 3.10: *JV -curve of the solar cell. Key performance parameters, namely V_{OC}, J_{SC} and FF are indicated. FF is given by the available power at the MPP of the real photovoltaic device divided by the theoretical maximum power.*

The FF is equal to 100% in an ideal device, where the I-V curve has a rectangle shape. The power conversion efficiency (PCE) is defined as the ratio of the device output power (P_{out}) and the irradiation input power (P_{in}):

$$PCE = \frac{P_{out}}{P_{in}} = \frac{V_{oc} J_{sc} FF}{P_{AM1.5}} \tag{3.6}$$

For the present measurements, a custom-made sample holder provides a shadow mask for the non-measuring area and ensures that only the probed pixel is under solar illumination. A distance of 320 mm is set between the solar cell and the light source. During measuring, the voltage seeps from -1 V to 0.2 V with 0.01 V increment and 0.01 s delay. Each pixel is measured several times to sort out the best device performance. After measuring, each metal pixel of the samples is mapped with optical microscopy (OM). Though OM images, the size the pixel is individually calculated with the aid of software ImageJ.

4 Sample preparation

In this chapter, the materials and manufacturing steps used for sample preparation for the entire study are presented.

4.1 Materials

In the sections for the mesoporous metal oxide thin film preparation, the used materials can be primarily classified in to the following three parts: the precursors used for the formation of the metal oxide, the diblock copolymer template, the poor solvent added in to the sol-gel solution and the different solvent used for the solution preparation. In the section for the solar cell fabrication, the materials can be classified in to the floowing three parts: the compact electron transport layer, the mesoporous electron transport layer, the light harvest perovskite layer, the hole-transport layer.

4.1.1 Precursors

Within the frame of this thesis, three kinds of precursors, namely, titanium isopropoxide (TTIP), tin chloride ($SnCl_4$), and iron chloride ($FeCl_3$) are used for the preparation of nanostructured metal oxide thin films.

TTIP is purchased from Carl Roth GmbH. It is a transparent or canary yellow liquid with a relative density of 0.96 g cm^{-3} and fumes in moist air. Its stoichiometric formula is referred as $Ti[OCH(CH_3)_2]_4$, which exists as a monomer with a titanium center having an octahedral coordination environment of isopropoxides, as shown in figure 4.1a. Titania, evolved from TTIP via hydrolysis and condensation reactions, typically requires a high-temperature treatment to be crystallized as anatase phase.

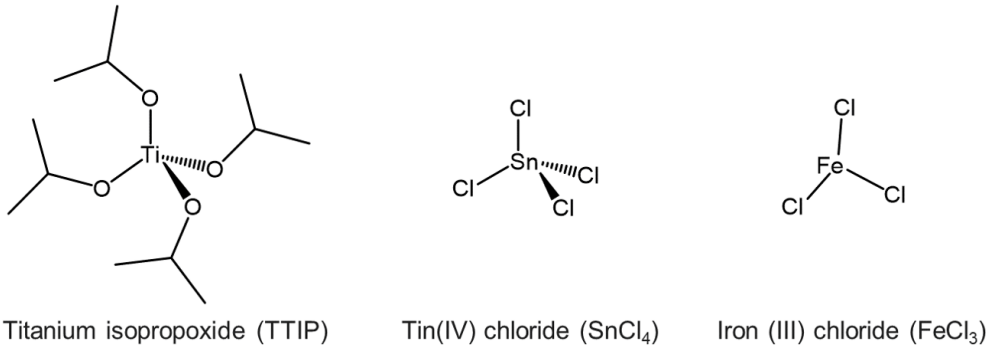

Figure 4.1: *The chemical structures of PS-b-PEO and PS-b-P4VP.*

Tin chloride ($SnCl_4$, 98%), also known as tin tetrachloride or stannic chloride, was purchased from Sigma-Aldrich. It is an inorganic compound with the formula $SnCl_4$. It is a colorless hygroscopic liquid, which fumes on contact with air. It is used as a precursor to other tin compounds. It is a strong Lewis acid, which is widely used as promoter or catalyst in organic synthesis and is soluble in most organic solvents. Anhydrous tin(IV) chloride solidifies at 33 °C to give monoclinic crystals with the P21/c space group. It is isostructural with $SnBr_4$. The molecules adopt near-perfect tetrahedral symmetry with average Sn–Cl distances of 227.9(3)pm. [48] Several hydrates of tin tetrachloride are known. The pentahydrate, $SnCl_4 \cdot 5H_2O$ was formerly known as butter of tin. They all consist of $[SnCl_4(H_2O)_2]$ molecules together with varying amounts of water of crystallization. The additional water molecules link together the molecules of $[SnCl_4(H_2O)_2]$ through hydrogen bonds. [49], Although the pentahydrate is the most common hydrate, lower hydrates have also been characterised. [50]

Iron (III) chloride ($FeCl_3$, 97%) is purchased from Sigma-Aldrich. Anhydrous iron (III) chloride is a black substance with a slightly pungent odor of hydrochloric acid. As an anhydrous compound, it is extremely hygroscopic, i.e. it removes water from the air. With increasing water content the hygroscopic nature decreases and the color changes from red-brownish to yellowish, the result is iron (III) chloride hexahydrate ($FeCl_36H_2O$).

4.1.2 Structure-directing templates

Two kinds of block polymers are used for conducting the morphologycal study of the mesoporous metal oxide thin films: Polystyrene-block-polyethylene oxide (PS20500-b-PEO8000) and Polystyrene-bolck-poly-4-vinyl pyridine (PS-b-P4VP). Both polymers are purchased from Polymer Source Inc.Canada. The polystyrene (PS) block is hydrophobic, and the polyethylene oxide or the Polystyrene-bolck-poly-4-vinyl pyridine segment is

polymer	M_n **(kg/mol)**	**PDI**	**polymer block**	M_n **(kg/mol)**	T_g **(°C)**
PS-b-PEO	28.5	1.02	PS	20.5	86
			PEO	8	-63
PS-b-P4VP	22.6	1.12	PS	11.8	104
			P4VP	10.8	153

Table 4.1: *Parameters of the diblock polymer templates, including name, number average molar mass M_n, polydispersity index (PDI), and glass transition temperature (T_g).*

hydrophilic, which acts as the polymer matrix to incorporate the precusor of the metal oxide. By tailoring the phase seperation beviour of the block polymerr, various mesoporous matal oxide thin films can be prepared. Due to the different physicochemical property of the hydrophilic segment and the precusor of the metal oxide, the morphology control of the motal oxide thin film differs alot from system to system. The chemical formula of the polymer template is shown in figure 4.2.

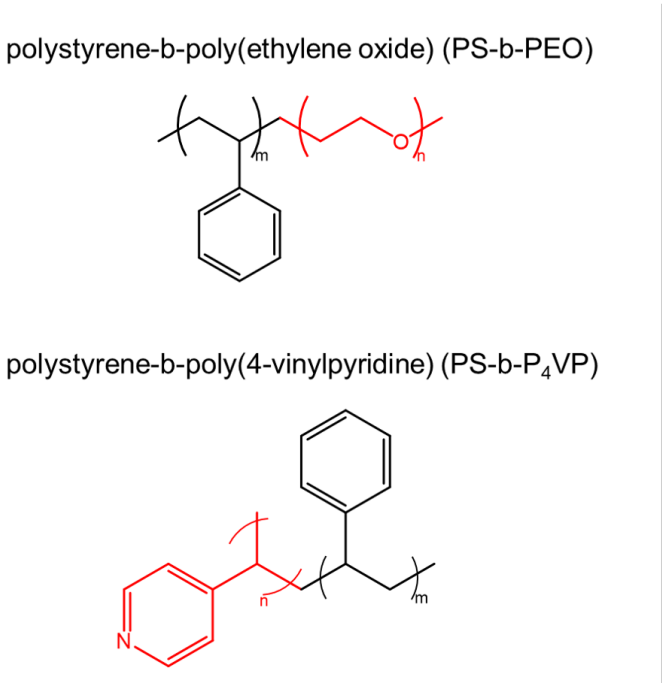

Figure 4.2: *The chemical structures of PS-b-PEO and PS-b-P4VP.*

4.1.3 Electron blocking materials

For the fabrication of the solar cells in the present thesis, we use 2,2',7,7'-tetrakis(N,N di-p-methoxyphenylamine)9,9'-spiro-bi-fluorene (spiro-OMeTAD) as the electron blocking materials. Its chemical structure is shown in figure 4.3a. It has a spiro-center (i.e. a tetrahedral carbon connects to phenyl moieties), which functions to prevent crystallization of this organic materials. Crystallization of the EBM is disadvantageous for solar cell performance as it would lead to a bad contact between the perovskite layer and the hole transport layer. The unique properties, including the amorphous nature, high solubility, ionization potential make spiro-OMeTAD one of the best performing hole transporting material in the solar cell up to now.

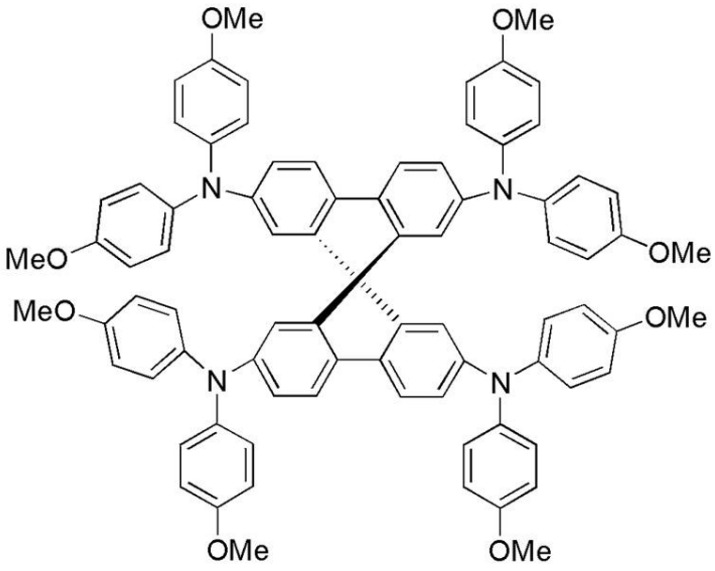

Figure 4.3: *The chemical structures of spiro-OMeTAD*

4.2 Thin film preparation

4.2.1 Substrate cleaning

To ensure that the deposited films are not contaminated by surface impurities on the substrate, silicon and glass sheets are cleaned in an acid bath before using them as substrates. Moreover, the cleaning process can keep a defined state of the substrate surface, which is essential to ensure reproducibility. The acid bath is prepared according to the procedure established in reference [51]. DI water (H_2O), hydrogen peroxide (H_2O_2) and

sulfuric acid (H_2SO_4, 98 %) are mixed in sequence in a glass beaker residing in a water bath at room temperature. The amounts of H_2O, H_2O_2 and H_2SO_4 in the solution are 54 ml, 84 ml and 198 ml, respectively. After mixing, the water bath is heated to 80 °C gradually. Separately, the substrates are loaded into a teflon holder and rinsed with DI water to remove dust particles from the substrate surface. Once the temperature reaches 80 °C, the teflon holder is immersed into the acid bath, and kept for 15 min. Thereafter, it is taken out and transferred to a beaker with pure DI water. Each substrate is rinsed with DI water to remove acidic traces before being dried under nitrogen flow. After drying, the substrates are stored in a clean sample box for further use.

4.2.2 Spin coating

Spin coating is a common technique for applying thin films to substrates. When a solution of a material and a solvent is spun at high speeds, the centripetal force and the surface tension of the liquid together create an even covering. After any remaining solvent has evaporated, spin coating results in a thin film ranging from a few nanometres to a few microns in thickness. Spin coating is used in a wide variety of industries and technology sectors. The primary advantage of spin coating over other methods is its ability to quickly and easily produce very uniform films. The use of spin coating in organic electronics and nanotechnology is widespread and has built upon many of the techniques used in other semiconductor industries. The relatively thin films and high uniformity required for effective device preparation, as well as the need for self-assembly and organisation to occur during the casting process, do however necessitate some differences in method. For spin coating, higher angular speed leads to thinner final films. Furthermore, film thickness also depends on the solvent, the viscosity and concentration of the solution. For the thin film deposition, a Delta 6 RC TT (Süss MicroTec Lithography GmbH) spin coater is applied. The parameters of spin coating including acceleration speed, angular speed of rotation and rotation time are first set. The pre-cleaned substrate is placed on the rotation table of the spin-coater and is then held via an applied vacuum. It is note that the samples prepared in the present thesis are mounted at the rotation tabe. A certain amount of solution is dripped on the substrate by a pipette. After the rotation stops, the sample is dismounted from the spin-coater and its back side is wiped with a clean tissue to remove residual solution.

4.2.3 Calcination

In the present thesis, we used a high temperature calciantion process for removing the polymeric template and promoting the crystallization process of metal oxide film. After calcination, crystalline patterned metal oxide thin films are achieved, which are desirable in mutiple applications [52]. In this work, the calcination is performed in a tube furnace (GERO or Hereaus instruments) under ambient conditions. A calcination protocol of heating ramp, calcination temperature, calcination time can be set according to different requirements. A standard calcination scheme in the present thesis consits of a heating ramp of 5 °C/min and a calcination temperature of 500 °C for 2 h.

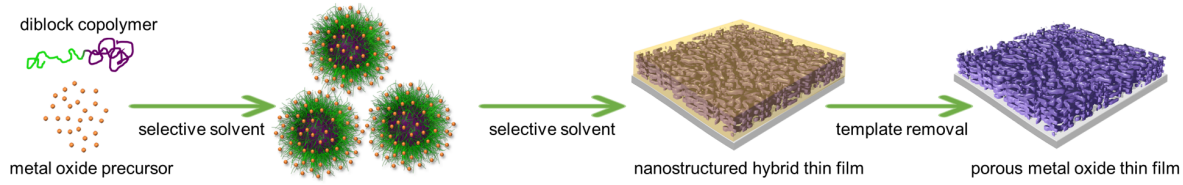

Figure 4.4: *Schematic illustration of fabricating mesoporous titania films with incorporated nanoparticles. It involves several steps: polymer template assisted sol-gel synthesis using the titania precursor TTIP, film deposition and high-temperature calcination.*

4.3 Fabrication of solar cells

The fabrication procedure of the perovskite solar cells comprises several steps, starting from the substrate cleaning, the compact α-Fe_2O_3 layer preparation, patterned α-Fe_2O_3 film, peroskite layer and electron blocking layer depossition, in the end the metal-electrode evaporation. The production procedure of the perovskite solar cell is demonstrated in figure 4.5. The individual steps are discussed in more detail below.

4.3.1 Substrate preparation and cleaning

The production of solar cells starts with the preparation of the bottom electrode. A transparent conductive oxide, namely fluorine-doped tin oxide (FTO), is used as the bottom electrode. Patterned FTO substrates were purchased from Youxuan (Liaoning, China). For the cleaning procedure, the FTO substrates were sequentially cleaned with Alconox® detergent solution (16 mg mL^{-1}), ethanol (99.8 %), acetone (99.9 %) and 2-propanol (99.8 %). Each ultrasonic bathing procedure lasts 15 min. Then the FTO

substrates were dried with N_2 gas. Prior to the thin film deposition, the substrates were treated with oxygen plasma for 10 min.

4.3.2 Synthesis of compact α-Fe_2O_3 layer

A compact α-Fe_2O_3 layer, acting as hole blocking layer of the pperoskite solar cells, is introduced between the fluorine-doped tin oxide (FTO) and the mesoporous α-Fe_2O_3 layer. The existence of the compact layer has been proven to be an effective approach to prevent recombination of charge carriers [53]. It is much denser than the mesoporous α-Fe_2O_3 film, circumvent the possibility of the short circuit. The manufacturing process of this blocking layer is the same as the reference [54]. Specificlly, 80 mg/ml $Fe(NO_3)_3 \cdot 9H_2O$/ethanol solution is spin coated on to the FTO substrate at 2000 rpm for 40 s. Afeter that, a calcination process was carried out at 500 °C for 30 mins for converting the $Fe(NO_3)_3 \cdot 9H_2O$ precursor into α-Fe_2O_3.

4.3.3 Depositon of patterned α-Fe_2O_3 film

To prevent moisture-induced deliquesce, the $FeCl_3$ powder used for the stock solution preparation is weighted in an N_2 glove box. Specifically, 42.7 mg $FeCl_3$ are weighed for preparing the stock solution. After taking out from the glovebox, the $FeCl_3$ powder is dissolved into 1 ml DMF solvent with continuous stirring for 30 mins. Afterward, the $FeCl_3$ solution is added into the pre-weighed 21 mg PS-b-PEO powder with further stirring for 30 mins to acquire the stock solution. The $FeCl_3$/PS-b-PEO composite thin films are deposited with a Delta 6 RC TT spin coater (SÜSS Micro-Tec Lithography GmbH) at 2000 rpm for 60 s. In contrast to the as deposited $FeCl_3$/PS-b-PEO composite thin film, a post treatment process is further performed at 200 °C for 5 mins in the air condition for obtaining a patterned α-Fe_2O_3 thin film.

4.3.4 Depositon of perovskite and electron blocking layer

Both the perovskite layer and the electron blocking layer are deposited in a N_2 gas golve box. The perovskite precursor solution was prepared by dissolving MAI (1.10 M), PbI2 (1.10 M) in to 1000 mL anhydrous DMF and DMSO (7:3, volume ratio) mixed solvent. The precursor was spin coated onto the prefabricated α-Fe_2O_3 thin films at 1000 rpm for 5 s and 5000 rpm for 20 s in the nitrogen glove box. Then, 180 μL chlorobenzene was dropped on to the substrates at the end of the fabrication progress (10 s). 72.3

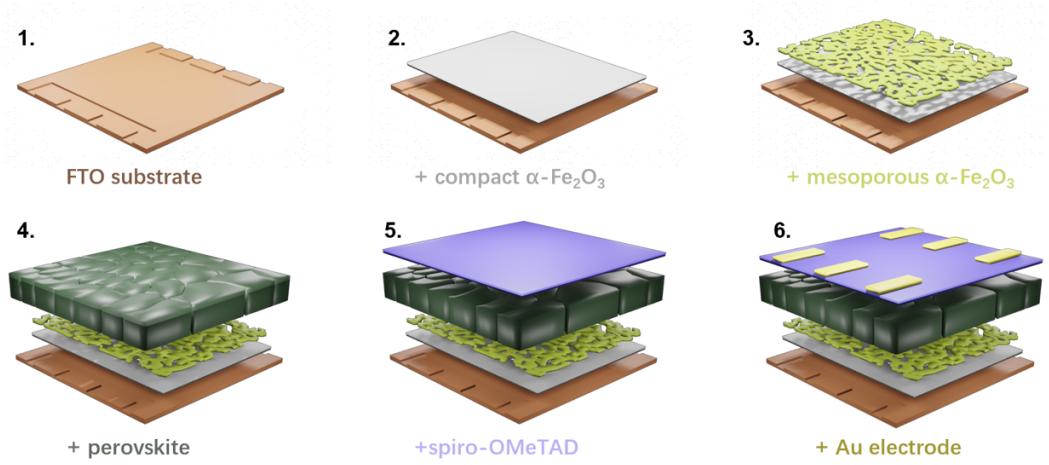

Figure 4.5: *Schematic illustration of the fabrication of the perovskite solar cells. Both cells start with a FTO-coated glass substrate. 1) The patterned FTO sheets are cleaned with organic solvent. 2) The compact α-Fe_2O_3 is deposited as electron blocking layer. 3) The patterned α-Fe_2O_3 films are deposited. 4) perovskite layer is added 5) electron blocking layer is deposited 6) The gold back contact is deposited on top to finalize the solar cells.*

mg Spiro-OMeTAD was dissolved in 1 mL chlorobenzene with additives of 17.5 μL Li-TFSI solution (520 mg mL^{-1} in acetonitrile), 28.8 μL tris (2-(1H-pyrazol-1-yl)-4-tert-butylpyridine) cobalt (III) tri [bis(trifluoromethane) sulfonimide] (FK 209 Co (III) TFSI) and 28.8 μL TBP. When the substrates were cooled down to room temperature, 50 μL of spiro- OMeTAD was dropped on the perovskite layers at 3500 rpm for 30 s.

4.3.5 Evapration of gold electrode

A gold electrode is used as the counter electrode of the perovskite solar cells. Producing the gold contact is the last step in the solar cell fabrication process, as shown in figure 4.5(6). In this work, the gold contact is deposited via thermal evaporation. The samples are placed upside down on into a shadow mask. During evaporation, the gold contact, in form of a pixel, can only be deposited onto the samples through these openings. The evaporation chamber is evacuated to a pressure of less than 3×10^{-5} mbar before about 180 mg of gold is thermally evaporated for 3 min. After the gold electrode is deposited successfully, the performance of solar cells is ready to be tested. The active area of one pixel is defined as the region where the gold contact overlaps with the FTO. During solar cell test, no shadow masks are applied. The accurate area is evaluated from its optical image via the software ImageJ v1.42q.

5 Template-oriented porous titania films

Parts of this chapter have been published in the article: Key factors for template-oriented porous titania synthesis: solvents and catalysts(YIN, Shanshan, et al. Key Factors for Template-Oriented Porous Titania Synthesis: Solvents and Catalysts. Small Methods, 2020, 4. Jg., Nr. 3, S. 1900689.) [55]

5.1 Preface

During the past decades, nanostructured titania thin films have been widely studied due to their attractive properties such as high electron mobility and mechanical flexibility. [56, 57] Main fields of application for nanostructured titania thin films include solar cells, gas sensing, lithium/sodium ion batteries, and photocatalysis. [58–62] When used as the anode material of lithium/sodium ion batteries, titania with a high surface-to-volume ratio facilitates penetration of electrolyte and intercalation of lithium or sodium ions. [63–66] In the case of organic-inorganic hybrid solar cells, the exciton diffusion length within typical backfilling materials is typically less than 20 nm. Mesoporous titania with uniform pore arrangement provides an excellent basis to suppress recombination losses of excitons. [62, 67–69] Although plenty of achievements were achieved in the preparation of porous metal oxide materials, current synthetic methods still have several inherent drawbacks from the perspective of thin film nanotechnology, such as time consuming processing conditions and the ill-defined powder form product. [14, 70–73] Among multiple preparation routes to porous inorganic nanostructures, amphiphilic block copolymer assisted sol-gel chemistry features a low cost, operation compatibility with ambient atmosphere and easy one-pot processing route, and therefore has been confirmed as a particularly promising approach. [74–79] In the block copolymer assisted synthetic route, the hydrolysis and condensation products of the organic precursors are preferentially incorporated

into one of the blocks via hydrogen bonds. Accordingly, the morphology control of the corresponding functional inorganic part can be realized by phase separation of the sol-gel solution. [19, 80–84]Templin and coauthors prepared a kind of organically modified aluminosilicate mesostructures from amphiphilic poly(isoprene-b-ethylene oxide) block copolymers (PI-b-PEO). Various morphologies corresponding to the phase diagrams of diblock copolymers were obtained by increasing the fraction of the inorganic precursors with respect to the polymer. [85] The Smarsly's group constructed a kind of highly crystalline mesoporous SnO_2 film by evaporation-induced self-assembly using a novel amphiphilic block-copolymer template. [86]Fisher and coauthors obtained a series of nano patterned titania thin films by organic/inorganic self-assembly and selective local functionalization. [87] Cheng et al. successfully synthesized nanowires, nanoparticles, flake-like structures, nano-doughnuts, worm-like and foam-like nanoscale networks by controlling the relative content of precursor, catalyst and solvent in a PS-b-PEO based casting solution. [18]Similarly, Hohn et al. demonstrated the strong influence of HCl addition on the thin film morphology. [67] However, to the best of our knowledge, the solvent effect regarding the block copolymer assisted sol-gel synthesis has been rarely studied, which is also crucial to the resulting titania morphologies. [88–90] In the microphase-separated sol-gel system, the swelling degree of the polymer chains in each domain is significantly influenced by the solvent nature. Typically, a neutral solvent is equally distributed into each domain, therefore swells both blocks to the same extent. Otherwise, a preferential swelling for a certain domain will be induced even with a slight solvent selectivity. [91, 92] In the present section, the morphology evolution of the template-oriented titania nanostructures has been systematically studied in terms of different solvents category and HCl content. The real space imaging method scanning electron microscopy (SEM) and the reciprocal space method grazing-incidence small angle X-ray scattering (GISAXS) are used for the thin film morphology characterization. Based on the detailed comparison and analysis of the multiscale characterization results, the relationship between the sol-gel components and final thin film morphology is unveiled.

5.2 Experimental: synthesis of mesoporous titania thin films

Tetrahydrofuran (THF), azeotrope of toluene and 1-butanol (TB), and 1, 4-dioxane are used for the stock sol-gel solution preparation, respectively. Five parallel samples with exponentially increased HCl content are prepared in each kind of solvent. For the preparation of the stock solution with THF as the solvent, PS-b-PEO (42.6 mg) was firstly

dissolved in THF (1.5 ml) under continuous stirring for 1 h. Then a certain amount of TTIP was added into the mixture dropwise. In order to avoid the formation of big clusters in the sol-gel solution, the catalyst (37% HCl) was dispersed into THF (0.5 ml) before addition. The final volume fraction of TTIP in all stock solution was kept at 7.5 vol.% for each sample, while the corresponding HCl content exponentially increased from 0.5 vol.% to 8.0 vol.%. The exact same preparation routine is carried out with 1, 4-dioxane or TB (toluene and 1-butanol) instead of THF to probe the impact of different solvent categories.The mixed stock solution was stirred for 1 hour to stabilize the hydrogen bond formed between PEO and Ti-O species. Afterwards, titania thin film deposition was performed with a Delta 6 RC TT spin coater at 2000 rpm for 60 s (SÜSS Micro Tec Lithography GmbH). In order to remove the polymer template, the as-spun thin films were calcined at 500 °C for 2h with a heating rate of 5°C min^{-1} in the air condition. After removing the polymer template by calcination, various titania scaffolds are obtained. Different types of micelle structures, such as sphere, cylinder, lamellae and vesicle, formed in the stock solution are schematically exhibited in figure 5.1a. Hydrolyzed titania nanodot arrays are depicted as green and polymer chains are represented as yellow, respectively. Figure 5.1b illustrates the thin film synthetic route utilized in the present work and figure 5.1c shows the hydrogen interaction between Ti-O- structures and PEO blocks.

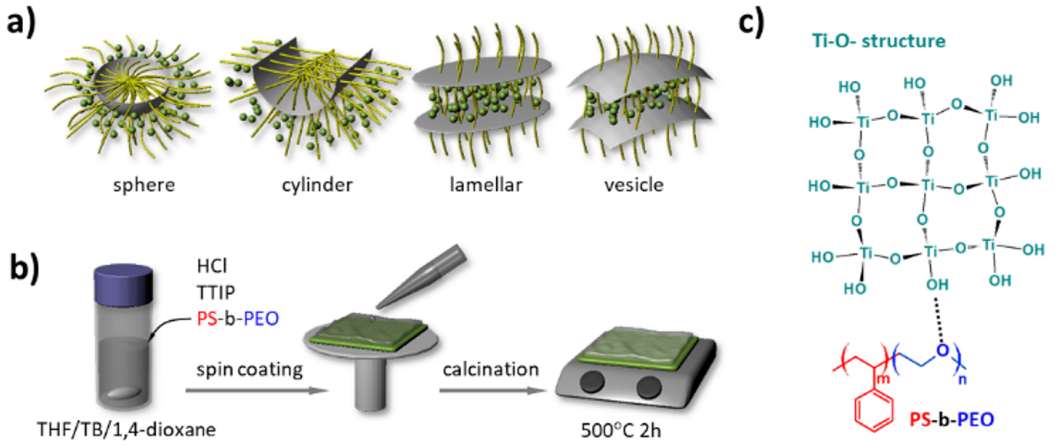

Figure 5.1: *a)Illustration of different polymer template (yellow chains) / titania nanodot array (green particles) arrangements formed in the sol-gel solution. b) Schematic overview of the preparation process of porous titania thin films. Casting solutions are based on different solvents and HCl content as indicated in the insets. Subsequent spin coating and high temperature annealing leads to the formation of porous and crystalline titania thin films.c) Representation of the linkage between titania species and the PEO block through hydrogen bonding. Reproduced from Ref [55] with permission from JOHN WILEY AND SONS, Copyright 2020.*

5.3 Thin film characterization

The surface morphology of the porous titania thin films was characterized by high-resolution field emission scanning electron microscope (SEM, Zeiss Gemini NVision 40) with working distance of 3.9 mm and acceleration voltage of 5 kV. Grazing-incidence small-angle scattering (GISAXS) measurements were carried out in house with a Ganesha SAXSLAB instrument at Technical University of Munich (TUM). The following parameters were used for the GISAXS measurement: a wavelength of 1.54 $\AA$, a sample to detector distance of 1056.2 mm, a horizontal beam size of 200 μm and a vertical beam size of 100 μm. A Pilatus 300K detector (Dectris Ltd.) was used for collecting the scattering data. An incident angle of 0.4 was set to probe inner structures of the thin film. X-ray diffraction (XRD) measurements were performed with X'Pert PRO PANanalytical instrument (Bragg-Brentano geometry with fixed divergence slits, continuous mode, position sensitive detector, Cu-K radiation, Ni filter).

5.4 TiO_2 with THF solvent: surface morphology

The self-assembly of the amphiphilic block polymers can be provoked by two approaches, progressive addition of poor solvent or solvent evaporation. For the poor solvent induced self-assembly, the micellization of polymer chains occurs when the poor solvent content increases to a critical value. This critical point is related to the concentration and molecular weight of the block polymer. [93]For the solvent evaporation induced self-assembly process, the microphase-separated structures can be formed at a critical polymer concentration. This micellization critical point varies with the Flory-Huggins interaction parameter and polymerization degree of the block polymer. [94,95] During the self-assembly process in aqueous solutions, the energetically unfavorable water-hydrophobe interactions are avoided for preventing a large enthalpy penalty. However, the degree of freedom of single chains is decreased significantly ($\Delta S < 0$). As a result, the phase separation is induced by the increased free energy in the system($\Delta G > 0$) [96, 97]

$$\Delta G = \Delta H - T\Delta S \tag{5.1}$$

Figure 5.3 are the SEM images of the titania thin films prepared with THF. As shown in the ternary phase diagram of the stock solution (Figure 5.3f), the HCl content increases from 0.5 vol.% to 1.0 vol.%, 2.0 vol.%, 4.0 vol.%, and 8.0 vol.% for sample shown in Figure 5.3a-e. The volume fraction of TTIP in each sample is kept the same at 7.5 vol.%. It can be seen that all SEM images in Figure 5.3 exhibit an interconnected, porous titania phase. [18] When the HCl content in the stock solution is increased from 0.5 vol.% to 1.0

vol.%, a significant enhancement of ordering can be observed (Figure 5.3a and b). The porous structure appears to be stable after the HCl content exceeds 2 vol.% (Figure 5.3c, d, and e). The structural evolution from Figure 5.3a to e can also be seen from the FFT patterns of the corresponding SEM images. The rather well defined ring-like pattern in Figure 5.3b-e indicate the presence of pores with similar size and enhanced ordering, while the smeared out pattern in Figure 5.3a indicates a rather broad size distribution with more disorder.

The underlying mechanism for governing the thin film structure evolution can be analysed with the following two approaches. Firstly, the chemical properties of each components in the sol-gel solution. Considering the superior miscibility of TTIP and PS-b-PEO in the THF solvent and the chemical stability of each component. The phase separation behavior is supposed to be less affected by these chemicals. However, TTIP is very prone to be hydrolyzed with the existence of H_2O molecules. The hydrolysis reaction mechanism between TTIP and H_2O molecules belongs to S_N2 nucleophilic substitution, which is schematically shown in figure 5.2. Considering the catalyst role of the H_2O molecules in the HCl solution, the lowest 0.5 vol.% HCl addition in the present work is assumed to be enough to stimulate the hydrolyse reaction. However, regarding the condensation process, a further growth and agglomeration of the condensed titania nanoparticles is prone to occurred with low HCl addition. Since the isoelectric point of TiO_2 lies at a pH of 5-7, charges on the particle surfaces in a weak acidic medium are not sufficient for keeping discrete particles in dispersed state, which facilitates the formation the randomly arranged large pore structures. [67,88] Secondly, the phase separation behivior of the block copolymer in the sol-gel solution. As mentioned above, the phase separation of block copolymer can be provoked by the solvent evaporation or poor solvent addition. The similar synthetic process in our previous work demonstrated the randomly arranged titania nanostructures formed without HCl addition, which suggested the weak effect of the solvent-induced self-assembly for the final titania nanostructures. [67] Therefore, the structure evolution in Figure 5.3 can be primarily assigned to the surface energy between PS blocks and surrounding solvent associated with poor solvent addition. For the titania structure in Figure 5.3a, 0.5 vol.% HCl addition within the sol-gel solution is far less than the critical value for micellization. Consequestly, a weak phase separated mixture of titania nano-dot array, polymer chains, and solvent are formed in the solution, which is converted in to a rather random structure after spin coating and calcination process. [98,99] On the other hand, the electrostatic repulsion among the condensed titania nano-dot array caused by low HCl content is not sufficient for preventing their further growth and agglomeration, which also facilitates the formation the randomly arranged pore structures. [67,88] With the increase of the HCl addition, a distinct phase separated structure is observed in Fig-

ure 5.3b, which suggests the critical poor solvent content is located between 0.5 vol.% and 1.0 vol.%. Closer observation shows that all of the phase-separated structures from Figure 5.3b to e are isoporous, which is assumed to be the result of ordered and spherical micelle formation in the respective sol-gel solution.The formation of spherical micelles at higher poor solvent content can be assigned to the enhanced surface energy between PS blocks and poor solvent. The stretch of hydrophobic PS blocks can be significantly inhibited with micellization. In addition, with higher HCl volume fraction, the aggregation process of hydrolyzed titania nano-dot arrays is effectively suppressed by an enhanced electrostatic repulsion force, which makes it easier to follow the microphase-separated structure of the polymer template. Interestingly, quite similar morphologies are exhibited if the HCl content increases from 1.0 vol.% to 8.0 vol.%, which indicates the superior stability of the phase-separated system under different poor solvent contents.

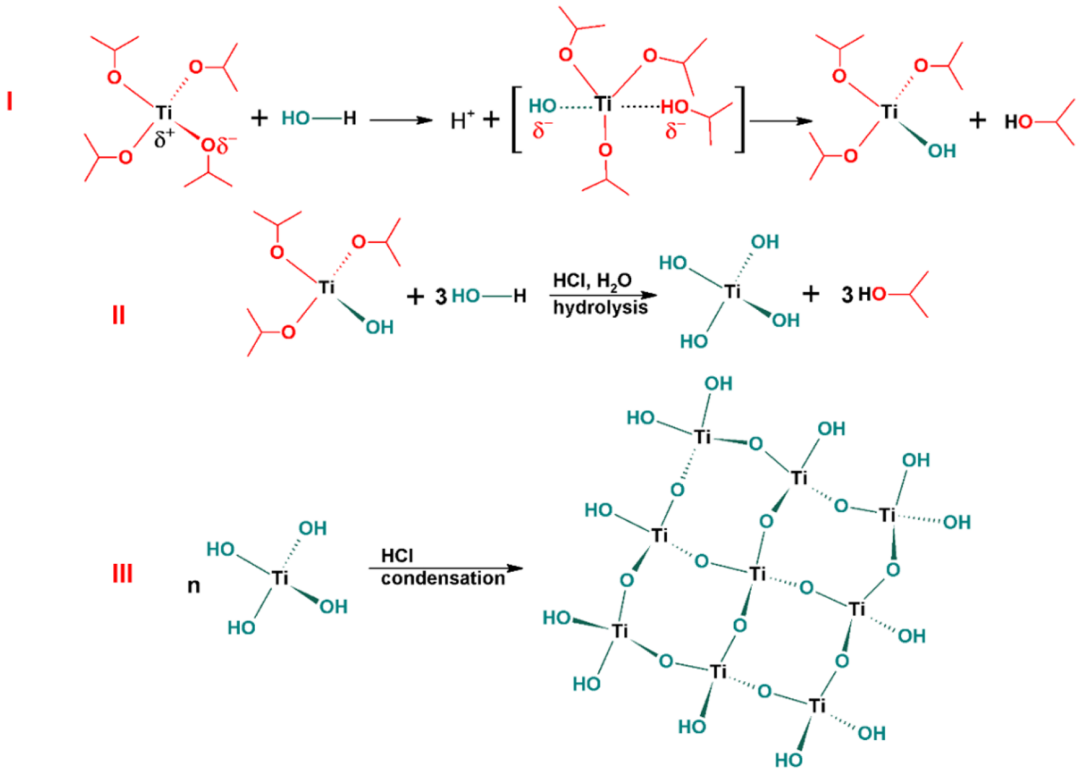

Figure 5.2: *Hydrolysis(I, II) and condensation (III) reaction mechanism of titanium tetraisopropoxide (TTIP).Reproduced from Ref [55] with permission from JOHN WILEY AND SONS, Copyright 2020.*

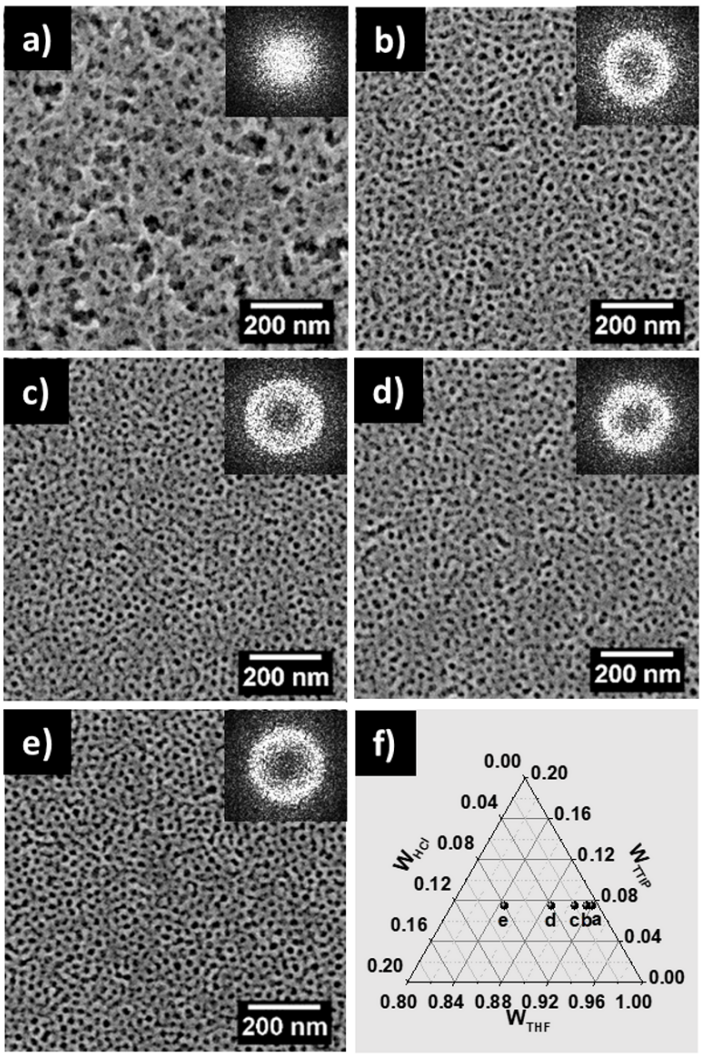

Figure 5.3: *SEM images of the titania thin films prepared with THF solvent. The u_p-right insets refer to the corresponding fast Fourier transform (FFT) patterns. The volume fraction of HCl is exponentially increased from a) 0.5 vol.% to e) 8.0 vol.%. f) Component phase diagram of the respective samples.Reproduced from Ref [55] with permission from JOHN WILEY AND SONS, Copyright 2020.*

5.5 TiO_2 with THF solvent: inner morphology

According to the SEM topography, the nanostructure evolution of the titania thin films is clearly demonstrated. Nevertheless, the thin film homogeneity over a large region is an important requirement for practical applications. Grazing incidence small angle X-ray scattering (GISAXS) is a powerful tool to detect the surface and buried structures in the

thin film. [100] Because of the very small incident angle, a macroscopic footprint of X-ray allows for gaining structure information with a high statistical relevance. [101]

Figure 5.5a to e refer to the 2D GISAXS data of the titania thin films prepared with different HCl content in the THF solvent. The observed maximum scattering intensity between the specular peak and sample horizon is the so called Yoneda peak, which is material characteristic. [69] The very pronounced horizontal scattering signal at the Yoneda region indicates the statistical average information of laterally ordered nanostructures. The shape of the scattering patterns from Figure 5.5a to e clearly demonstrates the variance of the structure within the thin film. Compared to the Figure 5.5a, the appearance of the pronounced vertical Brag rods in Figure 5.5b to e indicate the ordered pore arrangement within the probed thin film. [82]

For the quantitative analysis, the horizontal line cut at the Yoneda peak position are performed (the position indicated by the red arrow in Figure 5.5a). As shown in Figure 5.5f, the broad shoulder in the line cut of the thin film prepared with 0.5 vol.% HCl can be attributed to the nanostructures with relatively disordered spatial arrangement. In contrast, the conspicuous Bragg peaks appeared with the increased HCl content implys the narrow size distribution and ordered spatial arrangement of the nanostructures. The structure features obtained from the GISAXS data are in accordance with the observation in the SEM measurements (Figure 5.3). Moreover, the feature size variation can be manifested by a closer observation of the peak positions (vertical black dash lines in Figure 5.5f). The first order peak of the thin film prepared with 2.0 vol.%, 4.0 vol.% and 8.0 vol.% HCl are found at the same position, which are slightly right shifted with respect to the 1.0 vol.% HCl addition. The relatively lower q_y value for the thin film with 1.0 vol.% HCl indicates the larger structure distances.

In addition, when the HCl content increases from 1.0 vol.% to 8.0 vol.%, the peak position of the two lattice peaks in the GISAXS profiles remain in the same ratio of $1:\sqrt{3}$, which indicates the existence of hexagonally packed structures. [91] The average spacing d of the microphase-separated structures can be determined from the first-order Bragg diffraction peak q_m by using $d=2\pi \div q_m$. The calculated average spacing d of the thin films with HCl content of 1.0 vol.%, 2.0 vol.%, 4.0 vol.%, and 8.0 vol.% are 30 nm, 26 nm, 26 nm and 26 nm, respectively.

In order to extract the quantitative structure information along the lateral direction, horizontal line cuts are fitted within the framework of the Distorted-Wave Born Approximation (DWBA) using an Effective Interface and Local Monodisperse Approximation (EIA and LMA). Gaussian-distributed form factors in the applied model represent scattering centers placed on a one-dimensional (1D) paracrystal lattice. [102] The scattering

signal is approximated by incoherently superposing the scattering intensities of the individual standing cylindrical substructures(Figure 5.4). [22] Error bars indicate the scope of goodness of fitting. Within this model, all data in Figure 5.5f are fitted with two structure factors (center to center distances) and two form factors (radii). As marked by the gray area in Figure 5.5f, the pronounced scattering peaks in the high q region are well fitted with the small radii and center to center distances, which are indicated by the dark yellow circles in Figure 5.5g and h. Specifically, the center to center distance of the thin films with 0.5 vol.%, 1.0 vol.%, 2.0 vol.%, 4.0 vol.% and 8.0 vol.% HCl are fitted to be (30 ± 3) nm, (30 ± 1) nm, (26 ± 1)nm, (26 ± 1) nm and (26 ± 1) nm, which are well consistent with the preliminary calculation result by using d=$2\pi \div q_m$. [91] The corresponding structure radius are fitted to be (4.5 ± 0.3) nm, (3.9 ± 0.5) nm, (3.8 ± 0.3) nm, (3.6 ± 0.4) nm and (3.7 ± 0.4) nm. Therefore, the average pore sizes of the titania thin films can be extracted by the following equation: [68]

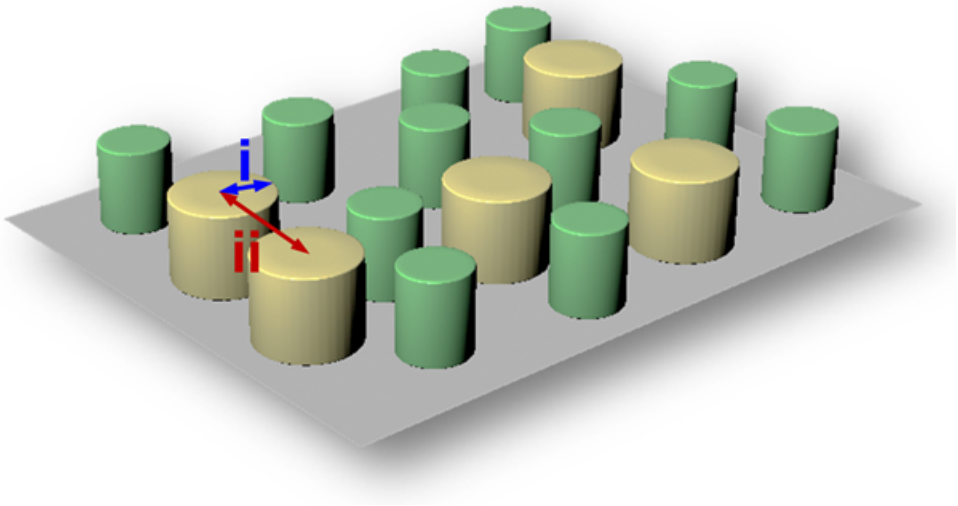

Figure 5.4: *Schematic illustration of the model used for the GISAXS fits. The scattering signal is approximated by incoherently superposing the scattering intensities of the individual standing cylinder substructures. Structure factors (center to center distances) and form factors (radii) of the scattering objects are represented as i and ii in the scheme. Reproduced from Ref [55] with permission from JOHN WILEY AND SONS, Copyright 2020.*

$$Pore\ size = center\ to\ center\ distance - 2\ \times structure\ radius \tag{5.2}$$

The pore sizes of the thin film prepared with 0.5 vol.%, 1.0 vol.%, 2.0 vol.%, 4.0 vol.% and 8.0 vol.% HCl are determined to be (21 ± 4) nm, (22 ± 2) nm, (18 ± 2) nm, (19 ± 2) nm and (19 ± 2) nm, respectively, which are in good agreement with the SEM topography shown in Figure 5.3.

The feature in the low q_y region, marked with the yellow part in Figure 5.5f, indicating the existence of large structures. The fitted center to center distances and radii are represented as purple circles as shown in Figure 5.5g and h, respectively. Specifically, the center to center distances of the thin films prepared with 0.5 vol.%, 1.0 vol.%, 2.0 vol.%, 4.0 vol.% and 8.0 vol.% HCl are (56 ± 4) nm, (32 ± 2) nm, (30 ± 2) nm, (28 ± 2) nm and (28 ± 2) nm. The corresponding radii are (11 ± 2) nm, (13 ± 1) nm, (12 ± 1) nm, (10 ± 1) nm and (11 ± 1) nm. With the same method mentioned above, the pore size calculated by the large structures for the samples with 0.5 vol.%, 1.0 vol.%, 2.0 vol.%, 4.0 vol.% and 8.0 vol.% HCl are (34 ± 7) nm, (4 ± 2) nm, (6 ± 4) nm, (7 ± 4) nm and (6 ± 4) nm, which are also visible in the SEM images. The good consistency of the SEM topography and the GISAXS data suggests that the surface morphology is also present within the bulk of the thin films.

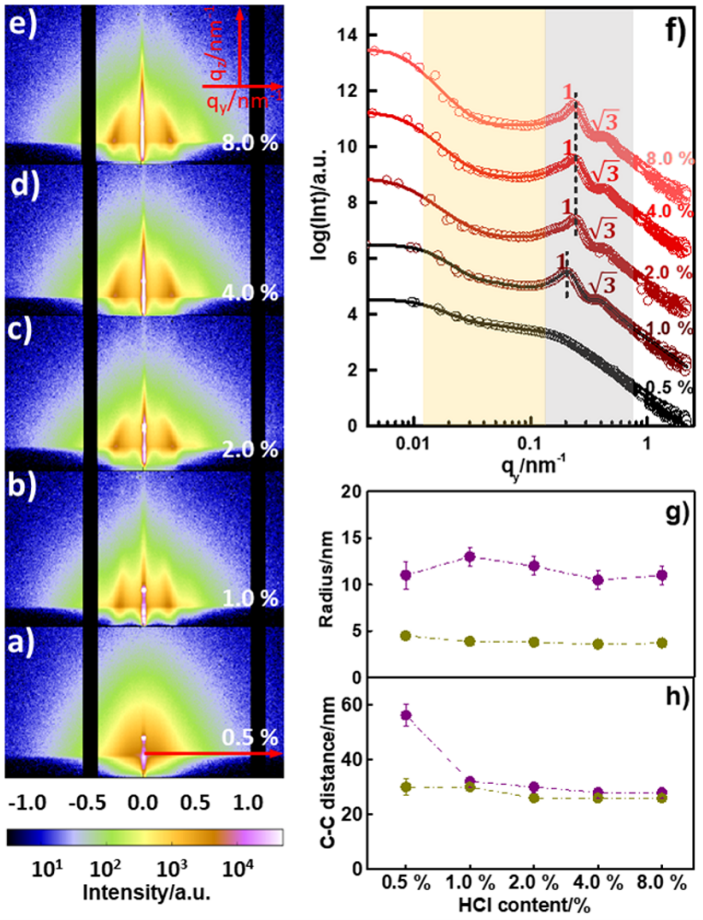

Figure 5.5: *a-e) 2D GISAXS data of the titania thin films prepared with THF solvent, the corresponding HCl content added in the sol-gel solution is noted in the lower right corner.f) horizontal line cuts of the 2D GISAXS data. The measured data are plotted as hollow circles and the fitting results are shown as solid lines, respectively. All curves are shifted along the intensity axis for clarity of presentation. Extracted structure g)radii and h) center-to-center distances as a function of the HCl content. Dark yellow circles refer to the small-sized structure and purple circles indicate the large-sized structure. Reproduced from Ref [55] with permission from JOHN WILEY AND SONS, Copyright 2020.*

5.6 TiO_2 with TB solvent: surface morphology

Figure 5.6 refers to the titania nanostructures prepared with different HCl addition in the TB solvent. As shown in Figure 5.6a and b, when the volume fraction of HCl increases from 0.5 vol.% to 2.0 vol.%, a significant structural transition from large clusters to isoporous structures is visible, which can also be reflected by the corresponding FFT patterns.

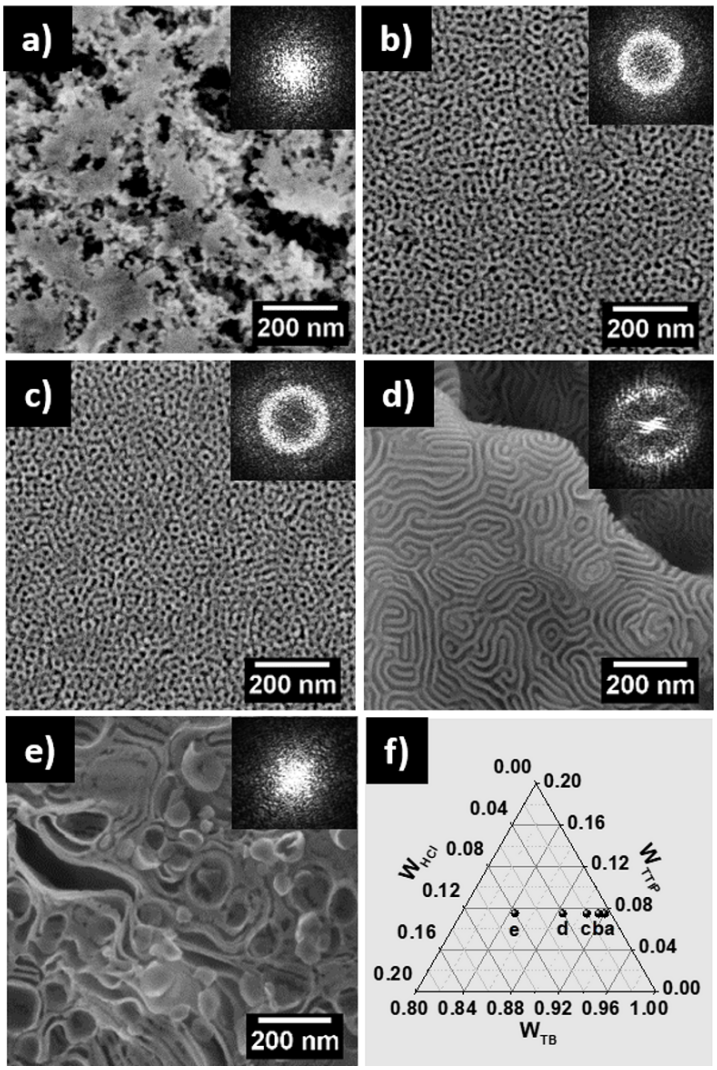

Figure 5.6: *SEM images of the titania thin films prepared with TB azeotrope solvent. The up-right insets refer to the corresponding fast Fourier transform (FFT) patterns. The volume fraction of HCl is exponentially increased from a) 0.5 vol.% to e) 8.0 vol.%. f) Component phase diagram of the respective samples. Reproduced from Ref [55] with permission from JOHN WILEY AND SONS, Copyright 2020.*

When the volume fraction of HCl reaches 4.0 vol.%, the sol-gel solution turns to turbid, which may result from the formation of micrometer-sized aggregates in the solution. [18] Due to the existence of these aggregates, the spin-coated thin films with 4.0 vol.% HCl exhibit discontinuous structures, which is well visible under low magnification in the SEM topography (Figure 5.7a). Figure 5.6d shows the uneven lamellar structure within a large aggregate. A further HCl addition yields a coexistence of the lamellae and vesicle structures (Figure 5.6e). The structure transition mechanism along with the HCl addition in Figure 5.6 can also be illustrated in the perspective of the surface energy between the

PS block and the poor solvent. The existence of the large cluster in Figure 5.7a could be attributed to the weak repulsion force among the hydrolyzed titania nano-dot arrays, which greatly reduced the template effect of the block copolymer. With the increase of the HCl content, the aggregation behavior is significantly suppressed. As a result, a morphology transition from sphere to cylinder, and then a hybrid structure of lamellae and vesicle is observed in the titania thin film. As mentioned before, the final morphology of titania is almost unaffected by the solvent-induced self-assemble process. Thus, it is reasonable to ascribe the titania morphology to the various micelle shapes in the solution.

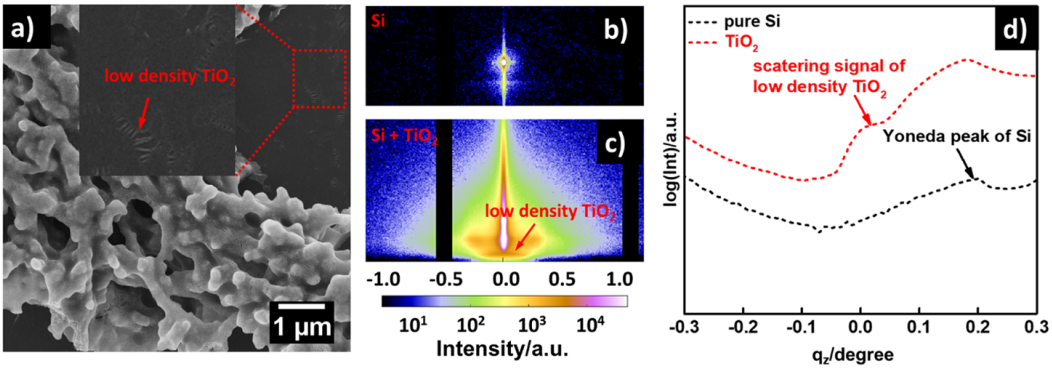

Figure 5.7: *a) Low magnified SEM topography of the titania thin films prepared with 4.0 vol.% HCl addition and TB solvent, b) 2D GISAXS data of bare silicon wafer and c) titania thin film prepared with 4.0 vol.% HCl addition and TB solvent; d) zoom-in the vertical line cuts of the 2D GISAXS patterns. Reproduced from Ref [55] with permission from JOHN WILEY AND SONS, Copyright 2020.*

It is worth to be noted that, with progressive poor solvent addition in the block copolymer solution, the spherical micelles are usually the first aggregates to form and they can be considered as the starting morphology for other aggregates, as the PS chains in spherical micelles are usually more stretched than in cylinders, lamellae or vesicles. [97] With the increased surface energy between PS blocks and poor solvent, the stretching of the PS chains is greatly reduced. As a result, more thermodynamically favorable morphology, such as lamellae and vesicles are formed. The coexistence structure of lamellae and vesicle in Figure 5.6e could be explained by the following three possibilities. Firstly, the stability boundaries for lamellae and vesicle are overlapping during the poor solvent addition process. [103] Secondly, the coexistence of lamellae and vesicle might be a true thermodynamic phenomenon which depends on the free energy difference between them. [104] Thirdly, the polydispersity of the bulk polymer may also account for the coexistence the structure. [105]

Compared to the morphologies shown in Figure 5.3, more intriguing structures, such as cylinder, lamellae and vesicle structures in Figure 5.6d and e, are obtained in the TB sol-gel system. Considering the low dielectric constant of the solvent (THF: 7.58, TB: 6.79, 1,4-dioxane: 2.25) and nonionizing properties of the PS and PEO blocks, the repulsion force among the polymer chains provoked by ionization is negligible. [97] Therefore the morphology variation of the titania thin film with respect to different solvent category can be analyzed in the perspective of the polymer-solvent interaction parameter(χ). [106]

$$\chi_{P-S} = V_S \left(\delta_S - \delta_P\right)^2 RT + 0.34 \tag{5.3}$$

Where V_S and δ_S are the molar volume and solubility parameter of the solvent, δ_P is the solubility parameter of the polymer, R is the gas constant, T is the Kelvin temperature. The characteristics of the different solvent and polymer can be taken from the literatures(e.g. polymer handbook, table 5.1). [107] As shown in table 5.1, the solubility parameter of the solvent (Hansen solubility parameterδ_H) consists of three parts: dispersive δ_d, permanent dipole–dipole interaction δ_p and hydrogen bonding forces δ_h.

$$\delta_H^2 = \delta_d^2 + \ \delta_p^2 + \ \delta_h^2 \tag{5.4}$$

In the case of the mixed TB solvent, the solubility parameter and molar volume are calculated by the sum of the products of the component value with their volume fractions. [108].

	$\delta(\mathrm{MPa}^{1/2})$				$V_S(\mathrm{cm}^2/\mathrm{mol})$
	δ_H	δ_d	δ_p	δ_h	
THF	19.4	16.8	5.7	8.0	79.7
TB	19.6	17.4	2.6	5.9	101.8
1,4-dioxane	20.5	19.0	1.8	7.4	88.5
PS	18.6	18.6	0.2	0.0	
PEO	19.9	17.3	3.0	9.4	

Table 5.1: *Characteristics of the different solvent and polymer. [109]*

The volume ratio of toluene and 1-butanol in the mixed solvent is 71.4 : 28.6 in the present work. Table 5.2 shows the corresponding polymer-solvent interaction parameters calculated by:equation 5.6 According to the Flory-Huggins theory, the polymer and solvent are completely miscible when χ_{P-S} is less than 0.5, and the smaller χ_{P-S} value means the better solubility of the polymer. As shown in table 5.2, all of the solvents used in this work are good solvents for both PS and PEO blocks. Nevertheless, the difference between $\chi_{S-PS}$and χ_{S-PEO} gives the preferential affinity of the solvent for a certain block:

$$\Delta\chi = \chi_{S-PS} - \chi_{S-PEO} \tag{5.5}$$

According to table 5.2 and equation 6.7, the $\Delta\chi$ of THF and TB are 0.01 and 0.04, respectively, which suggests both of the solvents have a slightly preferential affinity for the PEO block.

χ	THF	TB	1,4-dioxane
PS	0.36	0.38	0.47
PEO	0.35	0.34	0.35

Table 5.2: *Calculated polymer-solvent interaction parameters χ_{P-S} of different polymer-solvent pairs. [109]*

In addition, compared with THF, the relative higher $\Delta\chi$ of TB implies the stronger affinity between the PEO block and the TB solvent, which means a higher swelling degree of the PEO domain in the TB solvent. The different preferential affinity of THF and TB solvent for the polymer blocks might be the reason for the different morphologies seen in Figure 5.3 and Figure 5.6. The morphological difference is only conspicuous at 4.0 vol.% and 8.0 vol.% HCl content, and very similar morphologies are shown with 0.5 vol.% and 2.0 vol.% HCl addition. Thus, it is concluded that when two kinds of solvent possess comparable $\Delta\chi$ value, the spin coated thin films prefer to show similar micro-phase separated structures under relative low HCl content. While a distinct morphology deviation will be manifested with progressive HCl addition.

5.7 TiO_2 with TB solvent: innner morphology

The 2D GISAXS data of the titania thin films prepared with TB solvent are shown in Figure 5.8a to e. Regarding the thin films prepared with 0.5 vol.% and 8.0 vol.% HCl, the smeared scattering patterns in the lateral direction can be ascribed to the wide size distribution of the nanostructures parallel with the silicon substrate (corresponding to the SEM images of Figure 5.6a and e). In comparison, two symmetrically arranged Bragg peaks are shown for the thin film prepared with 1.0 vol.% and 2.0 vol.% HCl addition, which signifies a highly organized arrangement in the lateral direction. Compared to the 2D GISAXS data in Figure 5.8b and c, a greatly broadened scattering peak in the case of 4.0 vol.% HCl addition is observed in Figure 5.8d, which might result from the anisotropic structure of the cylinders (Figure 5.6d). Moreover, compared with other 2D GISAXS data, two intensity maxima are visible between the specular beam and the sample horizon in Figure 5.8d. As mentioned above, due to the formation of large aggregates, the thin film prepared with 4.0 vol.% HCl addition exhibits discontinuous structures on the

silicon substrate.Figure 5.7a demonstrates the significant structural difference between the aggregates and the region marked with the red frame. It is well known that the scattering signal in the vertical direction is associated with the material density, and the sporadic titania species scattered on the exposed silicon wafer possess much lower density than that of the aggregates. Thus, it is reasonable to ascribe the additional peak at lower scattering angle to these low-density titania structures. To determine whether the scattering signal comes from the silicon substrate or the titania layer, an additional GISAXS characterization of the bare silicon substrate is performed under the same incident angle. According to the 2D GISAXS data of bare silicon in Figure 5.7b, a weak Yoneda peak is visible between the specular beam and the sample horizon only. To further compare the Yoneda peak position of silicon and titania thin films, the vertical line cuts at the same q_y value are performed and shown in Figure 5.7d. It is observed that the silicon substrate and the titania thin film possess quite close Yoneda region at around 0.2, and the additional peak at low q_y position for titania is not found in the line cut of the silicon substrate. Therefore, the particular peak for titania at the low q_y region can be assigned to the discontinuous titania nanostructures on the silicon substrate.

For quantitative analysis, the horizontal line cuts are performed at the Yoneda region of porous titania and shown in Figure 5.8f. The horizontal line cuts in low q_y and high q_y region can be analyzed separately as a function of the shape and intensity difference of the scattering peaks. Regarding the high q_y region in the gray area, the significantly smeared peak seen in the horizontal line cuts of the thin films prepared with 0.5 vol.% and 8.0 vol.% HCl is cuased by the wide size distribution of the nanostructures. On the other hand, for the thin films prepared with 1.0 vol.%, 2.0 vol.% and 4.0 vol.% HCl, conspicuous scattering peaks are observed. The first-order peak of the three line cuts are marked with black dash lines, which can be used for estimating the spacing d of the microphase-separated structures by the equation of $d=2\pi q_m$. The calculated d value for the thin film prepared with 1.0 vol.%, 2.0 vol.% HCl are 24 nm, 22 nm, which can be assigned to the spacing between the neighboring nanowalls (Figure 5.6b and c). As mentioned above, the surface energy between the PS block and the surrounding solvent increases with continuous HCl addition. As a result, the stretch of the hydrophobic PS chains is progressively inhibited, which lead to the decrease of the pore size from Figure 5.6b (24 nm) to Figure 5.6c (22 nm). Furthermore, the relative positions of the first and second-order Bragg peaks of the samples prepared with 1.0 vol.% and 2.0 vol.% HCl are also following a $1:\sqrt{3}$ ratio, which suggests the presence of hexagonally organized structures over a macroscopic scale. The d value of the thin film prepared with 4.0 vol.% HCl are calculated to be 28 nm, which can be attributed to the distance between the adjacent cylinders (Figure 5.6d).

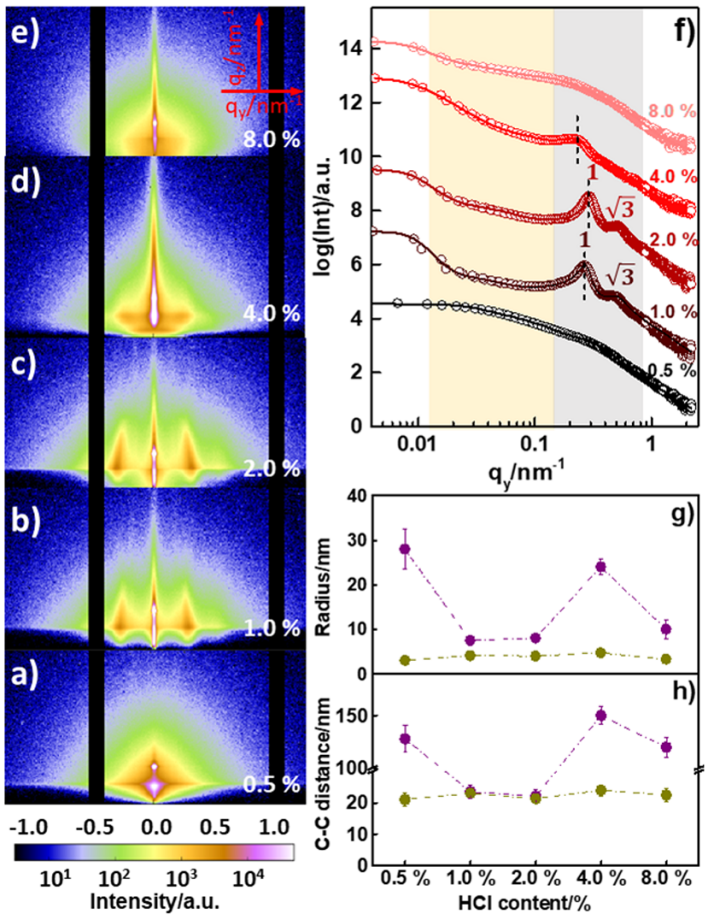

Figure 5.8: *a-e) 2D GISAXS data of the titania thin films prepared with TB solvent, the corresponding HCl content added in the sol-gel solution is noted in the lower right corner.f) horizontal line cuts of the 2D GISAXS data. The measured data are plotted as hollow circles and the fitting results are shown as solid lines, respectively. All curves are shifted along the intensity axis for clarity of presentation. Extracted structure g)radii and h) center-to-center distances as a function of the HCl content. Dark yellow circles refer to the small-sized structure and purple circles indicate the large-sized structure. Reproduced from Ref [55] with permission from JOHN WILEY AND SONS, Copyright 2020.*

Similarly, in the framework of the DWBA, all the line cuts in Figure 5.8f are well fitted with two structure factors and two form factors. The large structures are denoted as purple circles and small structures are represented as dark yellow circles, respectively (Figure 5.8g and h). The pronounced scattering signals in high q_y region are well fitted with the small structures. Specifically, the center to center distance of the thin films prepared with 0.5 vol.%, 1.0 vol.%, 2.0 vol.%, 4.0 vol.% and 8.0 vol.% HCl are fitted to be (21 ± 2) nm, (23 ± 1) nm, (21 ± 1) nm, (24 ± 2) nm and (22 ± 2) nm. The corresponding radius are (3.0 ± 0.3) nm, (4.1 ± 0.2) nm, (4.0 ± 0.1) nm, (4.7 ± 0.5) nm and (3.3 ± 0.5)

nm. With the method mentioned above, the calculated pore size contributed by the small structures are (15 ± 3) nm, (15 ± 2) nm, (13 ± 1) nm, (15 ± 3) nm and (16 ±3) nm. On the other hand, the scattering signals at low q_y region are fitted with large structures. The center to center distances of the large structures with 0.5 vol.%, 1.0 vol.%, 2.0 vol.%, 4.0 vol.% and 8.0 vol.% HCl addition are fitted to be (128 ± 13) nm, (25 ± 2) nm, (22 ± 2) nm, (150 ± 10) nm and (120 ± 10) nm. The corresponding radii are (28.0 ± 4.5) nm, (7.5 ± 0.4) nm, (8.0 ± 0.2) nm, (24.0 ± 1.8) nm and (10.0 ± 2.1) nm. As a result, the pore size afforded by the large structures are (72 ± 2) nm, (9 ± 3) nm, (6 ± 3) nm, (102 ± 12) nm and (100 ± 14) nm. The much higher pore radii within the thin films prepared with 0.5 vol.%, 4.0 vol.% and 8.0 vol.% HCl can be clearly observed in Figure 5.9.

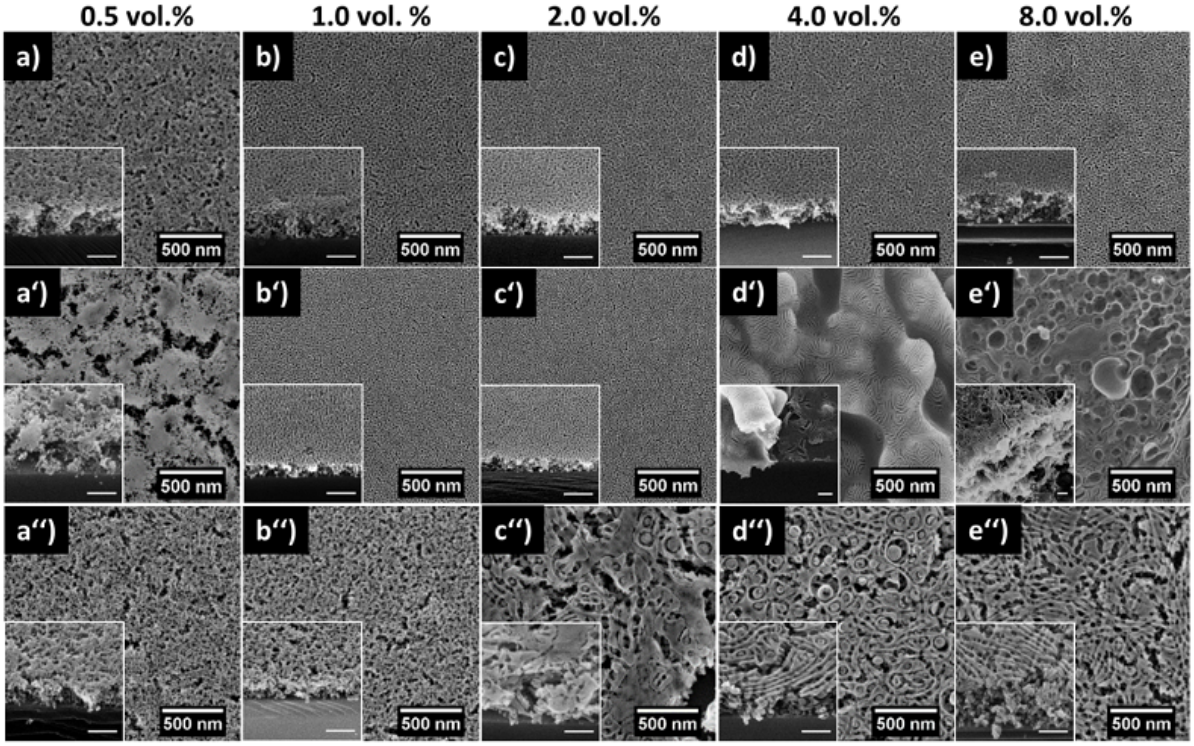

Figure 5.9: *SEM topography of the titania thin films prepared with THF (a-e), TB (a'-e'), and 1, 4-dioxane (a"-e"). Scale bar of the cross section images: 200 nm. The content of concentrated HCl added in corresponding sol-gel stock solutions are labeled on the top of each column. Reproduced from Ref [55] with permission from JOHN WILEY AND SONS, Copyright 2020.*

5.8 TiO_2 with 1,4-dioxane: surface morphology

Figure 5.10 refers to the SEM images of titania thin film prepared with 1, 4-dioxane. As shown in Figure 5.10a and b, the randomly stacked nanostructures similar with the THF and TB system are obtained with low HCl addition (0.5 vol.% and 1.0 vol.%), which can be assigned to the weak phase separation of the sol-gel solution and the aggregation of the nanoparticles. However, with increasing HCl addition, such as in case of the volume fraction of 2.0 vol.% in Figure 5.10c, a coexisting structure of nanowires and large aggregates is obtained. The formation of the inhomogeneous structures can be attributed to the variation of the surface energy between PS blocks and surrounding solvent. Compared to the random structures, the formation of the nanowires in Figure 5.10c effectively accommodates the extra surface energy resulting from the higher HCl content. However, the decreased surface energy associated with the phase transition makes it difficult to keep the stability of the new sol-gel system. As a consequence, some large aggregates are formed. With the further HCl addition, the aggregation process is significantly inhibited by the enhanced surface energy between the PS blocks and the surrounding solvent. Consequently, the structures with high specific surface area are formed as seen in Figure 5.10d and e. As mentioned above, for the micro-phase separated block polymer system, the spherical micelles are usually the first aggregates to form. However, unlike the thin film prepared with THF, and TB, the structure transition from random to sphere is not found in the case of 1, 4-dioxane. The direct structure transition from a random to a cylinder morphology might be attributed to the formation of large aggregates in case of 1.0 vol.% HCl addition. These aggregates possess much larger size than that of the microphase-separated cylinders, which consumes plenty of TTIP. Consequently, the TTIP or Ti-O- content in the microphase-separated regions is significantly decreased. Since the stretch of the PEO blocks region can be modified by the content of hydrophilic Ti-O-structures, a new microphase separated morphology might be provoked by the formation of the aggregates. In addition, compared with THF and TB, the much higher $\Delta\chi$ value of 1, 4-dioxane cause a full stretching of the PEO block, which also facilitates the formation of the more asymmetric micro-phase separated structures.

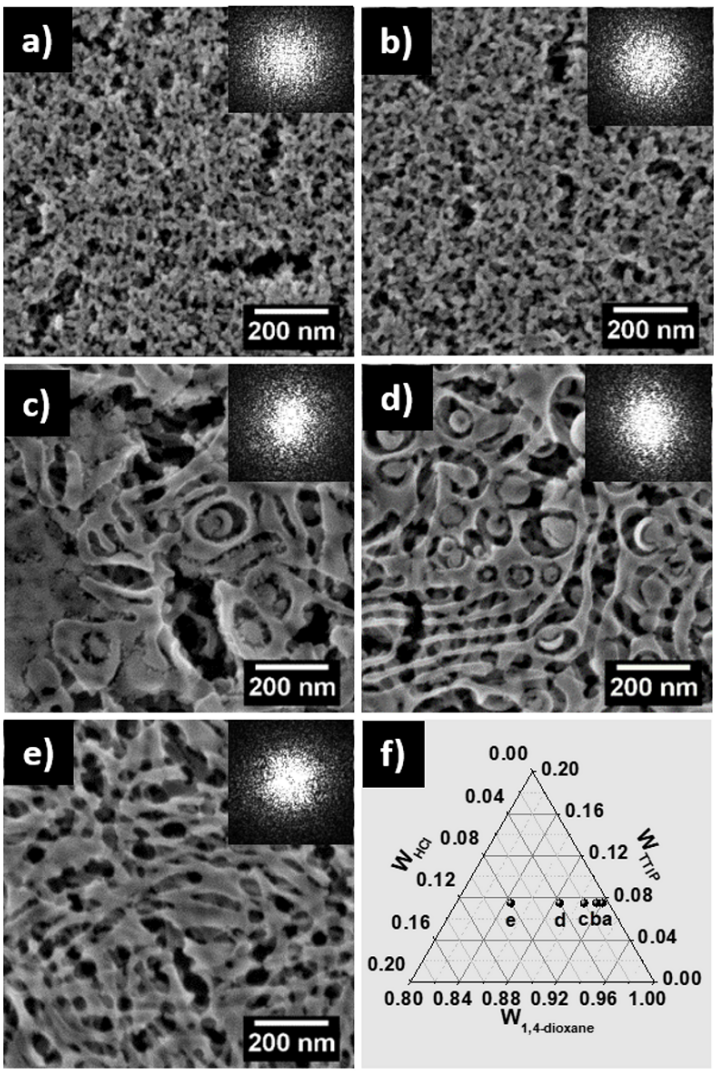

Figure 5.10: *SEM images of the titania thin films prepared with 1,4-dioxane solvent. The upright insets refer to the corresponding fast Fourier transform (FFT) patterns. The volume fraction of HCl is exponentially increased from a) 0.5 vol.% to e) 8.0 vol.%. f) Component phase diagram of the respective samples. Reproduced from Ref [55] with permission from JOHN WILEY AND SONS, Copyright 2020.*

5.9 TiO_2 with 1,4-dioxane: inner morphology

The 2D GISAXS data and corresponding horizontal line cuts are shown in Figure 5.11a to f. It is observed that for all samples a smeared peak along the q_y axis is present, which signifies the wide size distribution and random orientation of the structures within the thin film. [22]. However, a peak center can still be found for each horizontal line cut, which is marked out with black dash line in Figure 5.11f. The shift of the broad

peaks with progressive HCl addition suggests the increase of the pore size within the thin films.Similarly, for the quantitative analysis, all horizontal line cuts at the Yoneda position are fitted within the framework of the DWBA. As shown in Figure 5.11g and h, the thin films prepared with 0.5 vol.%, 1.0 vol.%, 4.0 vol.% and 8.0 vol.% HCl are fitted with two structure factors and two form factors. The large structures are denoted as purple circles and small structures are represented as dark yellow circles, respectively (Figure 5.11g and h). For the small structures, the center to center distance of the thin films with 0.5 vol.%, 1.0 vol.%, 2.0 vol.%, 4.0 vol.% and 8.0 vol.% HCl addition are fitted to be (42 ± 4) nm, (42 ± 3) nm, (43 ± 4) nm and (44 ± 5) nm. The corresponding radii are (3.5 ± 0.9) nm, (4.2 ± 1.0) nm, (3.4 ± 1.0) nm and (3.6 ± 1.0) nm. As a result, the pore size contributed by the small structures are (35 ± 5) nm, (34 ± 5) nm, (36 ± 6) nm and (37 ± 7) nm. For the large structures, the center to center distance of the thin films prepared with 0.5 vol.%, 1.0 vol.%, 4.0 vol.% and 8.0 vol.% HCl are fitted to be (51 ± 5) nm, (50 ± 5) nm, (74 ± 5) nm and (73 ± 5) nm. The corresponding radii are (7.5 ± 1.2) nm, (7.2 ± 1.1) nm, (9.5 ± 1.0) nm and (9.0 ± 1.0) nm. With the method mentioned above, the calculated pore size contributed by the large structures are (36 ± 7) nm, (36 ± 7) nm, (55 ± 7) nm and (55 ± 7) nm. However, for the thin film prepared with 4.0 vol.% HCl addition, an additional large structure factor and form factor in terms of the aggregates are introduced for getting a good fitting result. As shown in Figure 5.11g and h, the fitted small, middle and large structures are represented as dark yellow, purple and dark cyan colors, respectively. The center to center distance of the small, middle and large structures are fitted to be (39 ± 4) nm, (75 ± 5) nm and (500 ± 30) nm. The corresponding structures radius are (3.8 ± 1.0) nm, (9.7 ± 1.0) nm and (60 ± 5) nm. Therefore, the calculated pore size contributed by the small, middle and large structures are (31 ± 6) nm, (56 ± 7) nm and (380 ± 37) nm, respectively.

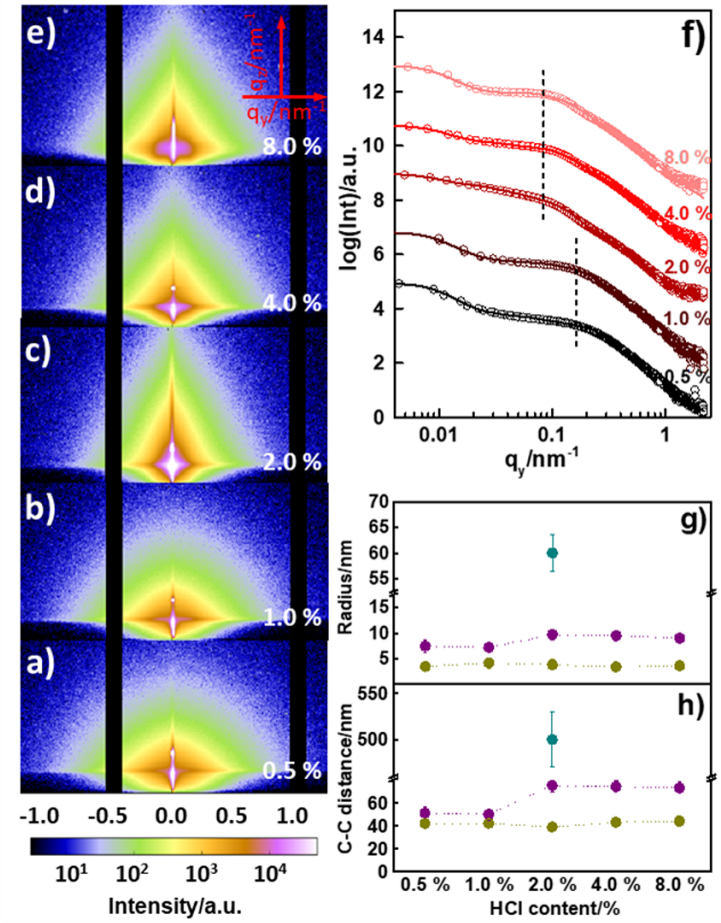

Figure 5.11: *a-e) 2D GISAXS data of the titania thin films prepared with 1,4-dioxane solvent, the corresponding HCl content added in the sol-gel solution is noted in the lower right corner.f) horizontal line cuts of the 2D GISAXS data. The measured data are plotted as hollow circles and the fitting results are shown as solid lines, respectively. All curves are shifted along the intensity axis for clarity of presentation. Extracted structure g)radii and h) center-to-center distances as a function of the HCl content. Dark yellow circles refer to the small-sized structure and purple circles indicate the large-sized structure. Reproduced from Ref [55] with permission from JOHN WILEY AND SONS, Copyright 2020.*

In order to comprehensively compare the nanostructures synthesized with different solvent category and HCl content, the combined surface and cross-section SEM images of all titania thin films are listed in Figure 5.9. According to Figure 5.9, the high structural consistency at the surface and cross-section suggests the isotropic characteristics of the nanostructures within the bulk of the thin films. Furthermore, it is found that the peak positions and broadness shown in the PSD profiles exhibit good consistency with the horizontal line cuts of the GISAXS data, which suggests the superior homogeneity of the thin films over a large area (Figure 5.12).

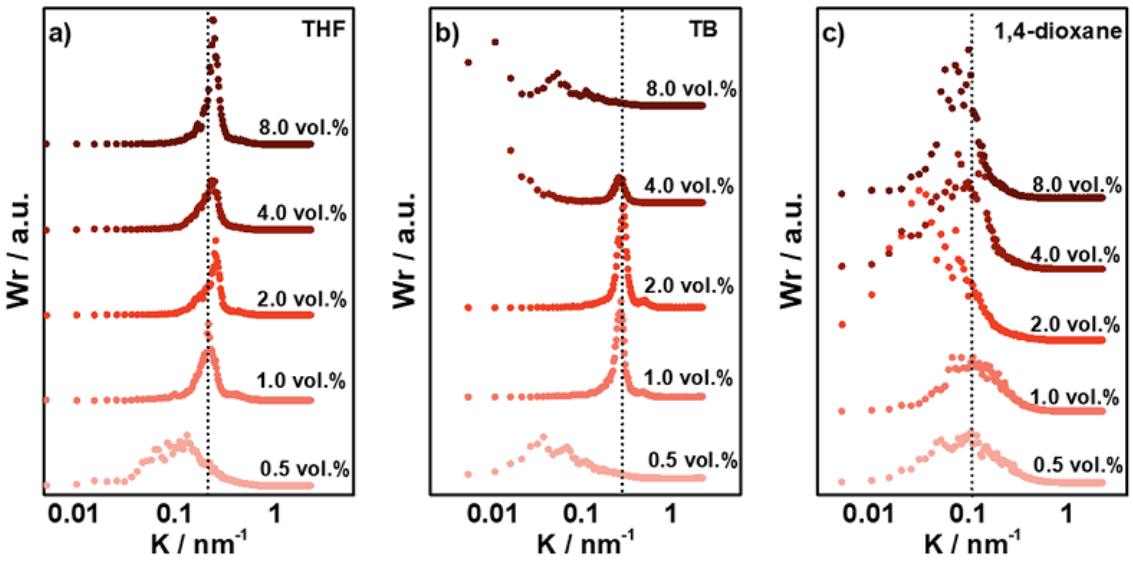

Figure 5.12: *Power spectral density (PSD) functions extracted from the SEM data. The volume fraction of HCl added into the solution is noted on the top of each data set and the utilized solvent category are noted at the upper-right of the each figure. The PSD profiles are shifted for clarity along y axis. The black dash lines are made to identify the difference of peak positions. Reproduced from Ref [55] with permission from JOHN WILEY AND SONS, Copyright 2020.*

Based on the SEM topography shown in Figure 5.9, a schematic phase diagram of PS-b-PEO/titania composite as a function of HCl content and $\Delta\chi$ value are plotted and shown in Figure 5.13a. It is observed that, when the HCl volume fraction is 0.5 vol.%, all of the thin films exhibit random structures, which can be assigned to the low surface energy between the PS blocks and the surrounding solvent. With the progressive addition of HCl, different phase separated nanostructures are formed. In the THF solvent, no obvious structure variation can be observed from 1.0 vol.% to 8.0 vol.% HCl addition, which suggests the weak influence of HCl content on thin film morphology under low $\Delta\chi$ value. However, a significant structure variation occurs at the region of $\Delta\chi > 0.01$ and $W_{HCl} > 0.5$ vol.%. In this region, a structure transition from sphere to cylinder, and then to lamellae-vesicle mixture is observed in the case of TB solvent. For 1,4-dioxane, a structure transition from random to cylinder-aggregates mixture, and then to pure cylinders is exhibited. The different structures formed with the same HCl content can be assigned to the different $\Delta\chi$ values of the solvent, which reflects the different preferential affinity of the solvent to a certain block.

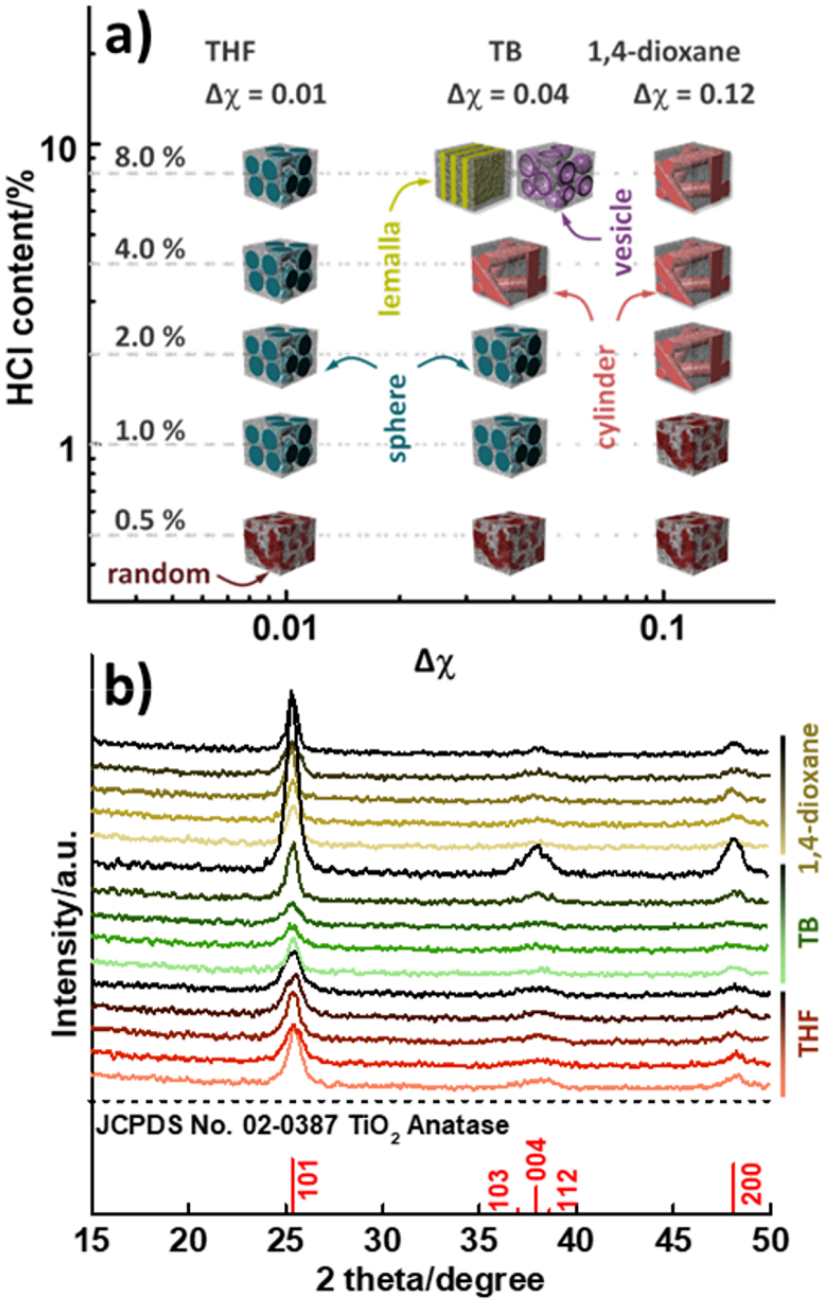

Figure 5.13: *a) Phase diagram of PS-b-PEO/titania composite prepared with different solvent and HCl content, b) X-ray diffraction (XRD) patterns of the calcined thin films. The HCl concentration from 0.5 vol.% to 8.0 vol.% in the stock solution is represented with gradient colors (the 8.0 vol.% HCl content is denoted as black color). Reproduced from Ref [55] with permission from JOHN WILEY AND SONS, Copyright 2020.*

It is reported that the crystallinity of titania can be modified by changing the pH value of the sol-gel solvent. [110] Therefore, X-ray diffraction (XRD) measurements are performed for all thin films within a two theta range from 15 to 50 degree. As shown in

Figure 5.13b, the diffraction peaks at 25.3°, 36.9°, 37.9°, 38.6° and 48.1° can be assigned to the (101), (103), (004), (112) and (200) crystal planes of anatase titania phase (JCPDS No. 02-0387). It is observed that the diffraction peaks of all thin films are found in the same position, which suggests no variation in the crystallinity is provoked by the HCl addition in the present work. Moreover, for the thin film prepared with 8.0 vol.% HCl addition in TB solvent, the integrally enhanced peak intensity might simply be caused by more material contributing to scattering. The titania grain size for all samples are calculated by using the Scherrer,s equation:

$$D = \frac{0.9\lambda}{\beta \cos\theta} \tag{5.6}$$

λ refers to the wavelength of the X rays. β denotes the full-width at half maximum in radians, and θ is the Bragg angle. The calculated grains size are listed in table 5.3. The calculated grain size of titania can be explained from the perspective of the thin film morphology and HCl content in the sol-gel solution. Regarding the thin films prepared with THF, it is observed that the grain size of titania is negatively related to the HCl content in the sol-gel solution. The smaller grain size of the titania prepared with higher HCl content can be ascribed to the enhanced electrostatic interactions among the particle surfaces. In contrast to the THF system, the larger grains size formed at relative higher HCl content can be assigned to the formation of new morphology. For instance, the large grain size of titania formed with 4.0 vol.% and 8.0 vol.% in the TB system can be attributed to the formation of cylinder and vesicle structures. Similarly, the big crystal size obtained with 2.0 vol.%, 4.0 vol.% and 8.0 vol.% HCl addition can be ascribed to the formation of novel cylinder structures.

	grain size of titania prepared with different HCl content/nm				
	0.5 vol.%	1.0 vol.%	2.0 vol.%	4.0 vol.%	8.0 vol.%
THF	9.8	7.8	7.4	7.2	7.1
TB	13.1	7.5	7.5	12.9	11.1
1,4-dioxane	10.5	10.2	13.8	12.9	11.3

Table 5.3: *The calculated grains size of different TiO_2 thin films. Reproduced from Ref [55] with permission from JOHN WILEY AND SONS, Copyright 2020.*

5.10 Conclusion

In this section, the synthesis of amphiphilic block co-polymer templated titania nanostructures is systematically investigated in terms of solvent category and HCl content. For

the pore structure characterization, real space SEM measurements and reciprocal space GISAXS measurements are performed. The detailed comparison and analysis demonstrate that the structure transformation for titania thin films in terms of different HCl addition and solvent category is governed by a synergistic effect of the following three factors: Firstly, the surface energy between PS blocks and surrounding solvent. Secondly, the aggregation behavior of the titania nanoparticles. Thirdly, the preferential affinity of solvent. As a poor solvent and catalyst for TTIP hydrolysis, the HCl content affects the degree of stretching of the hydrophilic PS blocks and the aggregation of the titania nanoparticles. The solvent selectivity determines the swelling degree of both blocks. Higher solvent selectivity signifies a more asymmetrical solvent distribution within the micro-phase separated domains, and higher HCl addition results in a more severe contraction of the PS blocks. When the volume fraction of HCl is 0.5 vol.%, a random structure is preferred to form regardless of the solvent selectivity, which can be ascribed to the unsuppressed aggregation of titania nanoparticles and weak phase separation within the thin films. With low solvent selectivity and proper HCl addition, such as the thin films prepared with THF and 1.0 vol.%, 2.0 vol.%, 4.0 vol.% and 8.0 vol.% HCl addition, the almost equally distributed solvent within the two phases and proper surface energy account for the formation of the iso-porous structures. Regarding the medium solvent selectivity of the TB solvent, a typical transition from sphere, cylinder, lamellae, to vesicle related to the variation of surface energy is provoked with the HCl addition. For the solvent with high selectivity, 1,4-dioxane, more asymmetric nanostructures, such as cylinder, are formed by the high preferential affinity of the solvent for the PEO blocks. Irrespective of the morphology, all titania thin films blong to pure anatase phase, which offers tremendous potential in the applications of gas sensor, photocatalytic, photovoltaic, and so on.

6 Templated mesoporous SnO_2 thin films

Parts of this chapter have been prepared as a manuscript:Key Factor Study for Amphiphilic Block Copolymer-Templated Mesoporous SnO_2 Thin Film Synthesis: Influence of Solvent and Catalyst. (YIN, Shanshan, et al. Key factor study for amphiphilic block copolymer-templated mesoporous SnO2 thin film synthesis: Influence of solvent and catalyst. Advanced materials interfaces, 2020, 7. Jg., Nr. 18, S. 2001002.) [111].

6.1 Preface

Nanostructured SnO_2 thin films were widely investigated during the past decades due to its wide band gap. Therefore, they are used in various applications, such as lithium-ion batteries, [112–122] solar cells, [123–131] solar water splitting, [132] gas sensing [133–142] and photoluminescence. [143] Methods reported in the literature for preparing nanostructured SnO_2 thin films include solvothermal synthesis, [114,144,145] reverse microemulsion synthesis, [146] sol-gel synthesis, [147–153] sputter deposition, [139, 154] chemical vapor deposition, [140, 143, 155]electro spinning [156] and electro deposition. [157] Among these preparation approaches, in particular the block copolymer assisted sol-gel chemistry approach features advantages for the large-scale production, since most of the sol-gel reaction can be performed without complicated equipment in the air conditions. Moreover, it is possible to assemble inorganic clusters into thin films with well-controlled crystal sizes, composition and homogeneity. [158] For example, Brezesinski and co-authors synthesized crack-free, mesoporous SnO_2 films by using the amphiphilic diblock copolymer poly(ethylene-co-butylene)-block-poly(ethylene oxide) and the crystallization mechanisms as well as the mesostructural evolution were investigated by a specially constructed 2D small-angle X-ray scattering setup. [82] Roose and co-authors fabricated mesoporous SnO_2

electron selective contacts of perovskite solar cells based on the block copolymer poly(1,4-isoprene-b-ethylene oxide) to achieve stable perovskite solar cells, which showed good performance under UV light in inert atmosphere. [126] Chi and co-authors synthesized a series of mesoporous SnO_2 thin films with the amphiphilic graft copolymer poly(vinyl chloride)-g-poly(oxyethylene methacrylate), which showed significantly different gas-sensing performances as function of the SnO_2 porosity. [141] Although mesoporous SnO_2 thin films prepared with block copolymer templates have shown applications in many fields, the key factors governing the final film morphology during the preparation process were rarely discussed. However, a more detailed understanding of the reaction conditions for the block copolymer assisted sol-gel chemistry approach to synthesize mesoporous SnO_2 thin films is a crucial factor for real-world application.

Typically, the following requirements should be met during the preparation of the metal oxide thin films with block copolymer assisted sol-gel chemistry. A good solvent for both polymer blocks is required for dissolving the block copolymer and a poor solvent for one of the blocks is required to stimulate the phase separation of the sol-gel system. To avoid the occurrence of macroscopic phase separation in the sol-gel solution, a good miscibility between good and poor solvent is necessary. In order to integrate the functional inorganic part into the micro-phase separated block polymer network, a hydrogen bond interaction between the precursor molecules and a specific segment of the block copolymer template is expected. [158] According to previous studies, the factors that affect the microstructure of the block copolymer templated metal oxide thin films include the reaction time, [82] the component content, [18,67,159] the surface conditions of the substrate, [14] the operational environment [160] and the way of removing the polymer template. [16]

In this section, the amphiphilic diblock copolymer polystyrene-block-poly(ethylene oxide) (PS-b-PEO) is used as template and $SnCl_4$ is utilized as precursor to fabricate mesoporous SnO_2 thin films. The morphology control of the SnO_2 thin films is realized by changing two key factors in the sol-gel stock solution: the content of hydrochloric acid catalyst and the category of the organic solvent (tetrahydrofuran or 1,4-dioxane). As a poor solvent for the PS blocks, the preferential affinity of the solvent to the different polymer blocks can be significantly changed with the addition of the hydrochloric acid. Through the complexation effect between $SnCl_4$ and the solvent molecules (here refers ro THF or 1,4-dioxane), the $SnCl_4$ precursor can be temporarily frozen before adding hydrochloric acid catalyst. This leads to the sustained release and a controlled hydrolysis of $SnCl_4$. As a result, the formation of big clusters due to the rapid hydrolysis of $SnCl_4$ is significantly inhibited and a mesoscale structure can be formed. Due to the synergistic effect of hydrochloric acid and the organic solvent, different mesopore structures such as spherical, cylindrical and vesical structures are successfully obtained. The thin film mor-

phology in the local and large area are probed with scanning electron microscopy (SEM) and grazing-incidence small angle X-ray scattering (GISAXS). By correlating different characterization results with the preparation method, the thin film morphology evolution is understood to originate from the preferential affinity of the utilized solvent mixture and the hydrogen bond interaction between the cycloether and H_2O molecules.

6.2 Experimental: synthesis of mesoporous SnO_2

To investigate the effect of the solvent category and poor solvent addition on the thin film morphology, two different solvents (THF and 1,4-dioxane) and four different hydrochloric acid volumes (50 μL, 100 μL, 150 μL and 200 μL) were utilized for the sol-gel stock solution preparation. In order to prevent the formation of big clusters due to the vigorous hydrolysis reaction of the $SnCl_4$ precursor, 2.0 mL THF or 1,4-dioxane solvent were divided in to smaller portions of 1.5 ml and 0.5 mL for the stock solution preparation. 1.5 mL THF or 1,4-dioxane was utilized for dispersing PS-b-PEO and $SnCl_4$ precursor, the rest 0.5 mL THF or 1,4-dioxane was assigned for diluting different volumes of hydrochloric acid (50 μL, 100μL, 150μL and 200μL). Firstly, 21.0 mg PS-b-PEO was added in to 1.5 mL THF or 1,4-dioxane solvent followed by 1 hour continuous stirring to fully dissolve it. Then, 33.8 μL $SnCl_4$ and 0.5 mL diluted hydrochloric acid solution were sequentially pipetted into the well dissolved PS-b-PEO solution.

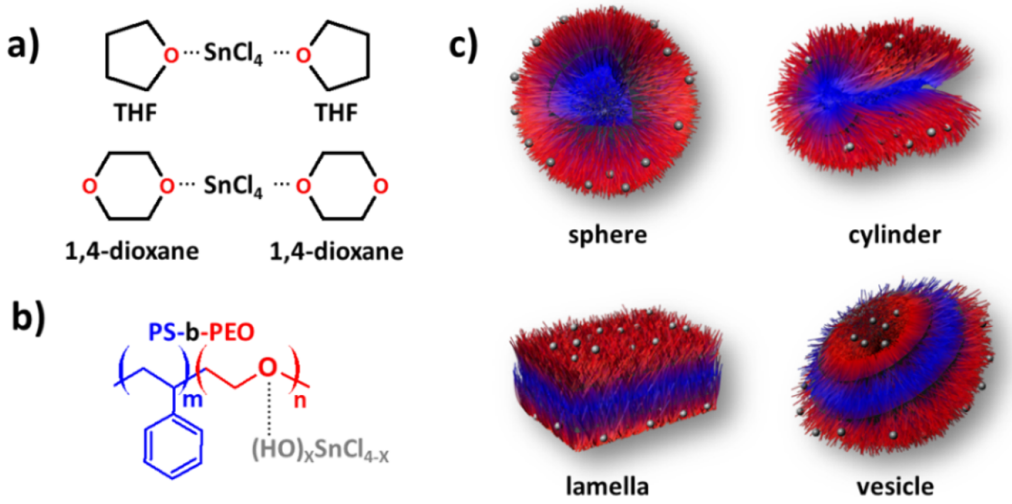

Figure 6.1: *a) Complexation between solvent molecules and $SnCl_4$ precursor; b) hydrogen-bond interaction between the hydrolyzed product of $SnCl_4$ and the PEO block;c) common phase-separated structures formed by amphiphilic diblock copolymers, PS blocks, PEO blocks and hydrolyzed $(HO)_X SnCl_{4-X}$ $(0 \leq x \leq 4)$ species are shown in blue, red and white colors, respectively. Reproduced from Ref [111] with permission from JOHN WILEY AND SONS, Copyright 2020.*

Because of the complexation effect between THF or 1,4-dioxane solvent and $SnCl_4$ molecules, white crystalline solids formed once adding $SnCl_4$ to the solution (figure 6.1a and figure 6.2).The existence of these complexes prevents the intense hydrolysis of $SnCl_4$ from the addition of hydrochloric acid, which accordingly restricts the aggregation of the hydrolyzed $(HO)_X SnCl_{4-X}$ $(0 \leq x \leq 4)$ species in the sol-gel solution. Through hydrogen bond interaction, the $(HO)_X SnCl_{4-X}$ species are specially confined into the hydrophilic PEO domains of the phase separated system (figure 6.1b). The common phase-separated structures, such as spheres, cylinders, lamella and vesicles, that can be formed by the PS-b-PEO polymer template and the hydrolyzed products in the sol-gel system are demonstrated in figure 6.1c. However, the complex crystals were moisture sensitive and rapidly vanished with the addition of diluted hydrochloric acid solution. [82, 161]

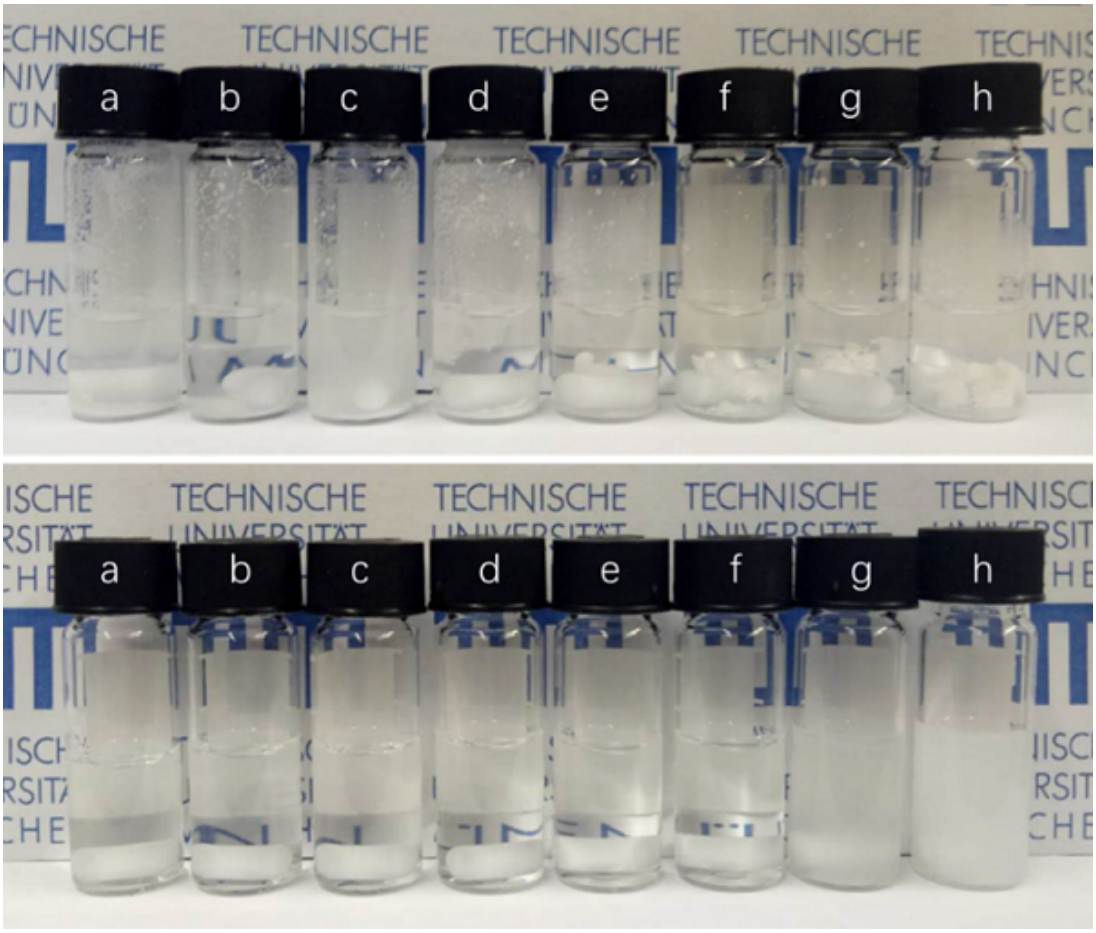

Figure 6.2: *Photographs of the sol-gel solutions prepared with THF (a to d) and 1,4-dioxane (e to h). The picture at the top clearly shows the white crystalline solids by adding $SnCl_4$ in to the cycloether solvent, and the picture below is the corresponding sol-gel solution after adding HCl catalyst. The HCl content added in to the sol-gel solution is 50 µl(a, e), 100µl(b, f), 150µl (c, g), and 200µl(d, h), respectively. Reproduced from Ref [111] with permission from JOHN WILEY AND SONS, Copyright 2020.*

The corresponding component phase diagram of the samples prepared with THF or 1,4-dioxane solvent is shown in figure 6.3). The as prepared sol-gel solution was further stirred for 1 hour to stabilize the hydrogen-bonds formed between the hydrophilic PEO blocks and the hydrolyzed $(HO)_X SnCl_{4-X}$ species. For the thin film deposition, the as prepared sol-gel solutions were spin coated on pre-cleaned silicon substrates with a Delta 6 RC TT spin coater (SÜSS Micro Tec Lithography GmbH) at 2000 rpm for 60 s. For removing the polymer template, the as-spun thin films were calcined at 500 °C for 2 hours with a heating rate of 1 °C min^{-1} in ambient atmosphere.

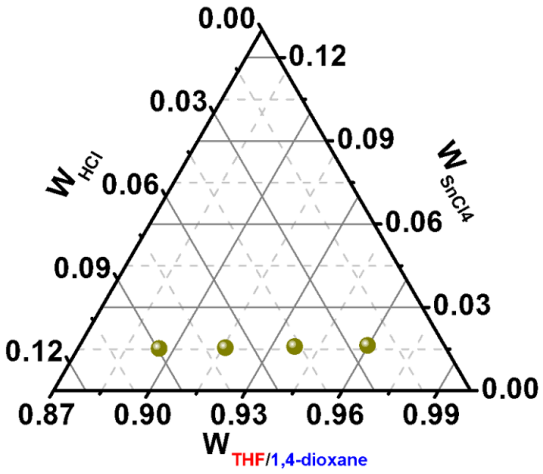

Figure 6.3: *Component phase diagram of the samples prepared with THF or 1,4-dioxane solvent.* $W_{component}$ *refers to the volume fraction of the component. Reproduced from Ref [111] with permission from JOHN WILEY AND SONS, Copyright 2020.*

6.3 Thin film characterization

The surface morphology of the prepared SnO_2 thin films was probed with a high resolution field emission scanning electron microscope (SEM, Zeiss Gemini NVision 40) at a working distance of 3.5 mm and an acceleration voltage of 5 kV. For the cross-section SEM measurement, the thin films were tilted 45° respective to the electron beam for a better view. The statistical average information of the porous structures within the bulk films was detected with grazing-incidence small angle X-ray scattering (GISAXS) at the P03 beamline of PETRA III storage ring. [162] The measurements were performed with a wavelength of 0.96 Å and at an incidence angle of 0.4°. A sample to detector distance of 4200 mm was utilized to obtain an appropriate q range. The scattering signal was recorded by a Pilatus 300K (Dectris Ltd.) detector with a pixel size of 172 μm. A python program named Directly Programmable Data Analysis Kit (DPDAK) was used for calibration and data analysis. [163] Horizontal line cuts of the 2D GISAXS data were performed at the Yoneda peak position of the SnO_2. The crystallinity of the prepared SnO_2 thin films was investigated with a D8 ADVANCE X-ray diffractometer using an X-ray wavelength of 1.54 $\AA$.

6.4 Crystallinity of the calcined thin films

For a specific chemical reaction, the equilibrium constant K is a measure of the ratio of the concentrations of products to the concentrations of reactants, which can be calculated by its corresponding standard Gibbs free energy (ΔG^0) with:

$$\ln \kappa = -\frac{\Delta G^0}{RT} \tag{6.1}$$

R is the gas constant with a value of 8.314 $JK^{-1}mol^{-1}$, T is the temperature of the reaction, ΔG^0 is the Gibbs free energy change per mole of reaction for unmixed reactants and products at standard conditions (i.e. 298 K, 100 kPa, 1 M of each reactant and product). A study about the temperature dependence of the equilibrium constant K showed that the $ln\kappa$ value for reaction (2) was positive after the temperature reached 100°C, which favors the formation of the SnO_2 product at equilibrium. [163]

$$SnCl_4(l) + 2H_2O(l) \rightarrow SnO_2 + 4HCl(g) \tag{6.2}$$

With a custom-built 2D small-angle X-ray scattering setup, Smarsly and co-authors demonstrated the pronounced crystallization of SnO_2 synthesized with poly(ethylene-co-butylene)-block-poly(ethylene oxide) template to occur at around 300-350°C. [158] In order to determine the crystallinity of the calcined SnO_2 thin films prepared in the present work, XRD measurement are performed (figure 6.3). The distinct diffraction peaks at 26.6, 33.9, 37.9, 39.0, 42.6, 51.7, 54.7 and 57.8 are assigned to the (110), (101), (200), (111), (210), (211), (220), and (002) crystal planes of the SnO_2 cassiterite phase (JCPDS NO.21-1250). The crystal size of the SnO_2 nanostructures can be calculated with the Debye-Scherrer equation 5.9.

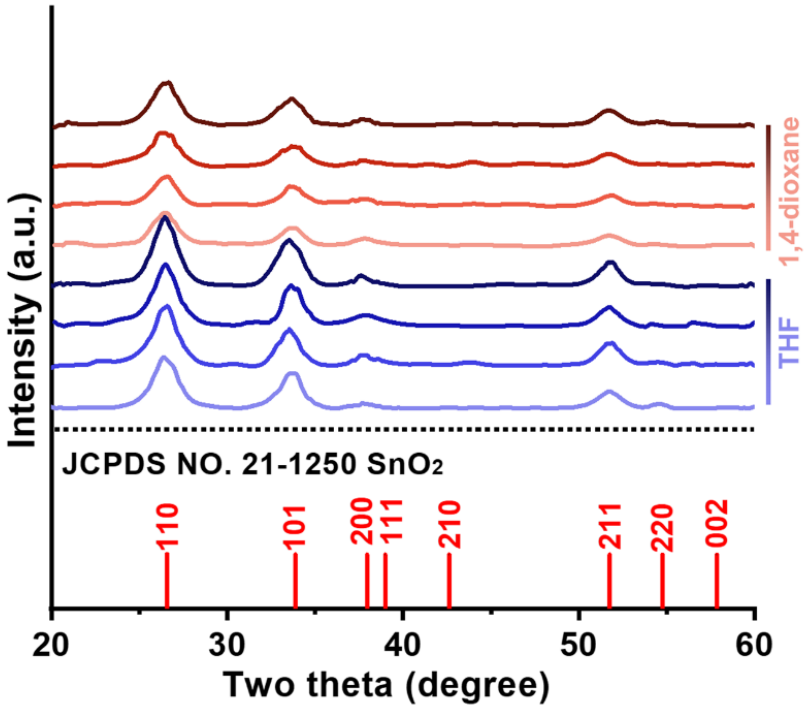

Figure 6.4: *XRD patterns of the calcined SnO_2 thin films. The SnO_2 thin films prepared with THF solvent and 1,4-dioxane solvent are represented as blue and red colors, respectively. The gradually darkening colors are utilized to represent the increment of the hydrochloric acid content. Reproduced from Ref [111] with permission from JOHN WILEY AND SONS, Copyright 2020.*

The average crystal sizes of the SnO_2 thin films are calculated from the (110), (101) and (211) peaks of the XRD patterns and the corresponding results are listed in Table 6.1. It is observed that the grain sizes of all SnO_2 thin films are around 5 nm and independent of the utilized solvent categories and hydrochloric acid content added in to the sol-gel solution. The grain sizes listed in table 6.1 are likely determined by the high calcination temperature, which is in accordance with the experimental result of previous work. [148]

	grain size of SnO_2/nm			
	50μl	100μl	150μl	200μl
THF	5.1±0.3	5.5±0.2	5.4±0.2	5.2±0.4
1,4-dioxnae	5.2±0.4	5.5±0.2	4.8±0.3	4.9±0.3

Table 6.1: *Calculated grains size of different SnO_2 thin films.*

In addition, the thin films acquired with THF solvent exhibit higher XRD peak intensities than that of the 1,4-dioaxne counterpart. This difference can be assigned to the relatively larger film thickness as indicated in the cross-section SEM images in figure 6.5. The different boiling points of the utilized solvents likely account for the thickness difference. Compared with the low boiling point THF system, the slower evaporation rate of the 1,4-dioxane solvent during the spin coating slackened the vitrification process of the thin film. As a consequence, more solution is lost at the same centripetal force level during the spin coating process, which in turn decreased the film thicknesses.

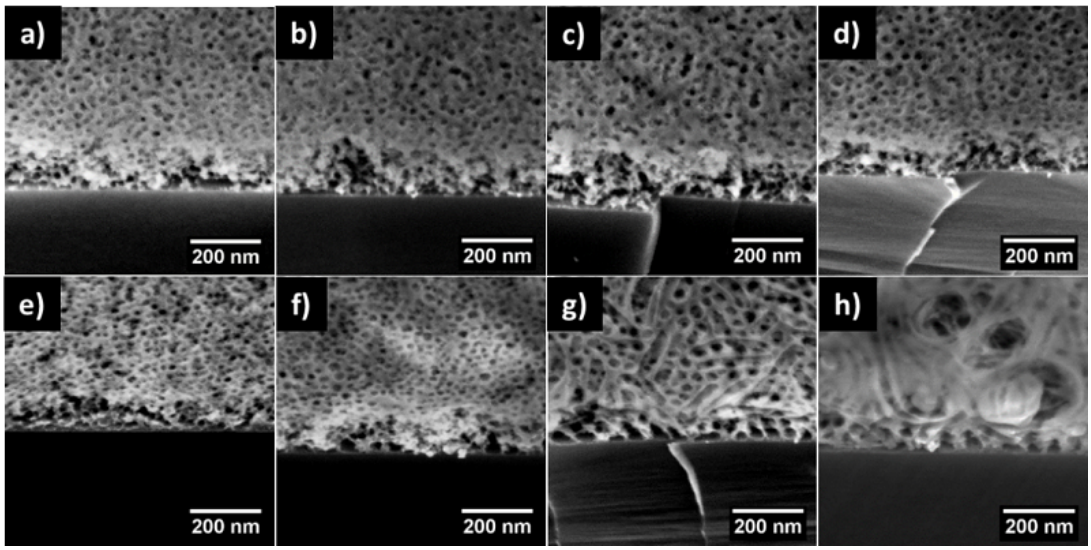

Figure 6.5: *Cross-section images of the SnO_2 thin films prepared with THF (a to d) and 1,4-dioxane (e to h). The corresponding HCl contents added in to the sol-gel stock solution are 50 μL(a, e), 100 μL(b, f) 150 μL(c, g) and 200 μL(d, h), respectively. Reproduced from Ref [111] with permission from JOHN WILEY AND SONS, Copyright 2020.*

6.5 Surface morphology of the SnO_2

Figure 6.6a-d show the SEM images and corresponding Fast Fourier transform (FFT) patterns of the SnO_2 thin films prepared with THF solvent. The hydrochloric acid content added in the sol-gel solution is 50 μl, 100 μl, 150 μl and 200 μl (Figure 6.6 a to d). All thin films prepared with THF solvent exhibit randomly distributed mesoporous structures. No significant structure variation is demonstrated with progressive hydrochloric acid addition. The weak order of the mesoporous structures can be further revealed by the corresponding blurred ring-like FFT patterns of the SEM images. In comparison with the THF system, the SnO_2 thin films prepared with 1,4-dioxane exhibit more intriguing microstructures, such as cylinders and vesicles. Moreover, the FFT pattern of the thin film prepared with

50 μl hydrochloric acid demonstrates conspicuous hexagonal symmetry patterns (Figure 6.6e), which suggests the existence of hexagonally ordered mesoporous structures of the thin film. In addition, a porous structure similar to Figure 6.6a is obtained when the hydrochloric acid amount is increased to 100 μL (Figure 6.6f). However, the relative blurred FFT patterns suggest the smearing of the hexagonally ordered mesopore arrangement. With further hydrochloric acid addition, a novel hybrid nanostructure consisting of spheres and cylinders is obtained (Figure 6.6g). The FFT pattern in Figure 6.6g reveals the random structure arrangement in the thin film. When the hydrochloric acid content utilized for sol-gel solution preparation is increased to 200 μl, a coexisting nanostructure of cylinders and vesicles is obtained (Figure 6.6h). The cross-section images shown in Figure 6.5 demonstrate that the thickness of all thin films is around 100 nm.

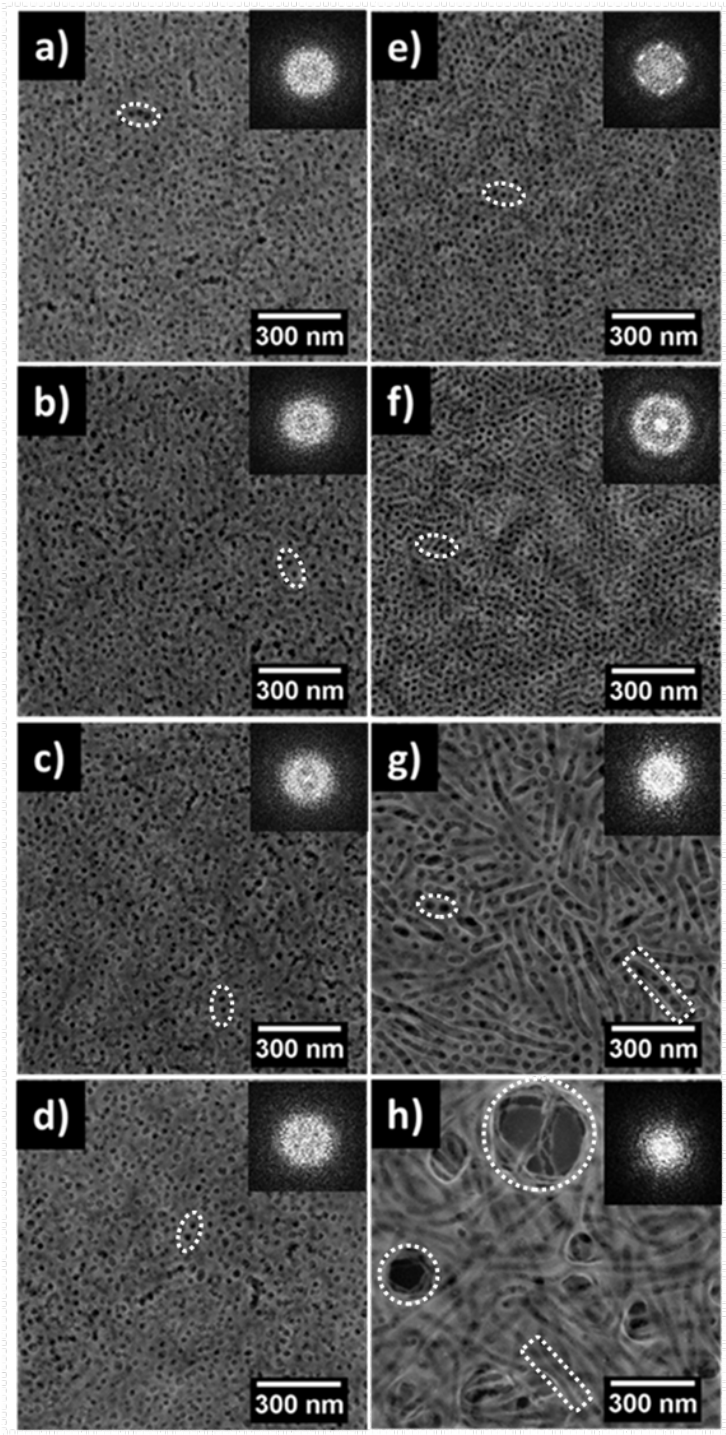

Figure 6.6: *SEM images and corresponding FFT patterns (upper right insets) of the samples prepared with THF (a-d) and 1,4-dioxane (e-h). The corresponding hydrochloric acid contents added into the sol-gel solution are 50µl (a and e), 100µl (b and f), 150µl (c and g) 200 µl (d and h). The spherical, cylindrical and vesicle nanostructures in the SEM images are marked with ellipse, rectangle and circle, respectively. Reproduced from Ref [111] with permission from JOHN WILEY AND SONS, Copyright 2020.*

To quantitatively extract contributions from different spatial frequencies, a power spectral density (PSD) function for each porous SnO_2 thin film is calculated from the SEM data. As shown in Figure 6.7, distinct PSD profile distributions are observed for the SnO_2 thin films prepared with different solvents and hydrochloric acid addition. Specifically, a clear broad single peak is observed in each PSD profile of the THF system. The peak positions at 0.1921 nm^{-1}, 0.1806 nm^{-1}, 0.1770 nm^{-1}, 0.1736 nm^{-1} for the thin films prepared with 50 μl, 100 μl, 150 μl and 200 μl hydrochloric acid addition correspond to an average inter domain spacing of 33 nm, 35 nm, 36 nm, 36 nm, respectively. For the 1,4-dioxane system, the PSD profiles of the thin films prepared with 50 μl and 100 μl hydrochloric acid feature a sharp single peak, and the peak position at 0.2380 nm^{-1} and 0.2174 nm^{-1} correspond to an average inter-domain spacing of 26 nm and 29 nm, respectively. In contrast, when the hydrochloric acid addition is further increased to 150 μl or 200 μl, multiple maxima in the PSD profile distribution are seen, which suggests the existence of polydisperse structures. The most pronounced peak is located at 0.1389 nm^{-1} and 0.0799 nm^{-1} for the thin films prepared with 150 μl and 200 μl hydrochloric acid. It corresponds to a dominant inter domain distance of 45 nm and 79 nm, respectively. Compared to the PSD profiles of the thin films prepared with THF solvent, a more pronounced variation of the peak width and position is observed for the 1,4-dioxane counterpart, which suggests a significant change of the order and inter-domain distances on the film surface.

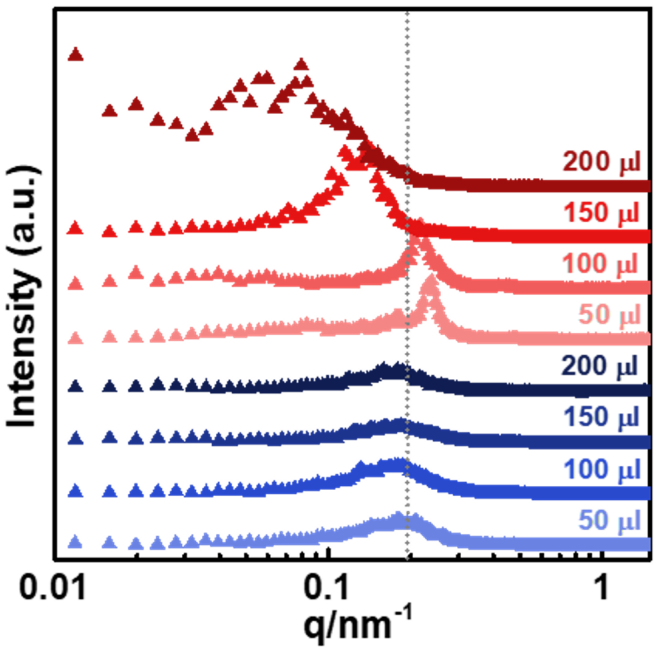

Figure 6.7: *PSD profiles of the SnO_2 thin films prepared with different HCl content and solvent category. The thin films prepared with THF and 1,4-dioxane solvent are presented with blue color and red color, respectively. The HCl content added to the stock solution is denoted on the upper right of each plot. The gray dash line is plotted as a guide to the eye. Reproduced from Ref [111] with permission from JOHN WILEY AND SONS, Copyright 2020.*

6.6 Inner morphology of the SnO_2

With SEM, the local surface morphologies of the prepared SnO_2 thin films are clearly visualized. However, the porosity for the buried structures is also of great importance for practical applications. Accordingly, GISAXS measurements are performed to probe both the surface and the inner structures of the thin films within a large sample area. [164] Figure 6.8a to d refer to the 2D GISAXS data of the SnO_2 thin films prepared with THF solvent and different hydrochloric acid addition content. The specular beam is blocked by a circular beam stop to prevent oversaturation of the detector. As indicated in Figure 6.8a to d, all of the scattering patterns show a distinct scattering signal in the Yoneda region, and the sectorial scattering patterns indicate the existence of randomly oriented nanostructures inside the entire films. [22] For a quantitative structure analysis in lateral direction, horizontal line cuts are performed for the 2D GISAXS data at the critical angle of SnO_2. The specific position is marked by a red arrow in Figure 6.8a. The

corresponding line cuts are plotted in Figure 6.9a. All line cuts exhibit multiple intensity peaks, as indicated with the black arrows. The prominent second order peak position of the thin film prepared with 50 μl hydrochloric acid addition is marked with a black dash line for reference. The gradual left shift of the second order peak position from bottom to top indicates a progressive expansion of the detected feature size with hydrochloric acid addition. Moreover, the gradual smearing of the peaks in the line cuts with increasing hydrochloric acid addition indicates an enhanced disorder, which is in good agreement with the characteristics of the PSD profiles shown in Figure 6.7.

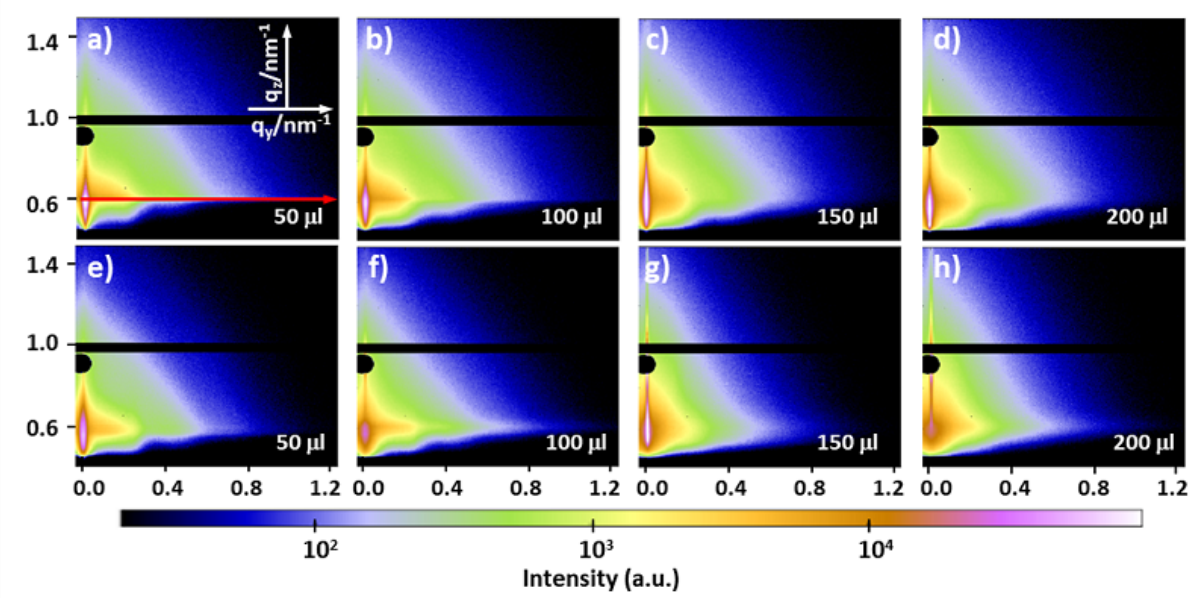

Figure 6.8: *2D GISAXS data of the SnO_2 thin films prepared with THF solvent (a to d) and 1,4-dioxane (e to h). The hydrochloric acid content utilized for the stock solution preparation is denoted on the lower right corner of each frame. Reproduced from Ref [111] with permission from JOHN WILEY AND SONS, Copyright 2020.*

Figure 6.8e to h refer to the 2D GISAXS data of the thin films prepared with 1,4-dioxane solvent. A distinct smearing of the Bragg peak is found with increasing hydrochloric acid addition, which can be more clearly revealed in the horizontal line cuts (Figure 6.9c). The prominent second order peak position of the thin film prepared with 50 μl hydrochloric acid addition is marked with a black dash line for reference. Apart from the second order peak, a distinct third order peak as marked with the black arrow is observed in the horizontal line cut of the sample prepared with 50 μl hydrochloric acid addition, which suggests the existence of well-ordered structures in the thin film. With further hydrochloric acid addition, the scattering peaks in the higher q-region are gradually smeared out

while an enhanced intensity in the lower q-region occurs simultaneously, which reflects the enhanced disorder of the small structures and increased contribution from large structures.

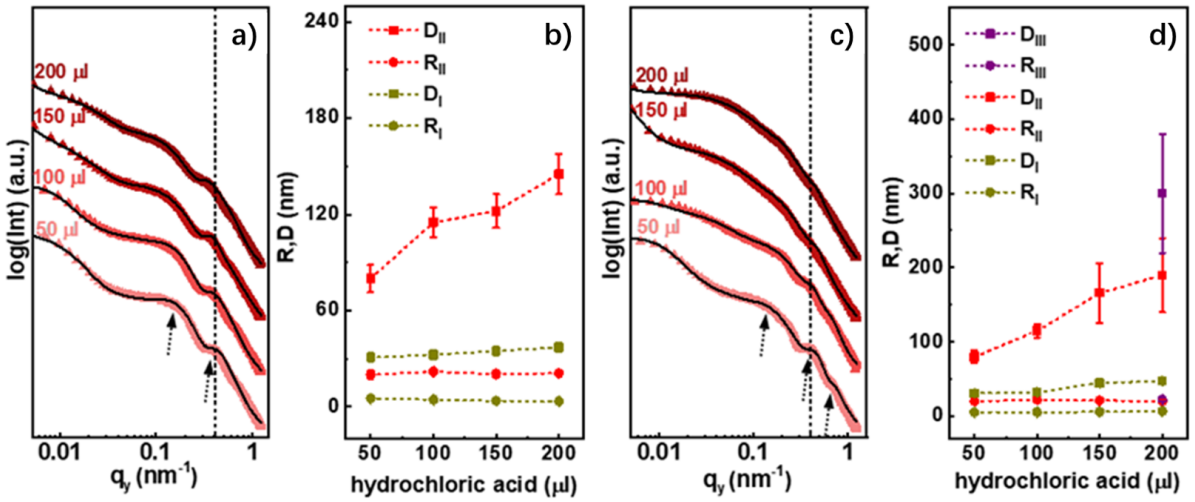

Figure 6.9: *Horizontal line cuts of the thin films prepared with a) THF solvent and c) 1,4-dioxane solvent, respectively. The measured data are plotted as solid triangles and the fit results are shown as black lines, respectively. All curves are shifted along the intensity axis for clarity of the presentation. Extracted structure radii (R) and center-to-center distances (D) are given as a function of the hydrochloric acid content are the extracted feature sizes of the thin films prepared with (j) THF solvent and (l) 1,4-dioxane solvent, respectively. The small-sized, medium-sized and large-sized structures are represented as dark yellow, red and purple color, respectively. Reproduced from Ref [111] with permission from JOHN WILEY AND SONS, Copyright 2020.*

In order to extract more detailed information of the nanostructures, the horizontal line cuts in Figure 6.9a and Figure 6.9c are modeled within the framework of the distorted-wave Born approximation (DWBA). A 1D paracrystalline lattice and a Gaussian size distribution are assumed for modeling the structure and form factors. The feature sizes including radii and center-to-center distances of the nanostructures are extracted by modeling. Based on the modeled radii and center-to-center distance, the pore sizes can be extracted with the equation 5.5 [165]

In order to obtain reasonable modeling result, two and three sets of feature sizes are used to model the line cuts in Figure 6.9a and Figure 6.9c, respectively. The specific modeling results for the line cuts in Figure 6.9a are shown in Figure 6.9b and table 6.2. With the progressive hydrochloric acid addition, the radii remain almost constant while the center-to-center distances increase gradually for both small and large structures. For the small structures, the center-to-center distances of the thin films prepared with 50 μl,

100 μl, 150 μl and 200 μl hydrochloric acid addition are determined to be (31 ± 3) nm, (33 ± 3) nm, (35 ± 3) nm and (37 ± 3) nm. The corresponding structure radii are (5.2 ± 0.5) nm, (4.4 ± 0.5) nm, (3.8 ± 0.4) nm and (3.4 ± 0.4) nm, respectively. For the medium-sized structures, the center-to-center distances of the thin films prepared with 50 μl, 100 μl, 150 μl and 200 μl hydrochloric acid addition are (80 ± 9) nm, (115 ± 9) nm, (122 ± 11) nm and (145 ± 13) nm. The corresponding structure radii are (20 ± 3) nm, (22 ± 2) nm, (21 ± 2) nm and (21 ± 2) nm, respectively. As a result, the small pore sizes of the thin films prepared with 50 μl, 100 μl, 150 μl and 200 μl hydrochloric acid are (20 ± 4) nm, (24 ± 4) nm, (27 ± 4) nm and (30 ± 4) nm, respectively. The medium pore sizes of these films are (40 ± 14) nm, (71 ± 13) nm, (81 ± 15) nm and (103 ± 16) nm.

hydrochloric acid μl	feature sizes/nm			
	D_I	R_I	D_{II}	R_{II}
50	31 ± 3	5.2 ± 0.5	80 ± 9	20 ± 3
100	33 ± 3	4.4 ± 0.5	115 ± 9	22 ± 2
150	35 ± 3	3.8 ± 0.4	122 ± 11	21 ± 2
200	37 ± 3	3.4 ± 0.4	145 ± 13	21 ± 2

Table 6.2: *Modeled structure radii (R) and center-to-center distances (D) of the thin films prepared with THF solvent.*

The specific modeling results for Figure 6.9c are shown in Figure 6.9d and table 6.3. The line cuts of the thin films prepared with 50 μl, 100 μl and 150 μl hydrochloric acid are fitted with two structure factors and form factors, and the thin film prepared with 200 μl hydrochloric acid is fitted with three structure factors and forms factors, respectively. For the small structures, the center-to-center distances of the thin films prepared with 50 μl, 100 μl, 150 μl and 200 μl hydrochloric acid are (31 ± 3) nm, (32 ± 3) nm, (45 ± 3) nm and (47 ± 3) nm. The corresponding structure radii are (5.4 ± 0.5) nm, (5.1 ± 0.5) nm, (6.0 ± 0.4) nm and (6.5 ± 0.5) nm. Using Equation 4, the pore sizes for the small structures are calculated to be (20 ± 4) nm, (22 ± 4) nm, (33 ± 3) nm and (34 ± 4) nm. For the medium-sized structures, the center-to-center distances of the thin films prepared with 50 μl, 100 μl, 150 μl and 200 μl hydrochloric acid are (80 ± 9) nm, (115 ± 9) nm, (166 ± 40) nm and (190 ± 50) nm. The corresponding structure radii are (20 ± 3) nm, (22 ± 2) nm, (21 ± 2) nm and (20 ± 2) nm. The calculated pore sizes are (40 ± 14) nm, (71 ± 13) nm, (124 ± 44) nm and (150 ± 54) nm. Due to the existence of large vesicles within the thin film prepared with 200 μl hydrochloric acid, an additional large structure

with center-to-center distance of (300 ± 80) nm and a radius of (22 ± 2) nm is used for modeling, which results in a calculated pore size of (256 ±84) nm.

hydrochloric acid μl	feature sizes/nm					
	D_I	R_I	D_{II}	R_{II}	D_{III}	R_{III}
50	31 ± 3	5.4 ± 0.5	80 ± 9	20 ± 3		
100	32 ± 3	5.1 ± 0.5	115 ± 9	22 ± 2		
150	45 ± 3	6.0 ± 0.4	166 ± 40	21 ± 2		
200	47 ± 3	6.5 ± 0.5	190 ± 50	20 ± 2	300 ± 80	22 ± 2

Table 6.3: *Modeled structure radii (R) and center-to-center distances (D) of the thin films prepared with 1,4-dioxane solvent.*

To compare with the calculated pore sizes based on the GISAXS modeling, the pore size distribution profiles are extracted through a binarization algorithm with the Image J software (Figure 6.10) for all SEM images in Figure 6.6. The peak center of the profiles is determined with a Gaussian function. For the THF system, a monotonic shift of the peak center from 21±3 nm to 25 ± 3 nm is observed, which is generally consistent with the GISAXS results (from 20 ± 4 nm to 30 ± 4 nm). For the 1,4-dioxane system, no distinct peak is detected for the thin film prepared with 200 μl hydrochloric acid addition, which can be attributed to the limited data points collected from the SEM images. However, it is noteworthy that more large pore sizes are detected for the thin films prepared with 150 μl and 200 μl hydrochloric acid, which arise from the cylindrical and vesicle structures shown in Figure 6.6g and h. When the hydrochloric acid addition is increased from 50 μl to 150 μl, the determined peak center shifts from 20±3 nm to 36 ± 4 nm, which is in a good agreement with the GISAXS results (from 20 ± 3 nm to 33 ± 3 nm) as well. The good consistency of the pore sizes acquired from the GISAXS modeling and the binarization algorithm is indicative of having similar surface and inner film morphologies as probed with SEM and GISAXS, respectively.

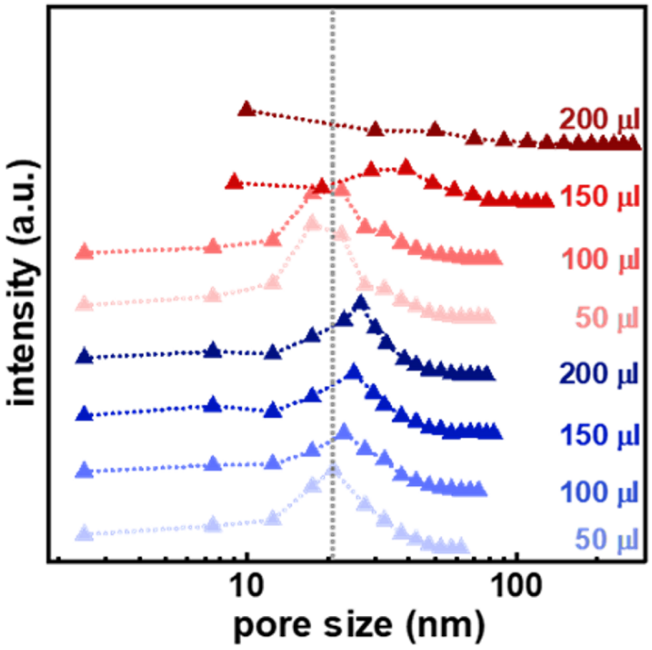

Figure 6.10: *Pore size distribution profiles of the SnO_2 thin films prepared with different HCl content and solvent category. The thin films prepared with THF and 1,4-dioxane solvent are presented with blue color and red color, respectively. The HCl content added to the stock solution is denoted on the right side of each plot. The gray dash line is plotted as a guide to the eye. Reproduced from Ref [111] with permission from JOHN WILEY AND SONS, Copyright 2020.*

6.7 Mechanism of morphology change

Considering the nonionizing properties of the PS and PEO blocks and the low dielectric constant of the solvent (THF: 7.58, 1,4-dioxane: 2.25) utilized in the present work, the repulsion force among the polymer chains provoked by ionization is negligible. [97] Accordingly, the morphology variation of the SnO_2 thin films is analyzed using the polymer-solvent interaction parameter.χ_{P-S} (equation 5.6) As described in the experimental section, the $SnCl_4$ content added in all solutions is 33.8 μl, and the corresponding hydrochloric acid content is linearly increased from 50 μl to 200 μl. Thus, 20.36 mg water is required for the hydrolysis of 33.8 μl $SnCl_4$, whereas 50 μl of 37% hydrochloric acid solution contains 37.8 mg water already. [166] Consequently, the water content in all prepared sol-gel solutions is in stoichiometric excess for the hydrolysis of $SnCl_4$. Accordingly, the following chemical reaction equilibrium is supposed to exist in the sol-gel solution:

$$SnCl_4 + xH_2O \rightleftharpoons Sn(OH)_xCl_{4-x} + xHCl(0 \leq x \leq 4) \tag{6.3}$$

As a poor solvent for the hydrophobic PS block of the diblock copolymer PS-b-PEO, the water content in the hydrochloric acid solution significantly affects the phase separation behavior of the sol-gel solution. Furthermore, superior miscibility of water in THF or 1,4-dioxane solvent can be achieved through hydrogen-bond interaction. [167–171] Accordingly, the water content in the hydrochloric acid solution is treated as solvent except for the part consumed by the complete hydrolysis of $SnCl_4$.

The characteristics of different solvents and polymers can be found in the polymer handbook (table 6.4)

	$\delta(\mathrm{MPa}^{1/2})$				$V_S(\mathrm{cm}^2/\mathrm{mol})$
	δ_H	δ_d	δ_p	δ_h	
THF	19.4	16.8	5.7	8.0	79.7
1,4-dioxane	20.5	19.0	1.8	7.4	88.5
H_2O	47.8	15.6	16.0	42.3	18.06
PS	18.6	18.6	0.2	0.0	
PEO	19.9	17.3	3.0	9.4	

Table 6.4: *Characteristics of the different solvent and polymer. [109]*

The solubility parameter $\delta_{H,mixture}$ and the molar volume $V_{S,mixture}$ of the binary mixture of THF/H_2O or 1,4-dioxane/ H_2O are taken as the sum of the products of the component value with their volume fractions:

$$\delta_{H,\ mixture} = \sum \delta_i \varphi_i; V_{S,\ mixture} = \sum V_i \varphi_i \tag{6.4}$$

δ_i, V_i and φ_i refer to the solubility parameter, molar volume and volume fraction of each single component in the solvent mixture, respectively. The calculated solubility parameter $\delta_{H,\ mixture}$ and the molar volume $V_{S,\ mixture}$ of different binary mixtures are listed in table 6.5. Water content (μl) in the table refers to the water content in the hydrochloride acid except for the portion consumed by $SnCl_4$.

solvent	THF				1,4-dioxane			
HCl contentμl	50	100	150	200	50	100	150	200
water contentμl	17	55	93	131	17	55	93	131
$\delta_{H,\ mixture}$	19.7	20.2	20.7	21.2	20.7	21.2	21.7	22.2
$V_{S,\ mixture}$	80.7	79.5	78.4	77.3	85.1	83.9	82.7	81.5

Table 6.5: *Calculated solubility parameter $\delta_{H,\ mixture}$ and molar volume $V_{S,\ mixture}$ of different binary mixtures.*

Based on the existing literature and calculated parameters (in table 6.4 and table 6.5), the polymer-solvent interaction parameters (χ_{P-S}) of different polymer-solvent pairs are determined (table 6.6).

solvent	THF				1,4-dioxane			
HCl contentμl	50	100	150	200	50	100	150	200
water contentμl	17	55	93	131	17	55	93	131
χ_{PS-S}	0.38	0.42	0.48	0.54	0.50	0.58	0.66	0.76
χ_{PEO-S}	0.34	0.34	0.36	0.39	0.36	0.40	0.45	0.51

Table 6.6: *Calculated solubility parameter $\delta_{H,\ mixture}$ and molar volume $V_{S,\ mixture}$ of different binary mixtures.*

The preferential affinity of a solvent for a certain block is represented by the expression of:

$$\Delta\chi = \chi_{S-PS} - \chi_{S-PEO} \tag{6.5}$$

Table 6.7 lists the $\Delta\chi$ values calculated from the different polymer-solvent interaction parameters (χ_{P-S}). According to the Flory-Huggins theory, the polymer can be completely dissolved in the solvent over the entire composition range when the $\Delta\chi$ value is lower than 0.5. [108], As shown in Table 6.7, the calculated $\Delta\chi$ values for all solvent mixtures utilized in the present work are less than 0.5, which suggests that both PS blocks and PEO blocks of the PS-b-PEO template can be well dissolved in the solvent. Since the water comprised in the hydrochloric acid is a significant factor affecting the preferential affinity of the solvent to the different polymer blocks, the morphology variation of the SnO_2 thin films is discussed in detail with respect to the water content in the sol-gel solution.

solvent	THF				1,4-dioxane			
HCl contentμl	50	100	150	200	50	100	150	200
water contentμl	17	55	93	131	17	55	93	131
$\Delta\chi$	0.04	0.08	0.12	0.15	0.14	0.18	0.21	0.25

Table 6.7: *Calculated solubility parameter $\delta_{H,\ mixture}$ and molar volume $V_{S,\ mixture}$ of different binary mixtures.*

Figure 6.11 shows the different film morphologies determined by the water content and $\Delta\chi$ values. It is observed that the $\Delta\chi$ values for both, THF and 1,4-dioxane mixture, monotonously increases with the increase of the water content. A spherical pore structure is preferentially formed for lower $\Delta\chi$ values ($0.04 \leq \Delta\chi \leq 0.18$). When the $\Delta\chi$ value reaches 0.21, a hybrid morphology consisting of spherical and cylindrical porous structures is observed. Further increasing the $\Delta\chi$ value to 0.25 leads to the appearance of vesicle structures. The structure transition from sphere to vesicle in terms of the $\Delta\chi$ values can be explained by the different stretching of the PS blocks in the sol-gel solution. The introduced water increases the surface energy between the PS chains and the surrounding solvent, which significantly inhibits the PS chain stretching in the solution. The PS chains in spherical micelles are typically more stretched than in cylinders or vesicles. Accordingly, they are usually the first aggregates to form and can be considered as the starting morphology for other aggregates. [97, 165, 166] It should be noted that, the calculated $\Delta\chi$ value for the SnO_2 thin film prepared with 50 μl hydrochloric acid (corresponding to 17μl water) and 1,4-dioxane solvent is located in the $\Delta\chi$ value range obtained with THF system ($0.04 \leq \Delta\chi \leq 0.15$). However, compared to the random porous structures shown in Figure 6.6a to d, a significantly enhanced order of the pore arrangement is observed in Figure 6.6e. This difference in order can be tentatively explained by a different hydrogen bond interaction type between the employed cycloether (THF or 1,4-dioxane) and H_2O. For a cycloether/H_2O binary mixture, the interactions between cycloether molecules can be mediated by H_2O molecules through bifunctional donor and acceptor hydrogen bond interactions. [108, 167–171] In contrast to the 1,4-dioxane/H_2O mixture, the smaller size of the THF molecule has an unfavorable effect on the hydrogen bond network formed between H_2O molecules. This leads to a significantly enhanced micro-heterogeneity in the THF/H_2O mixture system. As a result, THF/H_2O clusters enriched in THF are formed. [172] The formation of THF/H_2O clusters prevents the unfavorable interactions between water and the hydrophobic PS chains of the block copolymer, which weakens the phase separation tendency of the block copolymer. Accordingly, compared to the hexagonally packed pore arrangement obtained with 1,4-dioxane (Figure 6.6e), a reduction in

number and order of the pore structures is observed in the THF system (Figure 6.6a to d).

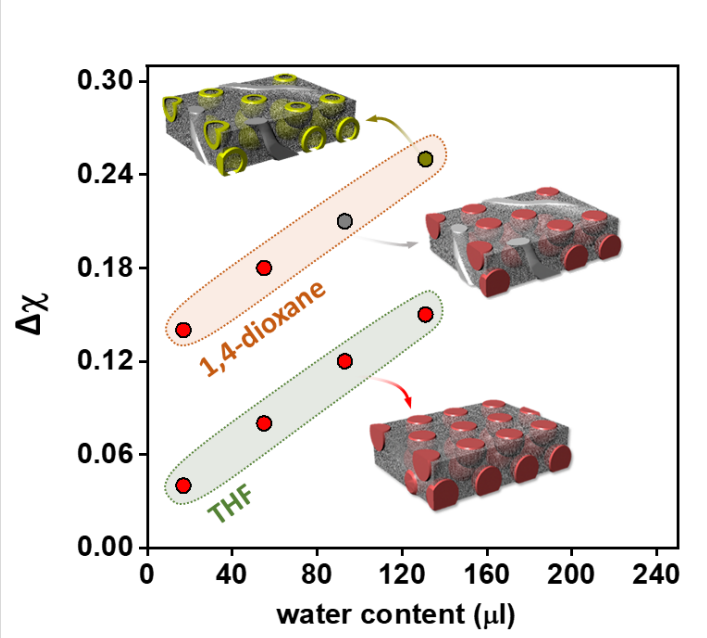

Figure 6.11: *Microstructure distribution of the SnO_2 thin films prepared with different solvent (THF or 1,4-dioxane) and water content (from hydrochloric acid), resulting in different film morphologies described as spheres (red), hybrid morphology of spheres and cylinders (grey) and vesicles (yellow). Reproduced from Ref [111] with permission from JOHN WILEY AND SONS, Copyright 2020.*

6.8 Conclusion

In this section, the amphiphilic block copolymer templated SnO_2 thin film synthesis is investigated by changing the solvent category and HCl content. Two kinds of cycloether solvents, THF and 1,4-dioxane, are utilized as good solvent for dissolution of the block copolymer PS-b-PEO. HCl is added as a poor solvent for stimulating the phase separation of the block polymer and to be the catalyst for the hydrolysis of $SnCl_4$. SEM and GISAXS measurements are performed to detect the mesoscale structure of the thin films at different length scales. A detailed comparison and analysis demonstrates that the structural transformation of the SnO_2 thin films in terms of different solvent category and HCl addition is governed by a synergistic effect of the following two factors: First, the preferential affinity of the solvent for a certain block; second, the hydrogen

bond between the employed cycloether and H_2O. By tuning the preferential affinity of the mixed solvent with different hydrochloric acid content, various structures including spheres, cylinders and vesicles are obtained. In addition, the spherical pore structure is preferentially formed at relative low $\Delta\chi$ value ($0.04 \leq \Delta\chi \leq 0.18$). A hybrid morphology consists of spherical and cylindrical pore structures can be obtained when the $\Delta\chi$ value reaches a value of 0.21. Further increasing the $\Delta\chi$ value to 0.25 provokes the formation of the vesicle structures. Compared to the 1,4-dioxane solvent, the smaller molecule size of THF leads to the enhanced micro-heterogeneity in the THF/H_2O mixture. As a result, all the thin films prepared with THF solvent show random structures. Irrespective to the morphology, all the prepared SnO_2 thin films are composed of cassiterite phase crystals with small sizes, which can be foreseen to have tremendous application potential in gas sensors, photocatalysis and photovoltaics.

7 Templated mesoporous iron (III) oxide thin films

Parts of this chapter have been published in the article: Multi-Dimensional Morphology Control for PS-b-P4VP Templated Mesoporous Iron (III) Oxide Thin Films.(YIN, Shanshan, et al. Multidimensional Morphology Control for PS-b-P4VP Templated Mesoporous Iron (III) Oxide Thin Films. Advanced Materials Interfaces, 2021, 8. Jg., Nr. 14, S. 2100141.). [173]

7.1 Preface

Hematite (α-Fe_2O_3), as the most common iron oxide polymorph, is characterized by its abundance, non-toxicity, good thermodynamic and chemical stability as well as large bandgap . [174–177] Compared to the bulk form, nanostructured α-Fe_2O_3 exhibits more size-dependent properties induced by the high surface area and quantum confinement. [178–181] Assembly of the α-Fe_2O_3 nanoparticles into periodic arrays has attracted high attention due to their potential applications in photoelectrochemical conversion, [182, 183] photovoltaic devices, [54, 184–186] lithium-ion batteries, [177, 180, 181, 187–189] gas sensors [179, 190, 191] and high-density nanoelectronic technologies. [192, 193] Especially, when used as the electron transport layer for photovoltaic devices, the pattern of the nanostructures might affects the charge carrier transport to the corresponding electrodes. [22] Current lithographic practices employed in the microelectronic industry face the escalating production cost by further decreasing the feature size. [194–196] As an inexpensive alternative, the block copolymer templated sol-gel method can produce various nanoscale structures with the assistance of self-assembly of block copolymers. [21, 97, 175, 192, 197–199] Typically, nanopatterning of the Fe_2O_3 NPs through block copolymer templates can be categorized into two types: directly accommodating the NPs inside the block copolymer matrix or in situ reducing block

copolymer coordinated metal precursors into NPs. To accommodate these NPs, a special surface treatment for the NPs for a proper dispersion in the block copolymer is required. For example, Barandiaran et al. [174] modified Fe_2O_3 maghemite NPs with polystyrene (PS) brushes and prepared hybrid polystyrene-block-poly(4-vinyl pyridine) (PS-b-P4VP)/Fe_2O_3 nanocomposites with tailored magnetic properties. The morphology change of the neat and composite thin films were systematically investigated with respect to a dioxane vapor annealing time. Abul Kashem et al. [200] prepared a series of polystyrene-block-polyisoprene/maghemite NPs (PS-b-PI/Fe_2O_3) composite thin films by grafting polystyrene chains on to maghemite NP surface and studied the structural evolution of the thin film structures with respect to the NP concentration. Yao et al. [201] controlled the alignment of polystyrene coated maghemite NPs within a block copolymer matrix by employing different external magnetic fields. The nano- and microstructure and the magnetic behavior of the hybrid films were investigated as a function of the NP concentration. Emrick et al. [202] modified CdSe NPs with trioctylphosphine oxide (TOPO) and polyethylene glycol polymer, which allowed for the specific location of the NPs in the PS and P2VP domains of the block polymer PS-b-P2VP. However, this method involves sophisticated NP preparation and modification processes and serious NP agglomeration can be provoked through a high loading of the polymer matrix with NPs. In the case of the in situ reduction approach, the metal precursors are specifically cooperated in one domain of the block copolymer and the metal oxide nanoparticles can be obtained by removing the organic species with pyrolysis or oxygen plasma treatment. Accordingly, the complex surface modification of the nanoparticles is circumvented. For example, Hardy et al. [178] synthesized highly ordered iron oxide NPs (α-Fe_2O_3) through well-defined ferrocene-containing triblock copolymers by UV/ozonolysis and thermal pyrolysis. Sohn et al. [175] realized the concurrent self-assembly of gold and iron oxide NPs by adding dodecanethiol-protected gold NPs and $FeCl_3$ to the toluene solution of PS-b-P4VP micelles. To the best of our knowledge, the polymer concentration and the solvent effect for block copolymer templated α-Fe_2O_3 thin film synthesis is rarely investigated. Related research in our group demonstrated the prominent influence of the PS-b-P4VP concentration on the ZnO morphology and the solvent effect during the polystyrene-block-polyethylene oxide (PS-b-PEO) templated TiO_2 and SnO_2 synthesis. [55, 55, 97] The formation of thermodynamically stable block polymer micelles is mainly governed by the following contributions: the stretching degree of the core-forming polymer chains, the interfacial tension between the micelle core and the surrounding solvent, and the repulsive interactions among the corona-forming chains. [196] The first two contributions can be affected by factors including copolymer composition and concentration, poor solvent content in the solution, and the preferential affinity of the common solvent. [203] The third contribution mainly refers

to block polymers which contain easily ionized chains during the micellization. In this situation, the electrostatic repulsions among the polymer chains turns to be the major component affecting the micellar structures. Accordingly, the morphology control for the block polymer can be realized via the addition of acids, bases, or salt. [204]

In this section, the PS-b-P4VP diblock copolymer templated α-Fe_2O_3 thin film synthesis is systematically investigated by changing the solvent category and PS-b-P4VP concentration. Two kinds of solvents with different preferential affinities to the polymer blocks (DMF and 1,4-dioxane) and three diblock copolymer (PS-b-P4VP) to precursor ($FeCl_3$) weight ratios ($\omega_{PS-b-P4VP}$:ω_{FeCl3}) are used for the solution preparation. Moreover, a series of DMF/1,4-dioxane mixtures with different compositions are confected for tuning the preferential affinity of the solvent for tracking the continuous evolution of the nanostructures. Due to the $FeCl_3$ concentrations in each sol-gel stock solution are identical, the influence of the ionization of the P4VP chains on the thin film morphology is ignored in the following analysis. Based on multiple characterization results, the underlying mechanism for governing the structural evolution of the thin films is revealed.

7.2 Experimental: synthesis of mesoporous α-Fe_2O_3

The preparation routine of PS-b-P4VP templated α-Fe_2O_3 thin films is schematically shown in Figure 7.1. For the sol-gel stock solution preparation, 2 mL solvent (DMF or 1,4-dioxane) was equally divided into two portions for dissolving $FeCl_3$ powder and PS-b-P4VP polymer, respectively. 20 mg $FeCl_3$ powder was weighed in a N_2 glove box to get rid of the effect of water in the air. After being taken out from the glove box, the $FeCl_3$ powder was dissolved by 1 mL DMF or 1,4-dioxane solvent. Meanwhile, PS-b-P4VP polymer solutions with different concentrations were prepared by dissolving 10 mg, 20 mg, or 40 mg PS-b-P4VP into 1 mL of the same solvent. The prepared $FeCl_3$ and PS-b-P4VP solutions were stirred for 1 hour for the complete dissolution. Afterwards, the $FeCl_3$ and polymer solutions were mixed and followed by further stirring for one hour to incorporate the inorganic $FeCl_3$ part into the micellar structures formed by PS-b-P4VP. Three $\omega_{PS-b-P4VP}$:ω_{FeCl3} ratios with fixed $FeCl_3$ concentrations, 1:2, 1:1, and 2:1, were used to investigate the polymer concentration effect in each solvent system.

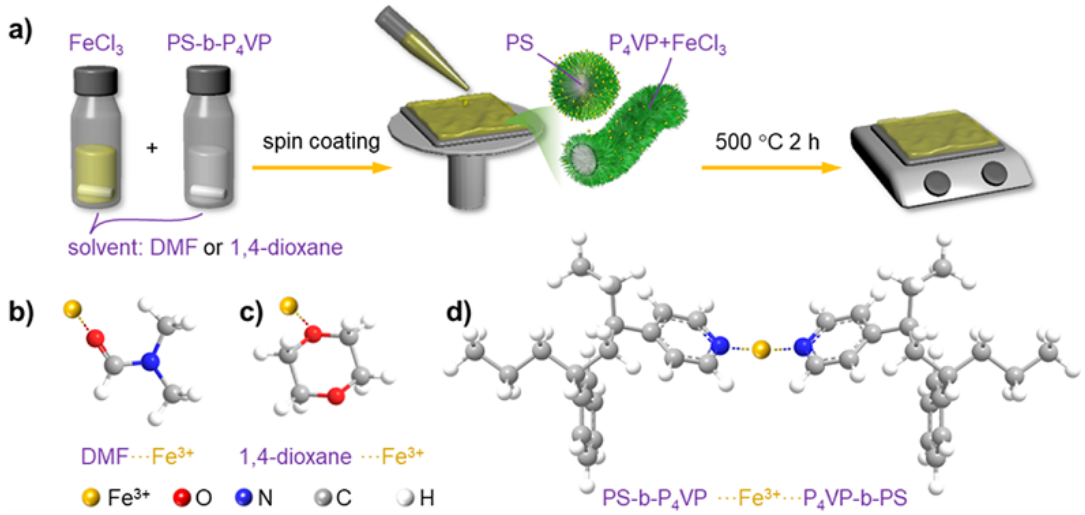

Figure 7.1: *Preparation routine of PS-b-P4VP templated α-Fe_2O_3 thin films (a). Complexation between $FeCl_3$ and solvent molecules: $DMF \cdots Fe^{3+}$ complex (b) and 1,4-dioxane $\cdots Fe^{3+}$ complex (c). Complexation between $FeCl_3$ and PS-b-P4VP polymer template(d). Reproduced from Ref [173] with permission from JOHN WILEY AND SONS, Copyright 2021.*

The component phase diagram of the different sol-gel solutions is shown in Figure 7.2. Figure 7.3 refers to the photograph of the prepared $FeCl_3$ and PS-b-P4VP/$FeCl_3$ sol-gel solutions. Through the complexation between the iron ions and the applied organic solvents (Figure 7.1b and c), the black-brown $FeCl_3$ powders were completely dissolved and clear solutions were obtained. Moreover, no precipitates were observed after mixing the $FeCl_3$ and PS-b-P4VP solutions. For the sol-gel solutions prepared with DMF/1,4-dioxane solvent mixture, 40 mg PS-b-P4VP and 20 mg $FeCl_3$ ($\omega_{PS-b-P4VP}$:ω_{FeCl3} = 2:1) were firstly dissolved with 1 ml DMF/1,4-dioxane mixture, respectively. Then, the sol-gel solution was prepared with the same routine as the pure solvent counterpart. For the thin film deposition, the prepared sol-gel solutions were spin-coated on to the pre-cleaned silicon substrates with a Delta 6 RC TT spin coater (SÜSS Micro-Tec Lithography GmbH) at 2000 rpm for 60 s. For removing the polymer template, the spin-coated thin films were calcined at 500 °C for 2 hours with a heating rate of 1 °C min^{-1} under ambient condition. Due to the preferential affinity of the solvent to the polymer blocks, various micellar structures can be formed in the sol-gel stock solution. Moreover, the vinyl pyridine side group on the P4VP chain has one free electron pair, which is not involved in bonding and therefore can bind or react with Fe^{3+} ion as a good ligand. [205] Accordingly, the Fe^{3+} species can be confined in the P4VP domains through complexation (Figure 7.1d). After the calcination treatement in the air condition, the polymer template PS-b-P4VP is removed and mesoporous α-Fe_2O_3 films formed simultaneously.

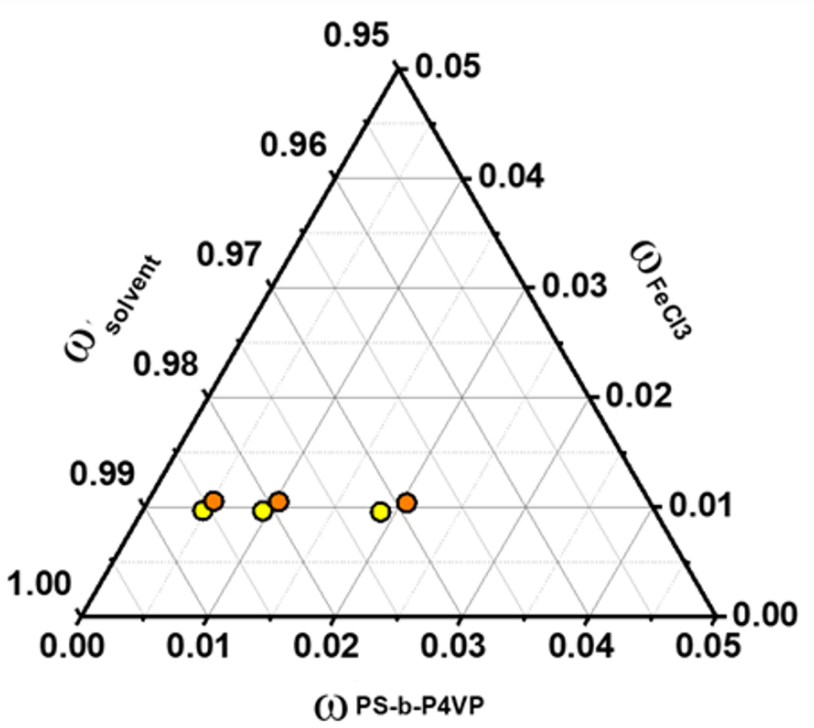

Figure 7.2: *Component phase diagram of the samples prepared with 1,4-dioxane (yellow) or DMF (orange) solvent. $\omega_x$refers to the weight fraction of the corresponding component. Reproduced from Ref [173] with permission from JOHN WILEY AND SONS, Copyright 2021.*

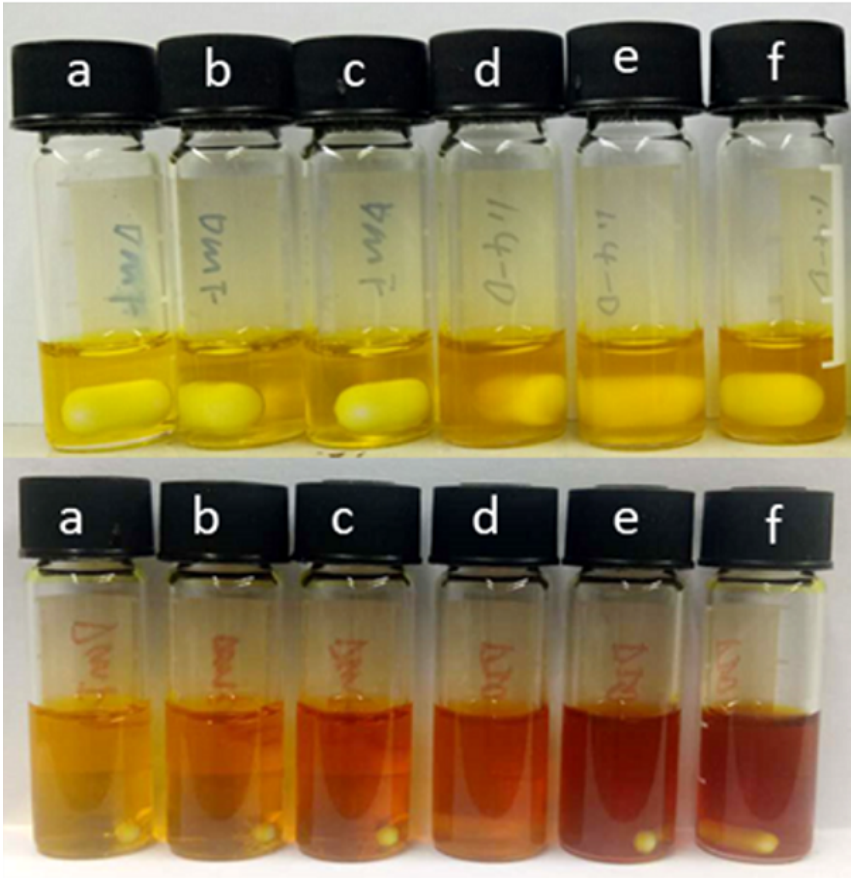

Figure 7.3: *Photographs of $FeCl_3$ solutions (top) prepared with different solvents (a-c: DMF; d-f: 1,4-dioxane) and corresponding sol-gel solutions after adding the PS-b-P4VP polymer template in to the $FeCl_3$ solution (bottom). Reproduced from Ref [173] with permission from JOHN WILEY AND SONS, Copyright 2021.*

7.3 Thin film characterization

The crystallinity of the α-Fe_2O_3 thin films was studied with a D8 ADVANCE X-ray diffractometer by using an X-ray wavelength of 1.54 $\AA$. Raman spectra were acquired with an "inVia Reflex Raman System", which consisted of a research-grade optical microscope (Leica DM2700M, Magnification 5x, 20x, 50x) and a high-performance Raman spectrometer (Renishaw). For the XRD and Raman characterization, drop-casting was used for the thin film preparation to enhance the measurement signal. X-ray photoelectron spectroscopy (XPS) measurements were performed with an ESCALAB 250Xi spectrometer (monochromatized Al K radiation, hν= 1486.6 eV) at ambient conditions. The surface morphology of the α-Fe_2O_3 thin films was probed with a high-resolution field emission scanning electron microscope (SEM, Zeiss Gemini NVision 40) at a working distance of 3.5

mm and an acceleration voltage of 5 kV. Grazing-incidence small-angle X-ray scattering (GISAXS) measurements for all samples were performed at the P03 beamline of PETRA III storage ring. [162] The wavelength and incidence angle used for the measurement was 0.96 $\AA$ and 0.35°. The sample to detector distance was 4340 mm and a Pilatus 300K (Dectris Ltd.) detector with a pixel size of 172 μm was used for recording the scattering signal. A python program called Directly Programmable Data Analysis Kit (DPDAK) was used for calibration and data analysis. [163]

7.4 Phase composition of the calcined thin films

Figure 7.4a shows the XRD patterns of the thin films with diffraction peaks at 24.2°, 33.3°, 41.0°, 49.5°, 54.2° and 57.6° corresponding to the (012), (104), (110), (113), (124), (116) and (122) lattice planes of the rhombohedral hematite (α-Fe_2O_3, JCPDS NO. of 01-1053). [206] The XRD characterization indicates that the crystallinity of the thin films is almost unaffected by the utilized solvent or $\omega_{PS-b-P4VP}$:ω_{FeCl3} ratios. Apart from the XRD characterization, the phase composition of the calcined thin films is further confirmed by the Raman spectra. The vibrational modes of hematite at the first Brillouin zone center can be represented by

$$\Gamma\text{vib} = 2\text{A1g} + 2\text{A1u} + 3\text{A2g} + 2\text{A2u} + 5\text{Eg} + 4\text{Eu} \quad (7.1)$$

The A1u and A2g modes in the equation are acoustic and optically silent. The remaining symmetrical (g) modes are active in Raman, and the asymmetrical (u) ones are active in infrared (IR) spectra. Figure 7.4b shows the Raman spectra of the calcined thin films prepared with different solvents and $\omega_{PS-b-P4VP}$:ω_{FeCl3} ratios. The peak located at 221 cm^{-1} corresponds to A1g mode and the remaining two peaks at 288 cm^{-1} and 405 cm^{-1} are attributed to the Eg modes. [183, 207]

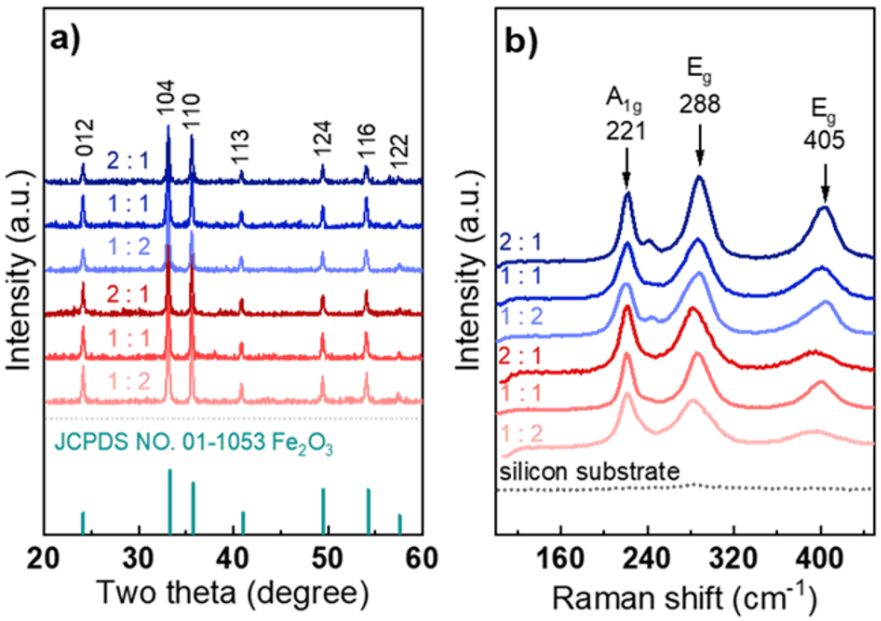

Figure 7.4: *Powder XRD patterns a) and Raman spectra b) of the α-Fe_2O_3 thin films prepared with DMF (red lines) and 1,4-dioxane solvent (blue lines). The indexed Bragg peaks of rhombohedral α-Fe_2O_3 (JCPDS NO. of 01-1053) are indicated with the vertical dark cyan lines at the bottom of a). The black dash line at the bottom of b) refers to the Raman spectra of the bare silicon substrate. The $\omega_{PS-b-P4VP}$:ω_{FeCl3} ratios used for the thin film preparation is labeled above the respective XRD or Raman data. Reproduced from Ref [173] with permission from JOHN WILEY AND SONS, Copyright 2021.*

The appearance of these three characteristic peaks indicates that the PS-b-P4VP $\cdot\cdot\cdot$ $FeCl_3$ complexes in all thin films are completely converted into α-Fe_2O_3 after the calcination process. Additionally, Figure 7.5a and b show the core-level Fe 2p XPS spectra for the calcined thin films prepared with $\omega_{PS-b-P4VP}$:ω_{FeCl3} of 2:1 in DMF and 1,4-dioxane solvent. The major Fe 2p1/2 and Fe 2p3/2 peaks of the two samples are observed centered at 710.8 eV and 724.4 eV with a spin energy separation of 13.6 eV. The two weak peaks that appear at 718.9 eV and 732.4 eV correspond to the shakeup satellites of Fe 2p3/2 and Fe 2p1/2. All peaks are typical characteristics of α-Fe_2O_3. [176, 208, 209] Apart from the Fe 2p peaks, prominent O 1s and C 1s peaks are also clearly visible in the full-range XPS survey spectra of both thin films, which can be ascribed to the organic functional group residues of the polymeric template. (Figure 7.5c)

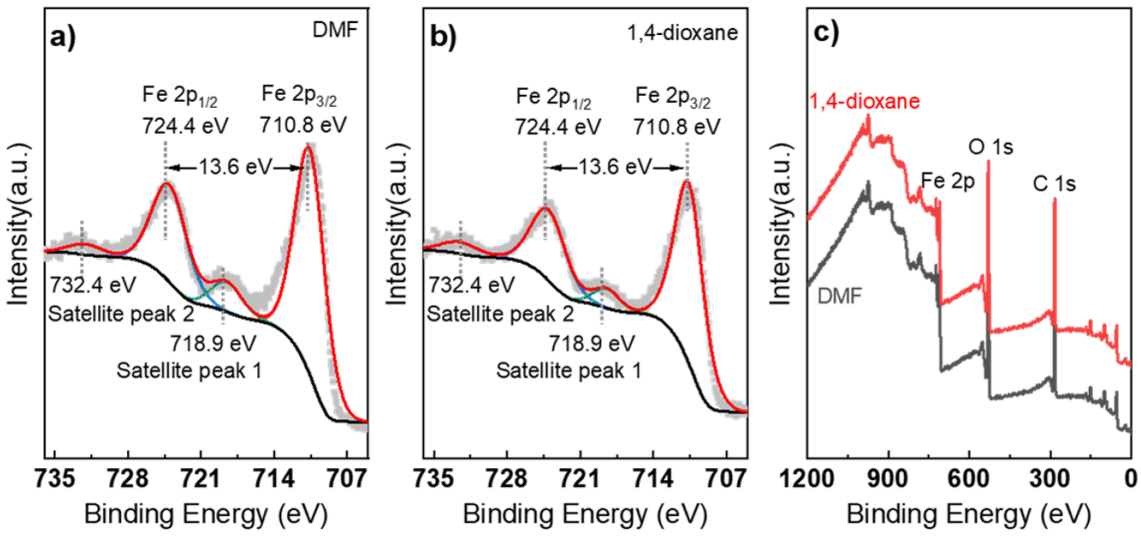

Figure 7.5: *Core-level Fe 2p XPS spectra a) and b) and full-range XPS survey spectra c) for the α-Fe_2O_3 thin films prepared with $\omega_{PS-b-P4VP}$:ω_{FeCl3} = 2:1 in DMF and 1,4-dioxane solvent. Reproduced from Ref [173] with permission from JOHN WILEY AND SONS, Copyright 2021.*

7.5 α-Fe_2O_3 with DMF: surface morphology

Figure 7.6a-c refers to the SEM images of the α-Fe_2O_3 thin films prepared with DMF solvent. The corresponding $\omega_{PS-b-P4VP}$:ω_{FeCl3} values used for the thin film preparation are 1:2, 1:1, and 2:1 for Figure 7.6a-c, respectively. The thin film prepared with $\omega_{PS-b-P4VP}$:ω_{FeCl3} of 1:2 is mainly composed of small nanoclusters (Figure 7.6a). When increasing the $\omega_{PS-b-P4VP}$:ω_{FeCl3} ratio to 1:1, a nanopattern consisting of spherical pore structures is formed. The porous structure of the thin film is directly associated with the template effect of the micelles in the solution. Due to the preferential affinity of the DMF solvent to the P4VP chains, spherical micelles consisting of PS cores and P4VP/Fe^{3+} coronas are prone to be formed, no matter in the DMF solution or in the final dry film. The structural transition from nanoclusters to the patterned nanostructures can be related to the micellization of the PS-b-P4VP template at the critical concentration, which is proportional to the concentration of the block copolymer. However, the formed micellar structures are labile at the early stage of the micellization due to the highly swollen condition of the core-forming chains by the solvent, which provides a strong probability for the micelle fusion. This fusion process might lead to the formation of the secondary large pore structures seen in Figure 7.6b. [93] By further increasing the $\omega_{PS-b-P4VP}$:ω_{FeCl3}

ratio to 2:1, a more uniform distribution of the pore structures and a slight increase of the pore size are observed within the thin film (Figure 7.6c). The influence of copolymer concentration on the micellar morphology can be explained by the equation from a theory that applied for small-molecule surfactant micelles. [196]

$$N_{agg} = 2(C/CMC)^{1/2} \tag{7.2}$$

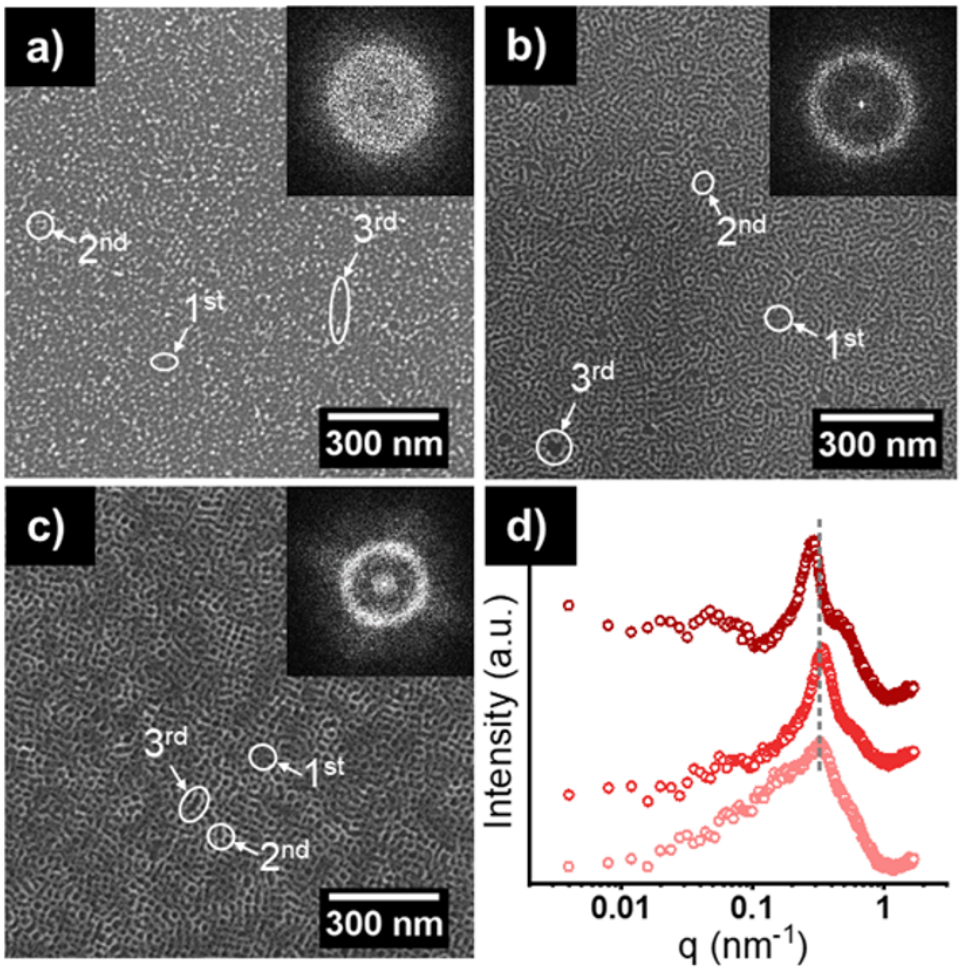

Figure 7.6: *SEM images and corresponding fast Fourier transform (FFT) patterns of the α-Fe_2O_3 thin films prepared by DMF solvent (a to c). The $\omega_{PS-b-P4VP}$:ω_{FeCl3} ratios are 1:2 a), 1:1 b) and 2:1 c), respectively. In the PSD functions calculated from the SEM images d), gradually darkening colors are utilized to represent the increase of the $\omega_{PS-b-P4VP}$:ω_{FeCl3} ratios from 1:2 to 2:1. The grey dash line in d is as a guide to the eye and the 1st, 2nd, and 3rd nanostructures used for the GISAXS data modeling are marked with white circles in a-c. Reproduced from Ref [173] with permission from JOHN WILEY AND SONS, Copyright 2021.*

N_{agg} is the average number of the polymer chains in an aggregate, C represents the copolymer concentration and CMC is the copolymer concentration at the critical water content. N_{agg} is proportional to the copolymer concentration C. For spherical micelles, the increase of the N_{agg} value yields larger core dimensions and an increase in the stretching degree of the core-forming blocks. This process is energetically favorable because the formation of a larger core size decreases the aggregate number and the total interfacial area within the system. Cross-section images of the α-Fe_2O_3 thin films are shown in Figure 7.7. It is observed that all the thin films are composed of a mesoporous α-Fe_2O_3 monolayer. Figure 7.6d shows the corresponding power spectral density (PSD) functions extracted from the SEM images. The enhanced ordering of the nanostructures can be manifested in the FFT patterns and the appearance of the second-order peak of the PSD functions. The sharp peaks of the PSD functions show the q values of the most dominant lateral feature sizes in the SEM images. [210] Specifically, the peak values of the thin films prepared with $\omega_{PS-b-P4VP}$:ω_{FeCl3} ratios of 1:2, 1:1, and 2:1 are determined to be 0.31 nm^{-1}, 0.34 nm^{-1}, and 0.28 nm^{-1}, which correspond to a feature sizes of 20.3 nm, 18.5 nm, and 22.4 nm, respectively. The correlation length is a measure for the lateral ordering of structures in the thin film, which is inversely proportional to the full width at half maximum (FWHM) of the first-order peak of the PSD functions. [211] The calculated correlation lengths for the nanostructures shown from Figure 7.6a to c are 4.8 nm, 10.4 nm, and 14.3 nm, which demonstrate the enhanced ordering with the increase of the $\omega_{PS-b-P4VP}$:ω_{FeCl3} ratio.

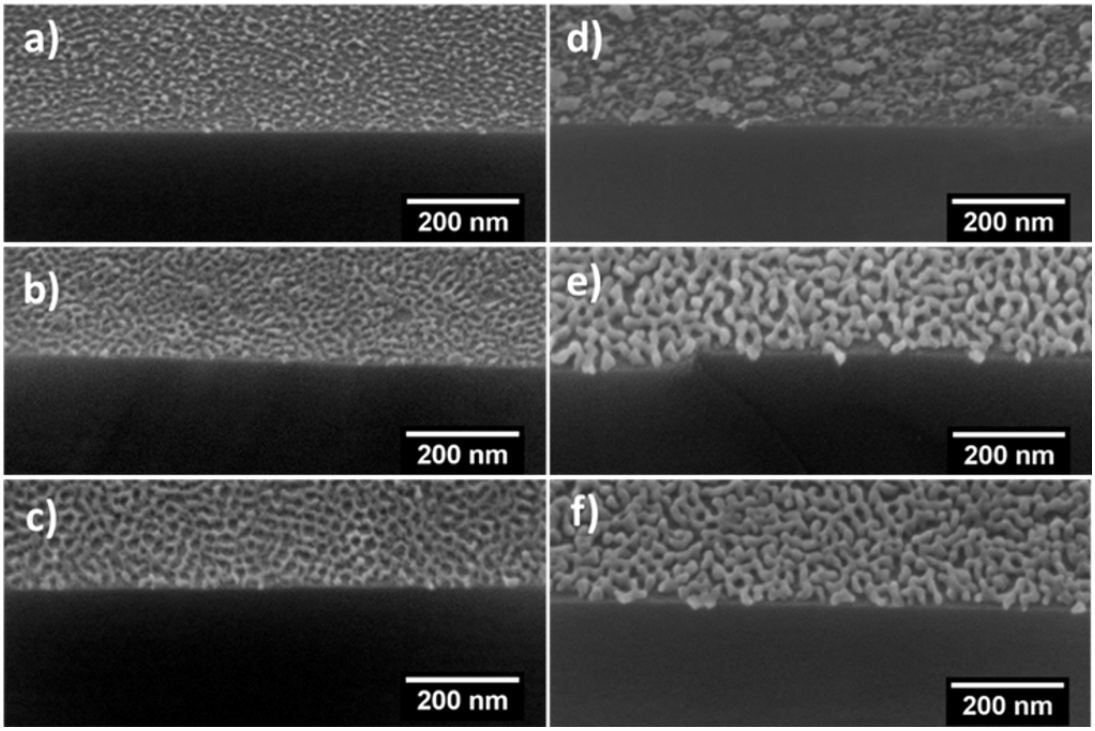

Figure 7.7: *Cross-section SEM images of the α-Fe_2O_3 thin films prepared with DMF a-c) and 1,4-dioxane d-f) solvent. The PS-b-P4VP content added in the sol-gel solution is 10 mg (a, d), 20 mg (b, e) and 40 mg (c, f), respectively. Reproduced from Ref [173] with permission from JOHN WILEY AND SONS, Copyright 2021.*

7.6 α-Fe_2O_3 with DMF: inner morphology

With the SEM measurements, the local structure on the film surface can be probed. However, in practical applications, the large area homogeneity and the inner structure of the thin film are also of great importance. Grazing-incidence small-angle X-ray scattering (GISAXS) ideally complements microscopic imaging techniques as it readily provides statistical structure information at the surface and the bulk of the thin film. [212] Figure 7.8a to c show the 2D GISAXS data of the α-Fe_2O_3 thin films prepared with DMF solvent. The shape of the Bragg peaks indicates the presence of well-ordered nanostructures in the horizontal direction of the thin films. [213] To extract the lateral structure information in the thin films, horizontal line cuts are performed at the material characteristic Yoneda peak positions as indicated by the white arrow in Figure 7.8a. Figure 7.8d shows the horizontal line cuts of the 2D GISAXS data. The additional broad peak in the low q_y region for the thin film prepared with $\omega_{PS-b-P4VP}$:ω_{FeCl3} of 1:1 can be assigned to the existence of the fused large pore structures within the film. Moreover, the shift of the most

pronounced scattering peaks in Figure 7.8d is in good accordance with the behavior of the PSD functions, which qualitatively reflects that the prepared thin films possess the same structural evolution trend within the local and large probed area. For quantitatively extracting the in-plane structure information of the α-Fe_2O_3 thin films, the horizontal line cuts in Figure 7.8d are fitted within the framework of the distorted-wave Born approximation (DWBA) by using a local monodisperse approximation (LMA). [62] In the modeling, Gaussian distributed form factors and structure factors are assumed. [214] The form factors refer to the shape and size of the scattering objects, which is assumed to be standing cylinders, and the structure factors denote the center-to-center distances between the scattering objects, respectively. Error bars indicate the scope of the goodness of fit. The fitted radii and distances are shown in Figure 7.8e and f. The most conspicuous scattering peak in the high q region is fitted to extract the 2^{nd} structure information. When the $\omega_{PS-b-P4VP}$:ω_{FeCl3} ratio increase from 1:2 to 2:1, the center-to-center distances of the 2nd structure are determined to be (20.0 ± 1.4) nm, (17 ± 3) nm and (22 ± 2) nm. The fitted center-to-center distances agree well with the feature sizes calculated from the main peak of the PSD functions, which reflects a good consistency of the main feature sizes in the local and large probed areas of the thin film. In addition, the corresponding radii of the 2^{nd} structure are fitted to be (5.6 ± 0.3) nm, (4.5 ± 0.4) nm, and (5.0 ± 0.4) nm. Based on the fitted center-to-center distances and radii, the pore sizes formed by the nanostructures can be calculated with the equation 5.5 [55, 215]

Considering the thin film prepared with a $\omega_{PS-b-P4VP}$:ω_{FeCl3} ratio of 1:2 is mainly composed of discrete nanoclusters and no distinct pore structures are observed, the pore size calculation is only performed for the rest two samples. Accordingly, the pore sizes calculated from the 2^{nd} center-to-center distances and radii are (8±4) nm and (12±3) nm for the samples prepared with $\omega_{PS-b-P4VP}$:ω_{FeCl3} of 1:1 and 2:1. In addition, the weak scattering intensity in the higher q_y region for all line cuts is fitted with a smaller 1st center-to-center distance and radius. The 1^{st} center-to-center distances for the thin films prepared with $\omega_{PS-b-P4VP}$:ω_{FeCl3} ratios of 1:2, 1:1 and 2:1 are determined to be (10.0 ± 1.5) nm, (8.6 ± 0.9) nm and (11.0 ± 1.2) nm, and the corresponding radii are fitted to be (2.6 ± 0.5) nm, (2.3 ± 0.4) nm and (2.6 ± 0.5) nm. According to equation 5.5, the 1^{st} pore sizes are calculated to be (4.0 ± 1.7) nm and (6 ± 2) nm for the thin films prepared with $\omega_{PS-b-P4VP}$:ω_{FeCl3} of 1:1 and 2:1. Moreover, the additional broad peak in the low q_y region for all thin films is fitted with the 3^{rd} distance and radius. Specifically, the center-to-center distance of the thin films prepared with $\omega_{PS-b-P4VP}$:ω_{FeCl3} ratios of 1:2, 1:1, and 2:1 is determined to be (210 ± 25) nm, (90 ± 19) nm and (120 ± 18) nm, and the corresponding radius is determined to be (6.5 ± 0.5) nm, (5.0 ± 0.5) nm and (5.5 ± 0.5) nm, respectively. The pore sizes generated by the third structure are calculated to be (80

$\pm$ 20) nm and (109 $\pm$ 19) nm for the thin films prepared with $\omega_{PS-b-P4VP}$:ω_{FeCl3} of 1:1 and 2:1. The small and large pore sizes calculated from the 1^{st} and 3^{rd} structure factors can be attributed to the locally collapsed or fused large pore structures in the thin film. Notably, all the modeled feature sizes in the GISAXS data analysis can be identified with surface features in the SEM images (see Figure 7.6). The good consistency between the GISAXS fitting result and the SEM topography demonstrates that the nanostructures observed in the micron size range extend all over the larger area on the thin film.

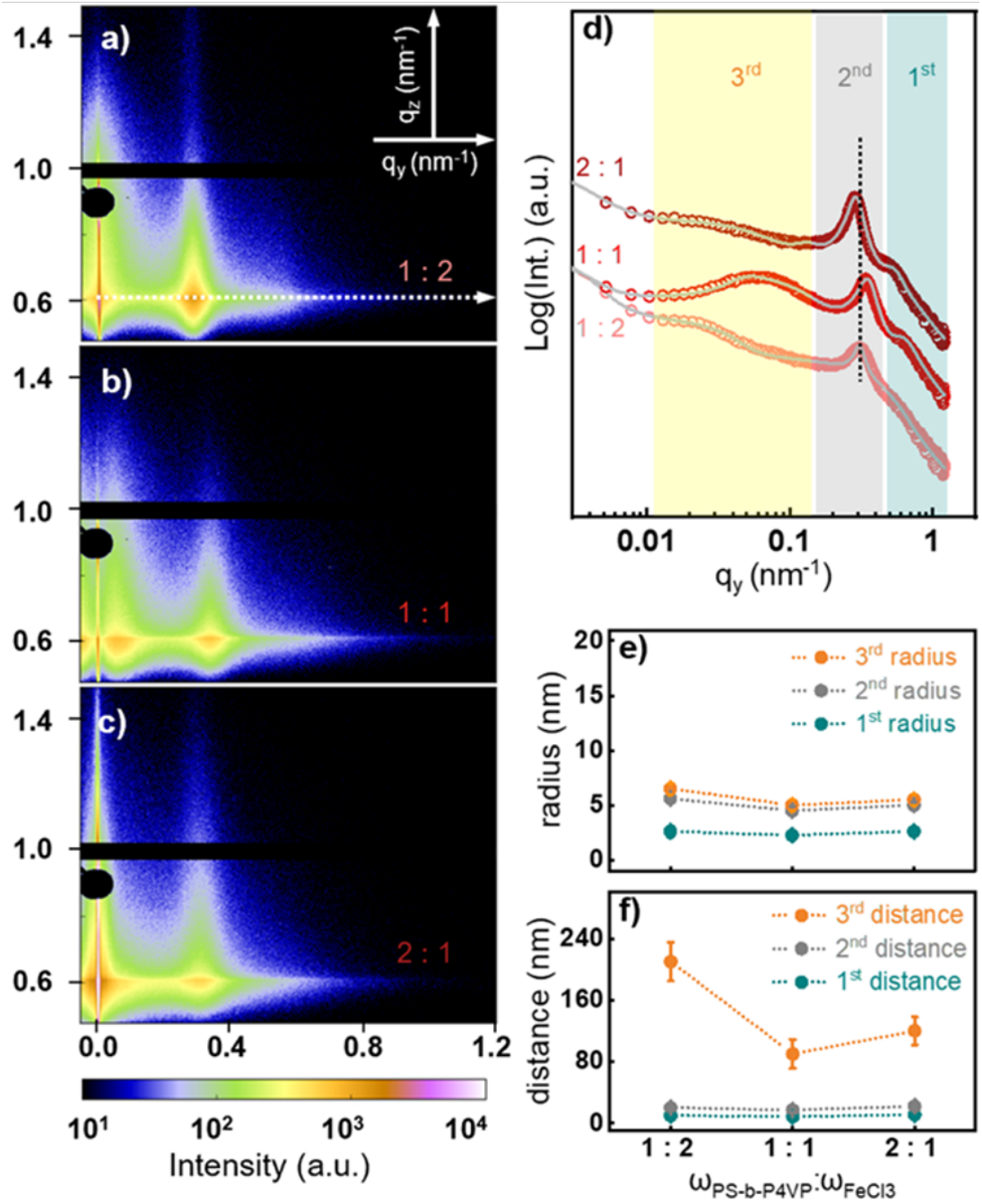

Figure 7.8: *2D GISAXS data (a to c) and corresponding horizontal line cuts (d) of the thin films prepared with DMF solvent. The $\omega_{PS-b-P4VP}$:ω_{FeCl3} ratios used for sample preparation are noted in the lower right corner of the 2D GISAXS data and the left side of the horizontal line cuts. The position for performing horizontal cuts is denoted as a white arrow in a. The black dash line in d is plotted as a guide to the eye. The scattering peaks appearing in the high, medium, and low qy regions are marked with cyan, grey and yellow rectangles, respectively. The radii (e) and center-to-center distances (f) for the different thin films are determined from the fits. Reproduced from Ref [173] with permission from JOHN WILEY AND SONS, Copyright 2021.*

7.7 α-Fe_2O_3 with 1,4-dioxane: surface morphology

Figure 7.9a to c show the SEM images of the α-Fe_2O_3 thin films prepared with 1,4-dioxane. Compared to the DMF counterpart samples, completely different morphologies can be observed in the 1,4-dioxane system. When the $\omega_{PS-b-P4VP}$:ω_{FeCl3} is 1:2, discrete nanoclusters accompanied with large aggregates are detected. Once increasing the $\omega_{PS-b-P4VP}$:ω_{FeCl3} ratio to 1:1 and 2:1, uniformly distributed worm-like structures with enhanced orderring, as verified by the FFT patterns, are formed. Figure 7.9d shows the corresponding PSD functions calculated from the SEM images. Due to the polydispersity of the nanostructures, no distinct peak is observed in the PSD function of the thin film prepared with a $\omega_{PS-b-P4VP}$:ω_{FeCl3} ratio of 1:2. The sharp peaks shown in the other two PSD functions can be used for determining the feature sizes and orderring. The peak centers of the thin films prepared with $\omega_{PS-b-P4VP}$:ω_{FeCl3} ratios of 1:1 and 2:1 are determined to be 0.23 nm^{-1} and 0.24 nm^{-1}, which corresponds to a feature sizes of 27.3 nm and 26.2 nm, respectively. The FWHM of the thin films prepared with $\omega_{PS-b-P4VP}$:ω_{FeCl3} ratios of 1:1 and 2:1 are determined to be 0.11 nm^{-1} and 0.13 nm^{-1}, which corresponds to correlation lengths of 9.1 nm and 7.7 nm, respectively. The fitted peak position and calculated correlation lengths indicate that the feature sizes and order of the thin films are damaged when increasing the $\omega_{PS-b-P4VP}$:ω_{FeCl3} ratios from 1:1 to 2:1. The drastic morphology variation of the thin films in terms of the solvent category can be tentatively explained by a preferential affinity theory. Based on the characteristic parameters of the different polymers and solvents, the polymer-solvent interaction parameters χ_{P-S} can be calculated via equation 5.6

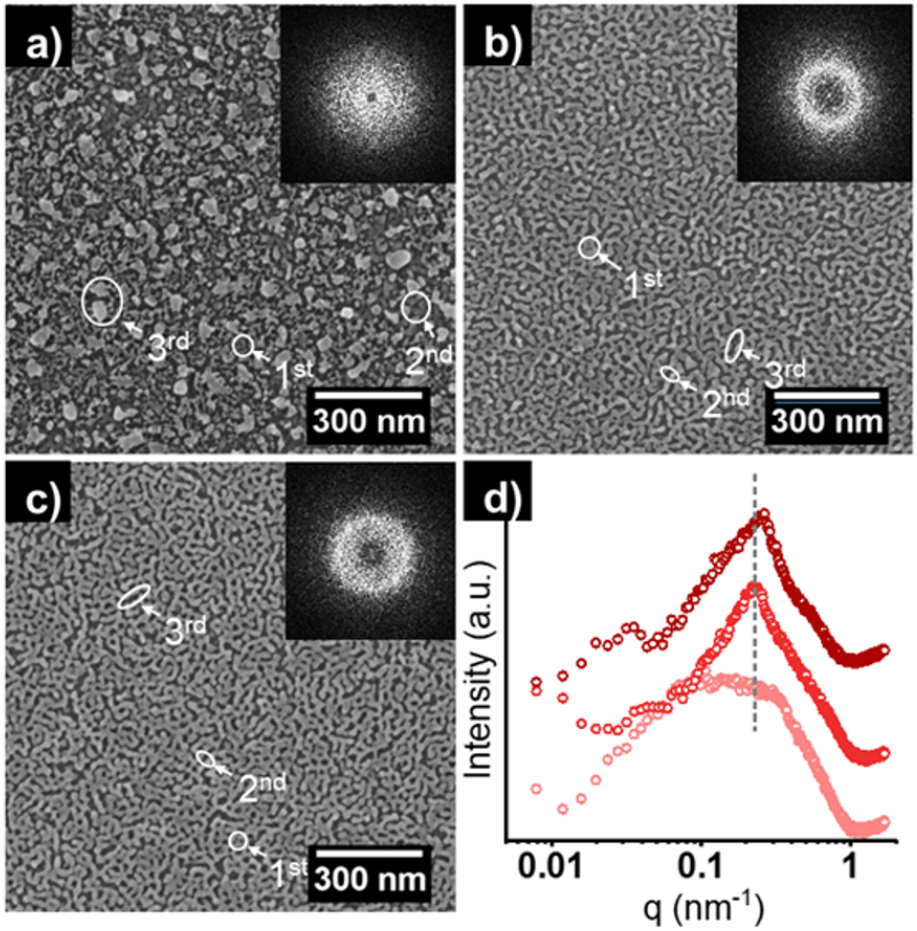

Figure 7.9: *SEM images and corresponding fast Fourier transform (FFT) patterns of the α-Fe_2O_3 thin films prepared by 1,4-dioxane solvent (a to c). The $\omega_{PS-b-P4VP}$:ω_{FeCl3} ratios are 1:2 a), 1:1 b) and 2:1 c), respectively. In the PSD functions calculated from the SEM images d), gradually darkening colors are utilized to represent the increase of the $\omega_{PS-b-P4VP}$:ω_{FeCl3} ratios from 1:2 to 2:1. The grey dash line in d is as a guide to the eye and the 1st, 2nd, and 3rd nanostructures used for the GISAXS data modeling are marked with white circles in a-c. Reproduced from Ref [173] with permission from JOHN WILEY AND SONS, Copyright 2021.*

According to the literature, the δ_H of PS and P4VP blocks are 18.6 $MPa^{1/2}$ and 23.0 $MPa^{1/2}$, respectively. [216] Table 7.1 shows the Hansen solubility parameters (δ_H) of DMF and 1,4-dioxane solvents.

	$\delta(\mathrm{MPa}^{1/2})$				$\mathrm{V}_S(\mathrm{cm}^2/\mathrm{mol})$
	δ_H	δ_d	δ_p	δ_h	
DMF	24.8	17.4	13.7	11.3	77.0
1,4-dioxane	20.5	19.0	1.8	7.4	85.7

Table 7.1: *Characteristics of the different solvent and polymer. [109]*

Table 7.2 are the corresponding χ_{P-S} values calculated by equation 5.6. According to the Flory-Huggins theory, the polymer and solvent are completely miscible when χ_{P-S} is less than 0.5. The preferential affinity of the solvent to a certain block can be calculated by the difference between the χ_{PS-S} and χ_{P4VP-S} (equation 6.7).

The calculated $\Delta\chi$ for the PS-b-P4VP/DMF and PS-b-P4VP/1,4-dioxane polymer-solvent pairs are 1.1 and -0.09. The high $\Delta\chi$ value of PS-b-P4VP/DMF means the inferior solubility of the PS blocks in DMF, which leads to the significantly inhibited stretching of the PS blocks and thus promotes the formation of spherical PS micellar cores. However, the negative $\Delta\chi$ value of PS-b-P4VP/1,4-dioxane polymer-solvent pair indicates that the 1,4-dioxane has a very slight preferential affinity to the PS block. Accordingly, the appearance of the aggregates in Figure 7.9a and the wormlike structures in Figure 7.9b and c can be ascribed to the weak selectivity of 1,4-dioxane and an increased stretching of the PS blocks. In addition, the inter-domain distances of the wormlike structure decreases by increasing the $\omega_{PS-b-P4VP}$:ω_{FeCl3} ratios from 1:1 to 2:1, which is against the trend shown in the DMF solvent system. The decreased inter-domain distance induced by the increase of the $\omega_{PS-b-P4VP}$:ω_{FeCl3} ratios can be assigned to the unique shape of the micellar structure. It is observed that the thin films prepared with $\omega_{PS-b-P4VP}$:ω_{FeCl3} of 1:1 and 2:1 are mainly composed of interconnected wormlike structures, which is prone to deform into more elongated wormlike micelles for accommodating more polymer chains and maintaining low surface energy in the monolayer geometry simultaneously.

χ	DMF	1,4-dioxane
PS	1.54	0.47
P4VP	0.44	0.56

Table 7.2: *Polymer-solvent interaction parameters χ_{P-S} of different polymer-solvent pairs. [109]*

7.8 α-Fe_2O_3 thin films with 1,4-dioxane: inner morphology

Figure 7.10a to c show the 2D GISAXS data of the α-Fe_2O_3 thin films prepared with 1,4-dioxane. Compared with the thin film prepared with a $\omega_{PS-b-P4VP}$:ω_{FeCl3} ratio of 1:2, the clearly visible Bragg rod in the lateral direction of the other two thin films can be attributed to an enhanced in-plane order of the nanostructures. Figure 7.10d shows the corresponding line cuts made from the 2D GISAXS data. The line cuts clearly show the sharpening of the Bragg peak by increasing $\omega_{PS-b-P4VP}$:ω_{FeCl3} ratio from 1:2 to 1:1. In addition, the Bragg peak shifts towards larger q_y values and broadens by further increasing the $\omega_{PS-b-P4VP}$:ω_{FeCl3} ratio from 1:1 to 2:1. The shift and width of the scattering peaks in Figure 7.10d is in good accordance with the PSD functions from Figure 7.9d, which demonstrates that the feature size variation trend is consistent in the local and large area of the thin film. Within the aforementioned fit model, the horizontal line cuts are fitted with three sets of nanostructures (radii and distances). The most pronounced scattering peak in the medium q_y region is fitted with the 2^{nd} nanostructure. Specifically, the 2^{nd} distances of the thin films prepared with $\omega_{PS-b-P4VP}$:ω_{FeCl3} ratios of 1:2, 1:1, and 2:1 are determined to be (20 ± 4) nm, (27 ± 3) nm, and (24 ± 2) nm, which are in substantial agreement with the feature sizes calculated from the PSD functions. The corresponding radii are (5.0 ± 1.5) nm, (5.1 ± 0.5) nm and (3.9 ± 0.5) nm. Based on equation 5.5, the pore sizes calculated from the 2^{nd} distance and radii are (10 ± 7) nm, (16 ± 4) nm, and (16 ± 4) nm, respectively. Apart from the most conspicuous scattering signal in the medium q_y region, the weak scattering in the high and low q_y regions are fitted with the 1^{st} and 3^{rd} nanostructures. The 1^{st} center-to-center distances of the thin films prepared with $\omega_{PS-b-P4VP}$:ω_{FeCl3} ratios of 1:2, 1:1, and 2:1 are determined to be (12 ± 2) nm, (14 ± 3) nm and (13 ± 2) nm and the corresponding 1st radius are (3.2 ± 0.2) nm, (3.3 ± 0.3) nm and (2.7 ± 0.2) nm, which yields the pore sizes of (6 ± 2) nm, (7 ± 3) nm and (8 ± 3) nm, respectively. Moreover, the 3^{rd} center-to-center distances of the thin films prepared with 1:2, 1:1, and 2:1 $\omega_{PS-b-P4VP}$:ω_{FeCl3} are determined to be (190 ± 55) nm, (100 ± 15) nm and (90 ± 12) nm and the corresponding 3^{rd} radii are (17 ± 2) nm, (5.5 ± 0.6) nm and (4.1 ± 0.6) nm, which yields the pore sizes of (156 ± 59) nm, (89 ± 16) nm and (82 ± 13) nm, respectively.

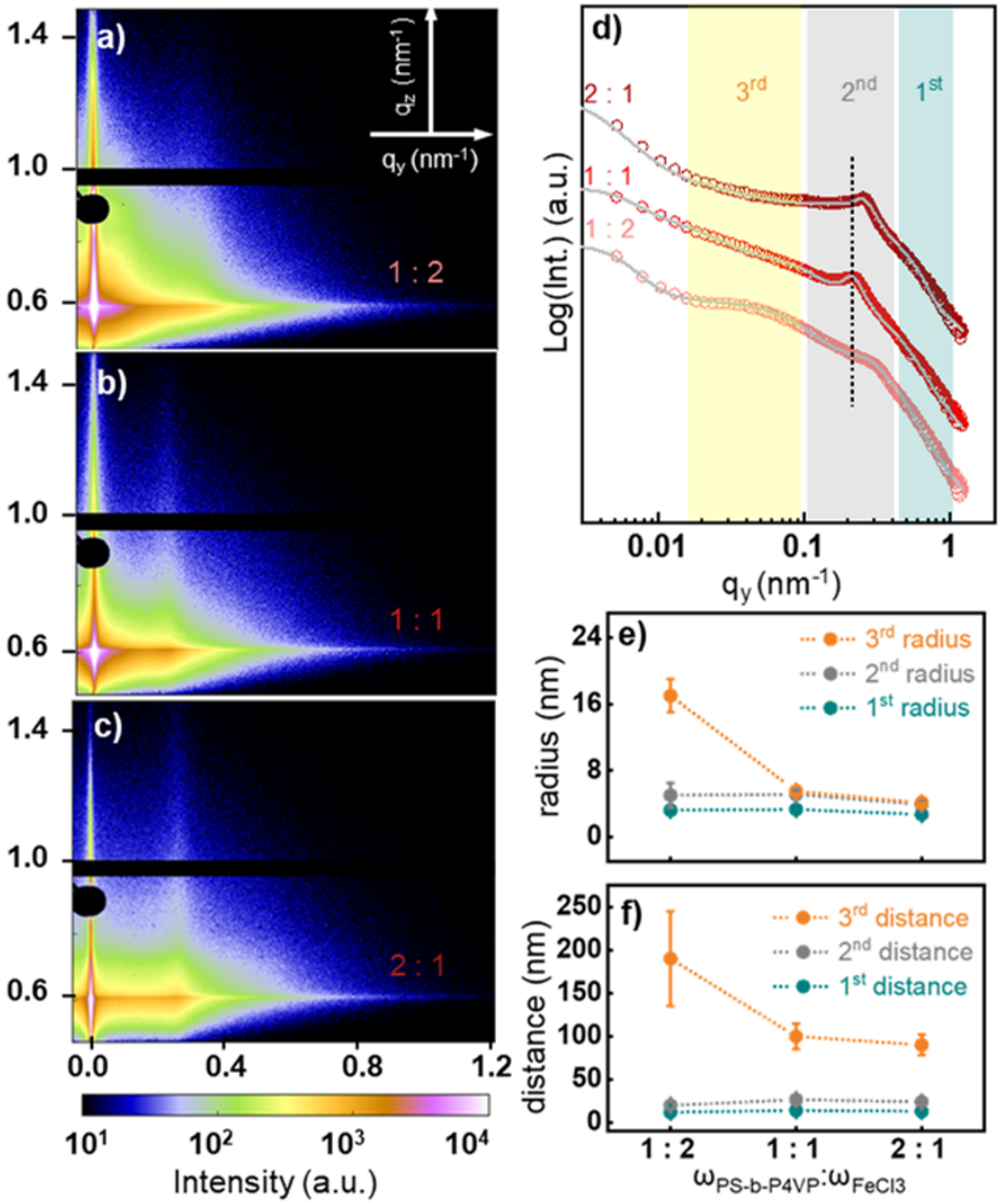

Figure 7.10: *2D GISAXS data (a to c) and corresponding horizontal line cuts (d) of the thin films prepared with 1,4-dioxane solvent. The $\omega_{PS-b-P4VP}$:ω_{FeCl3} ratios used for sample preparation are noted in the lower right corner of the 2D GISAXS data and the left side of the horizontal line cuts. The position for performing horizontal cuts is denoted as a white arrow in a. The black dash line in d is plotted as a guide to the eye. The scattering peaks appearing in the high, medium, and low q_y regions are marked with cyan, grey and yellow rectangles, respectively. The radii (e) and center-to-center distances (f) for the different thin films are determined from the fits. Reproduced from Ref [173] with permission from JOHN WILEY AND SONS, Copyright 2021.*

7.9 Morphology evolution

From the discussion above, the good consistency between the SEM topography and the structures extracted in the GISAXS data analysis demonstrates that a large area homogeneity is achieved for all α-Fe_2O_3 thin films. In addition, it is clearly demonstrated that the α-Fe_2O_3 thin films prepared with a $\omega_{PS-b-P4VP}$:ω_{FeCl3} ratio of 1:2 irrespective of the solvent, in DMF and 1,4-dioxane possess similar nanocluster structures. The main structural differences caused by the solvent category consist in the distinct spherical and worm-like nanostructures formed at higher $\omega_{PS-b-P4VP}$:ω_{FeCl3} ratios. Accordingly, a schematic illustration for the micellar structure evolution, which is directly related to the α-Fe_2O_3 nanostructures, is given with respect to the different solvent category and $\omega_{PS-b-P4VP}$:ω_{FeCl3} ratios in Figure 7.11. By increasing $\omega_{PS-b-P4VP}$:ω_{FeCl3} ratios from 1:1 to 2:1, a completely different structure evolution tendency is observed for the spherical and wormlike structures. Specifically, the expansion of the spherical micelles with the increase of the $\omega_{PS-b-P4VP}$:ω_{FeCl3} ratio can be explained by the theory for small molecule surfactant micelles. The average number of polymer chains in an aggregate (N_{agg}) is proportional to copolymer concentration, and the increased N_{agg} of the spherical micelles contributes to the enhanced stretching of the core-forming blocks and therefore the expansion of the micelles. However, for the interconnected wormlike structures acquired with the 1,4-dioxane solvent, the increase of the $\omega_{PS-b-P4VP}$:ω_{FeCl3} ratio promotes the formation of more elongated wormlike micelles for accommodating more polymer chains in the monolayer geometry.

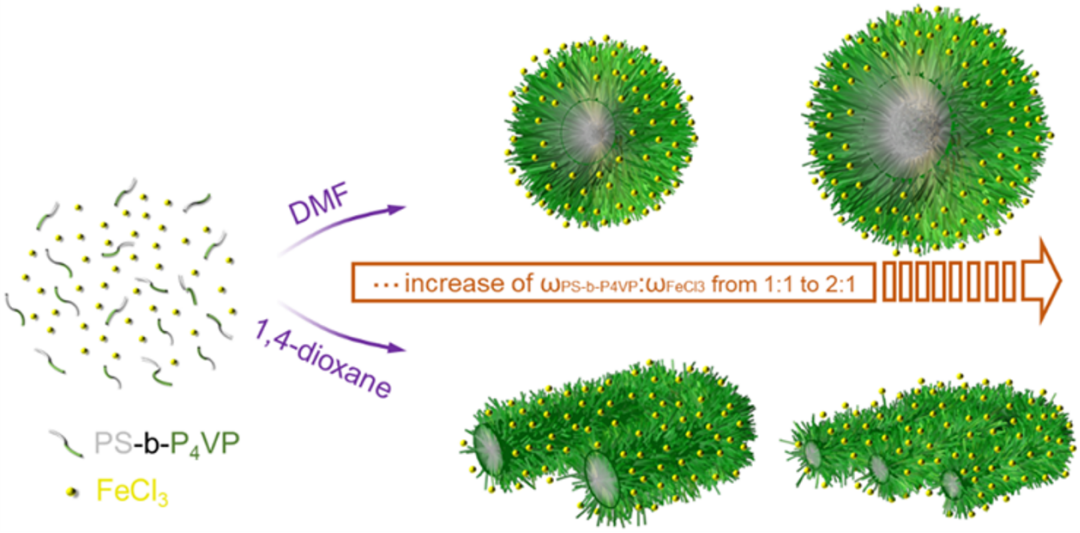

Figure 7.11: *Schematic illustration of the micellar structures in the thin films with respect to the different solvent category and $\omega_{PS-b-P4VP}$:ω_{FeCl3} ratios. Reproduced from Ref [173] with permission from JOHN WILEY AND SONS, Copyright 2021.*

7.10 Relationship between morphology and $\triangle\chi$ value

The solubility parameter of a solvent mixture can be tuned by changing its composition. [217] For tracking the successive morphology evolution with respect to the solubility parameter of a solvent, we study DMF/1,4-dioxane solvent mixtures with different compositions at a fixed $\omega_{PS-b-P4VP}$:ω_{FeCl3} ratio of 2:1 for the sol-gel solution preparation. The acquired thin film morphologies are shown in Figure 7.12. The morphology of the thin films remains almost constant when increasing the volume fraction of 1,4-dioxane from 0 to 20 vol.% (Figure 7.12a to c). The inflection from spherical to worm-like nanostructure is triggered, when the volume fraction of 1,4-dioxane reaches 30 vol.% (Figure 7.12d). As shown in Figure 7.12d, the wormlike structure appears in a form of micron-sized islands among the spherical pore structures. The formation of this unique hybrid structure is likely due to the incomplete micellar structural transformation in the sol-gel solution. By further increasing the volume fraction of 1,4-dioxane from 40 vol.% to 100 vol.%, the complete spherical-to-worm like micellar transformation occurs. As a result, thin films consisting of neat wormlike nanostructures are obtained (Figure 7.12e to k).

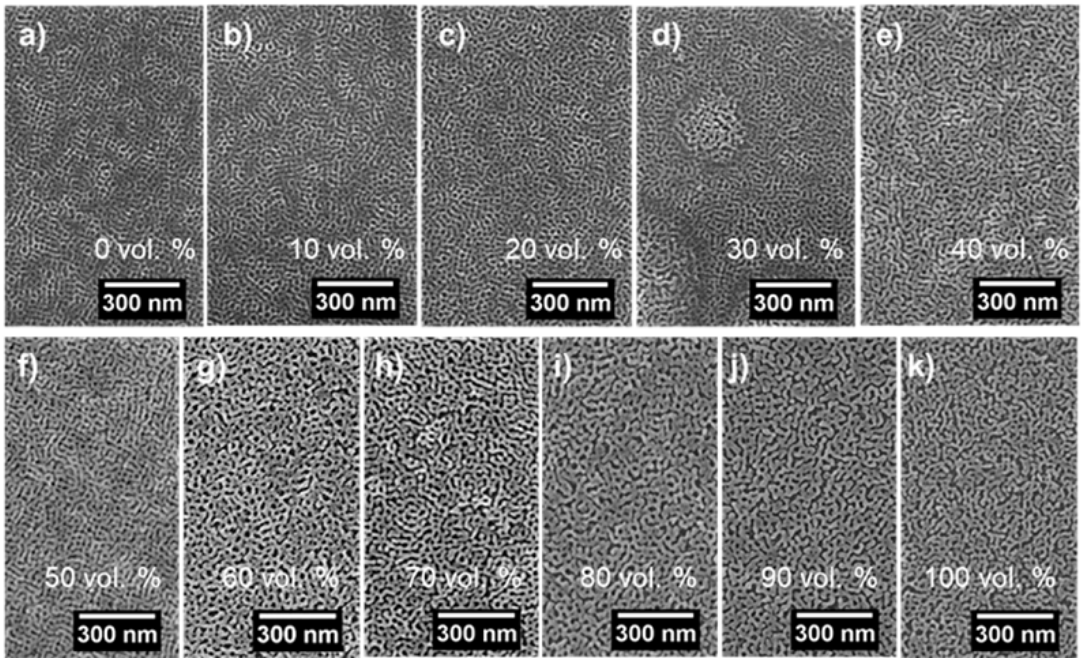

Figure 7.12: *SEM images of the α-Fe_2O_3 thin films prepared with different DMF/1,4-dioxane ratios. The volume fraction of 1,4-dioxane in the solvent mixture are marked in the images. The $\omega_{PS-b-P4VP}$:ω_{FeCl3} ratio used for solution preparation is 2:1. Reproduced from Ref [173] with permission from JOHN WILEY AND SONS, Copyright 2021.*

For unraveling the relationship between the thin film morphologies and the preferential

affinity of the co-solvent, a phase diagram of the α-Fe_2O_3 thin film morphologies is plotted as a function of the volume fractions of 1,4-dioxane and the $\Delta\chi$ values of different polymer-solvent pairs (Figure 7.13).

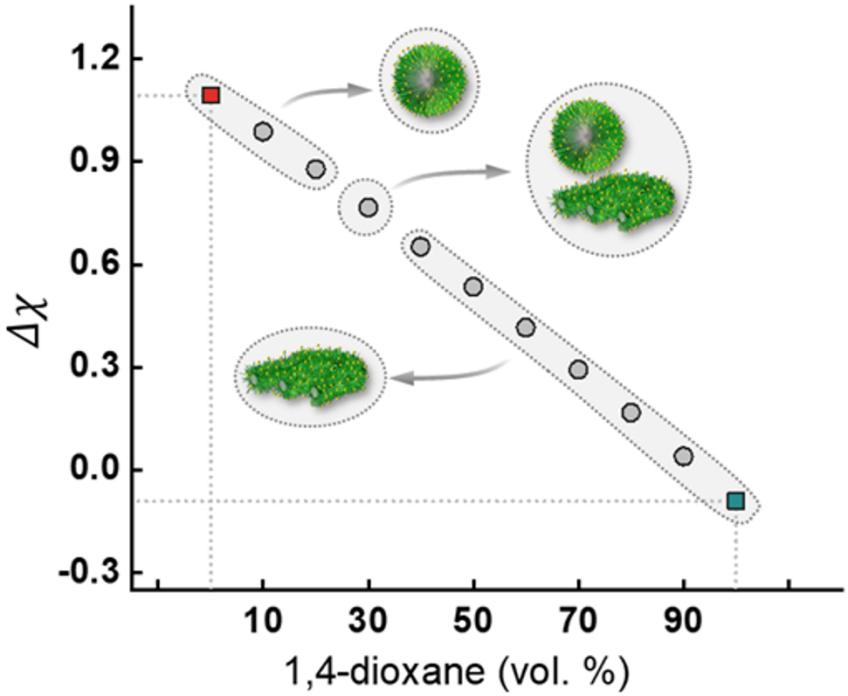

Figure 7.13: *Phase diagram of the α-Fe_2O_3 thin film morphologies with respect to the $\Delta\chi$ values of different polymer-solvent pairs and the volume fraction of 1,4-dioxane. Pure DMF and 1,4-dioxane solvent are represented with red and dark cyan squares. DMF/1,4-dioxane solvent mixtures are denoted with grey circles. The $\omega_{PS-b-P4VP}$:ω_{FeCl3} ratio used for solution preparation is 2:1. Reproduced from Ref [173] with permission from JOHN WILEY AND SONS, Copyright 2021.*

The specific polymer-solvent interaction parameters (χ_{P-S}) used for the $\Delta\chi$ calculation are listed in Table 7.3. According to the coordinate system, the thin film morphology is primarily templated by the spherical micelle structure in the region of $0.88 \leq \Delta\chi \leq 1.09$. The spherical-to-wormlike micellar transformation occurs at the $\Delta\chi$ value of 0.77. The further decrease of the $\Delta\chi$ value from 0.65 to -0.09 yields the neat wormlike nanostructures.

Volume ratio$_{DMF-1,4-dioxane}$	$\chi_{PS-Solvent}$	$\chi_{P4VP-Solvent}$	$\Delta\chi$
1.0:0.0	1.54	0.44	1.09
0.9:0.1	1.39	0.40	0.99
0.8:0.2	1.25	0.37	0.88
0.7:0.3	1.12	0.35	0.77
0.6:0.4	0.99	0.34	0.65
0.5:0.5	0.88	0.34	0.53
0.4:0.6	0.78	0.36	0.42
0.3:0.7	0.68	0.39	0.29
0.2:0.8	0.60	0.43	0.17
0.1:0.9	0.53	0.49	0.04
0.0:1.0	0.47	0.56	-0.09

Table 7.3: *Polymer-solvent interaction parameters (χ_{P-S}) and corresponding $\Delta\chi$ values of different polymer-solvent pairs. [109]*

For investigating the influence of the co-solvent compositions on the feature sizes and order of the α-Fe_2O_3 thin films, PSD functions of the SEM images from Figure 7.12 are calculated. As shown in Figure 7.14a, a significantly enhanced intensity in the low q region is observed for the thin film prepared with 30 vol.% 1,4-dioxane. This can be ascribed to the appearance of the micron-sized islands within the thin film. Figure 7.14b and c refer to the corresponding peak and FWHM values extracted from the PSD functions. A continuous shift of the peak position to smaller q values is observed by increasing the volume fraction of 1,4-dioxane from 0 vol.% to 90 vol.%, which indicates the continuous expansion of the feature sizes of the pore structures. However, a slight shift of the peak position towards larger q values is observed by increasing the 1,4-dioxane volume fraction from 90 vol.% to 100 vol.%. This shift is likely caused by the viscosity difference between the DMF/1,4-dioxane co-solvent and pure 1,4-dioxane. [218] Moreover, the extracted FWHM values (Figure 7.14c) indicate that the order of the nanostructure is decreased with the increase of the volume fraction of 1,4-dioxane. The highest FWHM value of the thin film prepared with 30 vol.% 1,4-dioxane can be ascribed to the mixture of the micron-sized island structures, which greatly diminishes the ordering of the thin film.

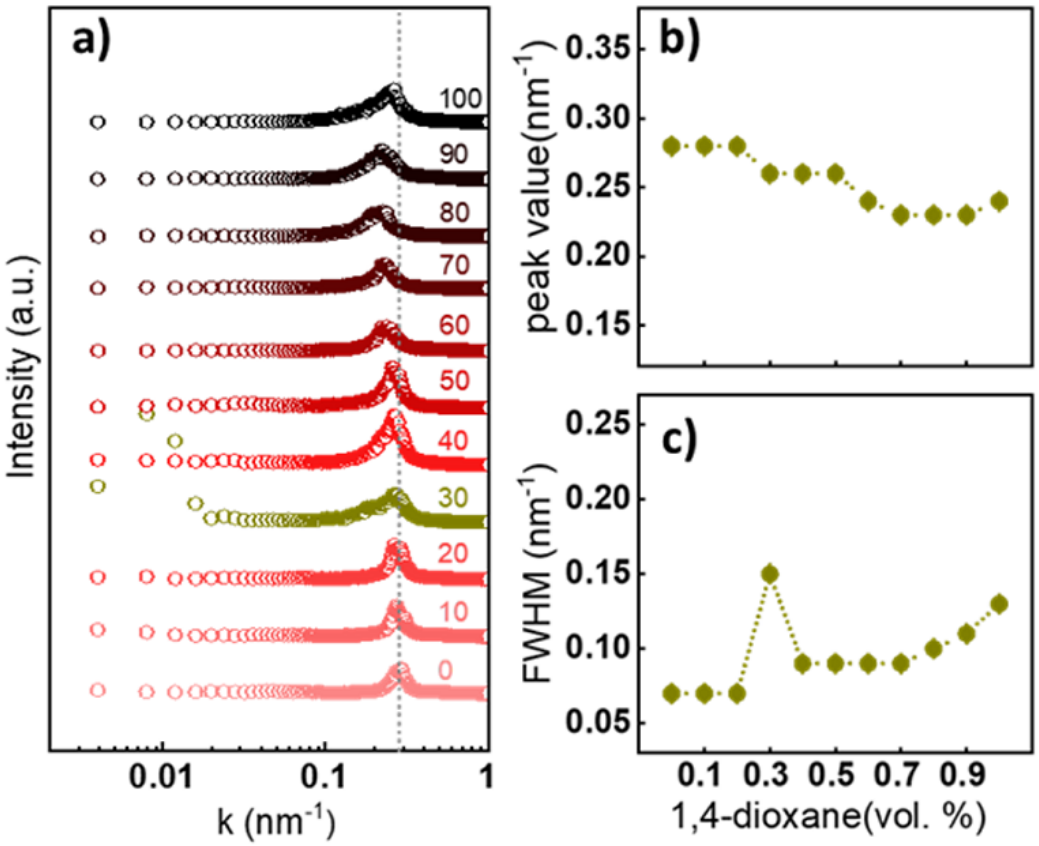

Figure 7.14: *PSD functions of the α-Fe_2O_3 thin films prepared with different DMF/1,4-dioxane ratios (a). The volume fractions of the 1,4-dioxane are marked above each PSD function and the grey dash line in a is plotted as a guide to the eye. The peak positions (b) and FWHM (c) for the different thin films are determined from the PSD functions. Reproduced from Ref [173] with permission from JOHN WILEY AND SONS, Copyright 2021.*

7.11 Conclusion

Mesoporous α-Fe_2O_3 thin films with different morphologies are synthesized by using $FeCl_3$ as the precursor and the amphiphilic diblock copolymer PS-b-P4VP as a template. The XRD, Raman, and XPS characterization results confirm the hematite phase in the thin films. The morphology control at the molecular level for the thin films is realized by changing the following two factors: the solvent category and the $\omega_{PS-b-P4VP}$:ω_{FeCl3} ratios. The SEM and GISAXS characterization results demonstrate the structural consistency on the local and large areas of the thin films. When the $\omega_{PS-b-P4VP}$:ω_{FeCl3} ratio used for sol-gel solution preparation is 1:2, nanocluster structures are observed in the case of the DMF and

1,4-dioxane solvent system. This nanostructures can be assigned to the weak templating effect of the low PS-b-P4VP concentration. By increasing the $\omega_{PS-b-P4VP}$:ω_{FeCl3} ratio to 1:1, the hierarchical spherical porous structure is formed in the DMF solvent system, whereas the wormlike structure is formed in the 1,4-dioxane system, which signifies the initiation of the phase separation of the PS-b-P4VP template in the sol-gel solution. The hierarchical structure in the DMF case can be assigned to the instability of the micellar structure, which leads to a partial fusion of the smaller spherical micelles. Moreover, the distinctly different morphologies present in the DMF and 1,4-dioxane system can be attributed to the different preferential affinity of the solvent. Further increasing the $\omega_{PS-b-P4VP}$:ω_{FeCl3} ratio to 2:1 leads to the expansion of the spherical pore structure, whereas the wormlike pore structure shrinks. The expansion of the spherical pore structure can be explained by the increased average number of polymer chains in an aggregate (N_{agg}). However, the unique interconnected wormlike structure tends to deform into more elongated wormlike structure for accommodating more polymer chains in the monolayer geometry. Moreover, DMF/1,4-dioxane solvent mixture with different component ratios are prepared for exploring the influence of the selectivity of the solvent on the nanostructure of the thin film. It is demonstrated that the spherical-to-wormlike porous structural transformation occurs at the critical $\Delta\chi$ value of 0.77 and the structural transformation leads to the expansion of the feature sizes of the nanostructures. The slight shrink of the feature size by increasing the volume fraction of 1,4-dioxane from 90 vol.% to 100 vol.% is likely due to the viscosity difference between the DMF/1,4-dioxane co-solvent and the pure 1,4-dioxane. Apart from the hybrid structure of the spherical and wormlike structure, the ordering of the nanostructures is gradually decreased by increasing the 1,4-dioxane component in the co-solvent. Given by the advantages of large area homogeneity and multiple morphologies, the α-Fe_2O_3 thin films prepared in the present work shows enormous application prospects in the photovoltaics and sensors fields.

8 Slot-die printed PS-b-P4VP and PS-b-P4VP/$FeCl_3$ thin films

Parts of this chapter have been published in the article: In-situ GISAXS observation and large area homogeneity study of slot-die printed PS-b-P4VP and PS-b-P4VP/$FeCl_3$ thin films.(YIN, Shanshan, et al. In Situ GISAXS Observation and Large Area Homogeneity Study of Slot-Die Printed PS-b-P4VP and PS-b-P4VP/FeCl3 Thin Films. ACS Applied Materials Interfaces, 2022, 14. Jg., Nr. 2, S. 3143-3155.) [219]

8.1 Preface

Nanostructured hematite (α-Fe_2O_3) thin films are highly promising for the applications as photoelectrodes or electrochemical electrodes in energy conversion and storage including photovoltaic devices, [220, 221] lithium-ion batteries, [187, 188, 222] sensors, [223–227] and photocatalysis [228–231] due to their non-toxicity, high abundance, and superior electrochemical stability. Several routes for synthesizing nanostructured α-Fe_2O_3 thin films were reported such as the hydrothermal method, [232] laser ablation, [233] and sol-gel method. [225, 234–238] Among the available physical or chemical synthesis approaches, solution-processable sol-gel method is particularly attractive due to their potential advantages such as simplicity, low-cost fabrication, and compatibility with large-scale thin film deposition techniques. [67, 220, 239–241] Moreover, the self-assembly of amphiphilic block copolymers was widely used for the synthesis of thin films with periodically ordered nanostructures, such as spheres, cylinders, and lamellae. [94, 242–245] Via block copolymer assisted sol-gel chemistry, various mesoporous metal oxide thin films have been prepared and the specific nanostructure was fine-adjusted by the components in the stock solution, the preferential affinity of the solvent to the polymer chains, and duration of the sol-gel reaction. [17, 18, 55, 246] To date, most amphiphilic block copolymer templated α-Fe_2O_3 thin film syntheses are still performed based on the lab-scale spin-coating

process, which is not suitable for the cost-effective fabrication of photoelectrodes or electrochemical electrodes in energy conversion and storage. Spray coating or printing are two well-established industrial-scale thin film deposition techniques. Compared to spray coating, printing techniques such as screen printing, [247] inkjet printing [248], slot-die printing [249], possess prominent advantages in terms of the crack resistance, tunable thicknesses and large area homogeneity of the deposited thin films. [240, 244] Moreover, grazing-incidence small-angle X-ray scattering (GISAXS) is a powerful tool for following the structure evolution in-situ and to detect the large area homogeneity of nanostructured thin films. [39, 250, 251] Recent investigations combined printing with the in-situ GISAXS technique for gaining an in-depth understanding of the film formation process during printing. For instance, Li et al. printed crack-free mesoporous TiO_2 thin films using a polystyrene-block-poly(ethylene oxide) templated wet chemistry method, which pioneered further investigations of printing block copolymer templated functional mesoporous metal oxide thin films. [252] Weinhold et al. followed the morphological evolution together with the optical properties of the active layers during the slot-die printing process and promoted the realization of large-scale production of high-efficiency organic solar cells. [253] Xia et al. fabricated magnetically anisotropic polystyrene-block-poly(methyl methacrylate)/γ-Fe_2O_3 hybrid thin films through applying an external magnetic field during the printing procedure. The structure formation perpendicular and parallel to the magnetic nanoparticle wires were characterized with GISAXS in detail. [240] Until now, a detailed investigation of the film formation kinetics and film homogeneity for block copolymer-templated α-Fe_2O_3 thin films are not yet performed.

In this section, we use slot-die coating to print PS-b-P4VP and hybrid PS-b-P4VP/$FeCl_3$ thin films. The film formation is followed with $in-situ$ GISAXS during printing and the large area homogeneity of the printed films are confirmed as well with GISAXS measurements. N, N-dimethylformamide (DMF), a selective solvent for the P4VP blocks of PS-b-P4VP and the coordination agent $FeCl_3$ are used for preparing the stock solutions of the sol-gel chemistry route. Dynamic light scattering (DLS) measurements are performed to probe the relationship between micellar structures in the stock solutions and the final structure of the printed thin films. Compared to the PS-b-P4VP control sample, the coordination effect between Fe^{3+} and the vinyl pyridine groups leads to an entanglement of the P4VP chains and the agglomeration of the micelles in the PS-b-P4VP/$FeCl_3$ composite solution. As a result, a different attachment property of the P4VP chains to the silicon substrate is induced. Thus, a distinct lateral domain size evolves and the ordering of structures occurs during the printing process. Due to the solvent convection and the preferential affinity of the DMF solvent to the P4VP blocks, dimple-type structures with vertically oriented PS cylinders dispersed in the P4VP host

develop in both, PS-b-P4VP and hybrid PS-b-P4VP/$FeCl_3$ printed films. By removing the polymer template from the hybrid PS-b-P4VP/$FeCl_3$ thin film after printing, a highly ordered, mesoporous and uniform α-Fe_2O_3 thin film is obtained. The successful printing of such α-Fe_2O_3 thin films is an important step toward real-world application of large area printed photoelectrodes or electrochemical electrodes in energy conversion and storage.

8.2 $In-situ$ and $ex-situ$ GISAXS measurements

Figure 8.1 shows the flow chart of the present experiments. For the PS-b-P4VP solution preparation, 20 mg PS-b-P4VP was added into 2 ml DMF solvent and stirred continuously for 2 hours. For the PS-b-P4VP/$FeCl_3$ counterpart, 20 mg PS-b-P4VP and 20 mg $FeCl_3$ were dissolved in 1 ml DMF and stirred for 1 hour, respectively. Then, the $FeCl_3$ and PS-b-P4VP solutions were mixed and stirred for another hour (Figure 8.1a). The $in-situ$ printing GISAXS experiment was performed at the P03 beamline of PETRA III storage ring with a beam-size of 10 x 27 μm^2 and X-ray energy of 12.92 keV (Figure 8.1b). [162] The sample-to-detector distance was determined to be 4200 mm by a calibration measurement using silver behenate and the incident angle was 0.35°. The scattering signal was recorded by a Dectris Pilatus 300K detector with a pixel size of 172 μm × 172 μm. The wet-chemical deposition via printing was performed with a homemade slot-die printer. The printer head was mounted and the sample stage was moved perpendicular to the X-ray beam. Accordingly, the thin film deposition was driven by the solution injection and simultaneous movement of the substrate holder. The solution was guided by a shim mask and a meniscus guide mask installed inside the printer head. A photograph of the set-up installed at the DESY beamline as well as a schematic diagram of the main parts of the printer is shown in Figure 8.2. The printing temperature was pre-regulated for ensuring a uniform thin film structure on both, macroscopic and microscopic length scales. Figure 8.3 shows the Fe_2O_3 thin films printed at 50 °C, 70 °C and 90 °C, respectively. Both, the degree of order and the homogeneity of the Fe_2O_3 thin films are significantly enhanced by increasing the printing temperature from 50 °C to 90 °C. Therefore, the sample stage is preheated to 90 °C before starting the $in-situ$ GISAXS measurements. The precleaned silicon substrates were fixed on the sample stage to avoid its possible displacement during the $in-situ$ printing process. After alignment, the sample stage was moved to the initial position for printing. The stock solution was infused into the printer head with a speed of 0.3 ml/min and the distance between the sample stage and the printing head was set as 0.5 mm. The sample stage was moved with a speed of 10 mm/s. To avoid radiation damage of the thin film, a minimized exposure time of 0.05 s was applied and the measurement position was laterally moved. The GISAXS data were recorded for the PS-b-P4VP thin

film from 12.7 s to 382.5 s and for the hybrid PS-b-P4VP/$FeCl_3$ film from 18.1 s to 543.8 s. Homogeneity scan for the printed thin films was performed over a span of 8.0 mm, which covered the entire range of the $in-situ$ printing experiment (Figure 8.1c). To remove the PS-b-P4VP template, the printed hybrid PS-b-P4VP/$FeCl_3$ thin film was calcined at 500°C for 2h in air (Figure 8.1d).

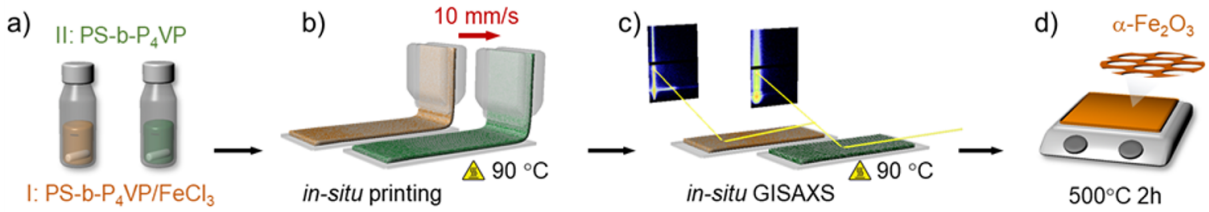

Figure 8.1: *Fabrication of mesoporous Fe_2O_3 films via slot die coating and high-temperature annealing: a) PS-b-P4VP/$FeCl_3$ and PS-b-P4VP are dissolved in DMF. b) The solutions are individually slot-die coated. c) The film formation of the printed films is followed by in-situ GISAXS. d) The slot die coated PS-b-P4VP/$FeCl_3$ thin film is calcined at 500 °C for 2h to finalize the α-Fe_2O_3 thin film. Adapted with permission from Ref [219] Copyright (2022) American Chemical Society.*

The static GISAXS measurement for the calcined thin film was carried out with a Ganesha SAXSLAB instrument with X-Ray energy of 8.05 keV. The incident angle was 0.42°, the sample-to-detector-distance was 1056 mm, the horizontal and vertical beam sizes were 200 μm, and 100 μm, and a Dectris Pilatus 300K detector was used for the scattering data acquisition. The GISAXS data was analyzed by a Python-based software, DPDAK (Directly Programmable Data Analysis Kit). [163]. Horizontal line cut of the 2D GISAXS data was performed at the critical angle of the material, the Yoneda peak position. The critical angle of PS, P4VP, $FeCl_3$ and Fe_2O_3 bulk were calculated to be 0.096°, 0.098°, 0.15°, and 0.32° with the X-ray energy of 8.05 keV. Considering the coordination effect between the Fe^{3+} and the vinyl pyridine groups on the P4VP chains, the critical angle of the Fe^{3+} complexed P4VP phase was determined as the average value of $FeCl_3$ and P4VP (0.12°).

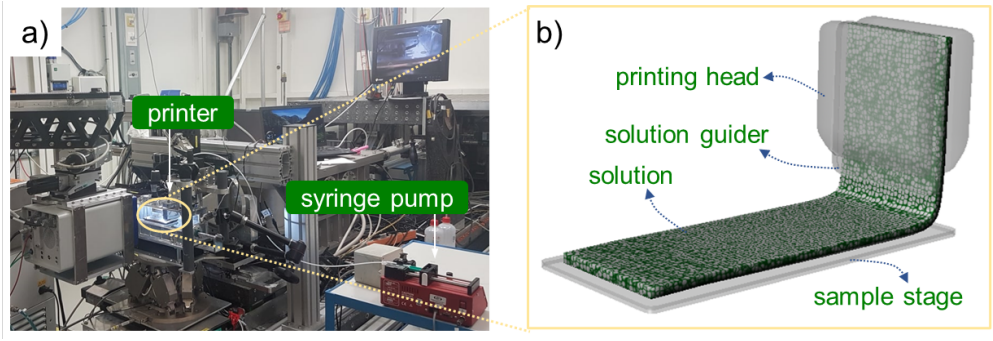

Figure 8.2: *a) Photograph of the in situ set-up installed at the MiNaXS/P03 beamline at DESY with labeled printer and syringe pump and b) schematic of the basic deposition principle showing the main parts of the printer. Adapted with permission from Ref [219] Copyright (2022) American Chemical Society.*

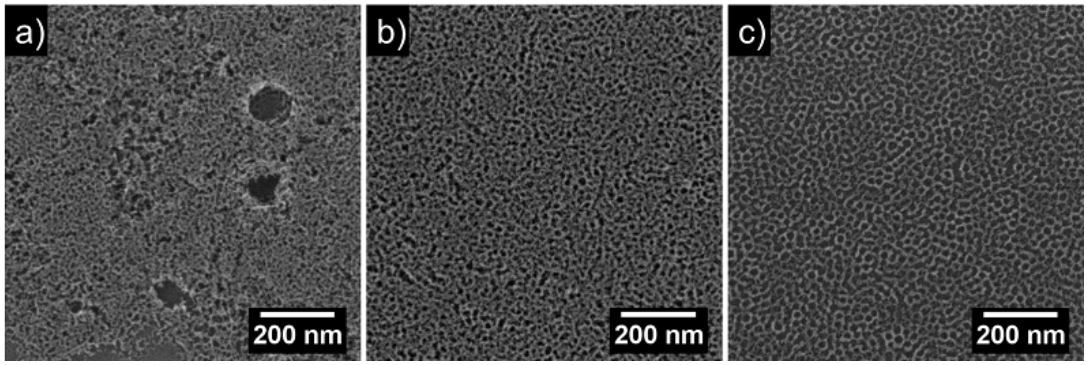

Figure 8.3: *SEM images of the Fe_2O_3 thin films printed with different substrate temperature: a) 50° C, b) 70 °C and c): 90 °C. Adapted with permission from Ref [219] Copyright (2022) American Chemical Society.*

The Yoneda peak positions of PS, P4VP and P4VP/$FeCl_3$ are marked in the vertical line cuts of the 2D GISAXS data of the printed film (Figure 8.4a and b). The critical angle of the mesoporous Fe_2O_3 is determined to be 0.22° (Figure 8.4c). Figure 8.5 shows the calculated scattering depth as a function of the incidence angle, and the X-ray energies and the density of the substance used for the calculation of the attenuation length profile are shown in table 8.1 Thus, at the selected incidence angles a probing of the full film thickness was ensured.

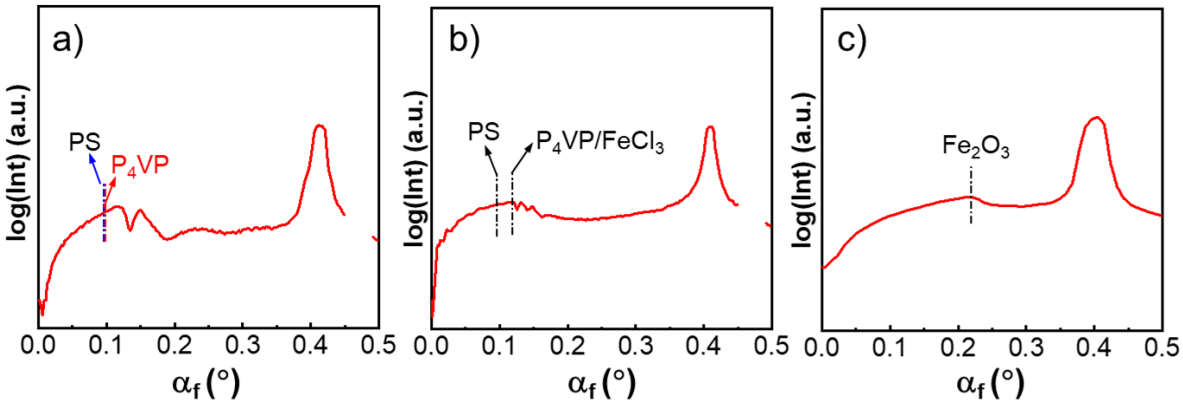

Figure 8.4: *Vertical line cuts of the 2D GISAXS data of PS-b-P4VP a), PS-b-P4VP/$FeCl_3$ b) and Fe_2O_3 c) thin films performed at $q_y = 0$ nm^{-1}. The critical angles of PS, P4VP, P4VP/$FeCl_3$ and Fe_2O_3 are marked with vertical dash lines. Adapted with permission from Ref [219] Copyright (2022) American Chemical Society.*

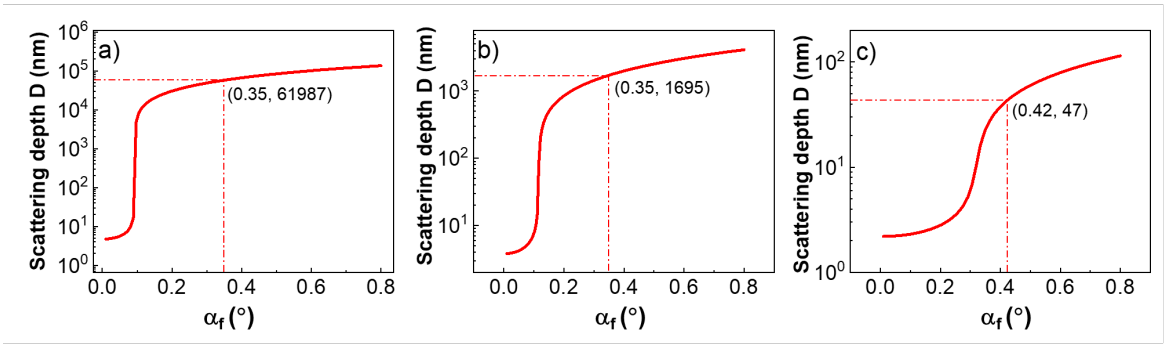

Figure 8.5: *Calculated scattering depth as a function of the incidence angle for (a) PS-b-P4VP and (b) PS-b-P4VP/$FeCl_3$ thin films at an x-ray energy of 12.92 keV as well as (c) α-Fe_2O_3 thin film at 8.05 keV. Adapted with permission from Ref [219] Copyright (2022) American Chemical Society.*

material	Energy (eV)	Density (g/cm^3)
PS-b-P4VP	12920	1.0
PS-b-P4VP/$FeCl_3$	12920	1.6
α-Fe_2O_3	8050	5.2

Table 8.1: *X-ray energies and the density of the material used for the calculation of the scattering depth. Adapted with permission from Ref [219] Copyright (2022) American Chemical Society.*

For a medium with the X-ray refractive index $n = 1 - \delta + i\beta$, the scattering depth is

$$D = \frac{\lambda}{\sqrt{2}\pi\,(l_i + l_f)} \tag{8.1}$$

with

$$l_{i,f} = \left[\mathbf{sin}\alpha_c{}^2 - \mathbf{sin}\alpha_{i,f}{}^2 + \sqrt{(\mathbf{sin}\alpha_{i,f}{}^2 - \mathbf{sin}\alpha_c{}^2)^2 + \left(\frac{\mu\lambda}{2\pi}\right)^2} \right]^{1/2} \tag{8.2}$$

8.3 Solution and thin film characterization

For determining the size distribution of the aggregates in the solution, dynamic light scattering measurements were performed with a LS spectrometer (LS Instruments, Fribourg, Switzerland). The instrument was equipped with a polarized helium-neon (HeNe) laser light source (Thorlabs, Dachau, Germany) with a maximum power output of 21 mW and provided a wavelength of 632.8 nm. The PS-b-P4VP and PS-b-P4VP/$FeCl_3$ solutions were filtered with a 0.45μm polytetrafluoroethylene (PTFE) sieve before the DLS measurements. Prior to the measurement, the PS-b-P4VP or PS-b-P4VP/$FeCl_3$ solution was filled into a glass cuvette with an outer diameter of 5 mm and a wall thickness of 0.4 mm. The temperature of the sample was controlled by placing the glass cuvette in a temperature-controlled decaline bath. Measurements were performed at 25 °C with a scattering angle of 90°. Normalized intensity autocorrelation functions $g_2(q,\tau)$ were recorded for 30 s and subsequently averaged after removing outliers. $q = 4\pi n \times \sin(\theta)/\lambda$ is the momentum transfer with n the refractive index of the solvent, 2θ the scattering angle, λ the wavelength of the laser light and τ the delay time. The normalized autocorrelation functions $g_2(q,\tau)$ were analyzed by the REPES algorithm implemented in the Gendist software. [254] A probability to reject of 0.5 was chosen. The distribution was normalized to the height of the most prominent peak, which gave the distribution of hydrodynamic radii A(Rh) in equal-area representation RhA(Rh) versus log(Rh). The average value of Rh, as well as the standard deviation, were determined from 5 measurements per sample.

The high-resolution field emission scanning electron microscope (SEM, Zeiss Gemini NVision 40) measurements were performed at a working distance of 3.5 mm and an acceleration voltage of 5 kV. The thin films were tilted (45°) respective to the electron beam for the cross-section SEM measurement. X-ray photoelectron spectroscopy (XPS) measurement was performed with a ESCALAB 250Xi spectrometer (monochromatized Al Kα radiation, hν= 1486.6 eV) in the air condition. Fourier transform infrared spectroscopy (FTIR) measurements was performed with an EQUINOX 55 FTIR instrument (BRUKER

CORPORATION, Billerica, United States of America). The spectrum was recorded in the range between 4000 and 400 cm^{-1}, with a resolution of 2 cm^{-1} and a scan number of 256. The crystallinity of the thin film was analyzed with a D8 ADVANCE X-ray diffractometer (XRD) using an X-ray wavelength of 1.54 $\AA$. To enhance the test signal of XRD and FTIR measurement, drop-casting was used for thin film deposition. Profilometry measurements were performed with a DektakXT Stylus Profiler (Bruker). Ten spots were measured to ensure sufficient experimental statistics for each sample.

8.4 Aggregate study in solution

For detecting the aggregation state of the polymer chains in the solution, DLS measurements are performed for the pure PS-b-P4VPand PS-b-P4VP/$FeCl_3$ solutions. Figure 8.6a shows the normalized autocorrelation curves acquired at a scattering angle of 90°, in which two and three decays are detected for PS-b-P4VP and PS-b-P4VP/$FeCl_3$ solutions, respectively. The first decay has a rather high amplitude and is ascribed to the diffusion of individual polymer chains. The slow second and third decay are rather weak and presumably result from the diffusion of larger objects. [243] The corresponding hydrodynamic radii Rh are shown in Figure 8.6b, the Rh values corresponding to the single PS-b-P4VP and the Fe^{3+} complexed PS-b-P4VP polymer chains are determined to be (4.1 ± 0.2) nm and (4.0 ± 0.2) nm, which suggests that the complexation of Fe^{3+} has almost no effect on the stretching state of individual PS-b-P4VP chains in the DMF solution. Moreover, the peak located at (166 ± 6) nm for the PS-b-P4VP solution and (72 ± 3) nm for the PS-b-P4VP/$FeCl_3$ solution can be ascribed to micelle assemblies as it is over large for single micelle. Since the PS-b-P4VP concentration studied in the present work is well above of reported critical micelle concentration (CMC) of the block copolymer, micelles as well as their corresponding assemblies can be expected in the solution. [255] Based on the contour lengths of the PS and P4VP blocks used in the present work, the size of simple spherical micelles with a PS core and a P4VP shell would be smaller than the values detected with DLS. [205] The molecular structure of PS and P4VP is shown in Figure 8.7 The calculated contour length and the polymer parameters used for the calculation is shown in table 8.2. Thus, the formed structure is more complex including a complexation structure between PS-b-P4VP and Fe^{3+} as schematically shown in the inset in Figure 8.6a. [256] Possibly, pre-assemblies of the polymer chains form 1D cylindrical micelles in the solution, which are larger than spherical micells. This kind of individual micelles can fuse into larger object as depicted in Figure 8.6c. Compared to the PS-b-P4VP/$FeCl_3$ solution, the fusion probability of the micelles in the pure PS-b-P4VP solution is relatively higher as no coordination effect between Fe^{3+} and the vinyl pyridine

groups exists. The coordination effect between Fe^{3+} and the vinyl pyridine groups might lead to the tangling of the P4VP chains in the micelle shell and the cementation between different micellar cell. Consequently, hard shell structure composed of tangled P4VP chains and Fe^{3+} can be formed around the PS cores, which hinders the fusion process of the single micelles and promotes the formation of the micellar assemblies in the solution. Thus, the detected peak positions at (72 ± 3) nm and (166 ± 6) nm in Figure 8.6b can be ascribed to the scattering of nonspherical micelles. Compared to the pure PS-b-P4VP solution, an additional weak scattering is detected in the micrometer range for the PS-b-P4VP/$FeCl_3$ solution, which can be ascribed to the small amount of micellar aggregates in the solution.

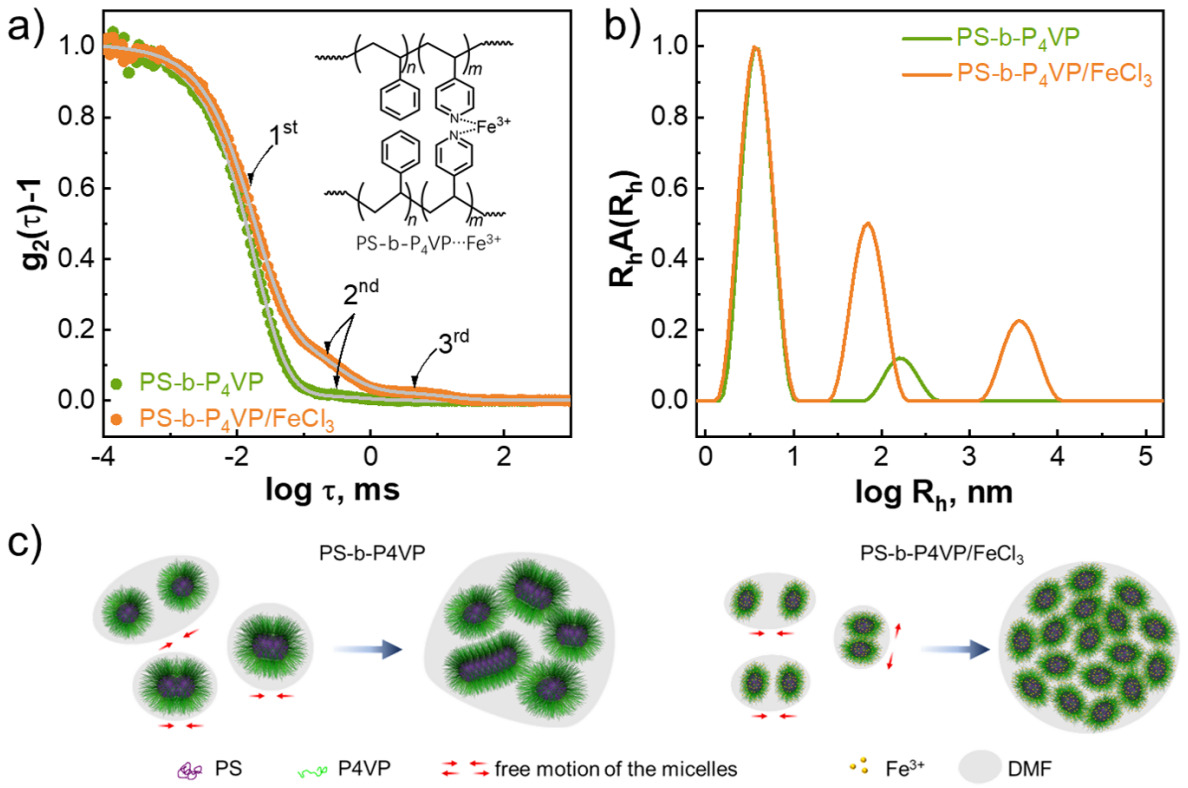

Figure 8.6: *Normalized autocorrelation functions at θ = 90° a) and the corresponding distribution functions of hydrodynamic radii Rh b) of the PS-b-P4VP (green) and PS-b-P4VP/$FeCl_3$ (orange) solutions. The decay positions of the autocorrelation functions are marked with arrows in a). The inset in a) shows the complexation between the PS-b-P4VP chains and the Fe^{3+}. Adapted with permission from Ref [219] Copyright (2022) American Chemical Society.*

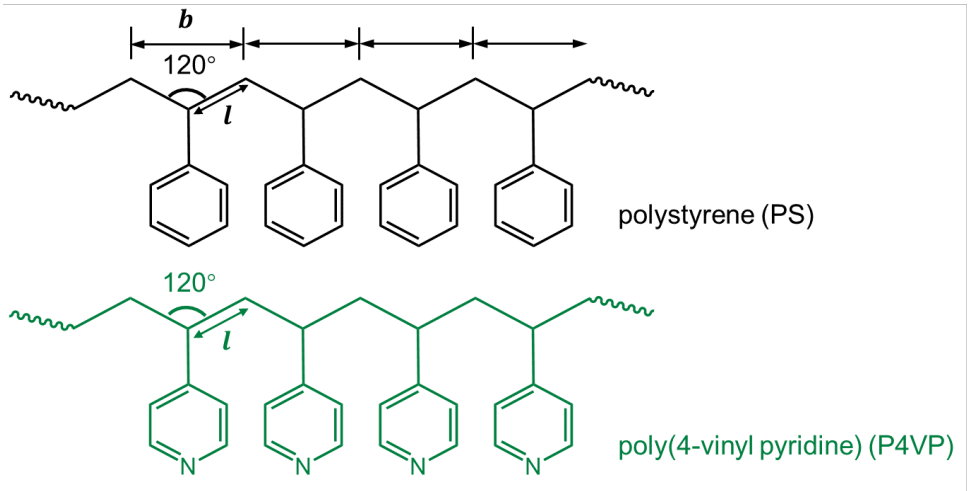

Figure 8.7: *Molecular structure and of PS (top) and P4VP (bottom). The length of the repeat unit is represented as b and the length of the signal bond between the carbon atoms is denoted as l. Adapted with permission from Ref [219] Copyright (2022) American Chemical Society.*

polymer	M(g/mol)	m(g/mol)	n	N	b(nm)	L_c(nm)
polystyrene (PS)	11800	104.1	113	57	0.267	15.2
poly(4-vinyl pyridine) (P4VP)	10800	105.14	103	52	0.267	13.9

Table 8.2: *Calculated contour length Lc of the PS and P4VP segments used in the present work based on molecular weight of the repeat unit m, degree of polymerization n, length of repeat cell b. Adapted with permission from Ref [219] Copyright (2022) American Chemical Society.*

8.5 In-situ film formation study

Thin films are prepared by printing the PS-b-P4VP and PS-b-P4VP/$FeCl_3$ solutions onto the silicon substrates. During the printing process, the thin film formation is followed with in-situ GISAXS. Selected 2D GISAXS data are shown in Figure 8.9. The lateral structure evolution during the printing process is shown as the two-dimensional (2D) color mapping of the horizontal line cuts (Figure 8.10a and d). Selected line cuts are shown in Figure 8.11a and b. Pure PS-b-P4VP film and hybrid PS-b-P4VP/$FeCl_3$ film printing differ markedly in terms of the temporal evolution, while the wet-to-dry process of both thin films can be divided into two phases (i and ii). The wet-to-dry boundary of the pure PS-b-P4VP thin film can be identified by the variation of the intensity in the

high q_y region (Figure 8.10a). In this region, intensity is hardly detectable up to 25.5 s (phase i). From 25.5 s to 382.5 s (phase ii), the intensity is increased, which can be ascribed to the fast evaporation of DMF solvent and the drying process of the thin film. However, an obvious intensity fluctuation is present in the low q_y value region of the pure PS-b-P4VP film during phase ii. Considering the temperature of the sample stage (90 °C) is lower than the glass transition temperature of PS (104°C) and P4VP (153°C) blocks, a significant restructuring of the polymer chains after the evaporation of the DMF solvent is negligible and the intensity fluctuation is likely induced by a spatial inhomogeneity of the thin film. [244] For obtaining detailed information on the film morphology, the line cuts of the 2D GISAXS data are analyzed with a model based on the distorted-wave Born approximation (DWBA) combined with the effective interface approximation (EIA) and the local monodisperse approximation (LMA) (Figure 8.11a). More details about data modeling can be found in Figure 5.4. One set of structure factor (center-to-center distance, D) and form factor (radius, R) is sufficient to model the data (Figure 8.10b and c). Within phase i (0 s - 25.5 s), the center-to-center distance and radius decrease from (460 ± 21) nm to (400 ± 20) nm and from (58 ± 3) nm to (54 ± 2) nm, which can be ascribed to the fast evaporation of the solvent. In contrast, the fluctuation of the feature size within phase ii are ascribed to the spatial inhomogeneity of the PS-b-P4VP film. During the printing process of the hybrid PS-b-P4VP/$FeCl_3$ film, a gradual increase in the scattering intensity at larger q_y values is noticeable in the first 36.2 s (phase i), which is caused by solvent evaporation. From 36.2 s to 543.8 s (phase ii), stable scattering features emerge and stay constant, reflecting a thorough removal of the DMF solvent from the film. For analysis, two sets of structure factors and form factors are used to model the horizontal line cuts (Figure 8.11b). The modeling results are shown in Figure 8.10e and f. Within phase i (from 0 s to 36.2 s), the D1 and D2 value decreases from (25.0 ± 1.0) nm to (24.0 ± 0.7) nm and from (30 ± 2) nm to (29.0 ± 1.6) nm, while R1 and R2 decreases from (10.5 ± 0.6) nm to (10.0 ± 0.5) nm and from (18 ± 2) nm to (16.6 ± 1.7) nm, respectively. Within phase ii, the D1, D2 value remain constant at (23.0 ± 0.5) nm, (28.0 ± 1.0) nm, and the R1, R2 value at (9.4 ± 0.3) nm, (15.9 ± 1.0) nm, respectively. Compared to the pure PS-b-P4VP counterpart, the slower film formation process identified in the hybrid film might be associated with the coordination between Fe^{3+} and the P4VP chains. Moreover, the dry PS-b-P4VP/$FeCl_3$ thin film features significantly enhanced structural homogeneity, decreased domain size in the lateral direction, and high structural orderring as evidenced by the appearance of a second-order peak in the high q_y region. The enhanced ordering of the deposited PS-b-P4VP/$FeCl_3$ film is likely determined by the interplay between effective segregation strengths of the polymer chains as well as the evaporation of the DMF solvent. Compared

to the pure PS-b-P4VP film, the coordination effect between Fe^{3+} and the P4VP chains restricts the stretching of the P4VP and influences the segregation strength of the PS-b-P4VP chains during the thin film deposition process. Moreover, since DMF is not a volatile solvent, the evaporation rate of DMF will be very slow, if the film is deposited at lower temperature. The prolonged evaporation of DMF at low temperature imparts high mobility for the PS-b-P4VP chains and increases the probability of the lateral flow of the solution on the substrate, which is detrimental for the self-assembly of the PS-b-P4VP chains from the free motion state into an ordered form. This effect can be evidenced by the structural evolution of the α-Fe_2O_3 films printed at different temperatures (Figure 8.3). In addition, it is observed that the radii obtained from the GISAXS modeling result are proportional to the hydrodynamic radii of the single micelles extracted from the DLS measurement, which further confirms that the morphology of the printed thin films can be affected by the conditions of the micelle structures in the solution.

Apart from the lateral structure evolutions, we also evaluate the Yoneda peak position evolution performed with the 2D color plots by integrating the individual vertical line cuts. As shown in Figure 8.8, no significant peak shift is observed in the Yoneda region during the entire printing process, which reflects that the refractive index of both PS-b-P4VP and PS-b-P4VP/$FeCl_3$ films is approximated during the dring process. The rapid solvent evaporation in the deposited PS-b-P4VP and PS-b-P4VP/$FeCl_3$ films can be ascribed to the high substrate temperature and the low thicknesses of the deposited films.

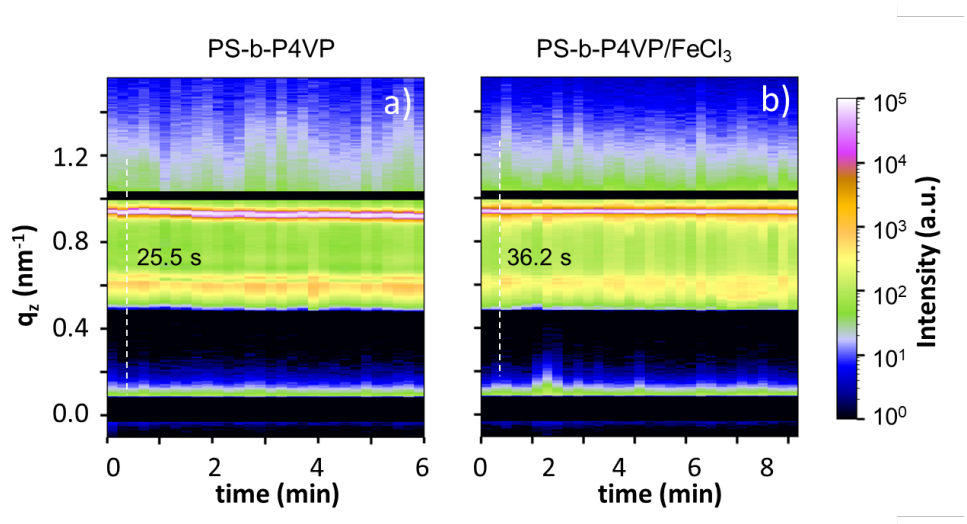

Figure 8.8: *2D mapping of the temporal evolution of the vertical line cuts from the 2D GISAXS data during printing of the (a) pure PS-b-P4VP and (b) hybrid PS-b-P4VP/$FeCl_3$ thin films. Characteristic times are indicated with vertical dashed lines at 25.5 and 36.2 s. Adapted with permission from Ref [219] Copyright (2022) American Chemical Society.*

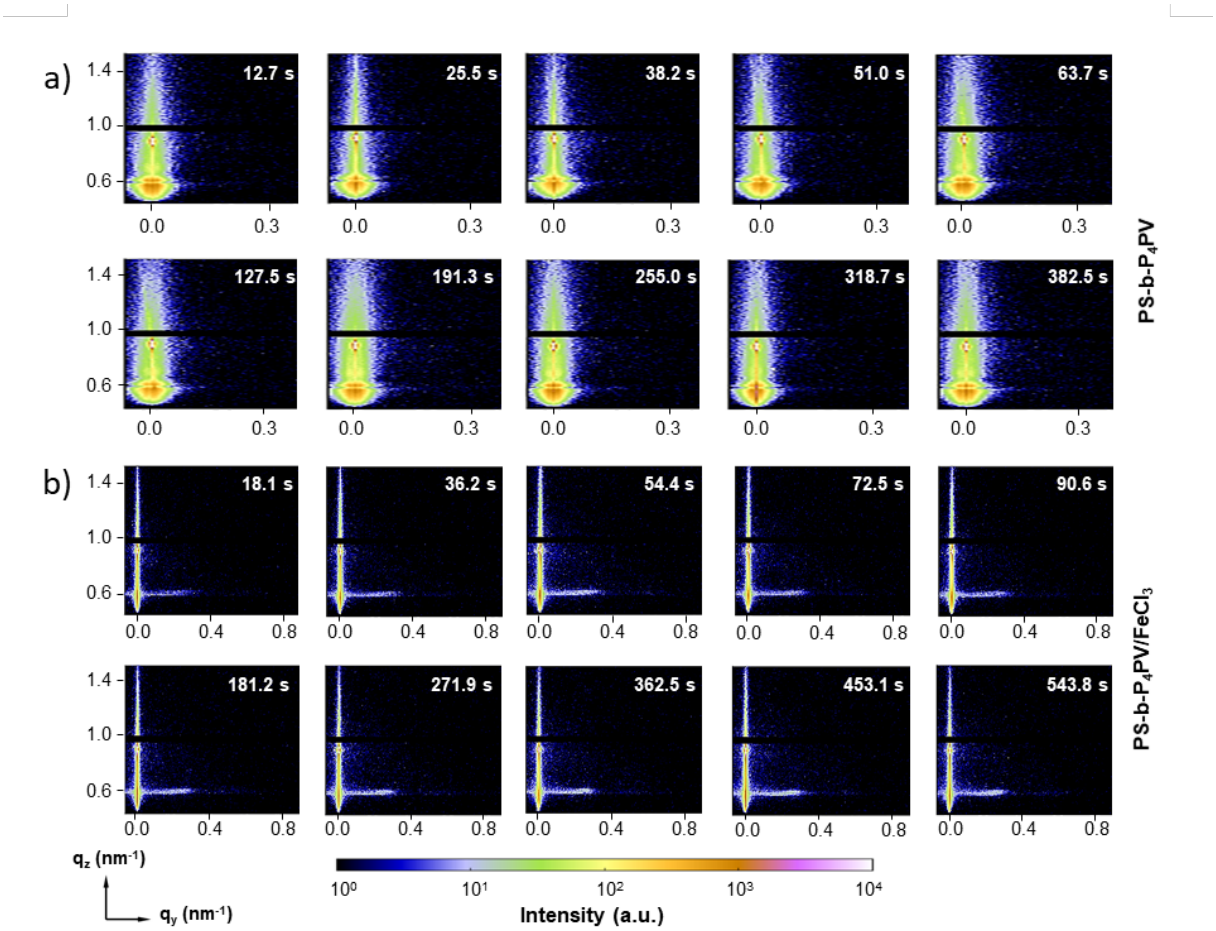

Figure 8.9: *2D GISAXS data measured during printing of the a) PS-b-P4VP and b) PS-b-P4VP/$FeCl_3$ thin films at different times as indicated. Adapted with permission from Ref [219] Copyright (2022) American Chemical Society.*

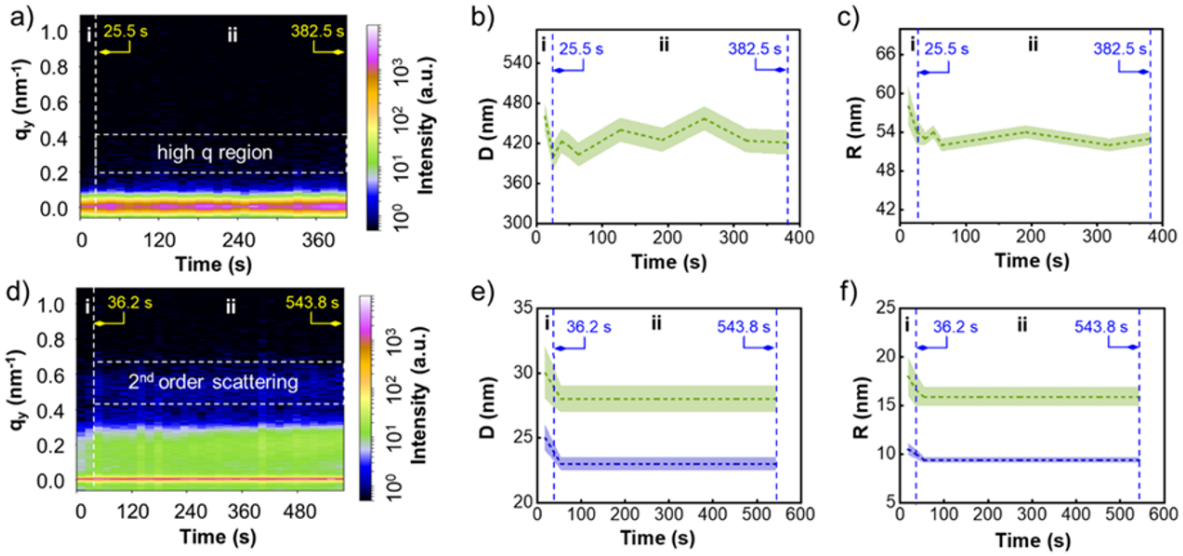

Figure 8.10: *2D mapping of the temporal evolution of the horizontal line cuts from the 2D GISAXS data during printing of the a) pure PS-b-P4VP and d) hybrid PS-b-P4VP/$FeCl_3$ thin film. The dashed white lines are plotted as guides to the eye to distinguish the wet-dry boundary of the printed thin film. The white dashed frames highlight the appearance of the second-order scattering in the high q_y region, respectively. Modeled center-to-center distances D b,e) and radii R c,f) of the PS-b-P4VP film b,c) and hybrid PS-b-P4VP/$FeCl_3$ film e,f). Adapted with permission from Ref [219] Copyright (2022) American Chemical Society.*

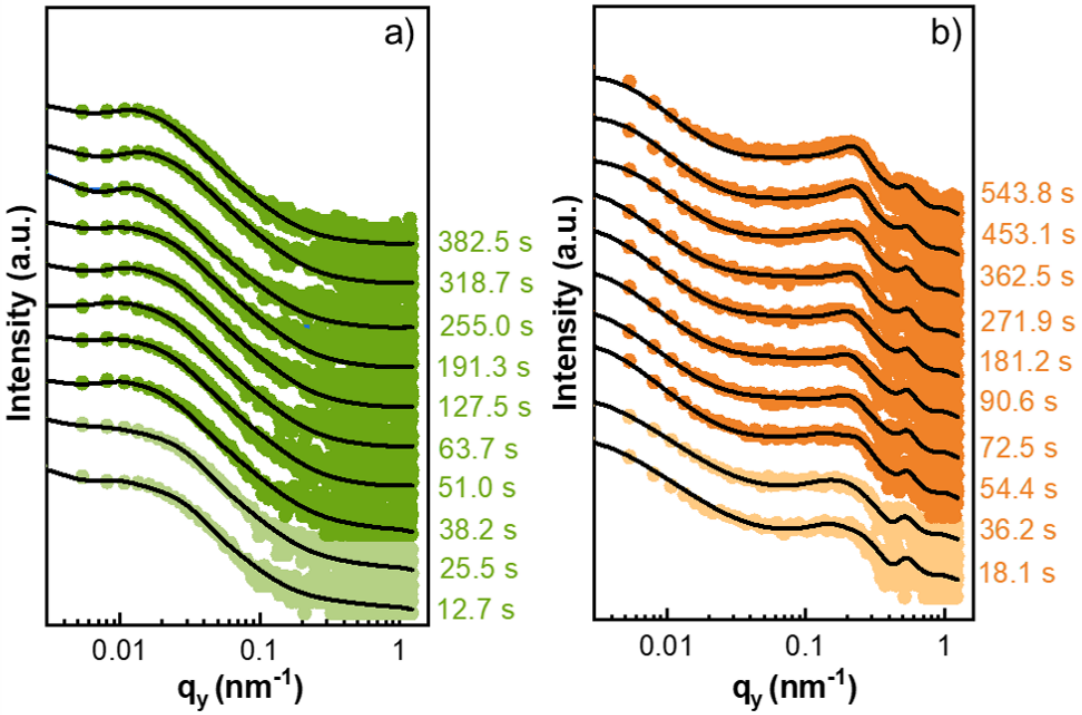

Figure 8.11: *Temporal evolution of horizontal line cuts of the 2D GISAXS data (symbols) shown together with the fits (solid lines) at selected times during the printing process. The line cuts are performed at the Yoneda peak positions of a) pure PS-b-P4VP and b) hybrid PS-b-P4VP/$FeCl_3$, respectively. Adapted with permission from Ref [219] Copyright (2022) American Chemical Society.*

8.6 Homogeneity of the PS-b-P4VP thin film

The microstructure of the dry PS-b-P4VP and PS-b-P4VP/$FeCl_3$ films is detected with the SEM measurement. Three distinct positions are selected for imaging. As shown in Figure 8.12, dimple-type structures consist of PS cores and a P4VP matrix for both thin films due to the poor solubility of the PS blocks in the DMF solvent. [256] Compared with the hybrid PS-b-P4VP/$FeCl_3$ thin film, the pure PS-b-P4VP thin film exhibits significantly enlarged domain sizes and conspicuous inhomogeneity along with the printing direction. For extracting more information about the diameter distribution of the PS cores, a binarization algorithm is performed for the SEM image via the Image J software. Taking the effect of the filter threshold into consideration, the statistics number obtained for the small sized objects is supposed to be slightly higher than the real value. As shown in Figure 8.15a, the majority diameter values extracted from the SEM images of the PS-b-P4VP film are less than 100 nm, and another discernable peak is located at around 500

nm. Moreover, a distinct difference in quantity is observed within each certain feature size range. In contrast, a comparative statistics number within each feature size range is obtained in the case of the PS-b-P4VP/$FeCl_3$ thin film (Figure 8.15b). Considering the large error of the statistics number in the range is less than 5 nm, the majority diameter values of the PS cores in the PS-b-P4VP/$FeCl_3$ thin films are determined in the range from 15 nm to 20 nm. Moreover, the PS-b-P4VP film mainly consists of randomly distributed microdomains, whereas distinct hexagonal lattices as marked with the yellow hexagons in Figure 8.15d-f can be identified on the PS-b-P4VP/$FeCl_3$ film surface. The structural differences in terms of the domain sizes, homogeneity, and regularity of the two films can be related to the aggregates in the solution and the interaction between the polymer chains and the polar silicon substrate. The DLS characterization demonstrates that the P4VP chains are more stretched in the pure PS-b-P4VP solution, and the P4VP block has a preferential interaction with the polar silicon substrate due to its smaller surface energy. [257] The high mobility of the P4VP chains in the pure PS-b-P4VP solution might induce the fusion of the micelles during the thin film deposition process, which is assumed to provoke the structural inhomogeneity shown in Figure 8.12a to c. Compared to the PS-b-P4VP film, the decreased domain sizes, enhanced homogeneity and structural order of the PS-b-P4VP/$FeCl_3$ counterpart can be primarily attributed to the decreased micellar sizes caused by the complexation of the Fe^{3+} and the P4VP chains. The complexation of the Fe^{3+} significantly restricts the stretching of the P4VP chains, which therefore inhibits their preferential interaction with the silicon substrate. As a consequence, smaller domain sizes are observed in SEM images (Figure 8.12d to f). It is worthy to be noted that the inter-domain distance in the printed PS-b-P4VP thin film is unusually large. Therefore, the P4VP chains should be in a highly-stretched conformation at such an inter micelle distances. Such conformation is very thermodynamically unfavorable due to the high entropic penalty. Therefore, the as printed thin films might possess unstable nanostructures. To study their thermal stability, an addition morphological characterization is performed after annealing of the as printed thin films at 100 °C for 30 mins. As shown in Figure 8.13, after the thermal annealing process, the substructures in the PS-b-P4VP thin film undergoes a reconstruction, whereas the nanodomains in the PS-b-P4VP/FeCl3 thin film are relatively persistent. The reconstruction of the substructures in the pure PS-b-P4VP thin film can be ascribed to the relaxation of the highly stretched polymer chains, which compensates the entropic penalties in the thin film. After the reconstruction process, a large number of sites within the continuous P4VP phase are interrupted. This might be caused by the more stretched state of the P4VP chains as they possess preferential interactions with the polar silicon substrate due to the smaller surface energy. Figure 8.14 shows the structural comparison and corresponding chain stretching model

in the PS-b-P4VP thin film occurred during the further thermal annealing process. The coordination effect between the Fe^{3+} and the P4VP chains in the final dry PS-b-P4VP and PS-b-P4VP/$FeCl_3$ thin films can be confirmed by the prominent shift of the pyridine ring from 1597 cm^{-1} to 1640 cm^{-1} in the FTIR spectra (Figure 8.16). [257]

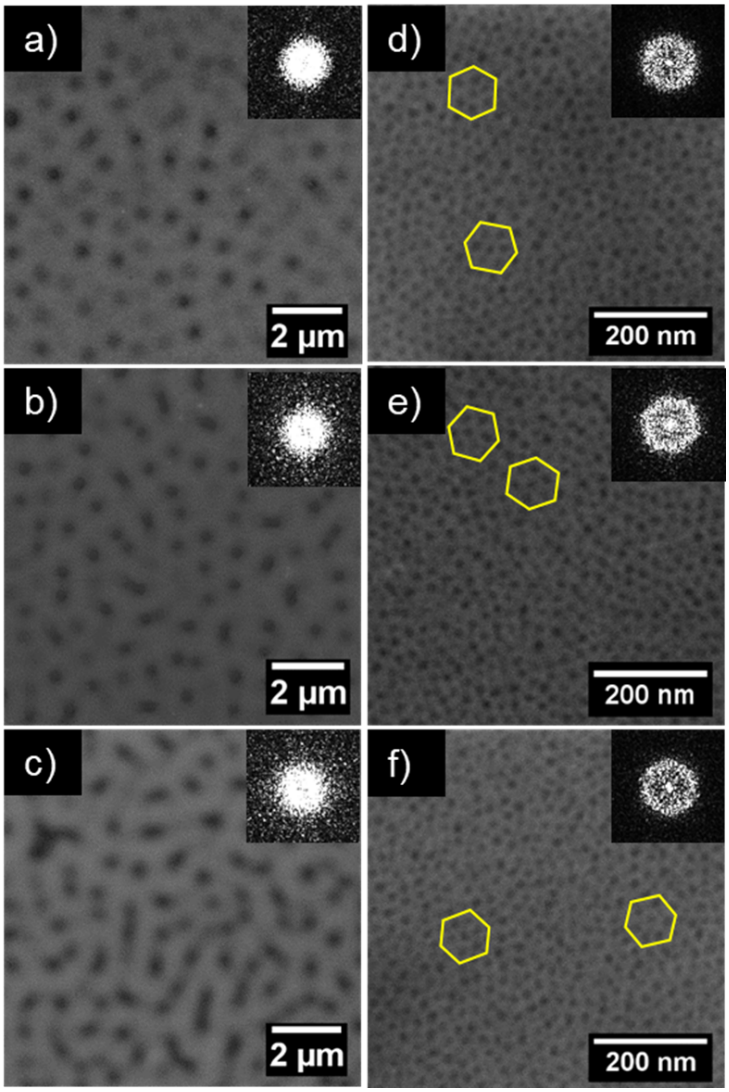

Figure 8.12: *SEM images show the surface morphologies at three different positions of a-c) the pure PS-b-P4VP and d-f) the hybrid PS-b-P4VP/$FeCl_3$ d to f) films. The images are shown sequentially in the printing direction and the corresponding distances between two adjacent SEM images are around 1 cm. Yellow hexagons are shown to illustrate the hexagonal lattice. Adapted with permission from Ref [219] Copyright (2022) American Chemical Society.*

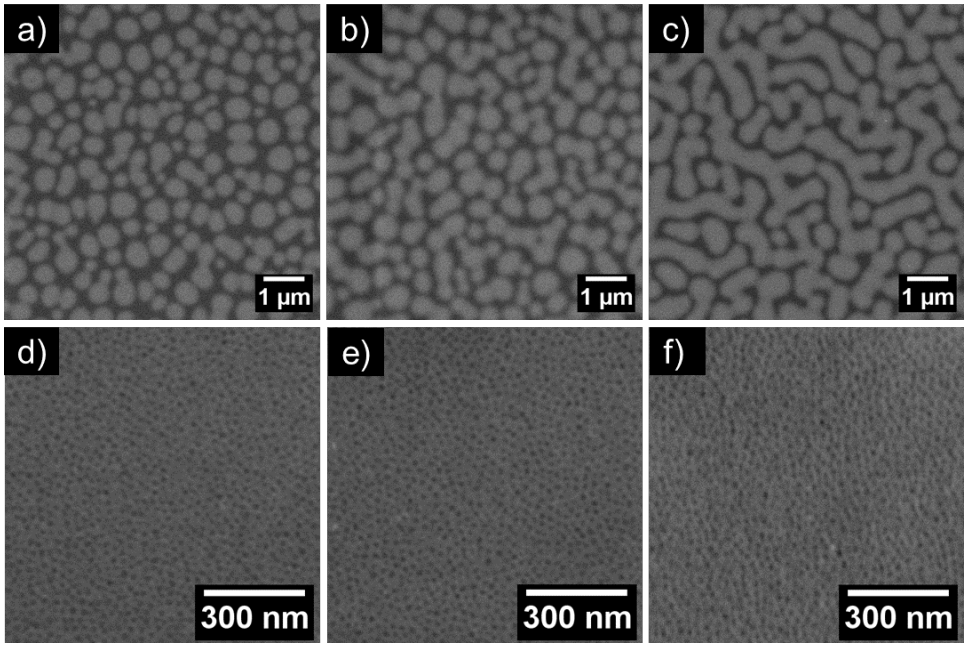

Figure 8.13: *SEM images of (a-c) the PS-b-P4VP and (d-f) PS-b-P4VP/FeCl3 thin films after annealing at 100 °C for 30 min. The images are shown sequentially in the printing direction and the corresponding distances between two adjacent SEM images are around 1 cm. Adapted with permission from Ref [219] Copyright (2022) American Chemical Society.*

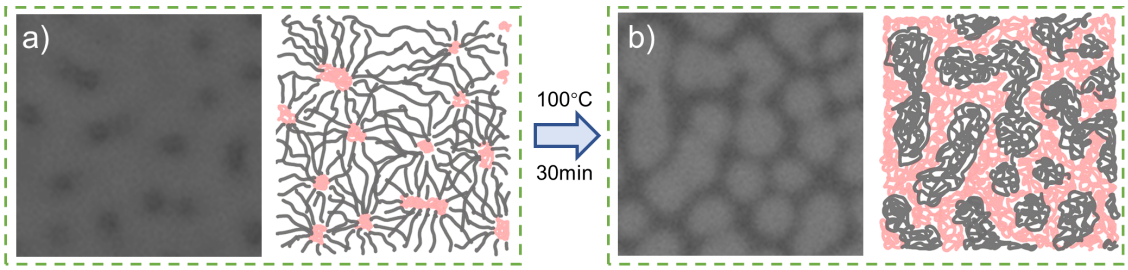

Figure 8.14: *Structural comparison and corresponding chain stretching model in the PS-b-P4VP thin film a) before and b) after annealing as seen with SEM and illustrated with a sketch. Adapted with permission from Ref [219] Copyright (2022) American Chemical Society.*

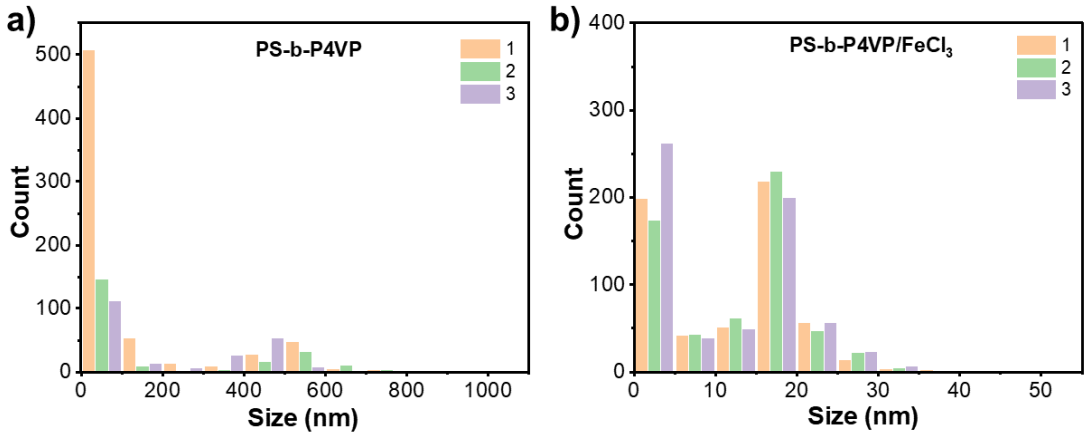

Figure 8.15: *Diameter distribution of the PS cylinders in the printed PS-b-P4VP and PS-b-P4VP/$FeCl_3$ thin films. The Histogram is plotted by performing the binarization algorithm for the SEM images via Image J software. The number in the legend represent the sequence of the SEM images. Adapted with permission from Ref [219] Copyright (2022) American Chemical Society.*

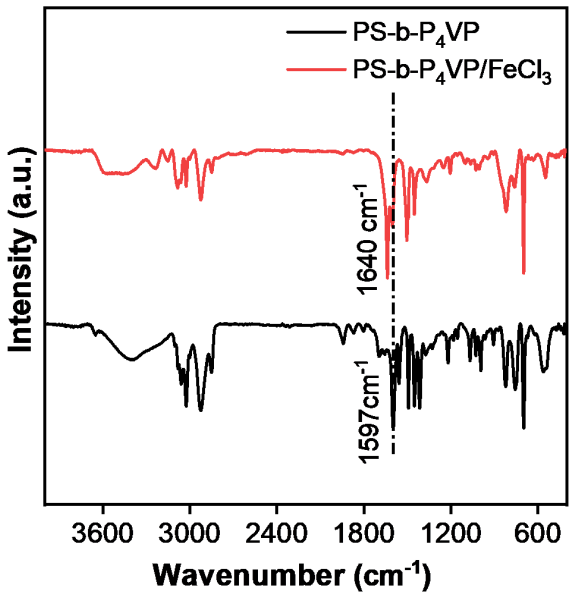

Figure 8.16: *FTIR spectrum of PS-b-P4VP (black) and PS-b-P4VP/$FeCl_3$ (red) films. The strong absorption peak of the pyridine ring at 1597 cm^{-1} is marked with a black dash line. Adapted with permission from Ref [219] Copyright (2022) American Chemical Society.*

With the SEM measurement, local structure information at the film surface can be resolved. However, the large-area homogeneity and the inner morphology of the thin

films are also of great importance in the real-world applications. [250] In the previous investigation, the homogeneity of the polymer colloids coating are quantified by the normalized average out-of-plane cuts. [258] Here, long-range GISAXS scans are performed over a span of 8 mm for checking the homogeneity of the printed thin films. The lateral scan is executed right after the in-situ experiments. Figure 8.17 shows the corresponding spatially resolved 2D color plot of the pure PS-b-P4VP thin film. Clearly visible intensity changes in the Bragg rod region, as indicated with the red boxes in Figure 8.17, are observed at all positions. This position dependence of the GISAXS signal is ascribed to the inhomogeneity of characteristic structures in the thin film. Figure 8.19 shows 2D GISAXS data equidistantly measured at different scan positions of the dry PS-b-P4VP film. The corresponding distance between two adjacent 2D GISAXS positions is 1 mm. Figure 8.18a shows the first 2D GISAXS data from Figure 8.19. The symmetrically distributed Bragg peaks in the low q_y range are marked with two orange arrows. The vertically aligned Bragg peaks are ascribed to the structure factor of the vertical cylindrical scattering objects in the thin film. [245, 259] According to the SEM images shown in Figure 8.12, these cylindrical scattering objects in the PS-b-P4VP and PS-b-P4VP/$FeCl_3$ thin films are supposed to consist of PS domains. The shape and location of the Bragg peaks in the 2D GISAXS data are related to the degree of order and the distance of the PS domains. A well-ordered nearest neighbor structure without any long-range order typically gives rise to two well-pronounced Bragg rods. [101] The well-distinguished Bragg peaks in Figure 8.19a-e, g, and h indicate the PS domains have a pronounced nearest-neighbor ordering. In contrast, the Bragg peaks in Figure 8.19f and i are significantly smeared and slightly shifted to the lower q_y range, which suggests a less defined order of the PS domains in the thin film. The elongation of the scattering spots in the q_z direction is caused by the film thickness, which limits the long-range order of the scattering objects in the perpendicular direction. [260]

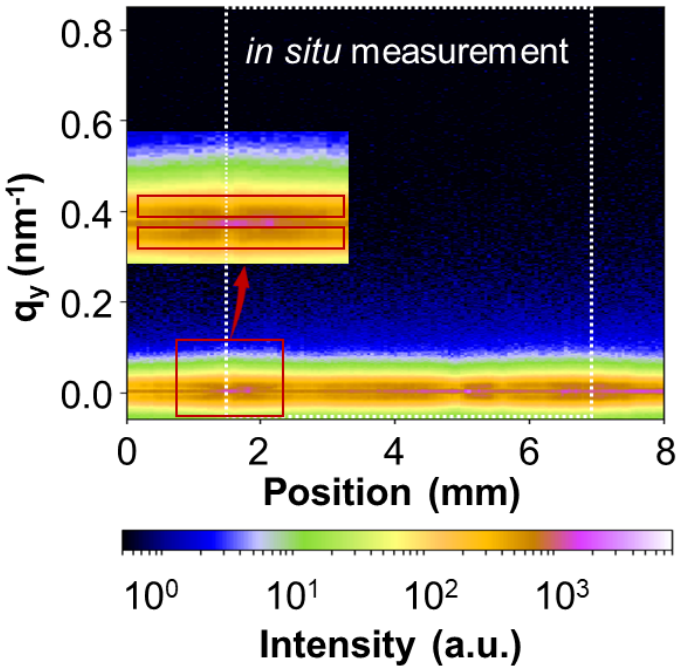

Figure 8.17: *Lateral GISAXS scan performed over a distance of 8 mm on the pure PS-b-P4VP thin film after the in situ measurement. The region of the in situ measurement is marked with a white rectangle. Adapted with permission from Ref [219] Copyright (2022) American Chemical Society.*

For further analysis, we performed horizontal line cuts at the critical angle of PS for all 2D GISAXS data. The horizontal line cut position is marked with a white arrow in Figure 8.18a. The line cuts acquired from Figure S10 a to S10 i are sequentially shown from bottom to top in Figure 8.18b. The difference in scattered intensity with respect to the first frame is shown in Figure 8.18c. [68] The line cuts in Figure 8.18b are fitted within the same model described before and the results are shown in Figure 8.18d and e. The extracted average values for the domain radius and distance are around 54 nm and 420 nm, respectively. We find that the domain radii change weakly within a range of 10 nm whereas the distances fluctuate largely within a range of 100 nm with respect to different positions. Thus, the inhomogeneity of pure PS-b-P4VP thin film is mainly attributed to the unevenly distributed PS domain distances, in agreement with the local SEM structure information (Figure 8.12a to c). Larger feature sizes up to micrometers seen in the SEM images are beyond the resolution limit of the GISAXS measurement.

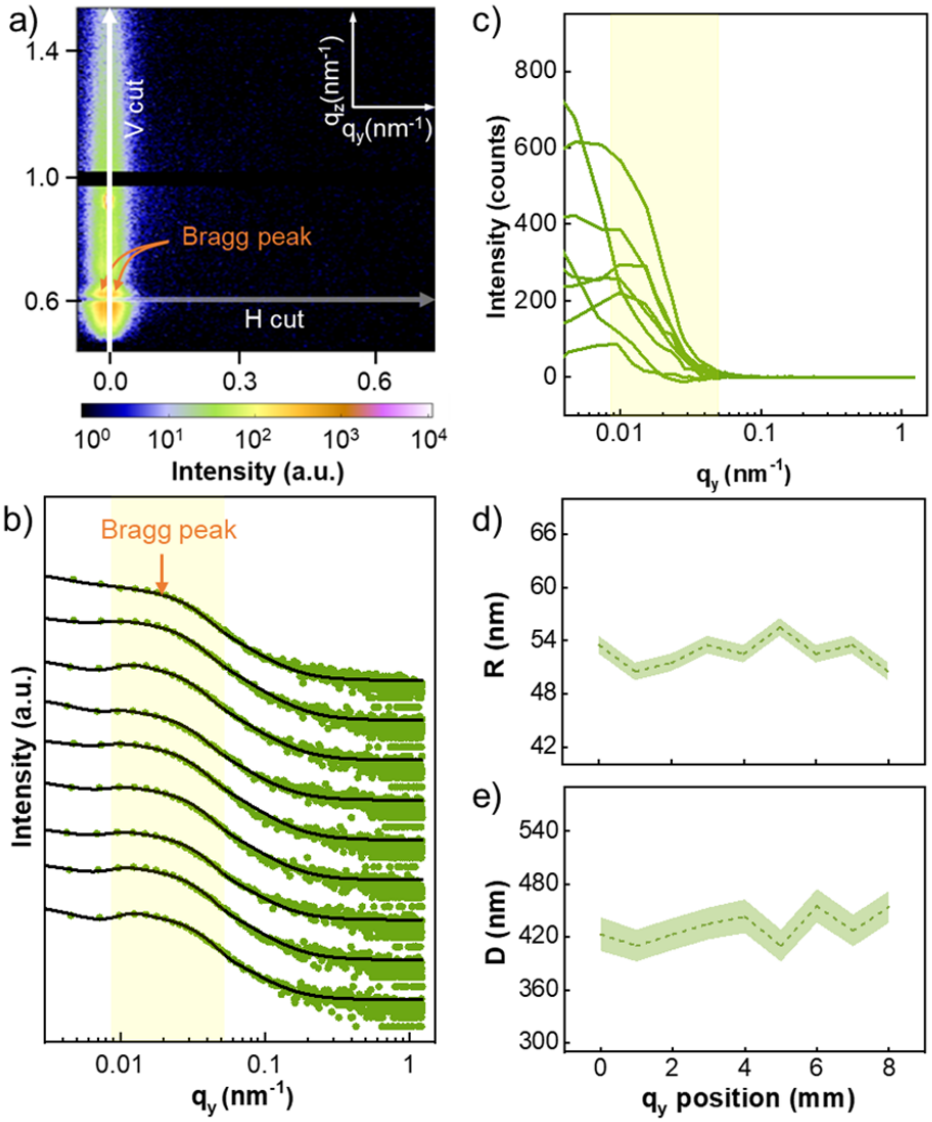

Figure 8.18: *a) Representative 2D GISAXS data of the printed PS-b-P4VP film. The Bragg rod position is marked with two orange arrows and the positions for performing the horizontal (H) and vertical (V) line cuts are denoted with white arrows. b) Selected horizontal line cuts (green circles) and corresponding fits (solid lines) of the 2D GISAXS data from a) to i) are sequentially shown from bottom to top, the Bragg peak position in the horizontal line cuts are marked with an orange arrow. c) The difference in scattered intensity with respect to the first frame. d) Characteristic radii R and e) distances D determined by modeling the horizontal line cuts. Adapted with permission from Ref [219] Copyright (2022) American Chemical Society.*

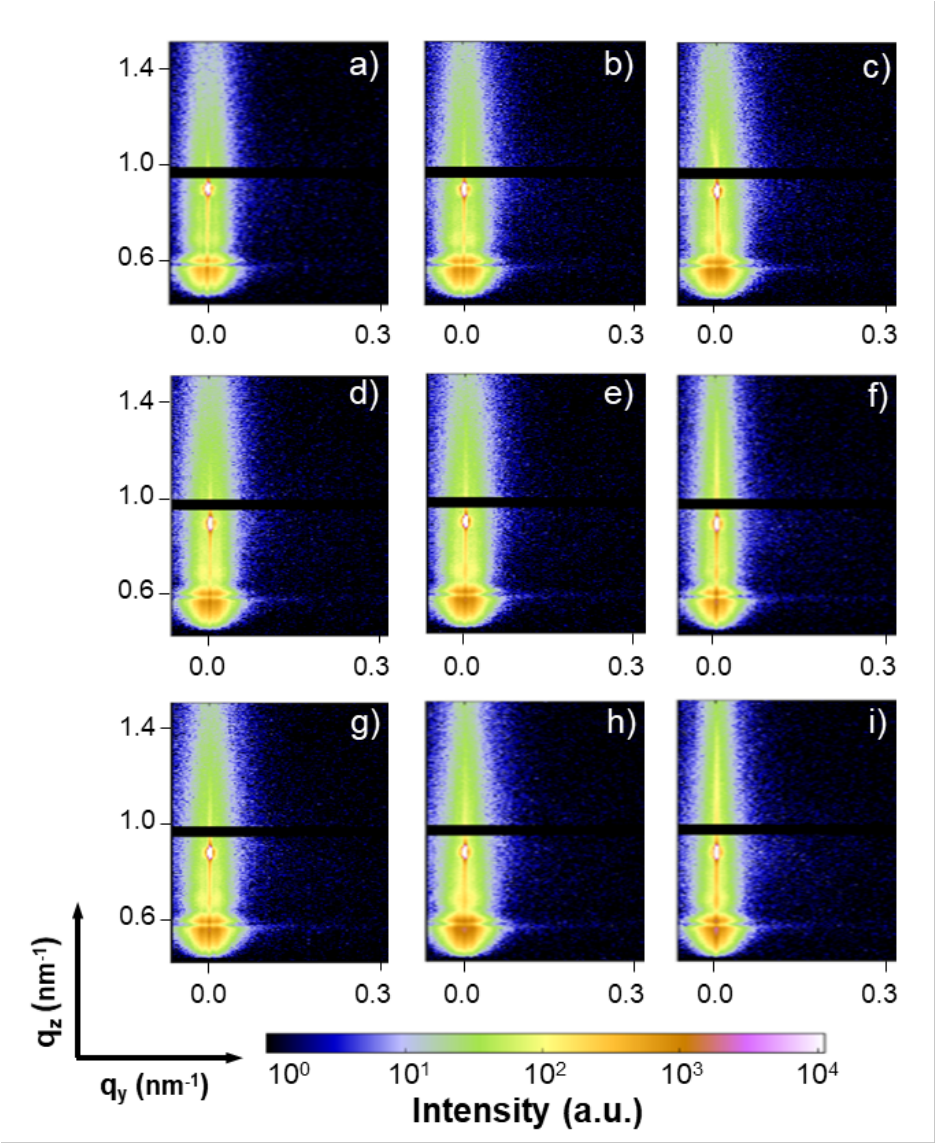

Figure 8.19: *2D GISAXS data equidistantly extracted at different measurement positions at the PS-b-P4VP film. The positions selected for extracting the 2D GISAXS data are in a distance of 1 mm to each other. Adapted with permission from Ref [219] Copyright (2022) American Chemical Society.*

8.7 Homogeneity of the PS-b-P4VP/$FeCl_3$ thin film

For comparison, a homogeneity study is also performed for the hybrid PS-b-P4VP/$FeCl_3$ thin film following the same measurement protocol. Figure 8.20 refers to the lateral GISAXS scan performed over a span of 8 mm on the hybrid PS-b-P4VP/$FeCl_3$ film after the in-situ GISAXS experiments. A high homogeneity of the hybrid film is seen. Com-

pared to the 2D color mapping of the pure PS-b-P4VP film, the hybrid PS-b-P4VP/$FeCl_3$ film shows significantly enhanced scattering at the higher q_y region, indicating the presence of smaller structures. The selected nine 2D GISAXS data from the GISAXS scans on the hybrid PS-b-P4VP/$FeCl_3$ film are shown in Figure 8.21. Without pronounced scattering changes in both horizontal and vertical directions, the 2D GISAXS data measured at different printing positions indicate that the obtained hybrid PS-b-P4VP/$FeCl_3$ film is homogeneous along the printing direction. In addition, we observe that the Bragg peaks appear only along the in-plane direction, and thus originate from the perpendicularly oriented cylinder structures in the thin film. Accordingly, the coordination effect between the Fe^{3+} and the P4VP chains restricts the orientation of the nanostructures significantly. Such a vertical alignment of cylindrical structures can be attributed to the perpendicular solvent concentration gradient established by solvent evaporation, which is also known as the solvent field and is beneficial for lateral ordering. [261] For quantitative analysis, horizontal line cuts along the critical angle of PS, as indicated with a white arrow in Figure 8.22a, are performed and shown in Figure 8.22b. All the horizontal line cuts show higher-order Bragg peaks. For a hexagonally packed cylinder array oriented normal to the substrate and truncated at the surface, scattering from specific lattice planes correspond to given peak position ratios in the lateral direction of the 2D GISAXS data. Specifically, scattering from the (h0) and (hk) planes, as denoted with I and II in Figure 8.22b, correspond to the 1:2:3 and 1:$\sqrt{3}$:$\sqrt{4}$:$\sqrt{7}$ lateral peak position ratios, respectively. [213] However, individual positions, which follow e.g. $\sqrt{3}q_y$, $2q_y$,$\sqrt{7}q_y$ and $3q_y$ relative to the first-order peak (marked with green arrows in Figure 8.22a and b) cannot be identified. The smearing of the Bragg peaks can be attributed to the misorientation of the hexagonal lattice over the large area probed by the X-ray beam. The misorientation of the hexagonal lattice can also be observed in the SEM images (Figure 8.12). To distinguish the scattering differences in the horizontal line cuts shown in Figure 8.22b, the first frame subtracted data are shown in Figure 8.22c within the same coordinate range as for the pure PS-b-P4VP (Figure 8.22c). Within the whole q_y range, only subtle scattering differences of the horizontal line cuts can be identified, confirming the large-area homogeneity of the printed PS-b-P4VP/$FeCl_3$ film. For the quantitative analysis, the corresponding horizontal line cuts are modeled with two sets of structure factors (distances) and form factors (radii). As shown in Figure 8.22d and e, the constant radii (R1 = 9.4 $\pm$ 0.3 nm, R2 = 15.9 $\pm$ 1 nm), and distances (D1 = 23 $\pm$ 0.5 nm, D2 = 28 $\pm$ 1 nm) for different measurement positions signify the good homogeneity of the hybrid film.

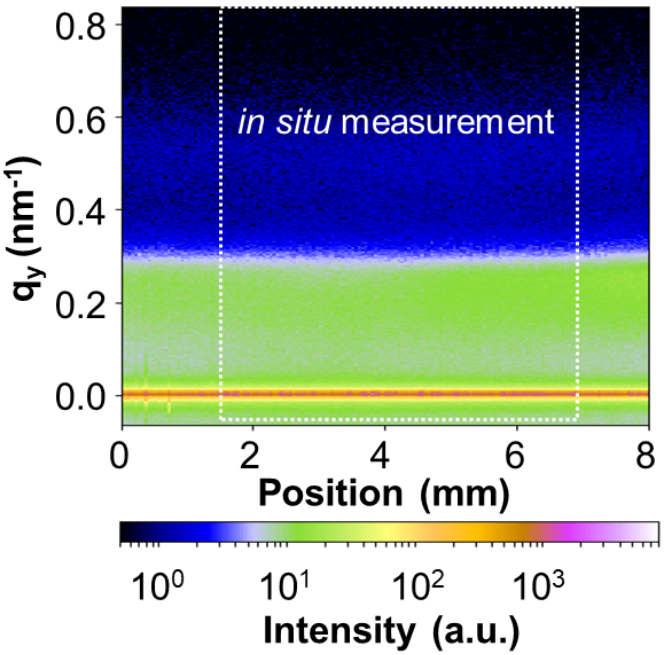

Figure 8.20: *Lateral GISAXS scan performed over a distance of 8 mm on the PS-b-P4VP/$FeCl_3$ thin film after the in situ measurement. The region of the in situ measurement is marked with a white rectangle. Adapted with permission from Ref [219] Copyright (2022) American Chemical Society.*

In addition to the large structures in the PS-b-P4VP thin film that are not resolvable via the GISAXS technique, the diameter values of the PS cores extracted from the SEM images of both PS-b-P4VP and PS-b-P4VP/$FeCl_3$ thin films (Figure 8.15) are fundamentally consistent with the GISAXS modeling result (Figure 8.18d and Figure 8.22d). The consistency between the binarization result of the SEM images and modeling result of the GISAXS data suggests the local structural information displayed in the SEM images is extended all over the thin film.

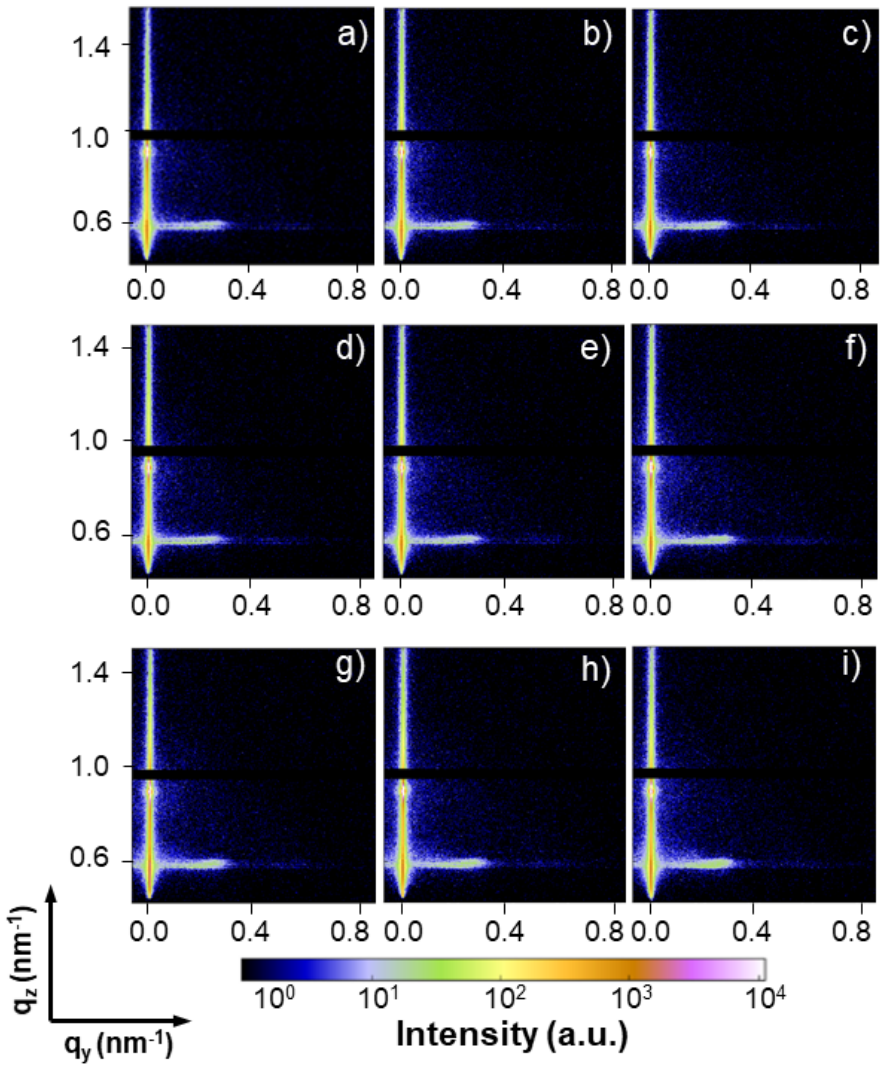

Figure 8.21: *2D GISAXS data equidistantly extracted at different measurement positions of the PS-b-P4VP/$FeCl_3$ film. The positions selected for extracting the 2D GISAXS data are located at a distance of 1 mm to each other. The positions for performing the horizontal (H) and vertical (V) line cuts are denoted with white arrows in a). Adapted with permission from Ref [219] Copyright (2022) American Chemical Society.*

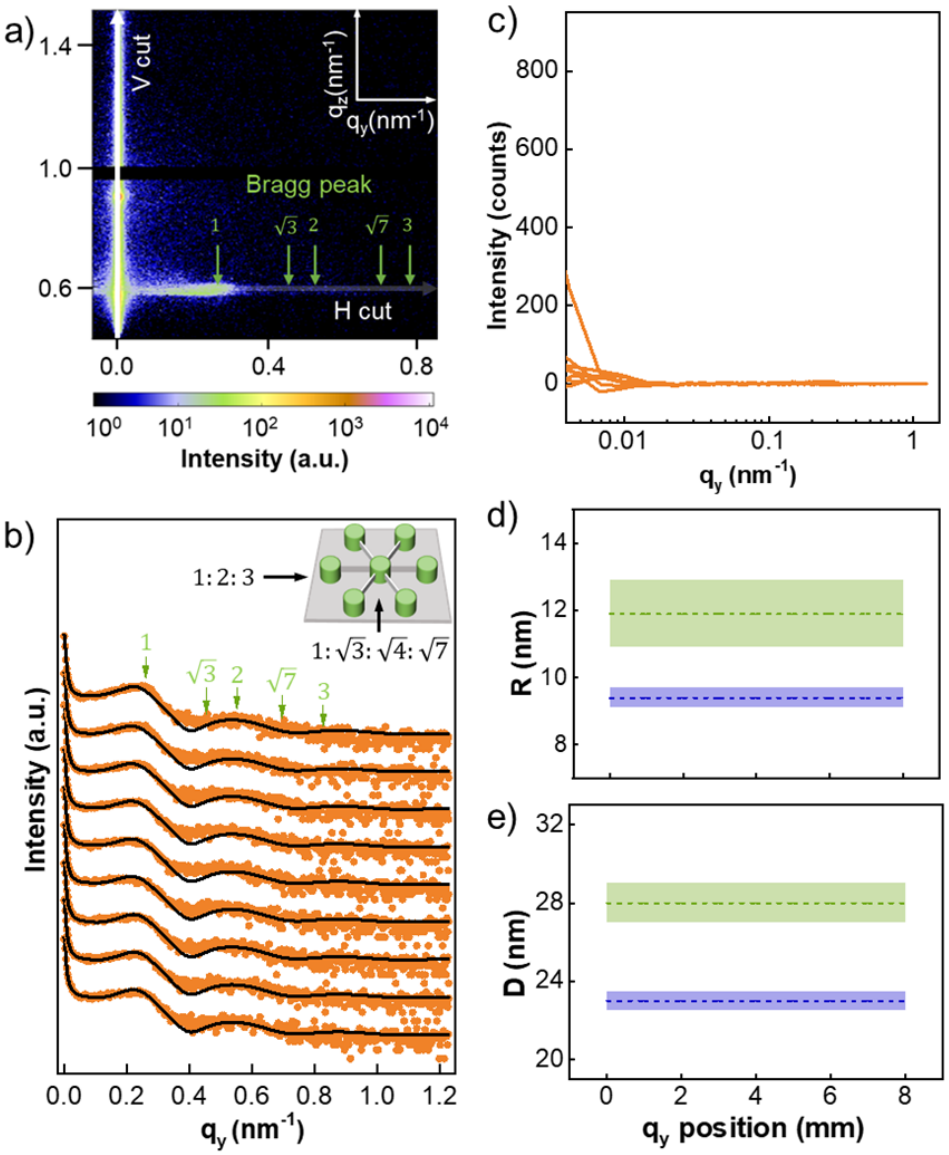

Figure 8.22: *a) Representative 2D GISAXS data of the printed hybrid PS-b-P4VP/$FeCl_3$ film. Positions for performing the horizontal (H) and vertical (V) line cuts are denoted with white arrows and the Bragg peak positions are denoted with green arrows. b) The horizontal line cuts (orange circles) and corresponding model fits (black lines) to fit the 2D GISAXS data from Figure 8.21a to i are sequentially shown from bottom to top. The inset is a schematic representation of different incident directions of the X-ray to the hexagonal lattice position. The (h0) and (hk) planes corresponding to a 1:2:3 and 1:$\sqrt{3}$:$\sqrt{3}$:$\sqrt{3}$ peak position ratios in the lateral direction and are denoted with black and red arrows, respectively. c) The difference in scattered intensity with respect to the first frame. d) Characteristic radii R and e) distances D extracted from modeling the horizontal cuts. Adapted with permission from Ref [219] Copyright (2022) American Chemical Society.*

8.8 Film thickness study

The average thickness of the final printed PS-b-P4VP and hybrid PS-b-P4VP/$FeCl_3$ films is determined to be 25.5 ± 1.6 nm and 90.3 ± 3.6 nm through profilometry measurement, respectively. Based on the thicknesses and the average feature sizes extracted from the SEM and GISAXS measurement, we plotted a scaled up schematic for the PS-b-P4VP and PS-b-P4VP/$FeCl_3$ thin films, the corresponding molecular chain arrangement in the cross-sectional direction of the cylindrical structures are shown on the right side of the schematic. (Figure 8.23a). It is observed that the change in the used ink during printing (addition of $FeCl_3$) causes a serious change in film thickness and film morphology. This difference in film morphology is also reflected in the vertical direction of the scattering data. Figure 8.23b and c show the vertical line cuts acquired from the 2D GISAXS data in Figure 8.19a-i and Figure 8.21a-i. The purple arrow marks oscillations in the line cuts originate from the dynamic effects in the diffuse scattering, reflection and refraction of the X-ray beams at the polymer/substrate and polymer/air interface. The relative positions of these oscillations is inversely proportional to the thickness and density of the polymer or hybrid layer. [262–264]Importantly, the position of the minima indicated by arrows in Figure 8.23b and c is independent of the scan positions, implying a well-preserved roughness, density and thickness for PS-b-P4VP and hybrid PS-b-P4VP/$FeCl_3$ films along the printing direction.

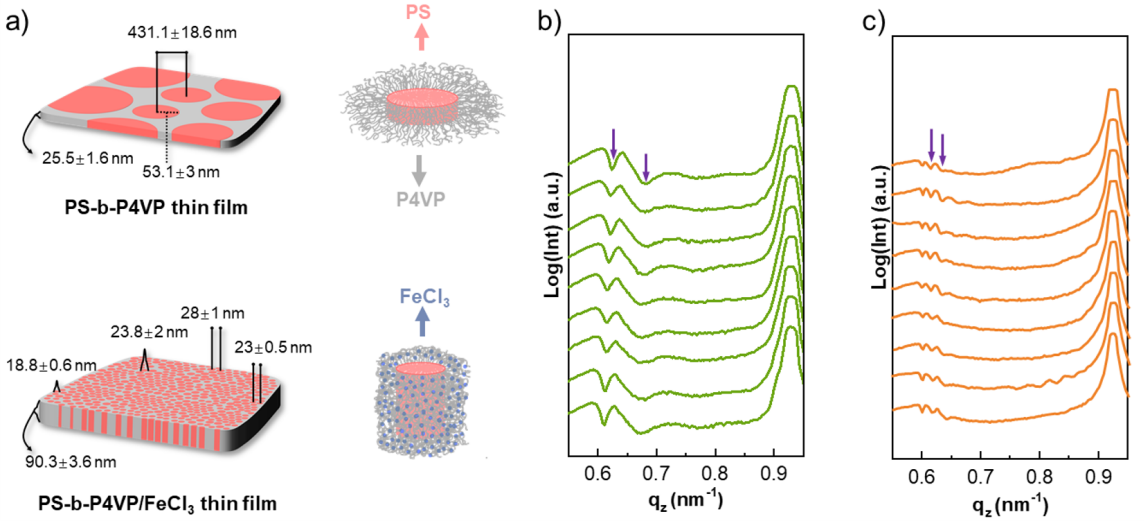

Figure 8.23: *a) Scaled up schematic and the corresponding molecular chain arrangement in the cross- sectional direction of the cylindrical structures in the PS-b-P4VP and PS-b-P4VP/FeCl3 thin films. Vertical line cuts are performed at qy = 0 nm-1 of the 2D GISAXS data of the printed b) pure PS-b-P4VP and c) hybrid PS-b-P4VP/FeCl$_3$ films. The line cuts shown from bottom to top in b) and c) are acquired from the 2D GISAXS data in Figure 8.19a-i and Figure 8.21a-i, respectively. The adjacent oscillation minima in the Yoneda peak region are marked with purple arrows. Adapted with permission from Ref [219] Copyright (2022) American Chemical Society.*

8.9 Morphology and composition of the calcined thin film

After the high-temperature calcination process, the polymer template is extracted and consequently the mesoporous Fe_2O_3 film is achieved. To obtain lateral and vertical structure information of the calcined thin film, surface and cross-section SEM measurements are performed. As shown in Figure 8.24a and b, the calcined thin film presents an ordered porous structure, which resembles the surface morphology of the as-deposited hybrid PS-b-P4VP/$FeCl_3$ film and has a thickness of around 10 nm. To analyze the large area homogeneity of the calcined Fe_2O_3 thin film, SEM characterization was performed at different length scales. As shown in Figure 8.25, neat porous structure is observed either in the local or the large area of the thin film, which is in line with the GISAXS characterization result of the uncalcined counterpart. The SEM images of the calcined thin-film suggest that the rearrangement of the cylinders within the lateral and vertical directions of the hybrid PS-b-P4VP/$FeCl_3$ thin film is negligible during the high-temperature calcination process. Figure 8.24c shows the 2D GISAXS data of the calcined thin film. The intensity streaks originate from the highly ordered, vertically oriented nanostructures within the

thin film. For further analysis, a horizontal line cut of the 2D GISAXS data is performed at the material-specific Yoneda peak position and shown in Figure 8.24d. The appearance of a third-order peak suggests the increased order of the nanostructure in the lateral direction. Agree with the horizontal line cut of the printed hybrid PS-b-P4VP/$FeCl_3$ film, the smearing of the Bragg peaks in the line cut is likely caused by the distortion of the lattice. Two bunches of hexagonal lattices with different orientations are marked with yellow hexagons in Figure 8.24a. However, in contrast to the hybrid PS-b-P4VP/$FeCl_3$ film, the narrowed Bragg peaks in mesoporous Fe_2O_3 film are indicative of improved structural order after calcination. To gain more insights into the size distribution of the scattering objects, the horizontal line cuts together with the modeled results are shown in Figure 8.24d. Three sets of structure factors and form factors are used for data modeling. The strong scattering signal located at higher q_y values is modeled with the first and second structures and the week scattering observed at smaller q_y values is modeled with the third structure. The modeled distances of the first, second, and third structures are (23.0 ± 1.6) nm, (23.0 ± 2.1) nm and (60.0 ± 2.1) nm. The corresponding radii are (3.2 ± 1.3) nm, (5.0 ± 1.2) nm and (15.0 ± 4.5) nm, respectively (Figure 8.24e). Based on equation 5.5, the pore size values calculated from the first, second, and third structures are (16.6 ± 4.2) nm, (13.0 ± 4.5) nm and (30.0 ± 19.0) nm. As marked out by the white circles, all structure sizes obtained by data modeling are also visible in the SEM image (Figure 8.24a), Therefore, the surface and inner morphologies are in good accordance, and the local structure shown in the SEM image is also representative for the large area of the thin film.

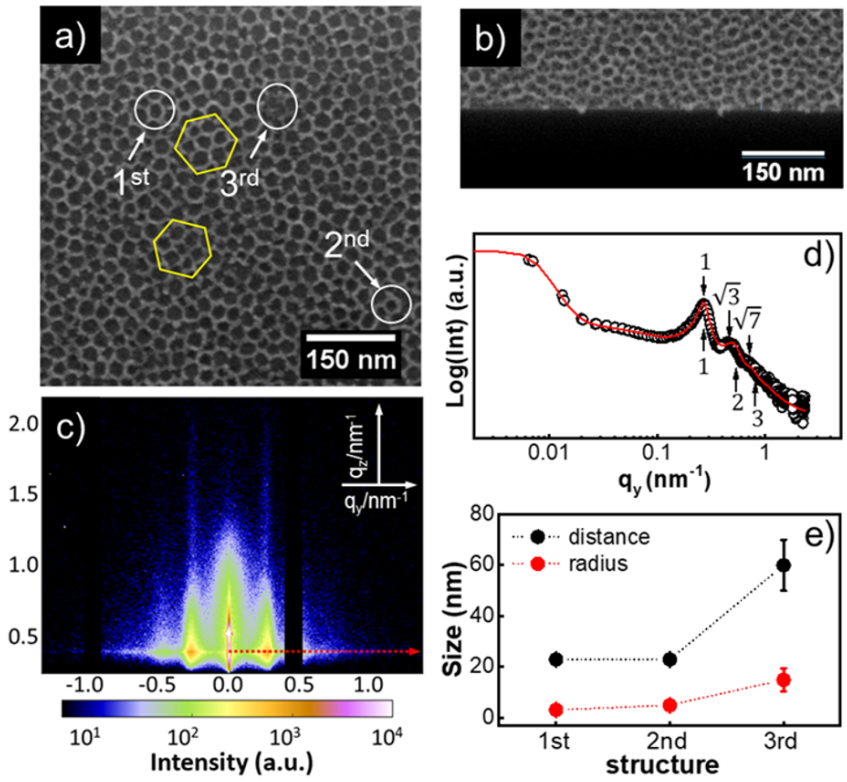

Figure 8.24: *a) Plan-view and b) cross-section SEM images of the mesoporous Fe_2O_3 thin film. c) Corresponding 2D GISAXS data and d) horizontal line cut. The Yoneda peak position for performing the horizontal line cut is denoted with a red arrow in c). The solid red line represents the fit to the data (hollow black symbols). e) Extracted characteristic structures are radii (red) and distances (black). Adapted with permission from Ref [219] Copyright (2022) American Chemical Society.*

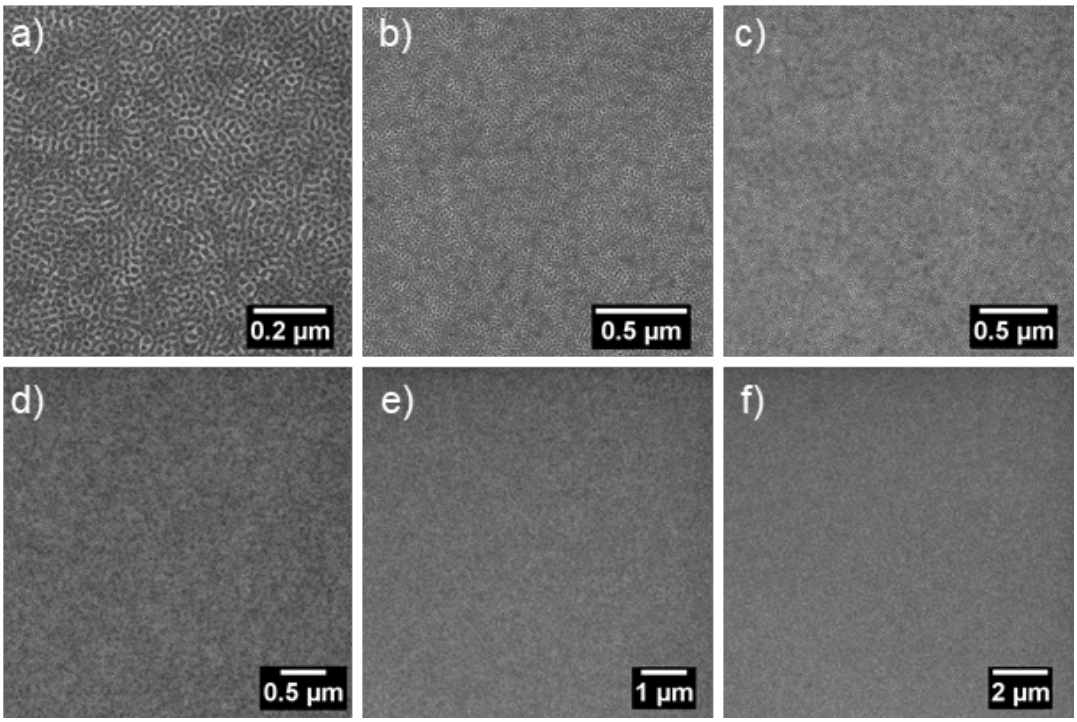

Figure 8.25: *SEM images taken at a magnification of (a) 80K, (b) 40K, (c) 30K, (d) 20K and (e) 10K of the calcined -Fe2O3 thin film. Adapted with permission from Ref [219] Copyright (2022) American Chemical Society.*

Important information about the surface electronic structure as well as the chemical element valence state is provided by the XPS measurement. Figure 8.26a shows the high-resolution Fe 2p spectrum of the calcined thin film. We can observe the distinct Fe(2p3/2) and Fe(2p1/2) peaks at 710.8 eV and 724.4 eV and two shake-up satellites at around 8 eV, which are higher than their corresponding main peaks. This observation is characteristic of Fe^{3+} in Fe_2O_3. [179] To gain further information on the crystallinity and phase of the calcined thin film, powder XRD measurement is performed. As shown in Figure 8.26b, all diffraction peaks are readily indexed to a pure rhombohedral phase of α-Fe_2O_3(JCPDS No. 890597). [265]

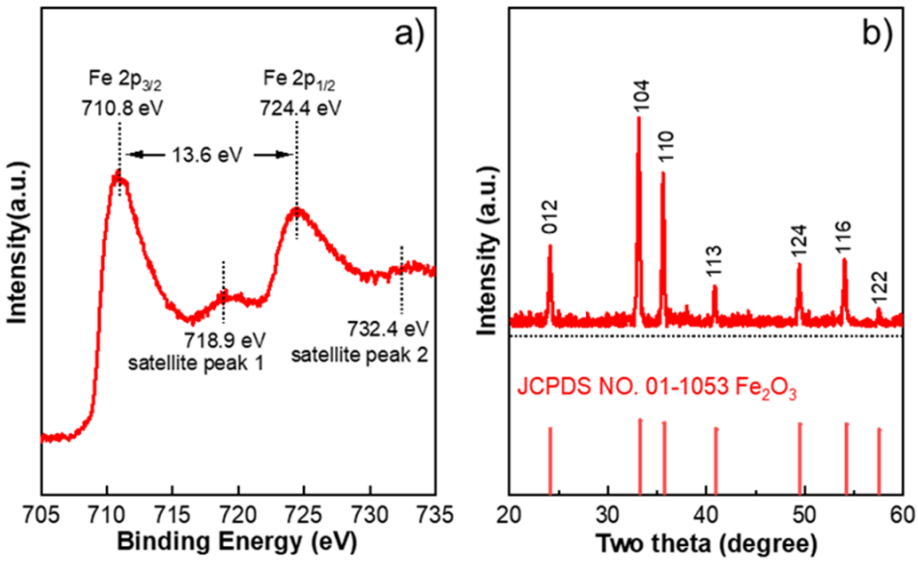

Figure 8.26: *Core-level Fe 2p XPS spectrum a) with marked characteristic peaks and powder XRD pattern b) of the calcined Fe_2O_3 thin film with standard JCPDS card (NO. 01-1053) of Fe_2O_3 as reference. Adapted with permission from Ref [219] Copyright (2022) American Chemical Society.*

8.10 Conclusions

In summary, we investigate the deposition process and large area homogeneity of printed pure PS-b-P4VP and hybrid PS-b-P4VP/$FeCl_3$ thin films with in-situ GISAXS. Multi-dimensional auxiliary characterizations, including DLS, SEM, FTIR, XPS, and XRD, are used for studing the aggregates in the sol-gel solution used for printing, the morphological, compositional, and crystalline information of the final printed and calcined thin films. Individually dissolved polymer chains with a size around 4 nm exist predominantly in both pure PS-b-P4VP and the PS-b-P4VP/$FeCl_3$ inks. Besides these individually dissolved polymer chains, micelle assemblies and aggregates are also detected. Compared to the pure PS-b-P4VP solution, decreased micelle assembly sizes and formation of aggregates are observed in the PS-b-P4VP/$FeCl_3$ counterpart due to the coordination effect between Fe^{3+} and the vinyl pyridine groups of the P4VP chains. Due to the attachment ability of the P4VP chains to the silicon substrate can be affected by the different micelle assemblys in the PS-b-P4VP and PS-b-P4VP/$FeCl_3$ solutions during the printing process, the film formation kinetics of the as-deposited thin films and corresponding morphologies in both lateral and vertical directions of the printed films differ pronouncedly. Compared to the pure PS-b-P4VP counterpart, an overall slower film formation process, decreased domain

sizes, and enhanced homogeneity in the lateral direction, and an increased thickness of the printed film is observed for hybrid PS-b-P4VP/$FeCl_3$. However, both printed films evidence an identical geometry with vertically oriented cylinders, which is likely induced by the perpendicular solvent convection during the rapid solvent evaporation process. After removing the polymeric template from the hybrid PS-b-P4VP/$FeCl_3$ thin film by calcination, a α-Fe_2O_3 layer with high degree of order is achieved, which holds considerable prospects in multiple fields such as energy conversion devices, sensors, or photocatalysis.

9 Hierarchical α-Fe_2O_3 thin films and their application in photovoltaic devices

Parts of this chapter have been composed in the article: Tailored Fabrication of Quasi-Isoporous and Double Layered α-Fe_2O_3 Thin Films and Their Application in Photovoltaic Devices, which is submitted to the journal:chemical engineering journal

9.1 Preface

Iron (III) oxide, α-Fe_2O_3, as the most thermodynamically stable polymorph, has attracted a great due of attention in the photovoltaic devices, [54, 184] lithium-ion batteries, [177] photoelectrochemical conversion, [182] gas sensors, [179] and high-density nanoelectronic technology applications, [193] during the past several decades. Especially when served as the electron transport layer in the perovskite solar cells, it is favorable for enhancing the UV stability as its low photocatalytic activity and diffusion lengths of hole. Literature reported preparation methods for the nanostructured α-Fe_2O_3 thin films involve thermal evaporation, [231] spray pyrolysis, [266–269] electron beam deposition, [270,271] chemical vapor deposition, [272,273] pulsed laser deposition, [274,275,275] sol-gel method, [276–278] liquid phase deposition, [279, 280] electrodeposition, [281, 282] sputtering. [283–285] Among the various preparation methods, solution processable sol-gel method features low cost and good compatibility with the large scale spray coating and printing techniques. Furthermore, with the assistance of templating effect of the diblock copolymers, diverse periodic metal oxide nanostructures can be achieved. [18, 19, 55, 246] The phase separation behavior of the diblock copolymer in the solvent or cosolvent is easily affected by the stretching degree of the core-forming polymer chains and the repulsive interactions among corona-forming chains. [97] Therefore, poor solvent, acid, base, or salt

addition are commonly adopted strategies for tuning the phase separated structures of the diblock copolymer thin films. Distinguished from the phase separation behavior of the pure block copolymer, the introduce of the metal oxide precursors in to the sol-gel solution make the phase separation process of the block copolymer more sophisticated. Cheng et al. have made a series of work for tuning the morphology of PS-b-PEO templated TiO_2 thin films by controlling the proportion of each component in the sol-gel solution and the formation mechanism of the morphologies are addressed. They demonstrated that the phase separation behavior of the TiO_2 thin film can not only be affected by the component ratio in the solution but also the aging time of the sol-gel solution and the calcination temperature for removing the polymeric template. [17, 18] Yin et al. have made a series of work for demonstrating the solvent effect in the diblock copolymer templated TiO_2, SnO_2 and α-Fe_2O_3 thin film synthesis process. [55, 173, 246] Saka et al. investigated the effect of the weight fractions of the solvents and ZAD on the PS-b-PEO templated ZnO nanostructures and constructed a ternary phase diagram for showing the compositional boundaries of the investigated morphologies. [286] Moreover, thermal annealing is testified to be an efficient channel for reconstructuring the morphology of the block copolymer thin film by affecting the interfacial interactions between the copolymers and substrate and the complex coupling and competition between dewetting and microphase separation. [287, 288] Park et al. fabricated a waferlevel antireflective nanostructure array via the combined action of dewetting and Oswald ripening of the spin-coated multilayer of nanosilver colloids. [289]

In the present section, the morphology control of the PS-b-PEO templated α-Fe_2O_3 thin films is realized from multi-dimensional approaches. H_2O, as a poor solvent, is added in to the sol-gel solution for tuning the stretching degree of the core and corona forming polymer segment. Different $FeCl_3$-to-PS-b-PEO ratios are designed for checking the templating effect of the PS-b-PEO block co-polymer to the α-Fe_2O_3 nanostructures. Thermal annealing post treatment is performed for reconstructuring the nanostructures of the α-Fe_2O_3. The structural information of the as deposited and calcined thin films is characterized by SEM and GISAXS measurements. The crystallinity, crystal orientation, and composition of the calcined α-Fe_2O_3 thin films are detected by XRD, GIWAXS and XPS measurements. In order to capitalize the unique properties of the distinct α-Fe_2O_3 nanostructures acquired in the present work, two representative α-Fe_2O_3 thin films prepared with medium $FeCl_3$ concentration, 0 μL H_2O addition and annealing/no annealing post treatment are employed as the electron transfer modification layer for investigating their morphological effect on the photovoltaic properties of the perovskite solar cells. Photovoltaic performance test result indicates that the V_{OC}, as well as the PCE values of the devices are significantly improved by capitalizing the unique hierarchical α-Fe_2O_3 nanos-

tructures as the electron transport modification layer of the PSCs. This improvement is supposed to be induced by the enhanced light transmittance and electron extraction ability of the electron transport layer. Moreover, the suppressed carrier recombination at the interfaces could also be the reason for the increased V_{OC} values.

9.2 Experimental section

Polystyrene-block-polyethylene oxide (PS_{20500}-b-PEO_{8000}) was purchased from Polymer Source Inc with a degree of polymerization of N_{PS}=20500 and N_{PEO}=8000. Iron(III) chloride ($FeCl_3$, 97%), Iron (III) nitrate nonahydrate ($Fe(NO_3)_3 \cdot 9H_2O$, 99.95%) and N, N-dimethylformamide (DMF, anhydrous, 99.8%) were purchased from Sigma-Aldrich. 2,2,7,7- tetrakis-(N,N-di-4-methoxyphenylamine)-9,9-spirobifluorene (Spiro-OMeTAD) were purchased from Sigma-Aldrich, Germany. All the chemicals are used as received without further treatment. Silicon substrates (Si 100, p-type) were purchased from Silchem (Freiburg, Germany). FTO substrates were purchased from Youxuan (Liaoning, China). The detailed cleaning procedure for the silicon and FTO substrates can be found in the Supporting information.

Figure 9.1 schematically shows the thin film preparation process in the present work. To prevent moisture-induced deliquesce, the $FeCl_3$ powder used for the stock solution preparation is weighted in an N_2 glove box. Specifically, 21.3 mg, 42.7 mg, and 85.3 mg $FeCl_3$ are weighed for preparing the stock solution with low, medium, and high $FeCl_3$ concentrations. After taking out from the glovebox, the $FeCl_3$ powder is dissolved into 700 μL DMF solvent with continuous stirring for 30 mins. Afterward, the $FeCl_3$ solution is added into the pre-weighed 21 mg PS-b-PEO powder with further stirring for 10 mins. Concerning the proper homogeneity and coverage of the thin films prepared with medium $FeCl_3$ concentration, different amount of H_2O is added into the solution to further investigate the poor solvent-induced phase separation behavior. Specifically, a set of H_2O/DMF mixtures are prepared by adding different amounts of H_2O (0 μL, 5 μL, 10 μL, 20 μL, 40 μL, 80 μL) into 300 μL DMF solvent. Then, the DMF/H_2O mixture is added into the $FeCl_3$/PS-b-PEO solution with further stirring for 30 mins to acquire the stock solution. The component phase diagram of the stock solution prepared with low, medium and high $FeCl_3$ concentration is shown in Figure 9.2. The $FeCl_3$/PS-b-PEO composite thin films are deposited with a Delta 6 RC TT spin coater (SÜSS Micro-Tec Lithography GmbH) at 2000 rpm for 60 s. To investigate the thermal induced restructuring effect of the deposited thin films, a post treatment process is performed at 200 °C for 5 mins in the air condition. For distinction, the α-Fe_2O_3 thin films prepared in the present work are denoted in the format of annealing/no annealing-low/medium/high $FeCl_3$ concentration.

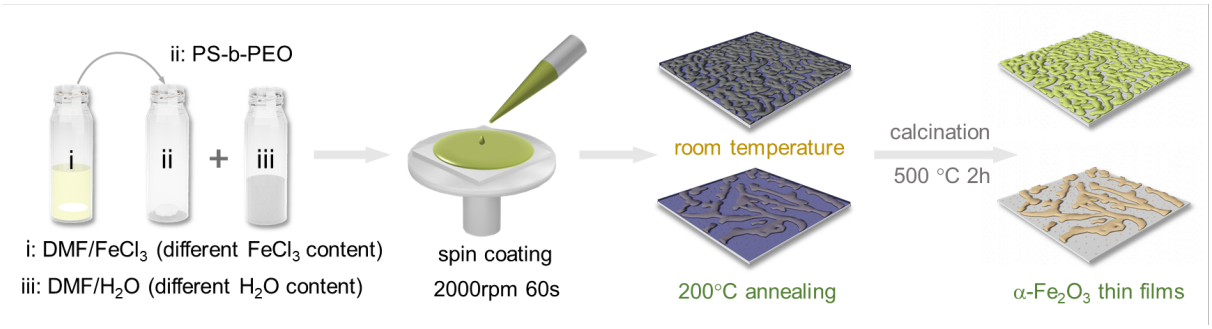

Figure 9.1: *Flow chart of patterned α-Fe_2O_3 thin film preparation in the present work.*

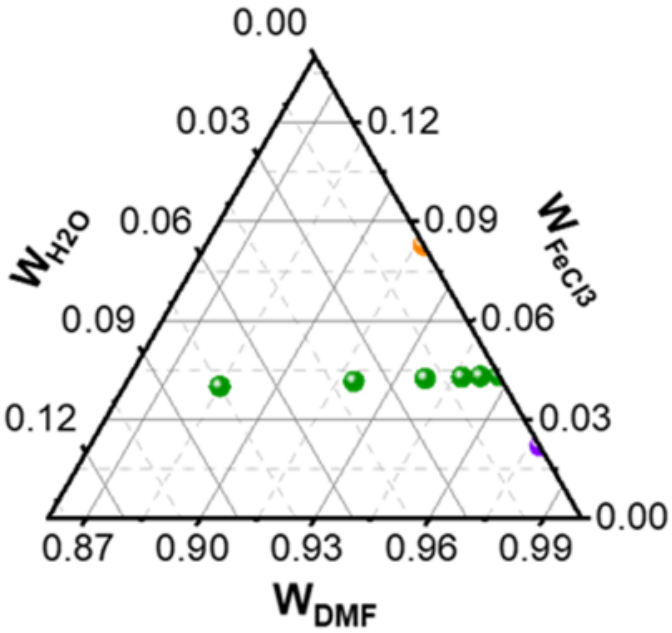

Figure 9.2: *Phase diagram of the α-Fe_2O_3 thin films prepared with different component ratios in the present work. The stock solution prepared with low, medium and high $FeCl_3$ concentration are denoted with purple, green and orange colors, respectively.*

The surface and cross-sectional morphology of the α-Fe_2O_3 thin films was probed with a high-resolution field emission scanning electron microscope (SEM, Zeiss Gemini NVision 40) at a working distance of 3.5 mm and an acceleration voltage of 5 kV. The Grazing-incidence small-angle X-ray scattering (GISAXS) measurements of the thin films prepared with medium $FeCl_3$ concentration Grazing-incidence small-angle X-ray scattering (GISAXS) measurements for all thin films were performed at the P03 beamline of PETRA

III storage ring. [162] The wavelength and incidence angle was 0.99 $\AA$ and 0.35°, respectively. The sample to detector distance was 4077 mm and a lambda 750k (X-Spectrum GmbH) detector with a pixel size of 55 μm was used for recording the scattering signal. 10 times single shots with an exposure time of 0.1 s are performed for doing the GISAXS measurements to avoid the X-ray induced beam damage on the thin films. For increasing the scattering intensity, the as obtained 10 2D GISAXS images are superimposed into one image. For the GISAXS measurement of the thin films prepared with low and high $FeCl_3$ concentration, the wavelength and incidence angle were 1.048 $\AA$ and 0.4°, respectively. The sample to detector distance was 4066 mm and a Pilatus detector with a pixel size of 172 μm was used for recording the scattering signal. A python program called Directly Programmable Data Analysis Kit (DPDAK) was used for calibration and data analysis. [163] Grazing-incidence wide-angle X-ray scattering (GIWAXS) measurements of the α-Fe_2O_3 thin films prepared with midium $FeCl_3$ concentration and 0 μl H_2O addition is performed at the same beamline with their corresponding GISAXS measurment. The sample to detector distance (SDD) was 180 mm and incident angle is 0.4°. The GIWAXS data were analyzed with a Matlab and GIXSGUI software. As a supplementary measurement, the calcined thin film was also analyzed with a D8 ADVANCE X-ray diffractometer using an X-ray wavelength of 1.54 $\AA$. To increase the test signal of XRD measurement, drop-casting was used for the thin film deposition. XPS measurement was performed with a SUPRA(XPS2) X-ray photoelectron spectrometer (Kratos, England) and UPS was performed with an Axis Ultra DLD X-ray photoelectron spectrometer (Kratos, England). The J-V curves of the exemplary perovskite solar cells were obtained with a Keithley 2450 SourceMeter. A scan rate of 10 mV/s is used under simulated AM 1.5 sunlight at 100 mW/cm^2. The light intensity was calibrated with a reference silicon solar cell. During the measurement, a metal aperture mask was used to define the active area of the solar cells (0.1 cm^2).

9.2.1 Films prepared with medium $FeCl_3$ concentration

Figure 9.3a show the SEM images of the α-Fe_2O_3 thin films prepared with no annealing-medium $FeCl_3$ concentration. The corresponding H_2O content added into the stock solution is marked on the top right corner of the images. Different substructures include spheres, cylinders and vesicles are detected in the calcined α-Fe_2O_3 thin films. The corresponding micellar structures for forming these porous nanostructures is schematically shown in Figure 9.3b.

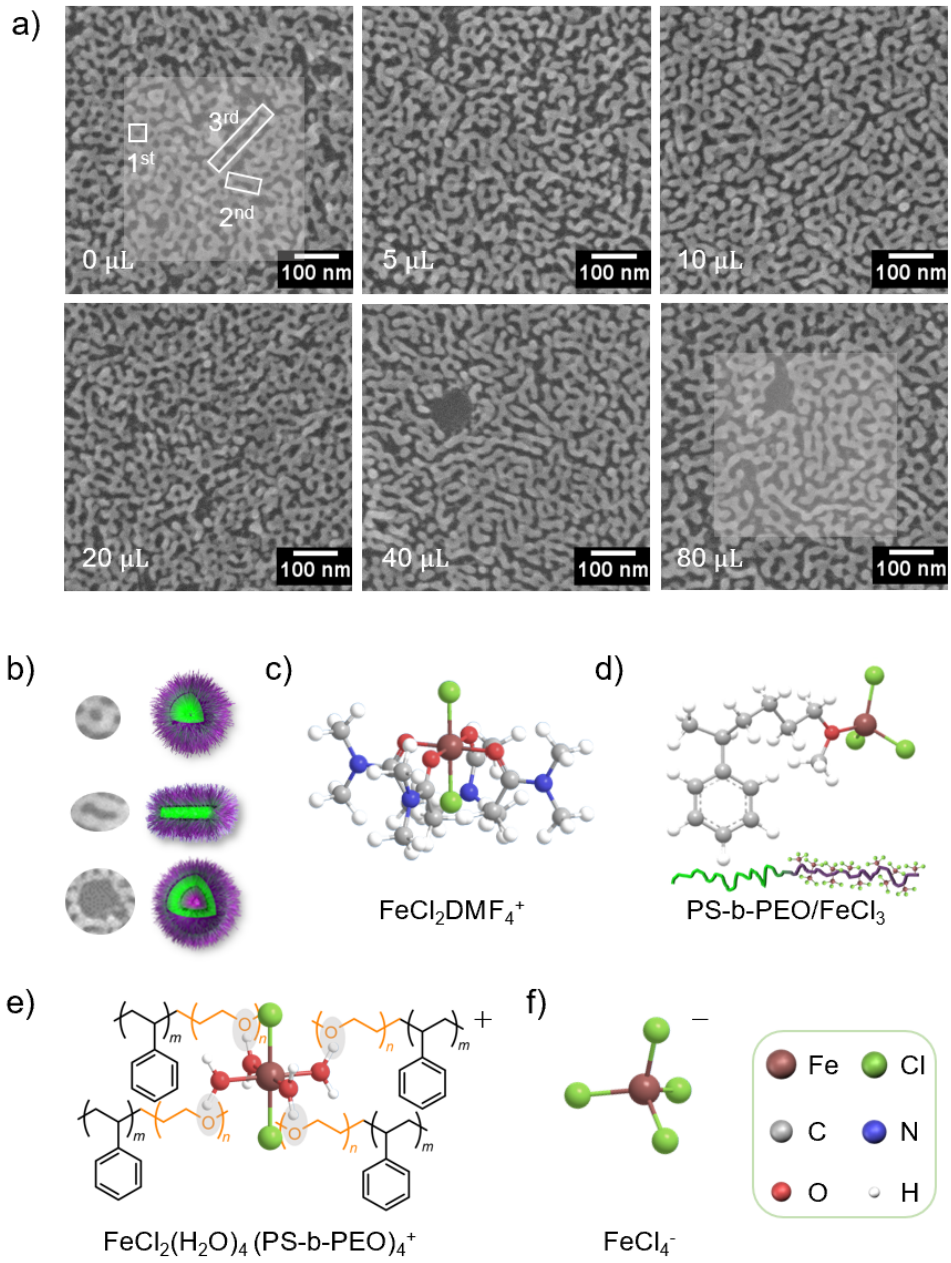

Figure 9.3: *a) SEM images of the α-Fe_2O_3 thin films prepared with no annealing-medium $FeCl_3$ concentration. The H_2O content added into the stock solutions is marked on the top right corner of the images. The 1^{st}, 2^{nd}, and 3^{rd} features sizes marked in a) are in good accordance with the structure factors and form factors extracted from the modeling result of the GISAXS data.The corresponding cross sectional and low magnification SEM images are shown in figure 9.4. b) The different nanostructures detected in the calcined α-Fe_2O_3 thin films and the corresponding micellar structures formed by the block copolymers. c) Molecular structure of the $FeCl_2DMF^{4+}$, d) PS-b-PEO/$FeCl_3$, e) $FeCl_2(H_2O)_4$ (PS-b-PEO)$^{4+}$ and f) $FeCl^{4-}$ complexes.*

Due to the presence of DMF and water molecules in the solvent, the main form of the Fe associated species are supposed to be $FeCl_2DMF^{4+}$, PS-b-PEO/$FeCl_3$, $FeCl_2(H_2O)_4$(PS-b-PEO)$^{4+}$ and tetrahedral $[FeCl_4]^-$ in the sol-gel solution. Figure 9.3b-e. [290, 291] With the proceed of spin coating, most of the solvent molecules are evaporated. The main complexes in the vitrified thin films become PS-b-PEO/$FeCl_3$, which will be in situ converted into α-Fe_2O_3 during the subsequent calcination process. It is observed that the thin films prepared with 0-20 μL H_2O addition are mainly composed of spherical and cylindrical structures and additional large vesicles with the size around 100 nm are detected by increasing the H_2O amount to 40 μL and 80 μL (Figure 9.3e and f). The pore structure evolution from spheres to vesicles can be ascribed to the increased surface energy between the PS blocks and the surrounding solvent, which resembles our previous investigations on the block copolymer templated TiO_2 and SnO_2 thin film synthesis. [55, 246] The coexistence of the spherical, cylindrical and vesicular structures within the thin film can be ascribed to the polydispersity of the block copolymer or the free energy difference within the sol-gel solution system. [104, 105] In spite of the high dielectric constant of DMF (36.7) and H_2O (80.1), the repulsion force among the polymer chains provoked by ionization can be negligible as the nonionizing properties of the PS and PEO blocks. [97] Therefore, the morphology variation of the α-Fe_2O_3 thin films induced by the H_2O addition can be analyzed from the perspective of the polymer-solvent interaction parameter (χ) (equation 5.6)

The characteristics of the different solvents and polymers can be taken from the literature, which are detailed in (table 9.1) [292, 293] The solubility parameter and molar volume of the DMF/H_2O solvent are calculated by the sum of the products of the component values with their volume fractions. As a poor solvent, the H_2O content in the sol-gel solvent can significantly affects the micellar structures. Concerning 18.9 μL H_2O will be consumed to completely convert 42.7 mg $FeCl_3$ into $FeCl_2(H_2O)^{4+}$ complexes, the actual H_2O content serves as solvent in the sol-gel solution is calculated by subtracting the portion consumed by forming $FeCl_2(H_2O)^{4+}$ complexes from the total H_2O addition amount. Based on the polymer-solvent interaction parameters χ, the selectivity of the cosolvent to the different blocks of the copolymer can be measured via the equation:(equation 6.7)

	$\delta(\mathrm{MPa}^{1/2})$				$V_S(\mathrm{cm}^2/\mathrm{mol})$
	δ_H	δ_d	δ_p	δ_h	
DMF	24.8	17.4	13.7	11.3	77.0
H_2O	47.8	15.6	16.0	42.3	18.06
PS	18.6	18.6	0.2	0.0	
PEO	19.9	17.3	3.0	9.4	

Table 9.1: *Characteristics of the different solvent and polymer.*

Table 9.2 shows the calculated polymer-solvent interaction parameters (χ_{P-S}) and the corresponding $\Delta\chi$ values of the different polymer-solvent pairs. The smallerχ value reflects the better solubility of the polymer chains in the solvent. It is observed that all the solvent mixtures show distinct preferential affinity to the PEO chains, which favors the formation of the micelles with PS cores and PEO coronas in the solution. [292] During the solvent evaporation induced self-assembly process, the Fe species integrated PEO blocks are inclined to fusion each other and a continuous α-Fe_2O_3 network can be obtained by removing the polymeric template. Moreover, the $\Delta\chi$ values of the polymer-solvent pairs are determined to be the same at 0.45 when the water content added in to the solution is increased from 0 μL to 20 μL, which signifies the comparable selectivity of the solvent to the different polymer blocks and explains the formation of the quite similar nanostructures from Figure 9.3a to d. Nevertheless, a prominent increase of the $\Delta\chi$ value is observed when the water content added in the solution is increased to 40 μL and 80 μL, which demonstrates the increased selectivity of the solvent and explains for the formation of the large vesicles in Figure 9.3e and f. The cross-sectional images shown in Figure 9.4 demonstrate that all the porous α-Fe_2O_3 thin films mentioned above are nearly unilaminar and bear a thickness of around 20 nm.

	DMF					
water content(μL)	0	5	10	20	40	80
χ_{PS-S}	1.53	1.53	1.53	1.53	1.71	2.01
χ_{PEO-S}	1.09	1.09	1.09	1.09	1.23	1.48
$\Delta\chi$	0.45	0.45	0.45	0.45	0.48	0.53

Table 9.2: *Polymer-solvent interaction parameters (χ_{P-S}) and the corresponding $\Delta\chi$ values of the different polymer-solvent pairs.*

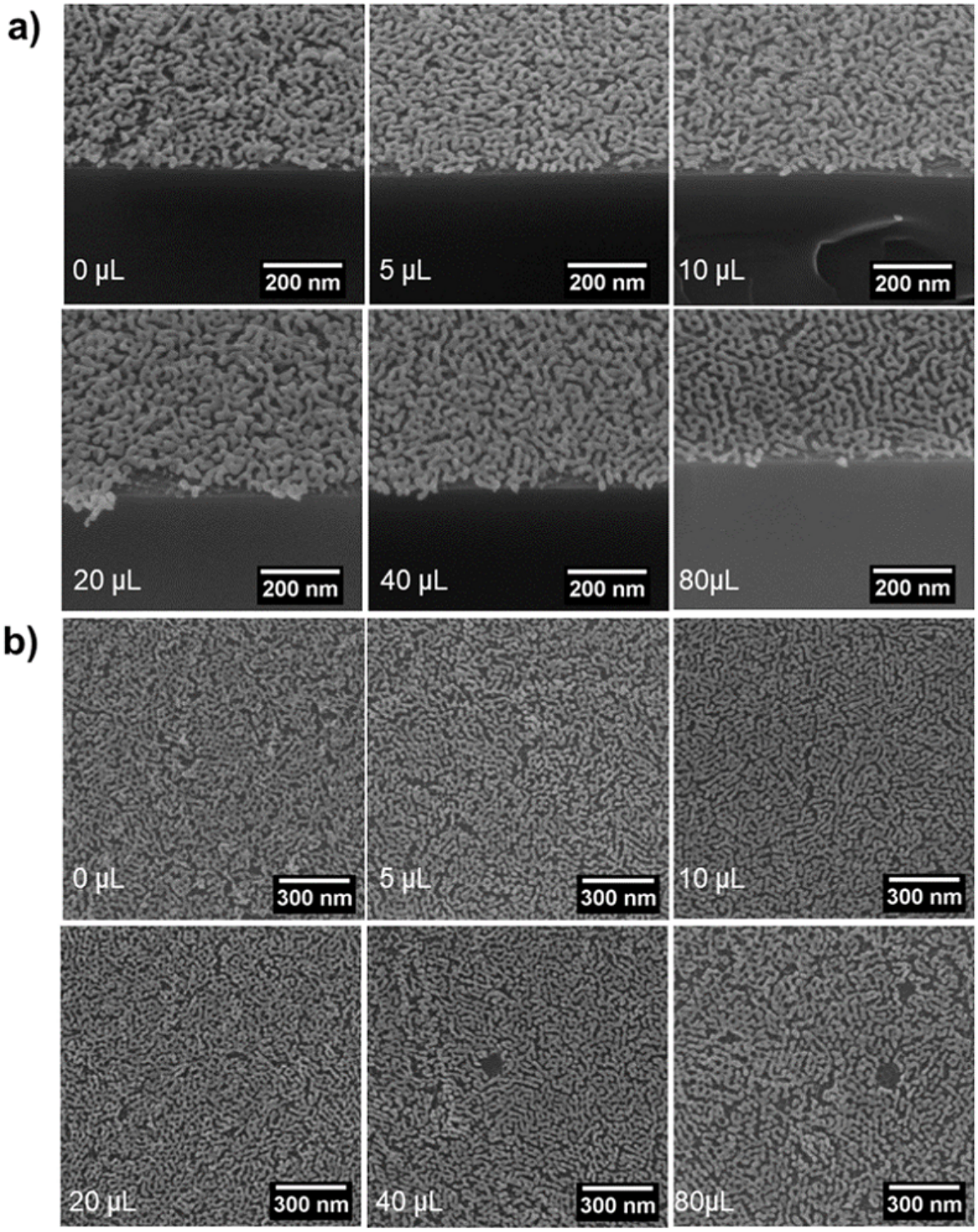

Figure 9.4: *Cross sectional a) and low magnification b) SEM images of the α-Fe_2O_3 thin films prepared with medium $FeCl_3$ concentration and without annealing post treatment. The H_2O content added in the stock solution are noted on the lower left corner of each image.*

Figure 9.4 refer to the SEM images of the α-Fe_2O_3 thin films prepared with annealing-medium $FeCl_3$ concentration. All the thin films demonstrate double layered structure with an interconnected cylindrical structure as the top layer and a finer nanocluster structure as the bottom layer. Compared to the thin films prepared without annealing, no significant structural difference is detected within the local area of the annealed thin films. However, the average distance between the cylinders is significantly decreased with the addition of H_2O. More detailed structural information along the surface normal of the double layered thin films is displayed in the cross-sectional SEM images. (Figure 9.6). The formation of the double layered structure during the annealing process is most likely thermodynamically driven by the combined effect of dewetting and Ostwald ripening. The formation of the finer and nearly compact bottom layer can be ascribed to the formation of a thin Fe species incorporated PEO layer induced by the strong preferential affinity of the PEO segments to the silicon substrate. [294] The selective interaction between PEO segments and Si substrate leads to the entropy difference between the chain conformations of the adsorbed and free molecules. [295, 296] Consequently, the excess destabilized di-block copolymer melts dewet the interlamellar layer adjacent to the Si substrate to form droplet, which is the so called autophobic behavior of PS-b-PEO copolymers during annealing. Figure 9.5 schematically shows a PS-b-PEO/$FeCl_3$ monolayer formed at the silicon substrate interface. Due to the high volatile property and low surface energy of the polar DMF and H_2O solvent used in the present work, the Ostwald ripening process of the droplets is significantly hindered. Consequently, interconnected cylinder structures rather than individual nanoislands are formed in the top dewetting layer of all thin films. [289] The narrowed distances between the neighboring cylinders induced by the H_2O addition can be ascribed to the higher polarity of H_2O than that of DMF, which accelerates the evaporation of the solvent and therefore hindered the further coalescence of the polymer chains and Ostwald ripening of the microdomains within the thin film during the annealing process.

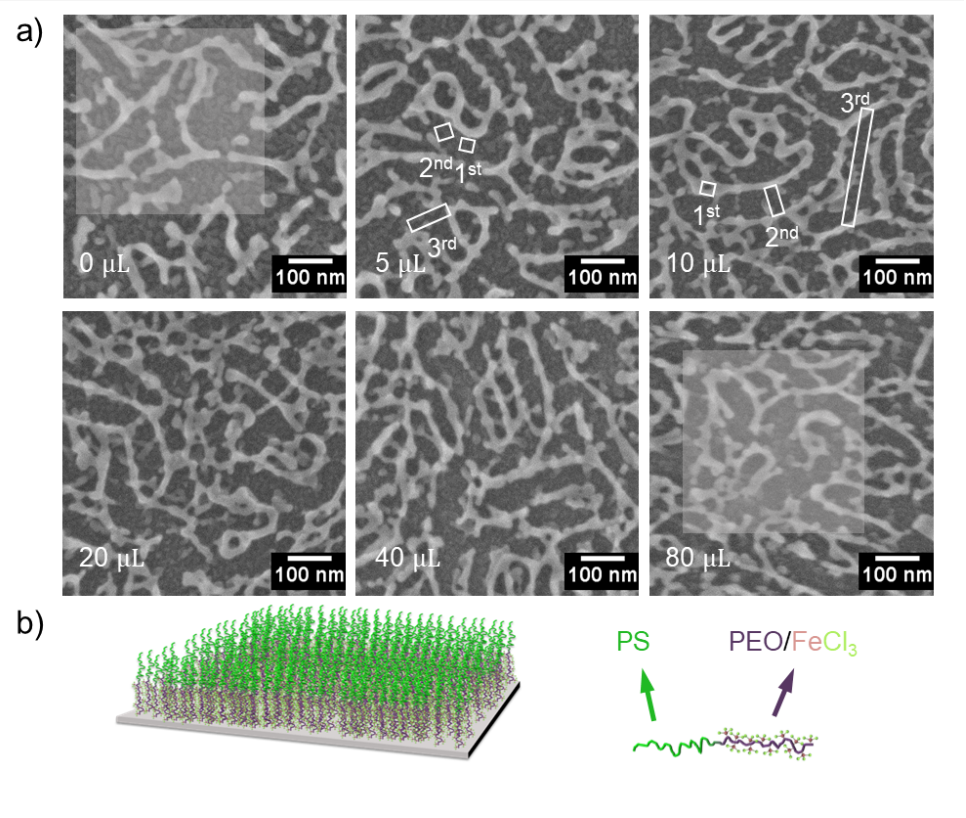

Figure 9.5: *a) SEM images of the α-Fe_2O_3 thin films prepared with annealing-medium $FeCl_3$ concentration. The corresponding H_2O content added into the stock solution is marked on the ocrner of each image. The corresponding cross sectional and low magnification SEM images are shown in Figure 9.6. b) Schematic diagram of the PS-b-PEO/$FeCl_3$ monolayer formed at the silicon substrate interface.*

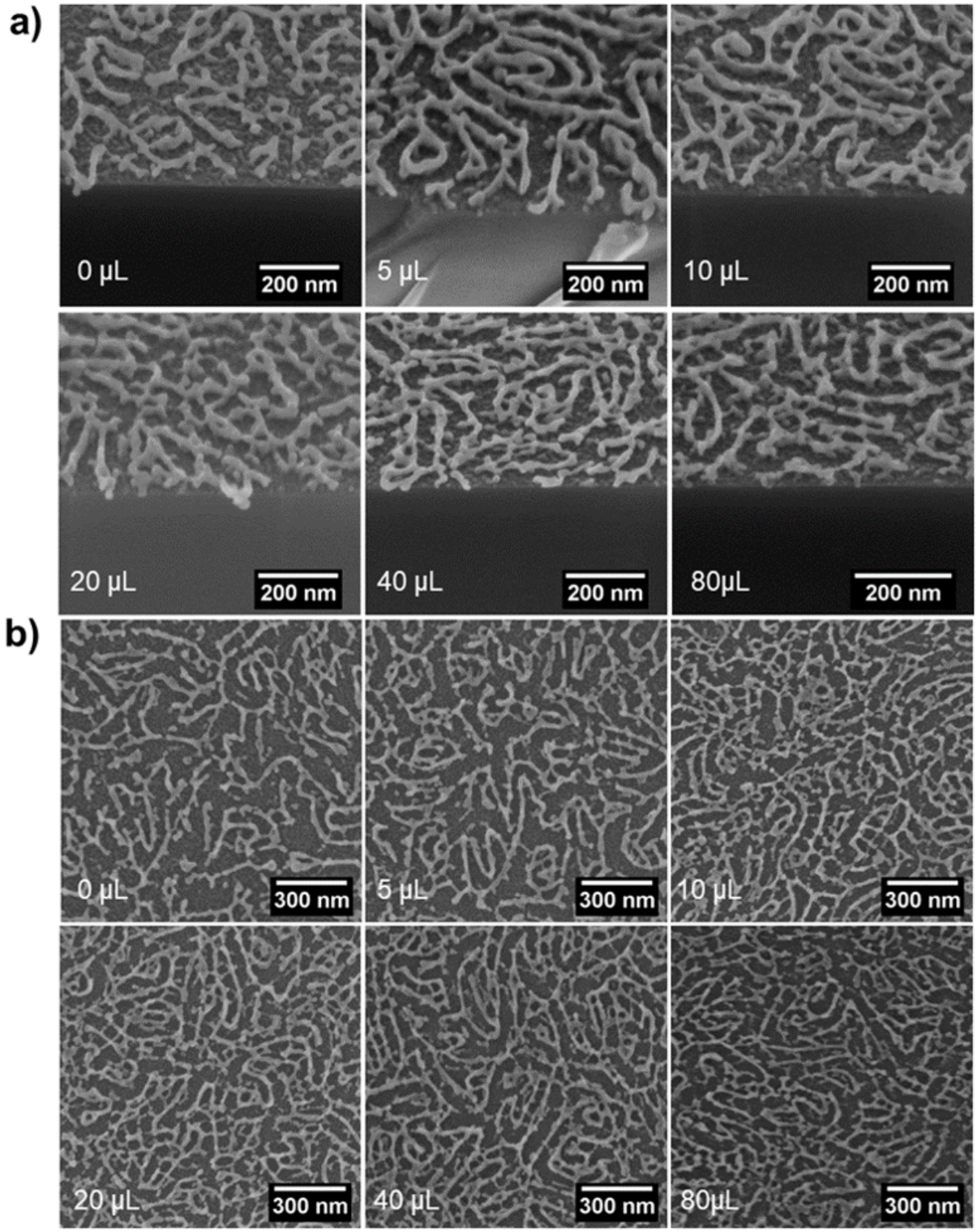

Figure 9.6: *Cross sectional a) and low magnification b) SEM images of the α-Fe_2O_3 thin films processed with annealing treatment. The H_2O content added in the stock solution are noted on the lower left corner of each image.*

For checking whether the phased separated nanostructures shown in Figure 9.3 and Figure 9.5 are already formed prior to the calcination procedure, SEM measurement is performed for the as deposited thin films prepared with no annealing/annealing-medium $FeCl_3$ and concentration 0 μL water addition. As shown in Figure 9.7, both the annealed and unannealed thin films possess analogous structures with the calcined counterpart. This observation indicates that the template effect of the PS-b-PEO polymer is fully manifested in the vitrified thin films and the high temperature calcination process doesn,t affect the self-assembly behavior of the PS-b-PEO polymer significantly and it mainly leads to the crystallization of the α-Fe_2O_3 and removal of the polymeric template.

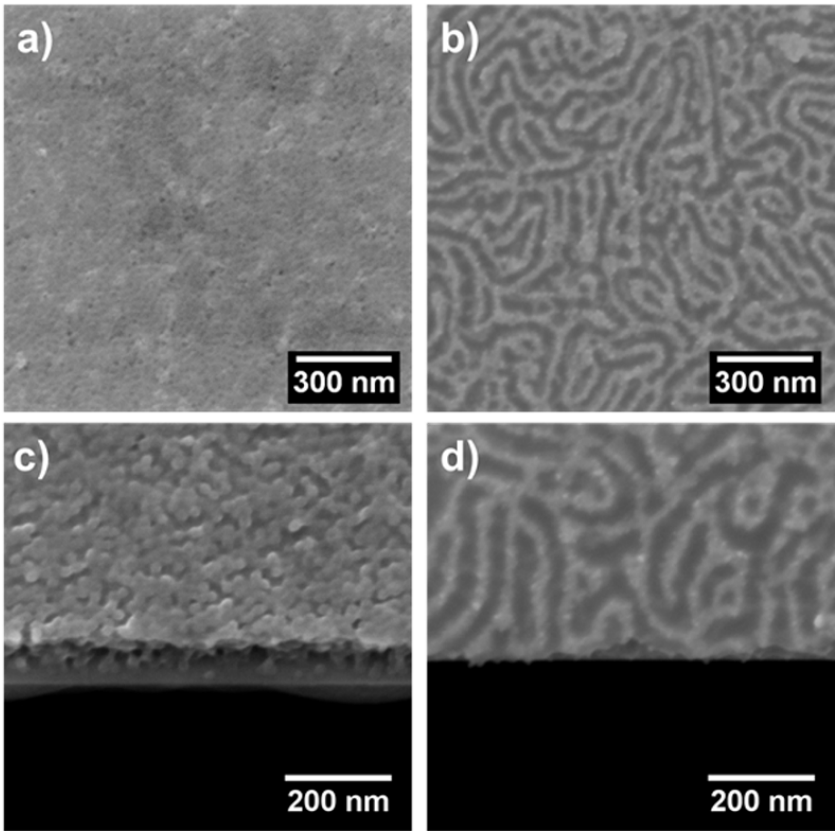

Figure 9.7: *(a,b) Surface and (c,d) cross-section SEM images of the as deposited thin films prepared (a,c) without annealing and (b,d) with annealing-medium $FeCl_3$ concentration and 0 μL water addition.*

Moreover, GIWAXS measurements are performed to study the effect of thermal annealing on the crystal form and grain orientation. Figure 9.8 show the calibrated 2D GIWAXS patterns of the α-Fe_2O_3 thin films prepared with no annealing/annealing-medium $FeCl_3$ concentration and 0 μL H_2O addition. [297] To explore the crystallinity of the α-Fe_2O_3 thin film, Azimuthal integration of the 2D GIWAXS data along q direction are performed

within a scattering angle range from -90° to 90° (Figure 9.9a). Both the room temperature prepared and annealed thin films feature four distinct characteristic peaks within the accessible q range, which can be assigned to the 012, 104, 110 and 113 crystal planes of the α-Fe_2O_3 phase. Based on the Scherrer equation in reciprocal space (1), the average grain sizes of the α-Fe_2O_3 thin films prepared with annealing and no annealing post treatment are estimated to be 6.2 nm and 6.7 nm.

$$D_{hkl} = \frac{2\pi K}{\Delta q_{hkl}} \tag{9.1}$$

Δq_{hkl} is the full width at half maximum of the scattering peak. K is the Scherrer constant with a value of 0.9. [298]

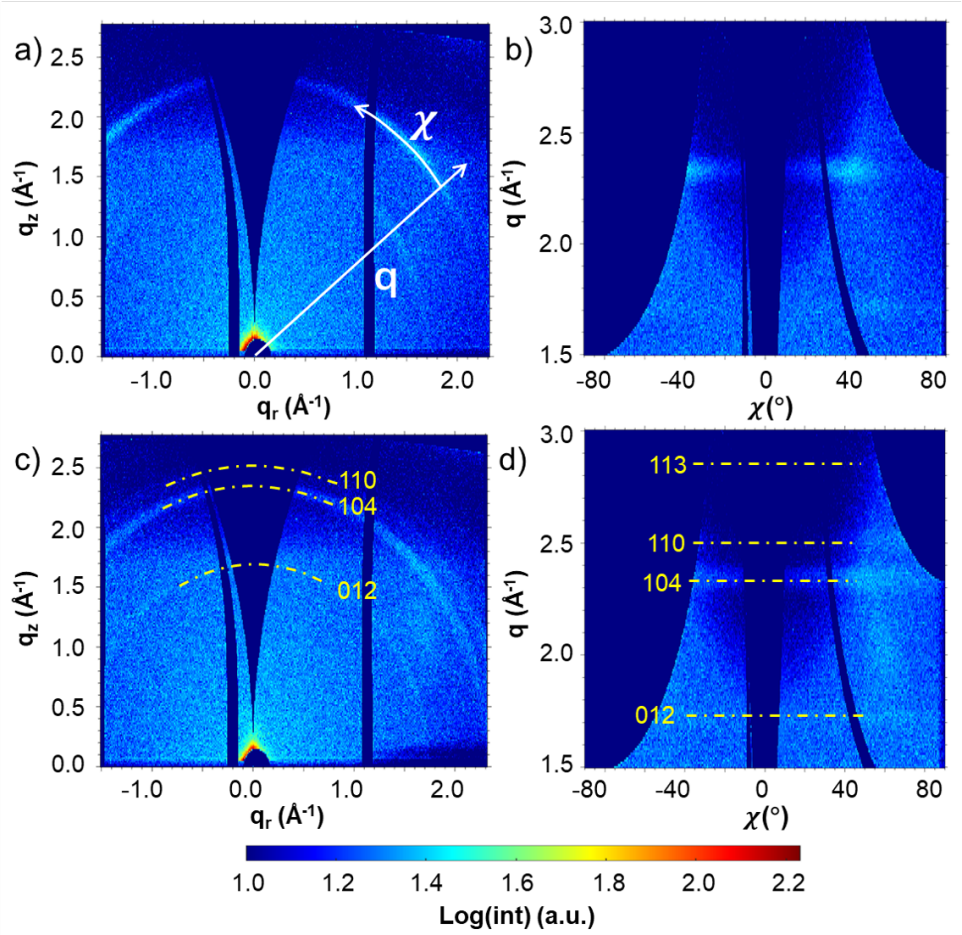

Figure 9.8: *2D GIWAXS patterns of the annealed and unannealed α-Fe_2O_3 thin films prepared on silicon substrate. Azimuthal integration of the 2D GIWAXS data are performed in the (q) direction and orientation distribution analysis are performed along the (χ) direction. The Bragg peak positions in the reshaped 2D GIWAXS patterns are represented with yellow dash lines in c)and d), respectively.*

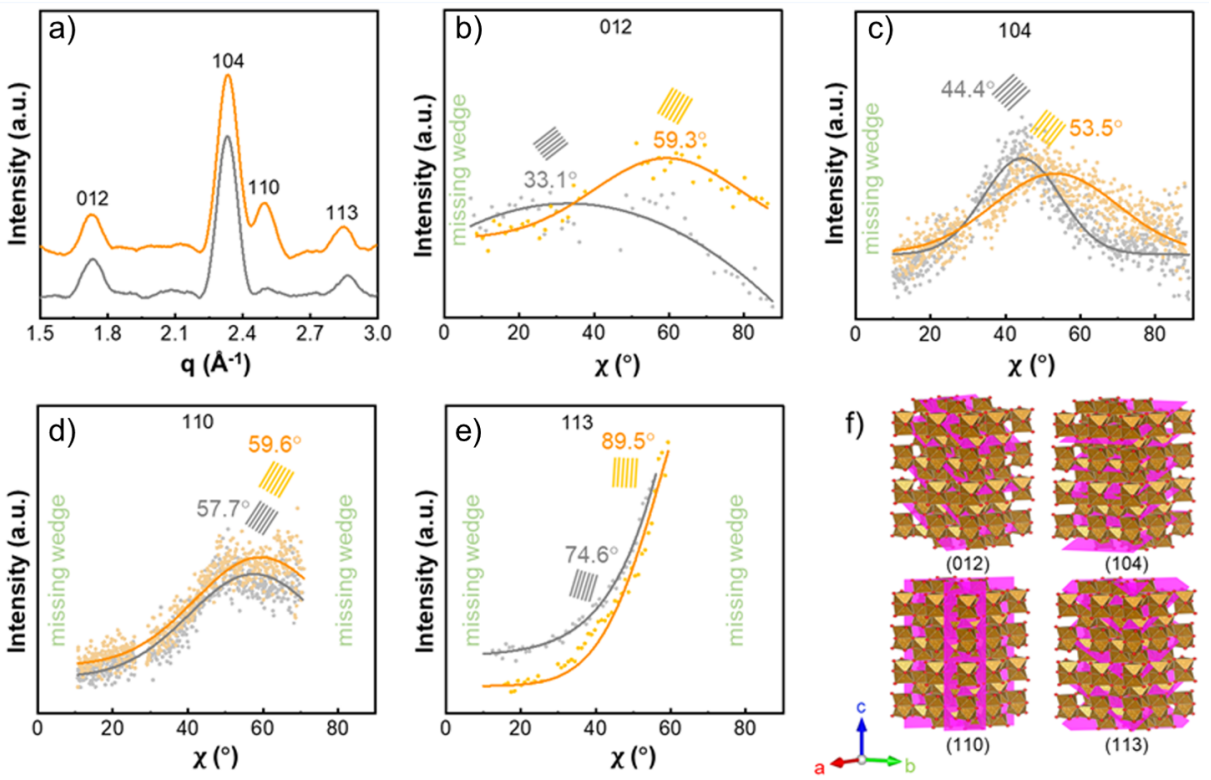

Figure 9.9: *GIWAXS data of the thin films prepared with medium $FeCl_3$ concentration and 0 µl H_2O addition. Azimuthal integration of the 2D GIWAXS data along q are performed at scattering angles from -90 to 90° a). Tube cuts for the 012, 104, 110 and 113 planes are performed in a q range of 1.6 - 1.8 $Å^{-1}$, 2.3 - 2.4 $Å^{-1}$, 2.45 - 2.55 $Å^{-1}$ and 2.8 - 2.9 $Å^{-1}$ for showing the orientation distribution, respectively b-e. The GIWAXS data of the unannealed and annealed samples are represented with grey and orange color, respectively. The original tube cuts and the fitting results in figure 6b-e are denoted as scattered dots and solid lines, respectively. Figure 6f is the crystal structure of α-Fe2O_3 and the 012, 104, 110 and 113 plans are marked with rosy rectangles.*

As a supplement to the GIWAXS measurement, XRD characterization further confirm the crystal phase of the calcined thin films. As shown in Figure 9.10a, all the diffraction peaks appeared in the XRD pattern can be indexed to the α-Fe_2O_3 (JCPDS card 01-1053). For extracting the orientation information of the crystal planes, we performed tube cut for each Bragg peak in Figure 9.11a. As shown in Figure 9.9b-e, the annealing process primarily affects the orientation of the 012, 104, and 113 planes and the orientation of the 110 plane is almost unchanged. The crystal structure of α-Fe_2O_3 is plotted and the corresponding 012, 104, 110 and 113 planes are denoted in Figure 9.9f. Additionally, XPS measurements are performed for checking the quantitative atomic composition information of the annealed and unannealed α-Fe_2O_3 thin films. Figure 9.10b and c show the

core-level Fe 2p XPS spectra of the unannealed and annealed α-Fe_2O_3 thin films. For both samples, the major Fe2p1/2 and Fe2p3/2 peaks are centered at 710.8 eV and 724.4 eV with a spin energy separation of 13.6 eV, and the two weak peaks appear at 718.9 eV and 732.4 eV are the shakeup satellites of Fe2p3/2 and Fe2p1/2.54 All peaks appeared in the Fe 2p spectrum are typical characteristics of α-Fe_2O_3. In addition to the Fe 2p peaks, prominent O 1s and C 1s peaks are also discernible in the survey spectra, which is likely derived from the organic functional group residues of the polymeric template in the α-Fe_2O_3 thin films (Figure 9.10d).

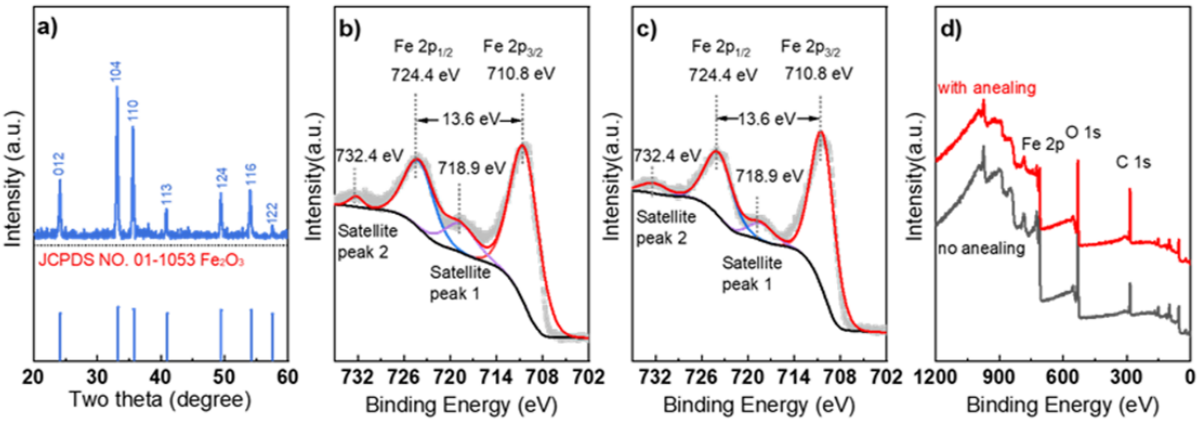

Figure 9.10: *XRD pattern and the corresponding JCPDS card of the thick α-Fe_2O_3 film prepared with drop casting a). Fe 2p spectrum of the α-Fe_2O_3 thin films prepared with no annealing/annealing-medium $FeCl_3$ concentration b) and c). Full-range XPS survey spectra of the α-Fe_2O_3 thin films prepared with no annealing/annealing-medium $FeCl_3$ concentration c).*

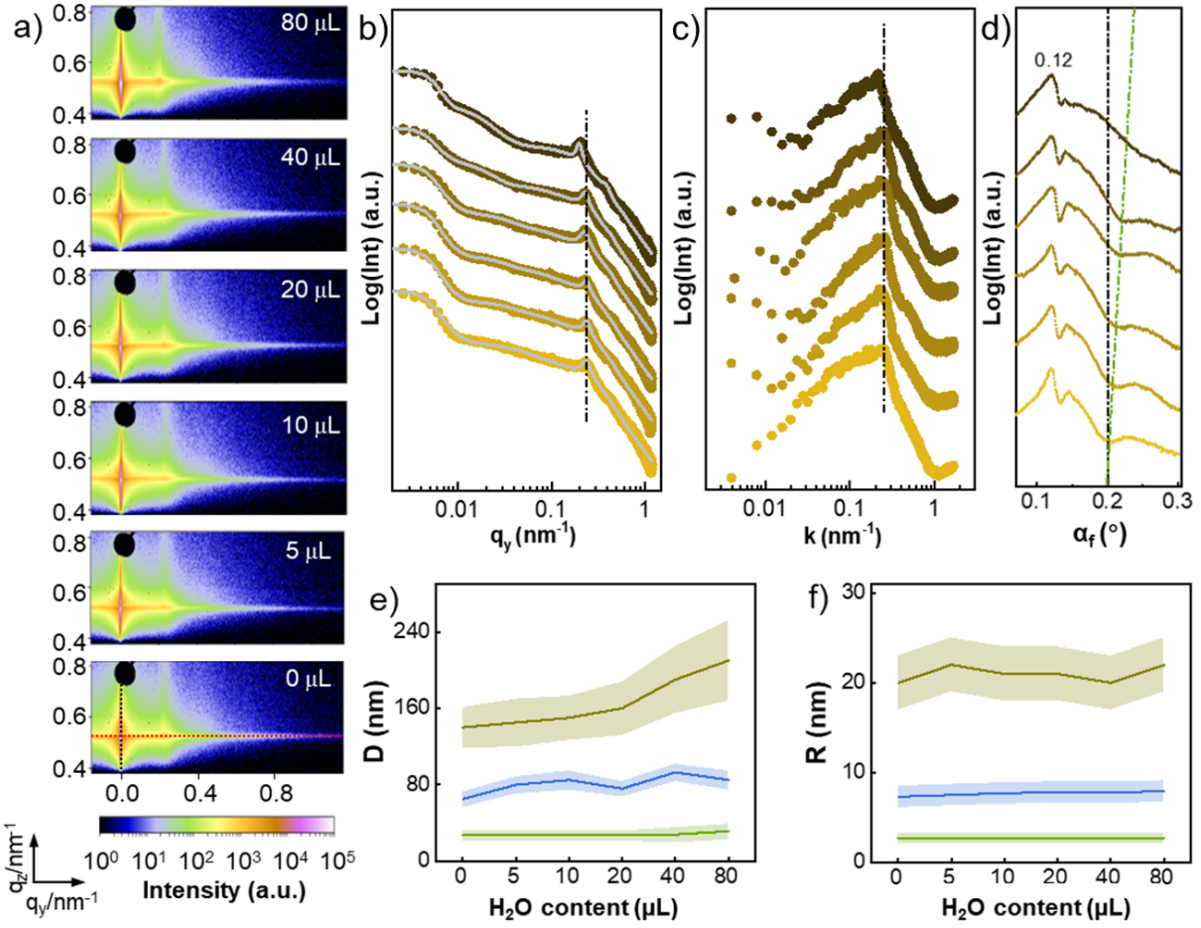

Figure 9.11: *2D GISAXS data of the α-Fe_2O_3 thin films prepared with no annealing-medium $FeCl_3$ concentration, the corresponding H_2O content added in the stock solution is marked on the right side of the 2D GISAXS data a). b) and c) are the horizontal line cuts performed at the Yoneda peak position and the PSD function extracted from the SEM data in Figure* **??**. *d) the vertical line cuts performed at the $q_y = 0$ nm^{-1} position of the 2D GISAXS data. The specific horizontal and vertical line cut position is schematically marked with a red dash line and a black dash line in a). The crescent H2O content added in the stock solution is represented with the deepened color in b)-d). The vertical black dash line and inclined green dash line are plotted as a guide to the eye. e) and f) is the extracted center to center distances (D) and radii (R) within the DWBA modeling framework. Three sets of structure sizes, which are represented as green, blue and yellow colors, are used for modeling the horizontal line cuts in b).*

Through SEM measurement, local structural information on the film surface can be resolved, whereas a large area homogeneity as well as the inner structure of the thin film are also of great importance for the practical applications. GISAXS involves a combination of grazing incidence diffraction (GID) and small angle scattering (SAS) techniques, which

allows for a simultaneously detection on the surface and inner structure of the thin film and provides information on size distributions and spatial correlations of the nanostructures with a high statistic relevance. [299, 300] Figure 9.11a shows the 2D GISAXS data of the α-Fe_2O_3 thin films prepared with no annealing-medium $FeCl_3$ concentration. As seen in the 2D data, the directly reflected X-ray is blocked by a beam-stop to prevent oversaturation of the detector. All 2D GISAXS data show pronounced scattering streak in the horizontal direction, which reflects the existence of the highly ordered structures in the lateral direction of the thin film. [301] The scattering maximum observed between the sample horizon and the specular beam is the so called Yoneda peak, which affords the critical angle information of the material. For quantitative analysis, horizontal line cuts are performed at the Yoneda peak position of α-Fe_2O_3. As shown in Figure 9.11b, the sharp Bragg peak in the high q region derives from the scattering of the most predominant feature size in the thin film. The Bragg peak position is almost constant when the H_2O content added in to the solution is increased from 0 μL to 40 μL, whereas a distinct shift towards the low q region is observed when the H_2O addition is further increased from 40 μL to 80 μL. The prominent left shift of the Bragg peak indicates the increase of the feature sizes, which can be ascribed to the enhanced coalescence of the PS domains induced by the enhanced surface energy between the PS segment and the co-solvent. [97] Figure 9.11c show the PSD distribution functions extracted from the SEM images. The consistent peak shift trend between the PSD distribution functions and horizontal line cuts qualitatively demonstrates the comparable feature sizes within the local and large area of the thin film. Based on the peak values extracted from the PSD distribution function and Bragg,s law d $= \frac{2\pi}{q}$, the inter domain distances are determined to be 31.4 $\pm$ 0.2 nm, 29.9 $\pm$ 0.2 nm, 28.5 $\pm$ 0.2 nm, 31.4 $\pm$ 0.2 nm, 28.5 $\pm$ 0.2 nm and 34.9 $\pm$ 0.2 nm for the thin films prepared with 0 μL, 5 μL, 10 μL, 20 μL, 40 μL, and 80 μL H_2O addition, respectively. For resolving the structure information of the α-Fe_2O_3 thin film in the depth direction, we performed the vertical line cuts at $q_y = 0$ nm^{-1} for the 2D GISAXS data. As shown in Figure 9.11d, the most conspicuous scattering at $q_z = 0.12°$ represents the Yoneda region of α-Fe_2O_3 and the green dash line marked intensity modulations come from the Kiessig fringes. [302]The continuous right shift of the minimum values in the Kiessig fringes indicates the decrease of the film thickness, which is discernable in the cross sectional SEM images in Figure 9.4. For quantitative analysis, we performed the modelling for the horizontal line cuts within the frame work of distorted wave Born approximation (DWBA). More details about the modelling are shown in the supporting information. Three sets of structure factors and form factors are introduced for getting a good modelling result and the specific values are shown in Table 9.3. As shown in Figure 9.11e and f, the most conspicuous Bragg peak in the high q region is modelled with the first order center-to-center distance (D) and radius

(R) values. Specifically, the D_1 values are 27 ± 5 nm, 27 ±5 nm, 27 ±5 nm, 27 ±5 nm, 28 ±5 nm, and 31.4 ± 5 nm and R_1 values are constant at 2.7 ± 0.6 nm for the α-Fe_2O_3 thin films prepared with 0 μL, 5 μL, 10 μL, 20 μL, 40 μL and 80 μL H_2O addition. The modelled center-to-center distance values for the predominant first order structures are approximate with the feature sizes calculated based on the PSD distribution functions. The rest two sets of feature sizes are used for modeling the scattering intensity in the lower q region. The D_2 and R_2 show a uniform fluctuation and possess an average value of 80.7 ± 9 nm and 7.7±1.2 nm within the whole H_2O addition frame. The D_3 values show a continuous growth and are 140 ± 21 nm, 145 ± 25 nm, 150 ± 23 nm, 160 ± 28 nm, 190 ± 35 nm, 210 ± 42 nm, R_3 values are uniformly fluctuating with an average value of 21 ± 3 nm for the α-Fe_2O_3 thin films prepared with 0 μL, 5 μL, 10 μL, 20 μL, 40 μL and 80 μL H_2O addition.

Water contentμl	D_1	R_1	D_2	R_2	D_3	R_3
0	27±5	2.7±6	65±8	7.3±1.2	140±21	20±3
5	27±5	2.7±0.6	80±9	7.5±1.2	145±25	22±3
10	27±5	2.7±0.6	85±10	7.7±1.2	150±23	21±3
20	27±5	2.7±0.6	76±8	7.8±1.2	160±28	21±3
40	28±5	2.7±0.6	93±9	7.8±1.2	190±35	20±3
80	31.4±5	2.7±0.6	85±10	7.9±1.2	210±42	22±3

Table 9.3: *Modelled center-to-center distance and radius values for α-Fe_2O_3 thin films prepared withwith no annealing-medium $FeCl_3$ concentration.*

Figure 9.12a show the 2D GISAXS data of the α-Fe_2O_3 thin films prepared with annealing-medium $FeCl_3$ concentration. Strikingly, all the 2D GISAXS data features stratified Yoneda regions in the vertical direction, which derives from the scattering of the α-Fe_2O_3 layers with different densities. Combined with the structural information displayed in the SEM images (Figure 9.3), the scattering intensity in the lower and higher Yoneda region can be generated by the loose bottom layer and the condensed cylindrical top layer, respectively. For quantitative analysis, horizontal line cuts are performed at the higher and lower Yoneda peak position, which are denoted with red dash lines in Figure 9.12a, of α-Fe_2O_3. As shown in Figure 9.12b, along with the water addition, the line cuts of the loose bottom layer feature a smeared scattering intensity distribution within the whole q_y region whereas a gradually protuberant Bragg peak is appeared in the high q region for the condensed α-Fe_2O_3 counterpart. The line cuts in Figure 9.12b qualitatively demonstrate the broad size distribution of the loose and condensed α-Fe_2O_3 layer, the

comparable ordering of the loose α-Fe_2O_3 layer and the enhanced ordering of the condensed α-Fe_2O_3 layer along with the water addition. For comparison, PSD distribution functions are extracted from the SEM images (Figure 9.12c). When the H_2O content added in to the solution is increased from 0 μL to 80 μL, the location of the main peak is sequentially determined to be 0.097 $\pm$ 0.0007 nm^{-1}, 0.100 $\pm$ 0.0007 nm^{-1}, 0.107 $\pm$ 0.0008 nm^{-1}, 0.109 $\pm$ 0.0009 nm^{-1}, 0.104 $\pm$ 0.0009 nm^{-1} and 0.115 $\pm$ 0.0008 nm^{-1}, which corresponds to an inter domain distance of 64.7 $\pm$ 0.47 nm, 62.8 $\pm$ 0.44 nm, 58.7 $\pm$ 0.44 nm, 57.6 $\pm$ 0.48 nm, 60.4 $\pm$ 0.52 nm and 54.6 $\pm$ 0.38 nm, respectively. The vertical line cuts in Figure 9.12d show that the relative position of the Yoneda peak is hardly altered along with the addition of H_2O, which demonstrates the comparable scattering length density among the different hierarchical α-Fe_2O_3 thin films. Considering the Yoneda peak positions of both annealed and unannealed α-Fe_2O_3 thin films are approximate with the silicon substrate. We performed an additional GISAXS measurement for the bare silicon substrate by using the same measurement parameters. As seen in Figure 9.13a, very weak scattering signal is detected for the bare substrate due to the low roughness. The critical angle of the substrate is determined to be 0.14° from the vertical line cut (Figure 9.13b). The corresponding horizontal line cut performed at the critical angle of the substrate is shown in Figure 9.13c. In addition to the low scattering intensity, the scattering characteristics of the bare silicon substrate and the α-Fe_2O_3 thin films in the whole q_y region is also significantly distinct with each other. Therefore, the scattering peaks recorded in the 2D GISAXS data of the α-Fe_2O_3 thin films can be primarily ascribed to the α-Fe_2O_3 nanostructure itself rather than the silicon substrate. For quantitative analysis, the horizontal line cuts are modelled within the frame work of DWBA and the modelling result is shown in Figure 9.12e and f. The modelled center-to-center distances and radii for the loose bottom layer are universally smaller than the top condensed layer. Within the whole H_2O addition range, both the distances and radii modeled for the loose α-Fe_2O_3 layer demonstrates uniform fluctuation with an average value of 9.2 $\pm$ 1 nm, 16.7 $\pm$ 1 nm, 62.5 $\pm$ 5.3 nm for D_1, D_2, D_3, and 3 $\pm$ 0.2 nm, 4.3 $\pm$ 0.3 nm, 8.7 $\pm$ 0.7 nm for R_1, R_2, R_3, respectively. For the top condensed α-Fe_2O_3 layer, the modeled distance and radius values show integrally decreased tendency from 45 $\pm$ 6nm to 26 $\pm$ 5 nm for D_1, from 74 $\pm$ 8 nm to 61 $\pm$ 9 nm for D_2 and from 421 $\pm$ 50 nm to 290 $\pm$ 21 nm for D_3, respectively. In contrast, R_1 and R_2 show uniform fluctuation with an average value of 7.3 $\pm$ 0.5 nm, 10.3 $\pm$ 1.5 nm, respectively. R_3 are integrally decreased from 29 $\pm$ 3 nm to 21 $\pm$ 3 nm, respectively. For the α-Fe_2O_3 thin films prepared either with annealing or without annealing post treatment, the structure and form factors extracted from the modeling of the GISAXS data are in good accordance with the features sizes marked in the SEM images. The good structural consistency between the SEM measurement and

the GISAXS modeling result demonstrates the good structural consistency in the local and large area of the thin film.

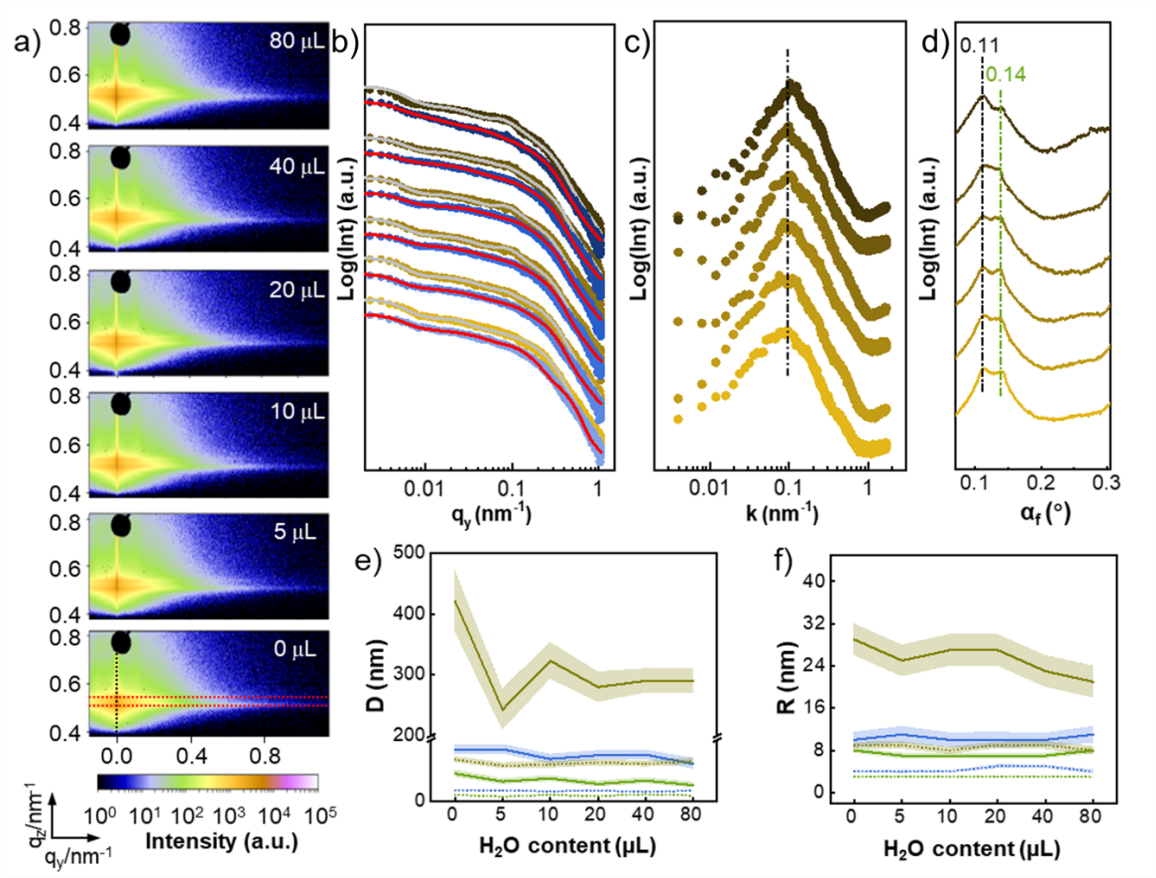

Figure 9.12: *2D GISAXS data of the bare silicon substrate (a). Vertical (b) and horizontal line cuts (c) performed at the qy=0 nm-1 (red dash line in figure S3a) and the Yoneda peak (white dash line in figure S8a) position of the silicon substrate.*

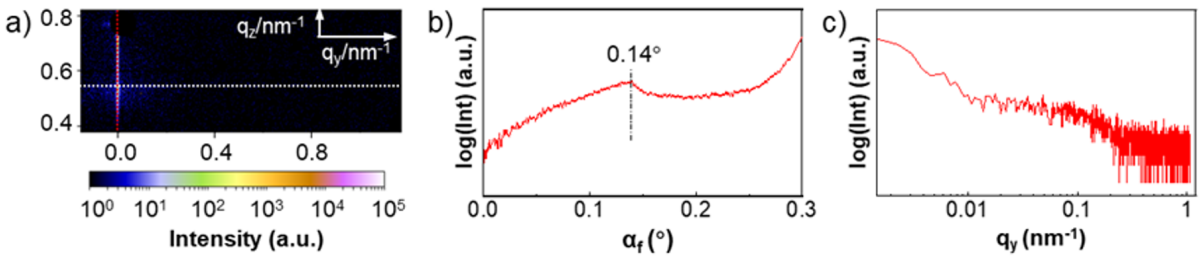

Figure 9.13: *2D GISAXS data of the bare silicon substrate a). Vertical b) and horizontal line cuts c) performed at the q_y=0 nm^{-1} (red dash line in a) and the Yoneda peak (white dash line in a) position of the silicon substrate.*

9.3 Films prepared with low/high $FeCl_3$ concentration and 0 μL H_2O

Figure 9.14a/b refer to the SEM images and 2D GISAXS data of the α-Fe_2O_3 thin films prepared low/high $FeCl_3$ concentration and 0 μL H_2O addition. For distinction, the -Fe2O3 thin films processed with thermal annealing are denoted via an additional subscript "a". As shown in Figure 9.14a, the α-Fe_2O_3 thin film prepared with low $FeCl_3$ content is composed of loose foam like structure and the homogeneity of the thin film is severely deteriorated after the annealing post treatment. By increasing the $FeCl_3$ content in the sol-gel solution, more ordered porous structures are formed whereas the coverage of the porous structures on the silicon substrate is not as good as the α-Fe_2O_3 thin films prepared by no annealing-low/medium $FeCl_3$ content. The local structural vacancy can be induced by the exfoliation of the excessive α-Fe_2O_3 during the high temperature calcination process. Due to the high mass loading of $FeCl_3$, the α-Fe_2O_3 thin film treated with thermal annealing is almost composed of dense structure, which is likely induced by the fusion and collapse of the PS-b-PEO/$FeCl_3$ micellar structures during the annealing process. The different morphologies of the α-Fe_2O_3 thin films prepared in the present work demonstrate that the templating effect of the PS-b-PEO block copolymer can be significantly weakened by the unmatched $FeCl_3$ precursor to PS-b-PEO weight fractions in the sol-gel solution. Due to the existence of the randomly distributed nanostructures in Figure 9.14a, all 2D GISAXS data in Figure 9.14b exhibit semicircular scattering patterns. [22] Besides, two distinct Bragg rods as denoted with white arrows, which symbolizes the existence of periodic structures, are observed in the 2D GISAXS data of the α-Fe_2O_3 thin film prepared with post annealing treatment and high $FeCl_3$ content. The cross sectional and low magnification SEM images are shown in figure S5 in detailed. The critical angle of the different porous α-Fe_2O_3 thin films can be determined from the vertical line cuts of the 2D GISAXS data. As shown in Figure 9.14c, a single sharp Yoneda peak located at around 0.15° is presented in the vertical line cut of the α-Fe_2O_3 thin films prepared with annealing/no annealing-low $FeCl_3$ concentration and no annealing-high $FeCl_3$ concentration. In addition, the Yoneda region is significantly broadened and splitted into two individual peaks at $q_z = 0.15°$ and $q_z = 0.21°$ for the α-Fe_2O_3 thin film prepared with annealing-high $FeCl_3$ concentration, which suggests the broadened scattering length density distribution and the formation of high density α-Fe_2O_3 within the thin film. To gain further structural information in the lateral direction, horizontal line cuts are performed at the Yoneda peak positions of the different α-Fe_2O_3 thin films. As shown in Figure 9.14d, for the α-Fe_2O_3 thin films prepared with no annealing-low $FeCl_3$ concentration, a broad scattering is observed in the high q region, which vanishes along with the appearance of a new scattering peak in the

higher q_y region and enhanced scattering in the lower q_y region after annealing. The peak shift can be ascribed to the formation of the extremely unevenly distributed feature sizes, as indicated in the SEM images in Figure 9.14a and Figure 9.8, in the annealed α-Fe_2O_3 thin film. In contrast, a sharp Bragg peak is discernible in the high qy region for the α-Fe_2O_3 thin films prepared with no annealing-high $FeCl_3$ concentration, which is again smeared along with the enhanced scattering in the lower q_y region after annealing. Due to the stratified Yoneda regions of the α-Fe_2O_3 thin film prepared with annealing-high $FeCl_3$ concentration, two horizontal line cuts are performed at each Yoneda peak center position. As seen in Figure 9.14d, the two horizontal line cuts characterize approximate shape within the whole detectable q_y range, which indicates the comparable feature size distribution of the density-stratified α-Fe_2O_3. Notably, no prominent annealing induced Bragg peak shift is observed for the α-Fe_2O_3 thin film prepared with high $FeCl_3$ concentration, which should be distinguished from the situation shown in the α-Fe_2O_3 thin film prepared with low $FeCl_3$ concentration. The broadened Bragg peak in the high qy region and the enhanced scattering in the low q_y region indicate the annealing treatment for the α-Fe_2O_3thin film prepared with high $FeCl_3$ concentration leads to the polydispersion of the pore structures and the formation of larger feature sizes within the thin film. As mentioned above, all the scattering characteristics in the horizontal line cuts can be retrieved from the structural information presented in the SEM images in Figure 9.14a and Figure 9.15, which confirm the structures shown in the SEM images spread all over the thin film.

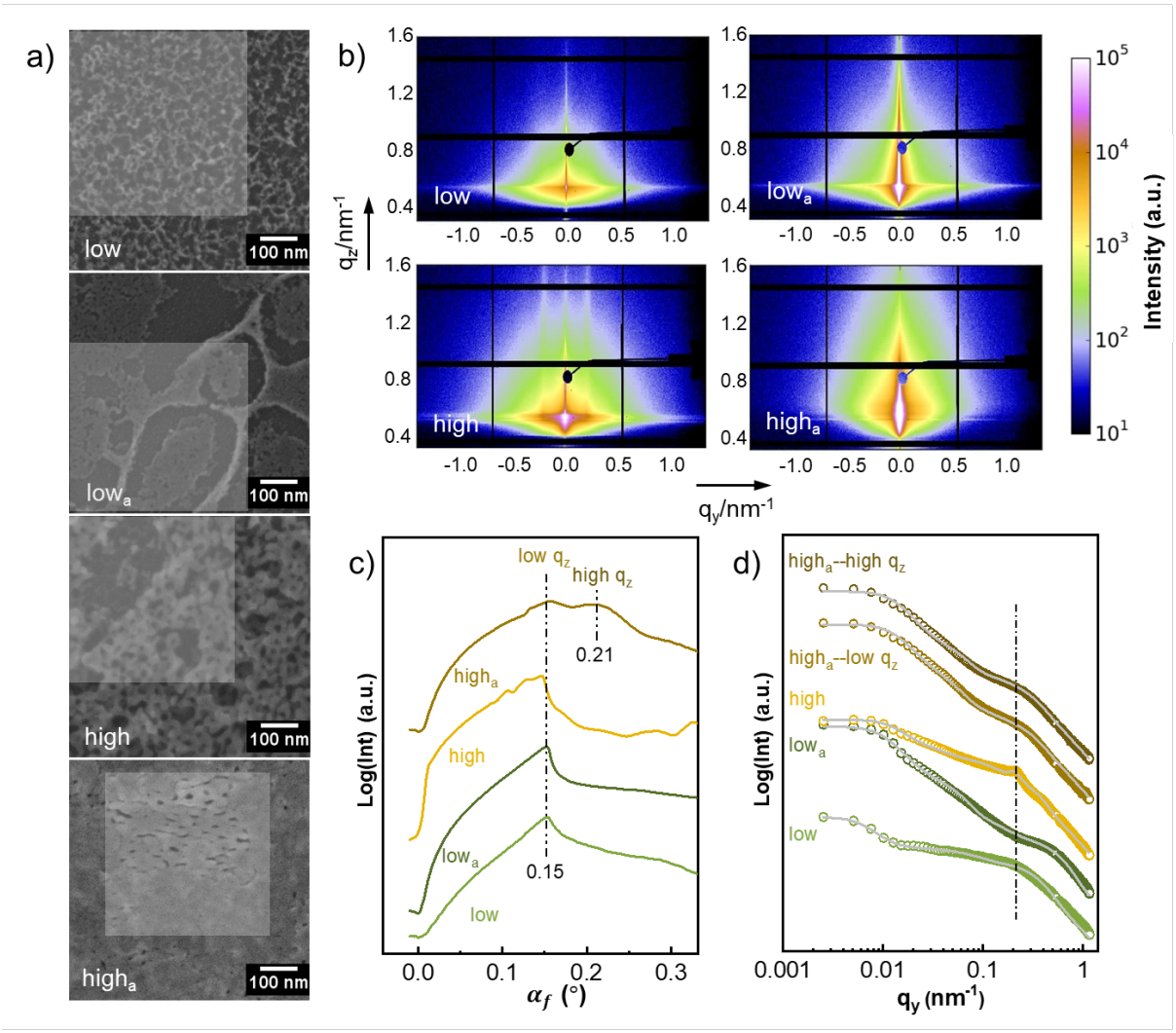

Figure 9.14: *SEM images a) and 2D GISAXS data b) of the α-Fe_2O_3 thin films prepared with annealing/no annealing, low/high $FeCl_3$ concenitration and 0 μL H_2O addition. For distinction, the annealed thin films are denoted with a subscript "a". The corresponding component weight fractions of the stock solutions used for preparing the α-Fe_2O_3 thin films with low/high $FeCl_3$ concentrations are denoted with purple/orange points in the phase diagram in figure 9.2. c) show the vertical line cuts performed at q_y=0 nm^{-1} of the 2D GISAXS data and d) refer to the horizontal line cuts performed at the Yoneda region of the different α-Fe_2O_3 thin films.*

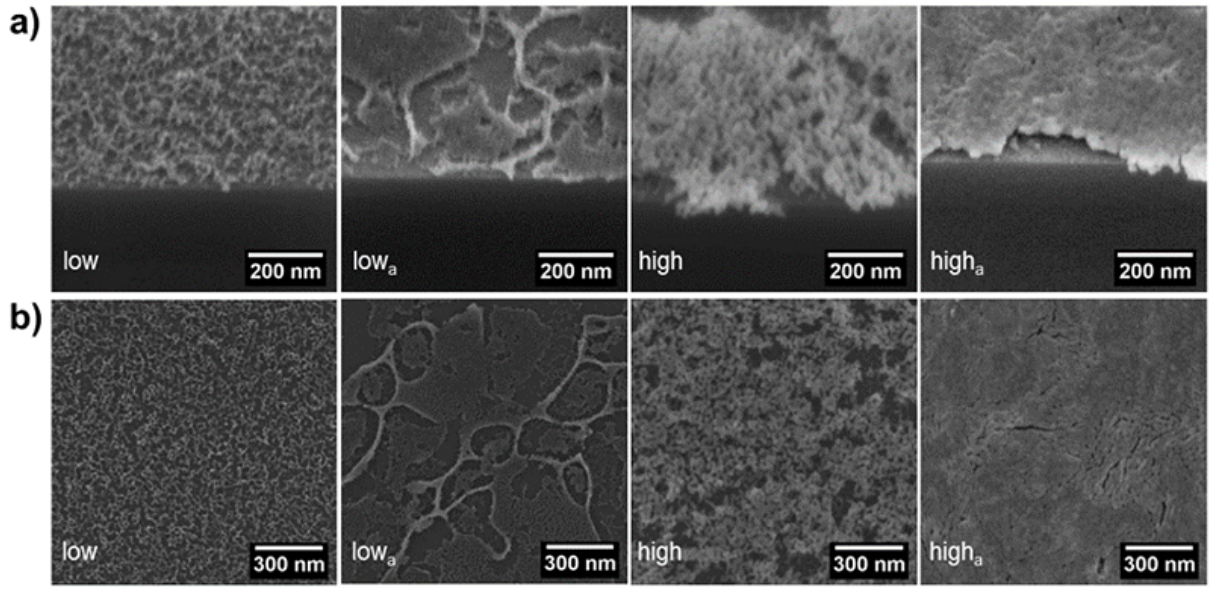

Figure 9.15: *Cross sectional and low magnification SEM images of the α-Fe_2O_3 thin films prepared with low and high $FeCl_3$ content. The α-Fe_2O_3 thin films processed with annealing treatment is denoted by subscript "a".*

9.4 Morphology evolution of the films

Based on the SEM images mentioned above, a simplified scheme is plotted and shown in Figure 9.16 for illustrating the structure variation of the α-Fe_2O_3 thin films caused by the H_2O addition, $FeCl_3$ content increasement and annealing treatment. The 3D thin film models shown in Figure 9.16 are duplicated from the local region of the SEM images, which is marked out with white squares in figure 9.3, figure 9.5 and figure 9.14. The primary structural varication caused by the $FeCl_3$ content increasement consists in the film thickness increasement, altered templating effect and exfoliation of the α-Fe_2O_3 materials, and the H_2O addition leads to the formation of large vesicles whereas the annealing post treatment mainly leads to the formation of the dewetted hierarchical structure.

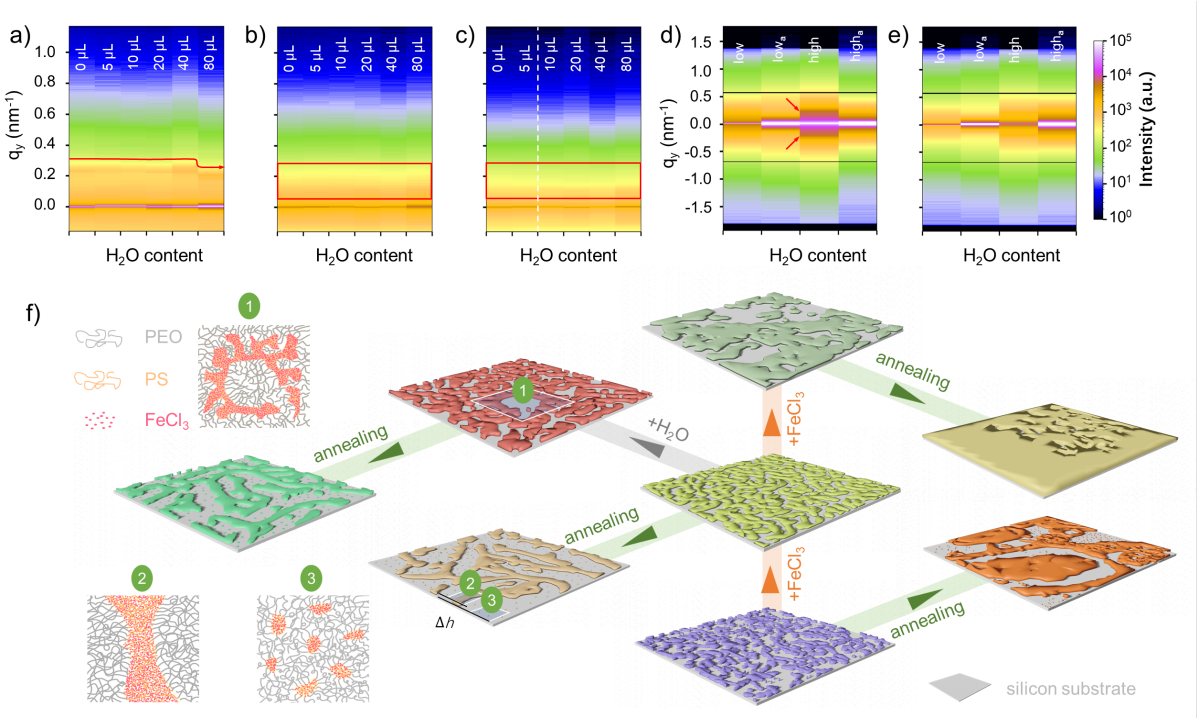

Figure 9.16: *Schematic illustration of the α-Fe_2O_3 nanostructures acquired at different preparation conditions. The 3D thin film structures are duplicated from the local SEM images marked with white dotted frames in figure 9.3, figure 9.5 and figure 9.14. The corresponding micellar structures of the uncalcined counterparts on the square marked local regions are shown on the top of the picture. The surface height difference of the hierarchical structure normal to the silicon substrate is marked with δh. The corresponding PEO/$FeCl_3$@PS micellar structures for forming the marked α-Fe_2O_3 nanostructures are shown on the right side of the picture, in which the PS segment is represented with grey line and the Fe/Cl_3 coordinated PEO segment is denoted with red dot and orange line, respectively.*

9.5 Current-voltage characteristics

Due to the most conspicuous morphological variation of the α-Fe_2O_3 thin films is induced via thermal annealing post treatment, two representative α-Fe_2O_3 thin films prepared with medium $FeCl_3$ concentration, 0 μL H_2O addition and annealing/no annealing post treatment are employed as the electron transport modification layer to investigate their morphological effect on the photovoltaic properties of the perovskite solar cells. More details about the solar cell fabrication can be found in the supporting information and simplified device preparation flowchart is shown in figure 9.17a. Figure 9.18 shows the compact α-Fe_2O_3 thin film doposited on the FTO substrate. Figure 9.17b and c show the compact α-Fe_2O_3 layer supported quasi-isoporous and double layered α-Fe_2O_3 thin films,

which are distinguished from the morphologies shown in Figure 9.3a and Figure 9.5a. This difference can be ascribed to the surface energy difference between the substrate and the film. [303] Altering substrate-polymer interactions can influence the wettability, the phase stability of the block polymers and thereby govern the pattern formation, [304] long-range microstructural alignment, [305] and defect density on the thin film. [306]

As shown in figure 9.17e, the double layered α-Fe_2O_3 nanostructure at the interface between the compact α-Fe_2O_3 layer and the perovskite layer is more bumpy than that of the quasi-isoporous nanostructure in figure 9.17d. Figure 9.17f compares the current-voltage (J-V) characteristics of these two types of solar cells. The extracted photovoltaic parameters (power conversion efficiency (PCE), short-circuit current density (I_{SC}), open-circuit voltage (V_{OC}), and fill factor (FF)) are shown in Table 9.4. The PSC devices fabricated with hierarchical α-Fe_2O_3 electron transport modification layer shows increased V_{OC} and PCE values. Statistical photovoltaic parameter distribution of the of the PVSCs prepared with quasi-isoporous, doulbe layered and compact α-Fe_2O_3 electron transport modification layer are shown in figure 9.19. The improved photoelectric property of the solar cells fabricated with double layered α-Fe_2O_3 electron transport modification layer can be ascribed to the enhanced light transmittance and electron extraction ability of the more bumpy double layered α-Fe_2O_3 electron transport modification layer. Moreover, the suppressed carrier recombination at the interfaces might also leads to the increase of the V_{OC}.

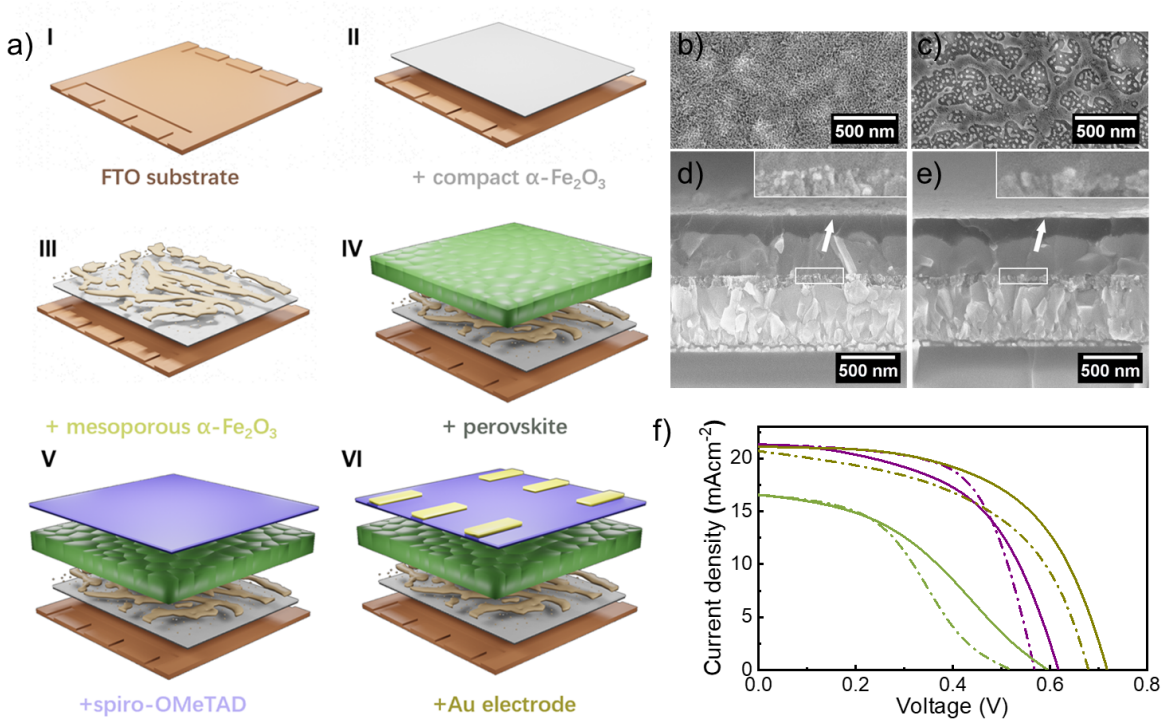

Figure 9.17: *Flow chart of the perovskite solar cell preparation. SEM images of the quasi-isoporous b) and hierarchical c) α-Fe_2O_3 modified α-Fe_2O_3 layer. The quasi-isoporous (b) and hierarchical (c) α-Fe_2O_3 layer are prepared via no annealing/annealing, medium $FeCl_3$ concentration and 0 μL H_2O addition.*

parameterr	α-Fe_2O_3-no anealing		α-Fe_2O_3-anealing	
	reverse	forward	reverse	forward
J_{sc}	21.345	21.305	21.12	20.71
V_{oc}	0.567	0.617	0.717	0.678
PCE(%)	7.647	7.038	8.587	7.141
FF(%)	63.134	53.554	56.715	50.888

Table 9.4: *Photovoltaic parameters extracted from J-V curves of the different studied types of solar cells.*

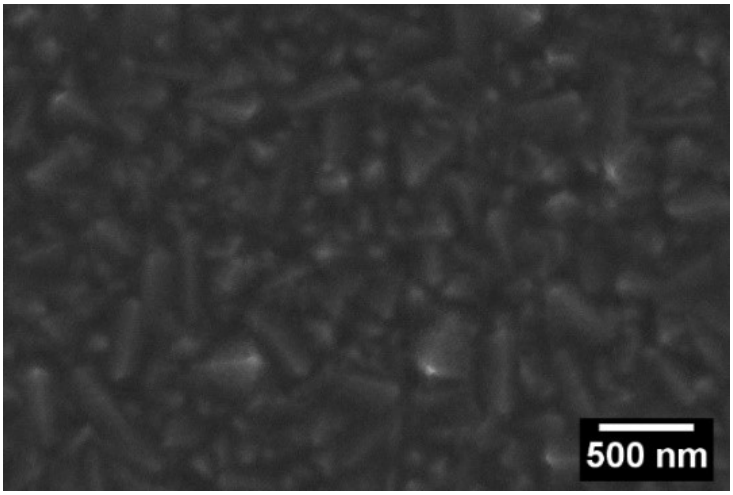

Figure 9.18: *SEM images of the compact -Fe2O3 thin films deposited on the FTO substrate.*

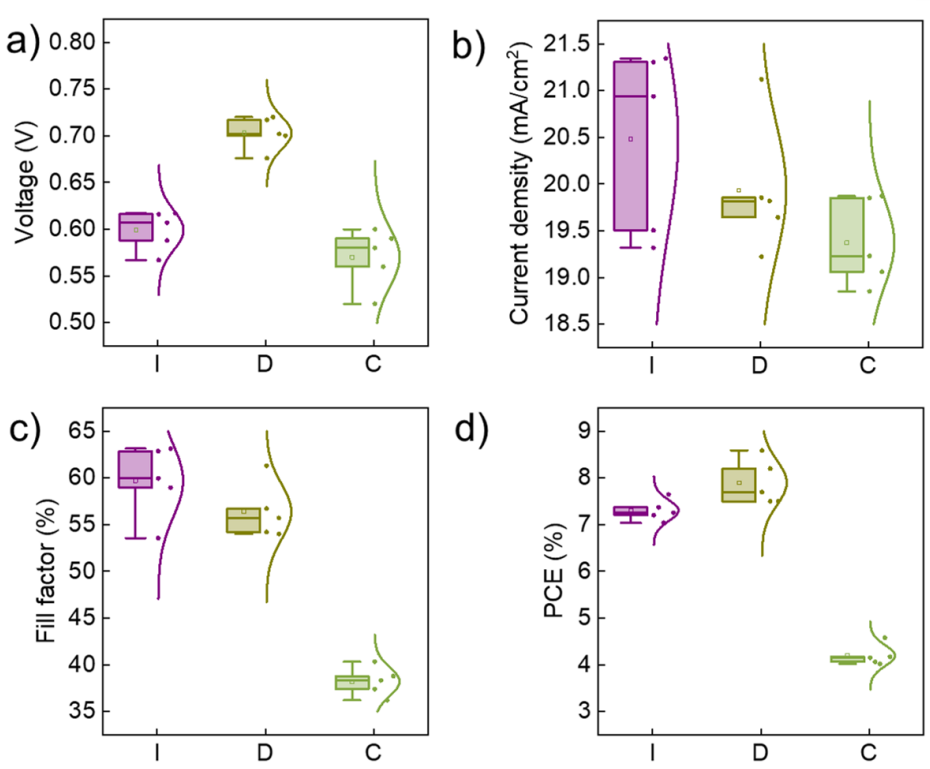

Figure 9.19: *Statistical photovoltaic parameter distribution of the of the PVSCs prepared with quasi-isoporous (purple, I) , double layered (dark yellow, D), and compact α-Fe_2O_3 (green) electron transport modification layer.*

9.6 Conclusion

In this work, a facile method involves block copolymer templated wet-chemistry and thermal annealing induced thin film dewetting is presented to synthesize ordered and hierarchical α-Fe_2O_3 nanostructures. By tuning the $FeCl_3$ to PS-b-PEO ratio, the poor solvent content in the sol-gel solution and the annealing temperature, various mesoporous and hierarchical α-Fe_2O_3 thin films are fabricated. The structural information within the local and large area are systematacially investigated via SEM and GISAXS measurement and the phase and orientation information about the α-Fe_2O_3 crystal is probed with GIWAXS and XRD measurement. Through the structural characterization, we conclude that the $FeCl_3$ addition mainly affects the templating effect of the PS-b-PEO, leads to the increasement of the film thickness and exfoliation of the α-Fe_2O_3 materials. The H_2O addition induces the formation of large vesicles whereas the annealing post treatment mainly cause the formation of the dewetted hierarchical structure. XRD characterizations confirm the crystal structure of α-Fe_2O_3 and GIWAXS characterization suggests that the annealing process primarily affects the orientation of the 012, 104, and 113 planes and the orientation of the 110 plane is almost unchanged. XPS measurement confirms the valence state of iron element and the existence of the organic functional group residues of the polymeric template in the α-Fe_2O_3 thin films. The present work is far from an optimization of the device parameters whereas it laid the foundation for further doping or surface modification of the thin films. Moreover, the simple synthesis method proposed in this work is also envisioned to the synthesis of other similar metal oxides or metal oxide composites, which provides a broad space for the research and development of a variety of novel porous functional materials applicable in the field of new energy, catalyst and sensor, etc..

10 Summary and outlook

In the present thesis, the synthesis of various kinds of metal oxide thin films is executed by controlling the composition of the sol-gel solutions and the post-processing conditions, and the applicability of the metal oxide thin films in photovoltaic devices are investigated. Within this scope, systematic morphology studies are conducted for block copolymer templated TiO_2, SnO_2, and α-Fe_2O_3 film synthesis. A fundamental understanding of the structure evolution and the large area homogeneity of the printed PS-b-P4VP and PS-b-P4VP/$FeCl_3$ thin films are revealed via in-situ GISAXS measurement. The aggregate state of the polymers in solution is also investigated. Moreover, the implications of the different kinds of patterned α-Fe_2O_3 thin films in perovskite solar cells are discussed. In the following part, some key issues put forward in the introduction part are addressed.

In the first result chapter, the preparation of mesoporous TiO_2 thin films is investigated by changing the solvent category and the HCl content in the sol-gel solution. Three kinds of solvent, THF, 1,4-dioxane, toluene/1-butanol, and 5 different HCl volume fractions are used for tuning the preferential affinity of the solvent to the polymer chains. By calcination, TiO_2 thin films with spherical, cylindrical, sac-like structures are obtained. The morphology evolution mechanism is explained from the perspective of the surface energy between PS blocks and the surrounding solvent, the aggregation behavior of the titania nanoparticles, and the preferential affinity of the solvent or solvent mixture. When the volume fraction of HCl is 0.5 vol.%, random structures are formed for all solvent categories due to the unsuppressed aggregation of titania nano-dot arrays and weak phase separation tendency of the block copolymer template. For the thin films prepared with THF and 1.0 vol.%, 2.0 vol.%, 4.0 vol.% and 8.0 vol.% HCl addition, the almost equally distributed solvent within two phases, and proper surface energy lead to the formation of the iso-porous structures. Regarding the medium solvent selectivity of TB, a typical transition from the sphere, cylinder, lamellae, to vesicle, related to the variation of surface energy, is provoked with the HCl addition. For the solvent with high selectivity, such as 1,4-dioxane, more asymmetric nanostructures, such as cylinder, are formed regardless of the amount of HCl added to the solution. Apart from the morphology study, the crystallinity of the TiO_2 thin films is also investigated with XRD, and it is found that all titania thin films consist of a pure anatase phase, irrespective of the morphology.

Compared with TiO_2, SnO_2 and α-Fe_2O_3 feature more advantages in the applications of the perovskite solar cells. Therefore, system morphology regulation for the SnO_2 and α-Fe_2O_3 thin films are conducted and recorded in the second and third result chapter.

For SnO_2 thin films, by choosing $SnCl_4$ as the precursor, THF and 1,4-dioxane as the solvent, large area uniform SnO_2 thin films with spherical, cylindrical, and saccate structures are acquired. It is demonstrated that the structural transformation of the SnO_2 thin films is governed by a synergistic effect of the preferential affinity of the solvent for a certain block and the hydrogen bond interaction between the employed cycloether and H_2O. The spherical pore structure is formed with a relatively lower $\Delta\chi$ value ($0.04 \leq \Delta\chi \leq 0.18$). A hybrid morphology consisting of spherical and cylindrical porous structures can be obtained when the $\Delta\chi$ value reaches 0.21. Further increasing the $\Delta\chi$ value to 0.25 leads to the formation of vesicle structures. Compared with 1,4-dioxane, the smaller molecular size of THF leads to enhanced microheterogeneity in the THF/H_2O mixture system, thus, all of the thin films prepared with THF solvent shows randomly porous structures, The crystallinity characterization results show that all of the prepared SnO_2 thin films consist of small crystal sizes and cassiterite phase.

For α-Fe_2O_3 thin films, PS-b-P4VP is selected as the polymer template, DMF and 1,4-dioxane are chosen as the selective solvent. Due to the strong phase separation tendency, no poor solvent like HCl or H_2O is added to the sol-gel solution to stimulate the phase separation of the PS-b-P4VP. The morphology control for the α-Fe_2O_3 thin films is realized by changing the solvent category and the template concentration. Nanocluster structures are observed in both DMF and 1,4-dioxane solvents at low template concentrations, which is due to the weak templating effect of the polymer. By increasing the template concentration, the hierarchical spherical pore structure is formed in the DMF solvent system, whereas the wormlike structure is formed in the 1,4-dioxane system, which signifies the initiation of the phase separation of the template. Due to the instability of the micellar structure at this stage, a partial fusion of the smaller spherical micelles is induced and a hierarchical structure is formed in the DMF system. The distinctly different morphologies observed in the DMF and 1,4-dioxane system can be attributed to the different preferential affinity of the solvent. Further increasing the template concentration leads to the expansion of the spherical pore structure and shrinkage of the wormlike structures. The expansion of the spherical pore structure is induced by the increased average number of polymer chains in an aggregate. In contrast, the unique interconnected wormlike structure tends to deform into a more elongated wormlike structure for accommodating more polymer chains in the monolayer geometry. Moreover, for tracking the morphology change of the thin film induced by the continuously varied selectivity of the solvent, DMF/1,4-dioxane solvent mixtures with different component ratios are prepared for the

sol-gel solution preparation. It is found that the spherical-to-wormlike porous structural transformation occurs at the critical $\Delta\chi$ value of 0.77 and the structural transformation leads to the expansion of the feature sizes and decreased ordering of the nanostructures.

The above-mentioned content involves the morphological regulation for TiO_2, SnO_2, and α-Fe_2O_3 thin films prepared via spin-coating deposition. Compared with the lab scale spin-coating deposition method, slot-die coating is a large-scale film production method, which is compatible with industrial printing facilities. Therefore, in the fourth result chapter, a fundamental understanding of the structural evolution of the PS-b-P4VP and PS-b-P4VP/$FeCl_3$ thin films during the slot-die coating process as well as the large area homogeneity of the thin films are revealed via the in situ GISAXS measurement. By properly choosing the printing temperature, large area homogeneous α-Fe_2O_3 thin films are printed out of the PS-b-P4VP/$FeCl_3$ solutions. For comparison, the pure PS-b-P4VP thin film is printed as a reference. Due to the sample stage is heated up to 90 °C prior to the printing process, the rapid evaporation of the solvent leads to a very ephemeral drying phase for both the PS-b-P4VP and PS-b-P4VP/$FeCl_3$ thin films. Totally different morphology and homogeneity are presented in the PS-b-P4VP and PS-b-P4VP/$FeCl_3$ thin films. These differences are mainly contributed by the configurations of the micelles in the solution. DLS measurement result shows that the micelles formed in the pure PS-b-P4VP solution are more stretched and therefore have a larger volume. In contrast, due to the complexation effect between the $FeCl_3$ species and the P4VP chains, the micelles formed in the PS-b-P4VP/$FeCl_3$ solution possess suppressed volume and the chains entanglement leads to the aggregation of the micelles in the solution. The high mobility of the stretched micelles in the pure PS-b-P4VP solution leads to the formation of the larger domain sizes and deteriorated homogeneity of the thin films along with the printing direction. Whereas the complexation between the P4VP and $FeCl_3$ species in the PS-b-P4VP/$FeCl_3$ solution restricted the favorable interaction between the P4VP segments and the silicon substrate and ensured the large area homogeneity of the deposited thin film. Accordingly, the thickness of the deposited PS-b-P4VP/$FeCl_3$ film is also larger than the pure PS-b-P4VP. This chapter provided detailed and comprehensive knowledge for the large area deposition of PS-b-P4VP and P4VP/$FeCl_3$ thin films, revealing the influence of the complexation effect between the P4VP and $FeCl_3$ species on the feature sizes as well as the homogeneity of the thin films.

In the fifth result chapter, quasi-isoporous and hierarchical α-Fe_2O_3 thin films are prepared to study the morphological effect of the electron transport layers on the optoelectronic properties of the perovskite solar cells. Three key factors, H_2O content, precursor content, and thermal annealing are applied for regulating the morphology of the α-Fe_2O_3 thin films. It is demonstrated that the primary structural varication caused by the $FeCl_3$

content mainly consists in the film thickness and the templating effect, the H_2O addition mainly leads to the formation of the sac-like structures, whereas the annealing post-treatment mainly leads to the formation of the dewetted hierarchical structure. Optoelectronic property test suggests that the perovskite solar cell devices prepared with hierarchical α-Fe_2O_3 electron transport modification layer show increased V_{OC} and PCE values, which can be ascribed to the enhanced light transmittance and electron extraction ability of the more bumpy hierarchical α-Fe_2O_3 electron transport modification layer.

Based on the experiments executed in the present these, further related investigations can be envisioned. For instance, the prepared TiO_2 and SnO_2 thin films in the present theses possess appropriate pore size and thicknesses, which is favorable in the applications of various kinds of solar cells. Therefore, based on the readily aviliable metal oxide thin films prepared in the present these, further modification, complexation with the second component for enhancing the conductivity of the electron transport layer or optimizing the energy level alignment of the devices can be carried out. Moreover, the unique wet chemistry method utilized in the present these is well adapted with the large area film deposition technique, which provided a large potential for the upscale fabrication of the comstom tailored functional metal oxide thin films. In another aspect, the wet chemistry method used in the present theses allows for the prepareation of various metal oxide/metal oxide composites via directly taliaing the component of the sol-gel solution, which provids various probability for exploring new functional composite thin films.

Bibliography

[1] M. Ni, M. K. Leung, D. Y. Leung, and K. Sumathy, "A review and recent developments in photocatalytic water-splitting using tio2 for hydrogen production," *Renewable and Sustainable Energy Reviews*, vol. 11, no. 3, pp. 401–425, 2007.

[2] B. Li, L. Wang, B. Kang, P. Wang, and Y. Qiu, "Review of recent progress in solid-state dye-sensitized solar cells," *Solar energy materials and solar cells*, vol. 90, no. 5, pp. 549–573, 2006.

[3] Y.-K. Jun, H.-S. Kim, J.-H. Lee, and S.-H. Hong, "Co sensing performance in micro-arc oxidized tio2 films for air quality control," *Sensors and Actuators B: Chemical*, vol. 120, no. 1, pp. 69–73, 2006.

[4] L. Fu, H. Liu, H. Zhang, C. Li, T. Zhang, Y. Wu, and H. Wu, "Novel tio2/c nanocomposites for anode materials of lithium ion batteries," *Journal of power sources*, vol. 159, no. 1, pp. 219–222, 2006.

[5] N. Yantara, D. Sabba, F. Yanan, J. M. Kadro, T. Moehl, P. P. Boix, S. Mhaisalkar, M. Grätzel, and C. Grätzel, "Loading of mesoporous titania films by ch 3 nh 3 pbi 3 perovskite, single step vs. sequential deposition," *Chemical Communications*, vol. 51, no. 22, pp. 4603–4606, 2015.

[6] A. K. Chandiran, A. Yella, M. Stefik, L.-P. Heiniger, P. Comte, M. K. Nazeeruddin, and M. Gratzel, "Low-temperature crystalline titanium dioxide by atomic layer deposition for dye-sensitized solar cells," *ACS applied materials & interfaces*, vol. 5, no. 8, pp. 3487–3493, 2013.

[7] W. Ke, G. Fang, J. Wang, P. Qin, H. Tao, H. Lei, Q. Liu, X. Dai, and X. Zhao, "Perovskite solar cell with an efficient tio2 compact film," *ACS applied materials & interfaces*, vol. 6, no. 18, pp. 15959–15965, 2014.

[8] T.-S. Su, T.-Y. Hsieh, C.-Y. Hong, and T.-C. Wei, "Electrodeposited ultrathin tio2 blocking layers for efficient perovskite solar cells," *Scientific reports*, vol. 5, no. 1, pp. 1–8, 2015.

[9] R. M. Pasquarelli, D. S. Ginley, and R. O'Hayre, "Solution processing of transparent conductors: from flask to film," *Chemical Society Reviews*, vol. 40, no. 11, pp. 5406–5441, 2011.

[10] G. Yang, C. Chen, F. Yao, Z. Chen, Q. Zhang, X. Zheng, J. Ma, H. Lei, P. Qin, L. Xiong, *et al.*, "Effective carrier-concentration tuning of sno2 quantum dot electron-selective layers for high-performance planar perovskite solar cells," *Advanced Materials*, vol. 30, no. 14, p. 1706023, 2018.

[11] F. Carn, A. Colin, M.-F. Achard, H. Deleuze, C. Sanchez, and R. Backov, "Anatase and rutile tio2 macrocellular foams: air–liquid foaming sol–gel process towards controlling cell sizes, morphologies, and topologies," *Advanced Materials*, vol. 17, no. 1, pp. 62–66, 2005.

[12] S. Y. Choi, M. Mamak, S. Speakman, N. Chopra, and G. A. Ozin, "Evolution of nanocrystallinity in periodic mesoporous anatase thin films," *Small*, vol. 1, no. 2, pp. 226–232, 2005.

[13] M. S. Doescher, J. J. Pietron, B. M. Dening, J. W. Long, C. P. Rhodes, C. A. Edmondson, and D. R. Rolison, "Using an oxide nanoarchitecture to make or break a proton wire," *Analytical chemistry*, vol. 77, no. 24, pp. 7924–7932, 2005.

[14] C. Sanchez, C. Boissiere, D. Grosso, C. Laberty, and L. Nicole, "Design, synthesis, and properties of inorganic and hybrid thin films having periodically organized nanoporosity," *Chemistry of materials*, vol. 20, no. 3, pp. 682–737, 2008.

[15] N. Chowdhury and B. Bhowmik, "Micro/nanostructured gas sensors: The physics behind the nanostructure growth, sensing and selectivity mechanisms," *Nanoscale Advances*, vol. 3, no. 1, pp. 73–93, 2021.

[16] Y.-J. Cheng, M. Wolkenhauer, G.-G. Bumbu, and J. S. Gutmann, "A facile route to reassemble titania nanoparticles into ordered chain-like networks on substrate," *Macromolecular rapid communications*, vol. 33, no. 3, pp. 218–224, 2012.

[17] Y.-J. Cheng, S. Zhou, M. Wolkenhauer, G.-G. Bumbu, S. Lenz, M. Memesa, S. Nett, S. Emmerling, W. Steffen, and J. S. Gutmann, "Morphology evolution in mesoporous titania block copolymer composite films with increasing sol–gel reaction time," *European Journal of Inorganic Chemistry*, vol. 2013, no. 7, pp. 1127–1133, 2013.

[18] Y.-J. Cheng and J. S. Gutmann, "Morphology phase diagram of ultrathin anatase tio2 films templated by a single ps-b-peo block copolymer," *Journal of the American Chemical Society*, vol. 128, no. 14, pp. 4658–4674, 2006.

[19] Y.-J. Cheng, L. Zhi, W. Steffen, and J. S. Gutmann, "Surface-supported, highly ordered macroporous crystalline tio2 thin films robust up to 1000 c," *Chemistry of Materials*, vol. 20, no. 21, pp. 6580–6582, 2008.

[20] Y.-J. Cheng, P. Müller-Buschbaum, and J. S. Gutmann, "Ultrathin anatase tio2 films with stable vesicle morphology templated by pmma-b-peo," *Small*, vol. 3, no. 8, pp. 1379–1382, 2007.

[21] K. Wang, S. Xia, W. Cao, N. Hohn, S. Grott, L. P. Kreuzer, M. Schwartzkopf, S. V. Roth, and P. Muller-Buschbaum, "Comparison of uv irradiation and sintering on mesoporous spongelike zno films prepared from ps-b-p4vp templated sol–gel synthesis," *ACS applied nano materials*, vol. 1, no. 12, pp. 7139–7148, 2018.

[22] K. Wang, V. Körstgens, D. Yang, N. Hohn, S. V. Roth, and P. Müller-Buschbaum, "Morphology control of low temperature fabricated zno nanostructures for transparent active layers in all solid-state dye-sensitized solar cells," *Journal of Materials Chemistry A*, vol. 6, no. 10, pp. 4405–4415, 2018.

[23] K. Wang, N. Hohn, L. P. Kreuzer, T. Widmann, M. Haese, J.-F. Moulin, and P. Muller-Buschbaum, "Morphology tuning of zno/p3ht/p3ht-b-peo hybrid films deposited via spray or spin coating," *ACS applied materials & interfaces*, vol. 11, no. 11, pp. 10998–11005, 2019.

[24] X. Wen, S. Wang, Y. Ding, Z. L. Wang, and S. Yang, "Controlled growth of large-area, uniform, vertically aligned arrays of α-fe2o3 nanobelts and nanowires," *The Journal of Physical Chemistry B*, vol. 109, no. 1, pp. 215–220, 2005.

[25] P. J. Flory, "Thermodynamics of high polymer solutions," *The Journal of chemical physics*, vol. 10, no. 1, pp. 51–61, 1942.

[26] M. A. Niedermeier, *Novel structuring routines of titania films for application in photovoltaics*. PhD thesis, Technische Universität München, 2013.

[27] M. D. Ward and M. J. Horner, "Structure and order in soft matter: symmetry transcending length scale," *CrystEngComm*, vol. 6, no. 67, pp. 401–407, 2004.

[28] L. Corvazier, L. Messé, C. L. Salou, R. N. Young, J. P. A. Fairclough, and A. J. Ryan, "Lamellar phases and microemulsions in model ternary blends containing amphiphilic block copolymersbasis of a presentation given at materials discussion no. 4, 11–14 september 2001, grasmere, uk.," *Journal of Materials Chemistry*, vol. 11, no. 11, pp. 2864–2874, 2001.

[29] N. Marinova, S. Valero, and J. L. Delgado, "Organic and perovskite solar cells: Working principles, materials and interfaces," *Journal of colloid and interface science*, vol. 488, pp. 373–389, 2017.

[30] F. Gao, Y. Zhao, X. Zhang, and J. You, "Recent progresses on defect passivation toward efficient perovskite solar cells," *Advanced Energy Materials*, vol. 10, no. 13, p. 1902650, 2020.

[31] W. Tress, N. Marinova, O. Inganäs, M. K. Nazeeruddin, S. M. Zakeeruddin, and M. Graetzel, "Predicting the open-circuit voltage of ch3nh3pbi3 perovskite solar cells using electroluminescence and photovoltaic quantum efficiency spectra: the role of radiative and non-radiative recombination," *Advanced Energy Materials*, vol. 5, no. 3, p. 1400812, 2015.

[32] K. K. Wong, A. Fakharuddin, P. Ehrenreich, T. Deckert, M. Abdi-Jalebi, R. H. Friend, and L. Schmidt-Mende, "Interface-dependent radiative and nonradiative recombination in perovskite solar cells," *The Journal of Physical Chemistry C*, vol. 122, no. 20, pp. 10691–10698, 2018.

[33] L. Lu, X. Han, J. Li, J. Hua, and M. Ouyang, "A review on the key issues for lithium-ion battery management in electric vehicles," *Journal of power sources*, vol. 226, pp. 272–288, 2013.

[34] A. Kudo and Y. Miseki, "Heterogeneous photocatalyst materials for water splitting," *Chemical Society Reviews*, vol. 38, no. 1, pp. 253–278, 2009.

[35] Z. Li, Y. Luan, Y. Qu, and L. Jing, "Modification strategies with inorganic acids for efficient photocatalysts by promoting the adsorption of o2," *ACS Applied Materials & Interfaces*, vol. 7, no. 41, pp. 22727–22740, 2015.

[36] C. Chen, W. Ma, and J. Zhao, "Semiconductor-mediated photodegradation of pollutants under visible-light irradiation," *Chemical Society Reviews*, vol. 39, no. 11, pp. 4206–4219, 2010.

[37] M. R. Hoffmann, S. T. Martin, W. Choi, and D. W. Bahnemann, "Environmental applications of semiconductor photocatalysis," *Chemical reviews*, vol. 95, no. 1, pp. 69–96, 1995.

[38] M. Tolan and M. Tolan, *X-ray scattering from soft-matter thin films: materials science and basic research*, vol. 148. Springer, 1999.

[39] P. Müller-Buschbaum, "Gisaxs and gisans as metrology technique for understanding the 3d morphology of block copolymer thin films," *European Polymer Journal*, vol. 81, pp. 470–493, 2016.

[40] G. Santoro and S. Yu, "Grazing incidence small angle x-ray scattering as a tool for in-situ time-resolved studies," *X-ray Scattering*, vol. 1, 2017.

[41] Y. Yoneda, "Anomalous surface reflection of x rays," *Physical review*, vol. 131, no. 5, p. 2010, 1963.

[42] Z. Jiang, "Gixsgui: a matlab toolbox for grazing-incidence x-ray scattering data visualization and reduction, and indexing of buried three-dimensional periodic nanostructured films," *Journal of Applied Crystallography*, vol. 48, no. 3, pp. 917–926, 2015.

[43] B. Inkson, "Scanning electron microscopy (sem) and transmission electron microscopy (tem) for materials characterization," in *Materials characterization using nondestructive evaluation (NDE) methods*, pp. 17–43, Elsevier, 2016.

[44] A. Hexemer and P. Müller-Buschbaum, "Advanced grazing-incidence techniques for modern soft-matter materials analysis," *IUCrJ*, vol. 2, no. 1, pp. 106–125, 2015.

[45] R. Hosemann, W. Vogel, D. Weick, and F. Balta-Calleja, "Novel aspects of the real paracrystal," *Acta Crystallographica Section A: Crystal Physics, Diffraction, Theoretical and General Crystallography*, vol. 37, no. 1, pp. 85–91, 1981.

[46] C. M. Palumbiny, *Polymeric PEDOT: PSS electrodes for organic electronics: Understanding the conductivity-structure relation*. PhD thesis, Technische Universität München, 2015.

[47] S. Tanuma, C. J. Powell, and D. R. Penn, "Calculations of electron inelastic mean free paths. v. data for 14 organic compounds over the 50–2000 ev range," *Surface and interface analysis*, vol. 21, no. 3, pp. 165–176, 1994.

[48] F. Sallusto, P. Schaerli, P. Loetscher, C. Schaniel, D. Lenig, and C. Mackay, "Qin advances in cell-based cancer immunotherapies 158 s, lanzavecchia a (1998) rapid and coordinated switch in chemokine receptor expression during dendritic cell maturation," *Eur J Immunol*, vol. 28, no. 9, pp. 2760–2769.

[49] J. C. Barnes, H. A. Sampson, and T. J. Weakley, "Structures of di-μ-hydroxobis (aquatrichlorotin (iv))-1, 4-dioxane (1/3), di-μ-hydroxobis (aquatrichlorotin (iv))-1, 8-epoxy-p-menthane (1/4), di-μ-hydroxobis (aquatribromotin (iv))-1, 8-epoxy-p-menthane (1/4), di-μ-hydroxobis (aquatrichlorotin (iv)), and cis-diaquatetrachlorotin (iv)," *Chemischer Informationsdienst*, vol. 11, no. 34, pp. no–no, 1980.

[50] A. R. Genge, W. Levason, R. Patel, G. Reid, and M. Webster, "Hydrates of tin tetrachloride," *Acta Crystallographica Section C: Crystal Structure Communications*, vol. 60, no. 4, pp. i47–i49, 2004.

[51] P. Müller-Buschbaum, "Influence of surface cleaning on dewetting of thin polystyrene films," *The European Physical Journal E*, vol. 12, no. 3, pp. 443–448, 2003.

[52] S. Costacurta, G. D. Maso, R. Gallo, M. Guglielmi, G. Brusatin, and P. Falcaro, "Influence of temperature on the photocatalytic activity of sol- gel tio2 films," *ACS applied materials & interfaces*, vol. 2, no. 5, pp. 1294–1298, 2010.

[53] S. A. Haque, E. Palomares, B. M. Cho, A. N. Green, N. Hirata, D. R. Klug, and J. R. Durrant, "Charge separation versus recombination in dye-sensitized nanocrystalline solar cells: the minimization of kinetic redundancy," *Journal of the American Chemical Society*, vol. 127, no. 10, pp. 3456–3462, 2005.

[54] Q. Luo, H. Chen, Y. Lin, H. Du, Q. Hou, F. Hao, N. Wang, Z. Guo, and J. Huang, "Discrete iron (iii) oxide nanoislands for efficient and photostable perovskite solar cells," *Advanced Functional Materials*, vol. 27, no. 34, p. 1702090, 2017.

[55] S. Yin, L. Song, S. Xia, Y. Cheng, N. Hohn, W. Chen, K. Wang, W. Cao, S. Hou, and P. Müller-Buschbaum, "Key factors for template-oriented porous titania synthesis: Solvents and catalysts," *Small Methods*, vol. 4, no. 3, p. 1900689, 2020.

[56] I. Dundar, M. Krichevskaya, A. Katerski, and I. O. Acik, "Tio2 thin films by ultrasonic spray pyrolysis as photocatalytic material for air purification," *Royal Society open science*, vol. 6, no. 2, p. 181578, 2019.

[57] A. Hagfeldt, G. Boschloo, L. Sun, L. Kloo, and H. Pettersson, "Dye-sensitized solar cells," *Chemical reviews*, vol. 110, no. 11, pp. 6595–6663, 2010.

[58] R. Terzian, N. Serpone, C. Minero, and E. Pelizzetti, "Photocatalyzed mineralization of cresols in aqueous media with irradiated titania," *Journal of Catalysis*, vol. 128, no. 2, pp. 352–365, 1991.

[59] C. Chu, J. Yang, Q. Zhang, N. Wang, F. Niu, X. Xu, J. Yang, W. Fan, and Y. Qian, "Biphase-interface enhanced sodium storage and accelerated charge transfer: flower-like anatase/bronze tio2/c as an advanced anode material for na-ion batteries," *ACS applied materials & interfaces*, vol. 9, no. 50, pp. 43648–43656, 2017.

[60] L. D. Birkefeld, A. M. Azad, and S. A. Akbar, "Carbon monoxide and hydrogen detection by anatase modification of titanium dioxide," *Journal of the American Ceramic Society*, vol. 75, no. 11, pp. 2964–2968, 1992.

[61] X. Wang, J.-Q. Meng, M. Wang, Y. Xiao, R. Liu, Y. Xia, Y. Yao, E. Metwalli, Q. Zhang, B. Qiu, *et al.*, "Facile scalable synthesis of tio2/carbon nanohybrids with ultrasmall tio2 nanoparticles homogeneously embedded in carbon matrix," *ACS applied materials & interfaces*, vol. 7, no. 43, pp. 24247–24255, 2015.

[62] N. Hohn, S. J. Schlosser, L. Bießmann, S. Grott, S. Xia, K. Wang, M. Schwartzkopf, S. V. Roth, and P. Müller-Buschbaum, "Readily available titania nanostructuring routines based on mobility and polarity controlled phase separation of an amphiphilic diblock copolymer," *Nanoscale*, vol. 10, no. 11, pp. 5325–5334, 2018.

[63] Y. Ren, L. J. Hardwick, and P. G. Bruce, "Lithium intercalation into mesoporous anatase with an ordered 3d pore structure," *Angewandte Chemie*, vol. 122, no. 14, pp. 2624–2628, 2010.

[64] J. Lee, Y. S. Jung, S. C. Warren, M. Kamperman, S. M. Oh, F. J. DiSalvo, and U. Wiesner, "Direct access to mesoporous crystalline tio2/carbon composites with large and uniform pores for use as anode materials in lithium ion batteries," *Macromolecular Chemistry and Physics*, vol. 212, no. 4, pp. 383–390, 2011.

[65] S.-M. Oh, J.-Y. Hwang, C. Yoon, J. Lu, K. Amine, I. Belharouak, and Y.-K. Sun, "High electrochemical performances of microsphere c-tio2 anode for sodium-ion battery," *ACS applied materials & interfaces*, vol. 6, no. 14, pp. 11295–11301, 2014.

[66] D. Fattakhova-Rohlfing, M. Wark, T. Brezesinski, B. M. Smarsly, and J. Rathouskỳ, "Highly organized mesoporous tio2 films with controlled crystallinity: A li-insertion study," *Advanced Functional Materials*, vol. 17, no. 1, pp. 123–132, 2007.

[67] N. Hohn, S. J. Schlosser, L. Bießmann, L. Song, S. Grott, S. Xia, K. Wang, M. Schwartzkopf, S. V. Roth, and P. Muller-Buschbaum, "Impact of catalytic additive on spray deposited and nanoporous titania thin films observed via in situ x-ray scattering: Implications for enhanced photovoltaics," *ACS applied nano materials*, vol. 1, no. 8, pp. 4227–4235, 2018.

[68] L. Song, W. Wang, V. Körstgens, D. M. González, F. C. Löhrer, C. J. Schaffer, J. Schlipf, K. Peters, T. Bein, D. Fattakhova-Rohlfing, *et al.*, "In situ study of spray deposited titania photoanodes for scalable fabrication of solid-state dye-sensitized solar cells," *Nano Energy*, vol. 40, pp. 317–326, 2017.

[69] L. Song, W. Wang, V. Körstgens, D. M. González, Y. Yao, N. K. Minar, J. M. Feckl, K. Peters, T. Bein, D. Fattakhova-Rohlfing, *et al.*, "Spray deposition of titania films with incorporated crystalline nanoparticles for all-solid-state dye-sensitized solar cells using p3ht," *Advanced Functional Materials*, vol. 26, no. 10, pp. 1498–1506, 2016.

[70] C. J. Brinker, Y. Lu, A. Sellinger, and H. Fan, "Evaporation-induced self-assembly: nanostructures made easy," *Advanced materials*, vol. 11, no. 7, pp. 579–585, 1999.

[71] J. Lee, M. C. Orilall, S. C. Warren, M. Kamperman, F. J. Disalvo, and U. Wiesner, "Direct access to thermally stable and highly crystalline mesoporous transition-metal oxides with uniform pores," *Nature materials*, vol. 7, no. 3, pp. 222–228, 2008.

[72] S. W. Robbins, P. A. Beaucage, H. Sai, K. W. Tan, J. G. Werner, J. P. Sethna, F. J. DiSalvo, S. M. Gruner, R. B. Van Dover, and U. Wiesner, "Block copolymer self-assembly–directed synthesis of mesoporous gyroidal superconductors," *Science advances*, vol. 2, no. 1, p. e1501119, 2016.

[73] T. Weller, L. Deilmann, J. Timm, T. S. Dörr, P. A. Beaucage, A. S. Cherevan, U. B. Wiesner, D. Eder, and R. Marschall, "A crystalline and 3d periodically ordered mesoporous quaternary semiconductor for photocatalytic hydrogen generation," *Nanoscale*, vol. 10, no. 7, pp. 3225–3234, 2018.

[74] G. Kaune, M. Memesa, R. Meier, M. A. Ruderer, A. Diethert, S. V. Roth, M. D'Acunzi, J. S. Gutmann, and P. Muller-Buschbaum, "Hierarchically structured titania films prepared by polymer/colloidal templating," *ACS applied materials & interfaces*, vol. 1, no. 12, pp. 2862–2869, 2009.

[75] T. S. Dörr, S. Fleischmann, M. Zeiger, I. Grobelsek, P. W. de Oliveira, and V. Presser, "Ordered mesoporous titania/carbon hybrid monoliths for lithium-ion battery anodes with high areal and volumetric capacity," *Chem.-Eur. J*, vol. 24, no. 24, pp. 6358–6363, 2018.

[76] J. Chen, Z. Hua, Y. Yan, A. A. Zakhidov, R. H. Baughman, and L. Xu, "Template synthesis of ordered arrays of mesoporous titania spheres," *Chemical communications*, vol. 46, no. 11, pp. 1872–1874, 2010.

[77] L. Kavan, J. Rathouskỳ, M. Grätzel, V. Shklover, and A. Zukal, "Surfactant-templated tio2 (anatase): Characteristic features of lithium insertion electrochemistry in organized nanostructures," *The Journal of Physical Chemistry B*, vol. 104, no. 50, pp. 12012–12020, 2000.

[78] M. G. Fischer, X. Hua, B. D. Wilts, I. Gunkel, T. M. Bennett, and U. Steiner, "Mesoporous titania microspheres with highly tunable pores as an anode material for lithium ion batteries," *ACS applied materials & interfaces*, vol. 9, no. 27, pp. 22388–22397, 2017.

[79] M. Rawolle, M. A. Niedermeier, G. Kaune, J. Perlich, P. Lellig, M. Memesa, Y.-J. Cheng, J. S. Gutmann, and P. Müller-Buschbaum, "Fabrication and characterization of nanostructured titania films with integrated function from inorganic–organic hybrid materials," *Chemical Society Reviews*, vol. 41, no. 15, pp. 5131–5142, 2012.

[80] J. H. Pan, X. Zhao, and W. I. Lee, "Block copolymer-templated synthesis of highly organized mesoporous tio2-based films and their photoelectrochemical applications," *Chemical engineering journal*, vol. 170, no. 2-3, pp. 363–380, 2011.

[81] Y. Xiao, S. You, Y. Yao, T. Zheng, C. Lin, S. V. Roth, P. Müller-Buschbaum, W. Steffen, L.-D. Sun, C.-H. Yan, *et al.*, "Generalized synthesis of mesoporous rare earth oxide thin films through amphiphilic ionic block copolymer templating," *European Journal of Inorganic Chemistry*, vol. 2013, no. 8, pp. 1251–1257, 2013.

[82] Y.-J. Cheng, S. Zhou, M. Wolkenhauer, G.-G. Bumbu, S. Lenz, M. Memesa, S. Nett, S. Emmerling, W. Steffen, S. V. Roth, *et al.*, "From spherical mesopores to worm-shaped mesopores: Morphology transition in titania–polystyrene-b-poly (ethylene oxide) composite films with increasing sol–gel reaction time," *European Journal of Inorganic Chemistry*, vol. 2014, no. 5, pp. 836–844, 2014.

[83] K. Nakanishi, "Hierarchically porous oxides, hybrids and polymers via sol-gel accompanied by phase separation," *MRS Online Proceedings Library (OPL)*, vol. 1007, 2007.

[84] M. C. Fuertes and G. J. Soler-Illia, "Processing of macroporous titania thin films: From multiscale functional porosity to nanocrystalline macroporous tio2," *Chemistry of materials*, vol. 18, no. 8, pp. 2109–2117, 2006.

[85] M. Templin, A. Franck, A. Du Chesne, H. Leist, Y. Zhang, R. Ulrich, V. Schädler, and U. Wiesner, "Organically modified aluminosilicate mesostructures from block copolymer phases," *Science*, vol. 278, no. 5344, pp. 1795–1798, 1997.

[86] T. Brezesinski, A. Fischer, K.-I. Iimura, C. Sanchez, D. Grosso, M. Antonietti, and B. M. Smarsly, "Generation of self-assembled 3d mesostructured sno2 thin films with highly crystalline frameworks," *Advanced Functional Materials*, vol. 16, no. 11, pp. 1433–1440, 2006.

[87] A. Fisher, M. Kuemmel, M. Järn, M. Linden, C. Boissière, L. Nicole, C. Sanchez, and D. Grosso, "Surface nanopatterning by organic/inorganic self-assembly and selective local functionalization," *small*, vol. 2, no. 4, pp. 569–574, 2006.

[88] C.-C. Wang and J. Y. Ying, "Sol- gel synthesis and hydrothermal processing of anatase and rutile titania nanocrystals," *Chemistry of materials*, vol. 11, no. 11, pp. 3113–3120, 1999.

[89] C. J. Brett, N. Mittal, W. Ohm, M. Gensch, L. P. Kreuzer, V. Korstgens, M. Månsson, H. Frielinghaus, P. Muller-Buschbaum, L. D. Soderberg, *et al.*, "Water-induced structural rearrangements on the nanoscale in ultrathin nanocellulose films," *Macromolecules*, vol. 52, no. 12, pp. 4721–4728, 2019.

[90] S. C. Warren, L. C. Messina, L. S. Slaughter, M. Kamperman, Q. Zhou, S. M. Gruner, F. J. DiSalvo, and U. Wiesner, "Ordered mesoporous materials from metal nanoparticle–block copolymer self-assembly," *Science*, vol. 320, no. 5884, pp. 1748–1752, 2008.

[91] B. Nandan, M. K. Vyas, M. Bohme, and M. Stamm, "Composition-dependent morphological transitions and pathways in switching of fine structure in thin films of block copolymer supramolecular assemblies," *Macromolecules*, vol. 43, no. 5, pp. 2463–2473, 2010.

[92] S. Kataoka, Y. Takeuchi, A. Kawai, M. Yamada, Y. Kamimura, and A. Endo, "Controlled formation of silica structures using siloxane/block copolymer complexes prepared in various solvent mixtures," *Langmuir*, vol. 29, no. 44, pp. 13562–13567, 2013.

[93] L. Zhang, H. Shen, and A. Eisenberg, "Phase separation behavior and crew-cut micelle formation of polystyrene-b-poly (acrylic acid) copolymers in solutions," *Macromolecules*, vol. 30, no. 4, pp. 1001–1011, 1997.

[94] T. Ghoshal, A. Chaudhari, C. Cummins, M. T. Shaw, J. D. Holmes, and M. A. Morris, "Morphological evolution of lamellar forming polystyrene-block-poly (4-vinylpyridine) copolymers under solvent annealing," *Soft Matter*, vol. 12, no. 24, pp. 5429–5437, 2016.

[95] Y. Funaki, K. Kumano, T. Nakao, H. Jinnai, H. Yoshida, K. Kimishima, K. Tsutsumi, Y. Hirokawa, and T. Hashimoto, "Influence of casting solvents on microphase-separated structures of poly (2-vinylpyridine)-block-polyisoprene," *Polymer*, vol. 40, no. 25, pp. 7147–7156, 1999.

[96] J. Hwang, C. Jo, K. Hur, J. Lim, S. Kim, and J. Lee, "Direct access to hierarchically porous inorganic oxide materials with three-dimensionally interconnected networks," *Journal of the American Chemical Society*, vol. 136, no. 45, pp. 16066–16072, 2014.

[97] Y. Mai and A. Eisenberg, "Self-assembly of block copolymers," *Chemical Society Reviews*, vol. 41, no. 18, pp. 5969–5985, 2012.

[98] G. H. Fredrickson and L. Leibler, "Theory of block copolymer solutions: nonselective good solvents," *Macromolecules*, vol. 22, no. 3, pp. 1238–1250, 1989.

[99] E. Helfand and Y. Tagami, "Theory of the interface between immiscible polymers. ii," *The Journal of chemical physics*, vol. 56, no. 7, pp. 3592–3601, 1972.

[100] P. Müller-Buschbaum, "A basic introduction to grazing incidence small-angle x-ray scattering," in *Applications of Synchrotron Light to Scattering and Diffraction in Materials and Life Sciences*, pp. 61–89, Springer, 2009.

[101] P. Müller-Buschbaum, "Grazing incidence small-angle x-ray scattering: an advanced scattering technique for the investigation of nanostructured polymer films," *Analytical and bioanalytical chemistry*, vol. 376, no. 1, pp. 3–10, 2003.

[102] T. Salditt, T. Metzger, J. Peisl, B. Reinker, M. Moske, and K. Samwer, "Determination of the height-height correlation function of rough surfaces from diffuse x-ray scattering," *EPL (Europhysics Letters)*, vol. 32, no. 4, p. 331, 1995.

[103] L. Zhang and A. Eisenberg, "Thermodynamic vs kinetic aspects in the formation and morphological transitions of crew-cut aggregates produced by self-assembly of polystyrene-b-poly (acrylic acid) block copolymers in dilute solution," *Macromolecules*, vol. 32, no. 7, pp. 2239–2249, 1999.

[104] H. Shen and A. Eisenberg, "Morphological phase diagram for a ternary system of block copolymer ps310-b-paa52/dioxane/h2o," *The Journal of Physical Chemistry B*, vol. 103, no. 44, pp. 9473–9487, 1999.

[105] O. Terreau, L. Luo, and A. Eisenberg, "Effect of poly (acrylic acid) block length distribution on polystyrene-b-poly (acrylic acid) aggregates in solution. 1. vesicles," *Langmuir*, vol. 19, no. 14, pp. 5601–5607, 2003.

[106] L. He, S. Pan, and J. Peng, "Morphology control of poly (3-hexylthiophene)-b-poly (ethylene oxide) block copolymer by solvent blending," *Journal of Polymer Science Part B: Polymer Physics*, vol. 54, no. 5, pp. 544–551, 2016.

[107] A. F. Barton, "Solubility parameters," *Chemical Reviews*, vol. 75, no. 6, pp. 731–753, 1975.

[108] Y. Li, H. Huang, T. He, and Y. Gong, "The effect of the preferential affinity of the solvent on the microstructure of solution-cast block copolymer thin films," *The Journal of Physical Chemistry B*, vol. 114, no. 3, pp. 1264–1270, 2010.

[109] C. M. Hansen, *Hansen solubility parameters: a user's handbook*. CRC press, 2007.

[110] W. Zhang, S. Chen, S. Yu, and Y. Yin, "Experimental and theoretical investigation of the ph effect on the titania phase transformation during the sol–gel process," *Journal of crystal growth*, vol. 308, no. 1, pp. 122–129, 2007.

[111] S. Yin, T. Tian, K. S. Wienhold, C. L. Weindl, R. Guo, M. Schwartzkopf, S. V. Roth, and P. Müller-Buschbaum, "Key factor study for amphiphilic block copolymer-templated mesoporous sno2 thin film synthesis: Influence of solvent and catalyst," *Advanced materials interfaces*, vol. 7, no. 18, p. 2001002, 2020.

[112] H.-X. Deng, S.-S. Li, and J. Li, "Quantum confinement effects and electronic properties of sno2 quantum wires and dots," *The Journal of Physical Chemistry C*, vol. 114, no. 11, pp. 4841–4845, 2010.

[113] Y. Luo, Y. Tang, S. Zheng, Y. Yan, H. Xue, and H. Pang, "Dual anode materials for lithium-and sodium-ion batteries," *Journal of Materials Chemistry A*, vol. 6, no. 10, pp. 4236–4259, 2018.

[114] D. Pan, N. Wan, Y. Ren, W. Zhang, X. Lu, Y. Wang, Y.-S. Hu, and Y. Bai, "Enhanced structural and electrochemical stability of self-similar rice-shaped sno2 nanoparticles," *ACS applied materials & interfaces*, vol. 9, no. 11, pp. 9747–9755, 2017.

[115] T. Ma, X. Yu, H. Li, W. Zhang, X. Cheng, W. Zhu, and X. Qiu, "High volumetric capacity of hollow structured sno2@ si nanospheres for lithium-ion batteries," *Nano letters*, vol. 17, no. 6, pp. 3959–3964, 2017.

[116] M. S. Faramarzi, A. Abnavi, S. Ghasemi, and Z. Sanaee, "Nanoribbons of sno2 as a high performance li-ion battery anode material," *Materials Research Express*, vol. 5, no. 6, p. 065040, 2018.

[117] F. Zoller, K. Peters, P. M. Zehetmaier, P. Zeller, M. Döblinger, T. Bein, Z. Sofer, and D. Fattakhova-Rohlfing, "Making ultrafast high-capacity anodes for lithium-ion batteries via antimony doping of nanosized tin oxide/graphene composites," *Advanced Functional Materials*, vol. 28, no. 23, p. 1706529, 2018.

[118] Y. Lee, M. R. Jo, K. Song, K. M. Nam, J. T. Park, and Y.-M. Kang, "Hollow sn–sno2 nanocrystal/graphite composites and their lithium storage properties," *ACS applied materials & interfaces*, vol. 4, no. 7, pp. 3459–3464, 2012.

[119] Z.-W. Zhou, Y.-T. Liu, X.-M. Xie, and X.-Y. Ye, "Constructing novel si@ sno2 core–shell heterostructures by facile self-assembly of sno2 nanowires on silicon hollow nanospheres for large, reversible lithium storage," *ACS applied materials & interfaces*, vol. 8, no. 11, pp. 7092–7100, 2016.

[120] W. Dong, J. Xu, C. Wang, Y. Lu, X. Liu, X. Wang, X. Yuan, Z. Wang, T. Lin, M. Sui, *et al.*, "A robust and conductive black tin oxide nanostructure makes efficient lithium-ion batteries possible," *Advanced Materials*, vol. 29, no. 24, p. 1700136, 2017.

[121] G. Du, Z. Guo, P. Zhang, Y. Li, M. Chen, D. Wexler, and H. Liu, "Sno 2 nanocrystals on self-organized tio 2 nanotube array as three-dimensional electrode for lithium ion microbatteries," *Journal of Materials Chemistry*, vol. 20, no. 27, pp. 5689–5694, 2010.

[122] Y. E. Roginskaya, F. K. Chibirova, T. Kulova, and A. Skundin, "Products of lithium interaction with nanostructured oxides sno 2-tio 2 and mechanism of charge-discharge of electrodes in a lithium-ion battery," *Russian Journal of Electrochemistry*, vol. 42, no. 4, pp. 355–362, 2006.

[123] B. Roose, C. M. Johansen, K. Dupraz, T. Jaouen, P. Aebi, U. Steiner, and A. Abate, "A ga-doped sno 2 mesoporous contact for uv stable highly efficient perovskite solar cells," *Journal of Materials Chemistry A*, vol. 6, no. 4, pp. 1850–1857, 2018.

[124] Y. Rui, H. Xiong, B. Su, H. Wang, Q. Zhang, J. Xu, and P. Müller-Buschbaum, "Liquid-liquid interface assisted synthesis of sno2 nanorods with tunable length for enhanced performance in dye-sensitized solar cells," *Electrochimica Acta*, vol. 227, pp. 49–60, 2017.

[125] N. Li, J. Yan, Y. Ai, E. Jiang, L. Lin, C. Shou, B. Yan, J. Sheng, and J. Ye, "A low-temperature tio 2/sno 2 electron transport layer for high-performance planar perovskite solar cells," *Science China Materials*, vol. 63, no. 2, pp. 207–215, 2020.

[126] B. Roose, J.-P. C. Baena, K. C. Gödel, M. Graetzel, A. Hagfeldt, U. Steiner, and A. Abate, "Mesoporous sno2 electron selective contact enables uv-stable perovskite solar cells," *Nano Energy*, vol. 30, pp. 517–522, 2016.

[127] A. Fakharuddin, F. Di Giacomo, I. Ahmed, Q. Wali, T. M. Brown, and R. Jose, "Role of morphology and crystallinity of nanorod and planar electron transport layers on the performance and long term durability of perovskite solar cells," *Journal of Power Sources*, vol. 283, pp. 61–67, 2015.

[128] Q. Jiang, X. Zhang, and J. You, "Sno2: a wonderful electron transport layer for perovskite solar cells," *Small*, vol. 14, no. 31, p. 1801154, 2018.

[129] X. Zhang, Y. Rui, Y. Wang, J. Xu, H. Wang, Q. Zhang, and P. Müller-Buschbaum, "Sno2 nanorod arrays with tailored area density as efficient electron transport layers for perovskite solar cells," *Journal of Power Sources*, vol. 402, pp. 460–467, 2018.

[130] Y. Chen, Q. Meng, L. Zhang, C. Han, H. Gao, Y. Zhang, and H. Yan, "Sno2-based electron transporting layer materials for perovskite solar cells: A review of recent progress," *Journal of Energy Chemistry*, vol. 35, pp. 144–167, 2019.

[131] D. Mohanta and M. Ahmaruzzaman, "Tin oxide nanostructured materials: an overview of recent developments in synthesis, modifications and potential applications. rsc adv 6: 110996–111015," 2016.

[132] Y. Gun, G. Y. Song, V. H. V. Quy, J. Heo, H. Lee, K.-S. Ahn, and S. H. Kang, "Joint effects of photoactive tio2 and fluoride-doping on sno2 inverse opal nanoarchitecture for solar water splitting," *ACS applied materials & interfaces*, vol. 7, no. 36, pp. 20292–20303, 2015.

[133] E. Brunet, T. Maier, G. C. Mutinati, S. Steinhauer, A. Köck, C. Gspan, and W. Grogger, "Comparison of the gas sensing performance of sno2 thin film and sno2 nanowire sensors," *Sensors and Actuators B: Chemical*, vol. 165, no. 1, pp. 110–118, 2012.

[134] T. Tharsika, M. Thanihaichelvan, A. Haseeb, and S. A. Akbar, "Highly sensitive and selective ethanol sensor based on zno nanorod on sno2 thin film fabricated by spray pyrolysis," *Frontiers in Materials*, vol. 6, p. 122, 2019.

[135] I. H. Kadhim, H. A. Hassan, and Q. Abdullah, "Hydrogen gas sensor based on nanocrystalline sno 2 thin film grown on bare si substrates," *Nano-micro letters*, vol. 8, no. 1, pp. 20–28, 2016.

[136] X. Xiao, L. Liu, J. Ma, Y. Ren, X. Cheng, Y. Zhu, D. Zhao, A. A. Elzatahry, A. Alghamdi, and Y. Deng, "Ordered mesoporous tin oxide semiconductors with large pores and crystallized walls for high-performance gas sensing," *ACS applied materials & interfaces*, vol. 10, no. 2, pp. 1871–1880, 2018.

[137] M. Bhuiyan, M. Hossain, T. Ueda, and T. Ikegami, "Preparation and characterization of sno2 thin film gas sensor for nox gas for environmental monitoring," in *Solid State Phenomena*, vol. 124, pp. 223–226, Trans Tech Publ, 2007.

[138] T. Oyabu, "Sensing characteristics of sno2 thin film gas sensor," *Journal of Applied Physics*, vol. 53, no. 4, pp. 2785–2787, 1982.

[139] M. Di Giulio, G. Micocci, A. Serra, A. Tepore, R. Rella, and P. Siciliano, "Sno2 thin films for gas sensor prepared by rf reactive sputtering," *Sensors and Actuators B: Chemical*, vol. 25, no. 1-3, pp. 465–468, 1995.

[140] K. Haddad, A. Abokifa, S. Kavadiya, B. Lee, S. Banerjee, B. Raman, P. Banerjee, C. Lo, J. Fortner, and P. Biswas, "Sno2 nanostructured thin films for room-temperature gas sensing of volatile organic compounds," *ACS applied materials & interfaces*, vol. 10, no. 35, pp. 29972–29981, 2018.

[141] W. S. Chi, C. S. Lee, H. Long, M. H. Oh, A. Zettl, C. Carraro, J. H. Kim, and R. Maboudian, "Direct organization of morphology-controllable mesoporous sno2 using amphiphilic graft copolymer for gas-sensing applications," *ACS applied materials & interfaces*, vol. 9, no. 42, pp. 37246–37253, 2017.

[142] S. Park, S. An, Y. Mun, and C. Lee, "Uv-enhanced no2 gas sensing properties of sno2-core/zno-shell nanowires at room temperature," *ACS applied materials & interfaces*, vol. 5, no. 10, pp. 4285–4292, 2013.

[143] J. Jeong, S.-P. Choi, C. I. Chang, D. C. Shin, J. S. Park, B. Lee, Y.-J. Park, and H.-J. Song, "Photoluminescence properties of sno2 thin films grown by thermal cvd," *Solid State Communications*, vol. 127, no. 9-10, pp. 595–597, 2003.

[144] M. A. Akhir, K. Mohamed, H. Lee, and S. A. Rezan, "Synthesis of tin oxide nanostructures using hydrothermal method and optimization of its crystal size by using statistical design of experiment," *Procedia Chemistry*, vol. 19, pp. 993–998, 2016.

[145] X. Zhou, L.-J. Wan, and Y.-G. Guo, "Binding sno2 nanocrystals in nitrogen-doped graphene sheets as anode materials for lithium-ion batteries," *Advanced materials*, vol. 25, no. 15, pp. 2152–2157, 2013.

[146] K. C. Song and J. H. Kim, "Preparation of nanosize tin oxide particles from water-in-oil microemulsions," *Journal of colloid and interface science*, vol. 212, no. 1, pp. 193–196, 1999.

[147] G. Zhang and M. Liu, "Preparation of nanostructured tin oxide using a sol-gel process based on tin tetrachloride and ethylene glycol," *Journal of materials science*, vol. 34, no. 13, pp. 3213–3219, 1999.

[148] S. M. Priya, A. Geetha, and K. Ramamurthi, "Structural, morphological and optical properties of tin oxide nanoparticles synthesized by sol–gel method adding hydrochloric acid," *Journal of Sol-Gel Science and Technology*, vol. 78, no. 2, pp. 365–372, 2016.

[149] M. Aziz, S. S. Abbas, W. R. W. Baharom, and W. Z. W. Mahmud, "Structure of sno2 nanoparticles by sol–gel method," *Materials letters*, vol. 74, pp. 62–64, 2012.

[150] M. Aziz, S. S. Abbas, and W. R. W. Baharom, "Size-controlled synthesis of sno2 nanoparticles by sol–gel method," *Materials Letters*, vol. 91, pp. 31–34, 2013.

[151] W. Luo, J. Deng, Q. Fu, D. Zhou, Y. Hu, S. Gong, and Z. Zheng, "Nanocrystalline sno2 film prepared by the aqueous sol–gel method and its application as sensing films of the resistance and saw h2s sensor," *Sensors and Actuators B: Chemical*, vol. 217, pp. 119–128, 2015.

[152] R. Dujardin, F. Delorme, B. Pintault, P. Belleville, C. Autret, I. Monot-Laffez, and F. Giovannelli, "A high yield one-pot aqueous synthesis of crystalline sno2 nanoparticles," *Materials Letters*, vol. 187, pp. 151–153, 2017.

[153] J. Zhang and L. Gao, "Synthesis and characterization of nanocrystalline tin oxide by sol–gel method," *Journal of solid state chemistry*, vol. 177, no. 4-5, pp. 1425–1430, 2004.

[154] S. Zhang, P. Zhang, Y. Wang, Y. Ma, J. Zhong, and X. Sun, "Facile fabrication of a well-ordered porous cu-doped sno2 thin film for h2s sensing," *ACS applied materials & interfaces*, vol. 6, no. 17, pp. 14975–14980, 2014.

[155] Y. Liu, E. Koep, and M. Liu, "A highly sensitive and fast-responding sno2 sensor fabricated by combustion chemical vapor deposition," *Chemistry of materials*, vol. 17, no. 15, pp. 3997–4000, 2005.

[156] A. Katoch, J.-H. Kim, Y. J. Kwon, H. W. Kim, and S. S. Kim, "Bifunctional sensing mechanism of sno2–zno composite nanofibers for drastically enhancing the sensing behavior in h2 gas," *ACS applied materials & interfaces*, vol. 7, no. 21, pp. 11351–11358, 2015.

[157] M. Dirican, Y. Lu, Y. Ge, O. Yildiz, and X. Zhang, "Carbon-confined sno2-electrodeposited porous carbon nanofiber composite as high-capacity sodium-ion battery anode material," *ACS applied materials & interfaces*, vol. 7, no. 33, pp. 18387–18396, 2015.

[158] W. Luo, T. Zhao, Y. Li, J. Wei, P. Xu, X. Li, Y. Wang, W. Zhang, A. A. Elzatahry, A. Alghamdi, *et al.*, "A micelle fusion–aggregation assembly approach to mesoporous carbon materials with rich active sites for ultrasensitive ammonia sensing," *Journal of the American Chemical Society*, vol. 138, no. 38, pp. 12586–12595, 2016.

[159] Y.-J. Cheng, S. Zhou, and J. S. Gutmann, "Morphology transition in ultrathin titania films: from pores to lamellae," *Macromolecular rapid communications*, vol. 28, no. 13, pp. 1392–1396, 2007.

[160] T. Brezesinski and A. Fischer, "K.-ichi iimura, c. sanchez, d. grosso, m. antonietti and bm smarsly, generation of self-assembled 3d mesostructured sno 2 thin films with highly crystalline frameworks," *Adv. Funct. Mater*, vol. 16, pp. 1433–1440, 2006.

[161] M. Bauer, J. Kouvetakis, and L. Groy, "Crystal structure of tin tetrabromodioxane, snbr4 · (c4h8o2), a one dimensional polymer of sn (iv)," *Zeitschrift für Kristallographie-New Crystal Structures*, vol. 217, no. 1, pp. 421–422, 2002.

[162] A. Buffet, A. Rothkirch, R. Döhrmann, V. Körstgens, M. M. Abul Kashem, J. Perlich, G. Herzog, M. Schwartzkopf, R. Gehrke, P. Müller-Buschbaum, *et al.*, "P03, the microfocus and nanofocus x-ray scattering (minaxs) beamline of the petra iii

storage ring: the microfocus endstation," *Journal of synchrotron radiation*, vol. 19, no. 4, pp. 647–653, 2012.

[163] G. Benecke, W. Wagermaier, C. Li, M. Schwartzkopf, G. Flucke, R. Hoerth, I. Zizak, M. Burghammer, E. Metwalli, P. Müller-Buschbaum, *et al.*, "A customizable software for fast reduction and analysis of large x-ray scattering data sets: applications of the new dpdak package to small-angle x-ray scattering and grazing-incidence small-angle x-ray scattering," *Journal of applied crystallography*, vol. 47, no. 5, pp. 1797–1803, 2014.

[164] J. J. van Franeker, D. Hermida-Merino, C. Gommes, K. Arapov, J. J. Michels, R. A. Janssen, and G. Portale, "Sub-micrometer structure formation during spin coating revealed by time-resolved in situ laser and x-ray scattering," *Advanced Functional Materials*, vol. 27, no. 46, p. 1702516, 2017.

[165] K. Sarkar, C. J. Schaffer, D. M. González, A. Naumann, J. Perlich, and P. Müller-Buschbaum, "Tuning the pore size of zno nano-grids via time-dependent solvent annealing," *Journal of Materials Chemistry A*, vol. 2, no. 19, pp. 6945–6951, 2014.

[166] N. S. Cameron, M. K. Corbierre, and A. Eisenberg, "1998 ewr steacie award lecture asymmetric amphiphilic block copolymers in solution: a morphological wonderland," *Canadian journal of chemistry*, vol. 77, no. 8, pp. 1311–1326, 1999.

[167] A. Kumbharkhane, Y. Joshi, S. C. Mehrotra, S. Yagihara, and S. Sudo, "Study of hydrogen bonding and thermodynamic behavior in water–1, 4-dioxane mixture using time domain reflectometry," *Physica B: Condensed Matter*, vol. 421, pp. 1–7, 2013.

[168] D. Sharma, S. Sahoo, and B. K. Mishra, "Molecular modeling in dioxane methanol interaction," *Journal of molecular modeling*, vol. 20, no. 9, pp. 1–10, 2014.

[169] A. Chaudhari, "Hydrogen bonding interaction between 1, 4-dioxane and water," *International Journal of Quantum Chemistry*, vol. 110, no. 5, pp. 1092–1099, 2010.

[170] M. J. Shultz and T. H. Vu, "Hydrogen bonding between water and tetrahydrofuran relevant to clathrate formation," *The Journal of Physical Chemistry B*, vol. 119, no. 29, pp. 9167–9172, 2015.

[171] K. Mizuno, S. Imafuji, T. Fujiwara, T. Ohta, and Y. Tamiya, "Hydration of the ch groups in 1, 4-dioxane probed by nmr and ir: Contribution of blue-shifting ch oh2 hydrogen bonds," *The Journal of Physical Chemistry B*, vol. 107, no. 16, pp. 3972–3978, 2003.

[172] T. Takamuku, A. Nakamizo, M. Tabata, K. Yoshida, T. Yamaguchi, and T. Otomo, "Large-angle x-ray scattering, small-angle neutron scattering, and nmr relaxation studies on mixing states of 1, 4-dioxane-water, 1, 3-dioxane-water, and tetrahydrofuran-water mixtures," *Journal of molecular liquids*, vol. 103, pp. 143–159, 2003.

[173] S. Yin, W. Cao, Q. Ji, Y. Cheng, L. Song, N. Li, C. L. Weindl, M. Schwartzkopf, S. V. Roth, and P. Müller-Buschbaum, "Multidimensional morphology control for ps-b-p4vp templated mesoporous iron (iii) oxide thin films," *Advanced Materials Interfaces*, p. 2100141, 2021.

[174] I. Barandiaran and G. Kortaberria, "Synthesis and characterization of nanostructured ps-b-p4vp/fe 2 o 3 thin films with magnetic properties prepared by solvent vapor annealing," *RSC advances*, vol. 5, no. 116, pp. 95840–95846, 2015.

[175] B.-H. Sohn, J.-M. Choi, S. I. Yoo, S.-H. Yun, W.-C. Zin, J. C. Jung, M. Kanehara, T. Hirata, and T. Teranishi, "Directed self-assembly of two kinds of nanoparticles utilizing monolayer films of diblock copolymer micelles," *Journal of the American Chemical Society*, vol. 125, no. 21, pp. 6368–6369, 2003.

[176] H. G. Cha, J. Song, H. S. Kim, W. Shin, K. B. Yoon, and Y. S. Kang, "Facile preparation of fe 2 o 3 thin film with photoelectrochemical properties," *Chemical Communications*, vol. 47, no. 8, pp. 2441–2443, 2011.

[177] S. Hou, P. Wang, Y. Li, F. Pang, M. Liu, Y. Luo, L. Zhuang, and L. Zhao, "Podocarpus-like -fe2o3/tio2 composite with balsam pear texture for enhanced lithium storage," *Applied Surface Science*, vol. 476, pp. 959–965, 2019.

[178] C. G. Hardy, L. Ren, S. Ma, and C. Tang, "Self-assembly of well-defined ferrocene triblock copolymers and their template synthesis of ordered iron oxide nanoparticles," *Chemical Communications*, vol. 49, no. 39, pp. 4373–4375, 2013.

[179] X. Hu, J. C. Yu, J. Gong, Q. Li, and G. Li, "α-fe2o3 nanorings prepared by a microwave-assisted hydrothermal process and their sensing properties," *Advanced Materials*, vol. 19, no. 17, pp. 2324–2329, 2007.

[180] D. Lei, M. Zhang, B. Qu, L. Chen, Y. Wang, E. Zhang, Z. Xu, Q. Li, and T. Wang, "α-fe 2 o 3 nanowall arrays: hydrothermal preparation, growth mechanism and excellent rate performances for lithium ion batteries," *Nanoscale*, vol. 4, no. 11, pp. 3422–3426, 2012.

[181] Z. Li, Y. Mao, Q. Tian, W. Zhang, and L. Yang, "Extremely facile preparation of high-performance fe2o3 anode for lithium-ion batteries," *Journal of Alloys and Compounds*, vol. 784, pp. 125–133, 2019.

[182] Y. Liu, Y.-X. Yu, and W.-D. Zhang, "Photoelectrochemical study on charge transfer properties of nanostructured fe2o3 modified by g-c3n4," *International journal of hydrogen energy*, vol. 39, no. 17, pp. 9105–9113, 2014.

[183] A. M. Jubb and H. C. Allen, "Vibrational spectroscopic characterization of hematite, maghemite, and magnetite thin films produced by vapor deposition," *ACS Applied Materials & Interfaces*, vol. 2, no. 10, pp. 2804–2812, 2010.

[184] W. Hu, T. Liu, X. Yin, H. Liu, X. Zhao, S. Luo, Y. Guo, Z. Yao, J. Wang, N. Wang, *et al.*, "Hematite electron-transporting layers for environmentally stable planar perovskite solar cells with enhanced energy conversion and lower hysteresis," *Journal of Materials Chemistry A*, vol. 5, no. 4, pp. 1434–1441, 2017.

[185] M. Shahpari, A. Behjat, M. Khajaminian, and N. Torabi, "The influence of morphology of hematite (α-fe2o3) counter electrodes on the efficiency of dye-sensitized solar cells," *Solar Energy*, vol. 119, pp. 45–53, 2015.

[186] A. Manikandan, A. Saravanan, S. A. Antony, and M. Bououdina, "One-pot low temperature synthesis and characterization studies of nanocrystalline α-fe2o3 based dye sensitized solar cells," *Journal of nanoscience and nanotechnology*, vol. 15, no. 6, pp. 4358–4366, 2015.

[187] Y. Jiang, D. Zhang, Y. Li, T. Yuan, N. Bahlawane, C. Liang, W. Sun, Y. Lu, and M. Yan, "Amorphous fe2o3 as a high-capacity, high-rate and long-life anode material for lithium ion batteries," *Nano Energy*, vol. 4, pp. 23–30, 2014.

[188] T. Jiang, F. Bu, X. Feng, I. Shakir, G. Hao, and Y. Xu, "Porous fe2o3 nanoframeworks encapsulated within three-dimensional graphene as high-performance flexible anode for lithium-ion battery," *ACS nano*, vol. 11, no. 5, pp. 5140–5147, 2017.

[189] S. Li, Y. Zhang, and J. Huang, "Three-dimensional tio2 nanotubes immobilized with fe2o3 nanoparticles as an anode material for lithium-ion batteries," *Journal of Alloys and Compounds*, vol. 783, pp. 793–800, 2019.

[190] K. Fan, J. Guo, L. Cha, Q. Chen, and J. Ma, "Atomic layer deposition of zno onto fe2o3 nanoplates for enhanced h2s sensing," *Journal of Alloys and Compounds*, vol. 698, pp. 336–340, 2017.

[191] S. S. Sangale, V. V. Jadhav, S. F. Shaikh, P. V. Shinde, B. G. Ghule, S. D. Raut, M. S. Tamboli, A. M. Al-Enizi, and R. S. Mane, "Facile one-step hydrothermal synthesis and room-temperature no2 sensing application of α-fe2o3 sensor," *Materials Chemistry and Physics*, vol. 246, p. 122799, 2020.

[192] S.-H. Yun, B.-H. Sohn, J. C. Jung, W.-C. Zin, J.-K. Lee, and O. Song, "Tunable magnetic arrangement of iron oxide nanoparticles in situ synthesized on the solid substrate from diblock copolymer micelles," *Langmuir*, vol. 21, no. 14, pp. 6548–6552, 2005.

[193] Y. Yin, J. Zhao, L. Qin, Y. Yang, and L. He, "Synthesis of an ordered nanoporous fe 2 o 3/au film for application in ascorbic acid detection," *RSC advances*, vol. 6, no. 68, pp. 63358–63364, 2016.

[194] C. Zhang, J. Li, A. Belianinov, Z. Ma, C. K. Renshaw, and R. M. Gelfand, "Nanoaperture fabrication in ultra-smooth single-grain gold films with helium ion beam lithography," *Nanotechnology*, vol. 31, no. 46, p. 465302, 2020.

[195] T. Tamai, N. Ichinose, S. Kawanishi, M. Nishii, T. Sasuga, I. Hashida, and K. Mizuno, "Patterning of sno2 thin films by combination of lithographic photoir-radiation and pyrolysis of an organotin polymer," *Chemistry of materials*, vol. 9, no. 12, pp. 2674–2675, 1997.

[196] M. Domonkos, P. Demo, and A. Kromka, "Nanosphere lithography for structuring polycrystalline diamond films," *Crystals*, vol. 10, no. 2, p. 118, 2020.

[197] S. Park, B. Kim, O. Yavuzcetin, M. T. Tuominen, and T. P. Russell, "Ordering of ps-b-p4vp on patterned silicon surfaces," *ACS nano*, vol. 2, no. 7, pp. 1363–1370, 2008.

[198] J. P. Spatz, S. Mössmer, C. Hartmann, M. Möller, T. Herzog, M. Krieger, H.-G. Boyen, P. Ziemann, and B. Kabius, "Ordered deposition of inorganic clusters from micellar block copolymer films," *Langmuir*, vol. 16, no. 2, pp. 407–415, 2000.

[199] A. Rahikkala, A. J. Soininen, J. Ruokolainen, R. Mezzenga, J. Raula, and E. I. Kauppinen, "Self-assembly of ps-b-p4vp block copolymers of varying architectures in aerosol nanospheres," *Soft Matter*, vol. 9, no. 5, pp. 1492–1499, 2013.

[200] M. Abul Kashem, J. Perlich, L. Schulz, S. Roth, W. Petry, and P. Müller-Buschbaum, "Maghemite nanoparticles on supported diblock copolymer nanostructures," *Macromolecules*, vol. 40, no. 14, pp. 5075–5083, 2007.

[201] Y. Yao, E. Metwalli, M. A. Niedermeier, M. Opel, C. Lin, J. Ning, J. Perlich, S. V. Roth, and P. Muller-Buschbaum, "Nano-and microstructures of magnetic field-guided maghemite nanoparticles in diblock copolymer films," *ACS applied materials & interfaces*, vol. 6, no. 7, pp. 5244–5254, 2014.

[202] S. Zou, R. Hong, T. Emrick, and G. C. Walker, "Ordered cdse nanoparticles within self-assembled block copolymer domains on surfaces," *Langmuir*, vol. 23, no. 4, pp. 1612–1614, 2007.

[203] L. Zhang and A. Eisenberg, "Formation of crew-cut aggregates of various morphologies from amphiphilic block copolymers in solution," *Polymers for Advanced Technologies*, vol. 9, no. 10-11, pp. 677–699, 1998.

[204] L. Zhang, K. Yu, and A. Eisenberg, "Ion-induced morphological changes in "crew-cut" aggregates of amphiphilic block copolymers," *Science*, vol. 272, no. 5269, pp. 1777–1779, 1996.

[205] Y. Chen, W. Zhao, and J. Zhang, "Preparation of 4-vinylpyridine (4vp) resin and its adsorption performance for heavy metal ions," *RSC advances*, vol. 7, no. 8, pp. 4226–4236, 2017.

[206] T. Ahmad, A. Ganguly, J. Ahmed, A. K. Ganguli, and O. A. A. Alhartomy, "Nanorods of transition metal oxalates: A versatile route to the oxide nanoparticles," *Arabian Journal of Chemistry*, vol. 4, no. 2, pp. 125–134, 2011.

[207] L. Wang, X. Lu, C. Han, R. Lu, S. Yang, and X. Song, "Electrospun hollow cage-like α-fe 2 o 3 microspheres: synthesis, formation mechanism, and morphology-preserved conversion to fe nanostructures," *CrystEngComm*, vol. 16, no. 46, pp. 10618–10623, 2014.

[208] Y. Yan, H. Tang, F. Wu, R. Wang, and M. Pan, "One-step self-assembly synthesis α-fe2o3 with carbon-coated nanoparticles for stabilized and enhanced supercapacitors electrode," *Energies*, vol. 10, no. 9, p. 1296, 2017.

[209] X.-F. Lu, X.-Y. Chen, W. Zhou, Y.-X. Tong, and G.-R. Li, "α-fe2o3@ pani core–shell nanowire arrays as negative electrodes for asymmetric supercapacitors," *ACS applied materials & interfaces*, vol. 7, no. 27, pp. 14843–14850, 2015.

[210] S. Bakaul, W. Lin, and T. Wu, "Evolution of magnetic bubble domains in manganite films," *Applied Physics Letters*, vol. 99, no. 4, p. 042503, 2011.

[211] B. Ziberi, F. Frost, T. Höche, and B. Rauschenbach, "Ripple pattern formation on silicon surfaces by low-energy ion-beam erosion: Experiment and theory," *Physical Review B*, vol. 72, no. 23, p. 235310, 2005.

[212] K. Wang, L. Bießmann, M. Schwartzkopf, S. V. Roth, and P. Muller-Buschbaum, "Tuning of the morphology and optoelectronic properties of zno/p3ht/p3ht-b-peo hybrid films via spray deposition method," *ACS applied materials & interfaces*, vol. 10, no. 24, pp. 20569–20577, 2018.

[213] S. Park, D. H. Lee, J. Xu, B. Kim, S. W. Hong, U. Jeong, T. Xu, and T. P. Russell, "Macroscopic 10-terabit–per–square-inch arrays from block copolymers with lateral order," *Science*, vol. 323, no. 5917, pp. 1030–1033, 2009.

[214] R. Hosemann and S. Bagchi, "The interference theory of ideal paracrystals," *Acta Crystallographica*, vol. 5, no. 5, pp. 612–614, 1952.

[215] G. Santoro, A. Buffet, R. Döhrmann, S. Yu, V. Körstgens, P. Müller-Buschbaum, U. Gedde, M. Hedenqvist, and S. Roth, "Use of intermediate focus for grazing incidence small and wide angle x-ray scattering experiments at the beamline p03 of petra iii, desy," *Review of Scientific Instruments*, vol. 85, no. 4, p. 043901, 2014.

[216] S. O'Driscoll, G. Demirel, R. A. Farrell, T. G. Fitzgerald, C. O'Mahony, J. D. Holmes, and M. A. Morris, "The morphology and structure of ps-b-p4vp block copolymer films by solvent annealing: effect of the solvent parameter," *Polymers for Advanced Technologies*, vol. 22, no. 6, pp. 915–923, 2011.

[217] Y. Yu, L. Zhang, and A. Eisenberg, "Morphogenic effect of solvent on crew-cut aggregates of apmphiphilic diblock copolymers," *Macromolecules*, vol. 31, no. 4, pp. 1144–1154, 1998.

[218] B. Jiang, B. Wang, L. Zhang, Y. Sun, X. Xiao, N. Yang, and H. Dou, "Preparation of poly (l-lactic acid) membrane from solvent mixture via immersion precipitation," *Separation Science and Technology*, vol. 51, no. 18, pp. 2940–2947, 2016.

[219] S. Yin, T. Tian, C. L. Weindl, K. S. Wienhold, Q. Ji, Y. Cheng, Y. Li, C. M. Papadakis, M. Schwartzkopf, S. V. Roth, *et al.*, "In situ gisaxs observation and large area homogeneity study of slot-die printed ps-b-p4vp and ps-b-p4vp/fecl3 thin films," *ACS Applied Materials & Interfaces*, 2022.

[220] M. Congiu, M. L. De Marco, M. Bonomo, O. Nunes-Neto, D. Dini, and C. F. Graeff, "Pristine and al-doped hematite printed films as photoanodes of p-type dye-sensitized solar cells," *Journal of Nanoparticle Research*, vol. 19, no. 1, p. 7, 2017.

[221] W. Zhu, Q. Zhang, C. Zhang, D. Chen, L. Zhou, Z. Lin, J. Chang, J. Zhang, and Y. Hao, "A non-equilibrium ti 4+ doping strategy for an efficient hematite electron transport layer in perovskite solar cells," *Dalton Transactions*, vol. 47, no. 18, pp. 6404–6411, 2018.

[222] Y. Yang, X. Fan, G. Casillas, Z. Peng, G. Ruan, G. Wang, M. J. Yacaman, and J. M. Tour, "Three-dimensional nanoporous fe2o3/fe3c-graphene heterogeneous thin films for lithium-ion batteries," *ACS nano*, vol. 8, no. 4, pp. 3939–3946, 2014.

[223] O. Tan, W. Zhu, Q. Yan, and L. Kong, "Size effect and gas sensing characteristics of nanocrystalline xsno2-(1- x) α-fe2o3 ethanol sensors," *Sensors and Actuators B: Chemical*, vol. 65, no. 1-3, pp. 361–365, 2000.

[224] S. Leonardi, A. Mirzaei, A. Bonavita, S. Santangelo, P. Frontera, F. Pantò, P. Antonucci, and G. Neri, "A comparison of the ethanol sensing properties of α-iron oxide nanostructures prepared via the sol–gel and electrospinning techniques," *Nanotechnology*, vol. 27, no. 7, p. 075502, 2016.

[225] R. Tongpool and S. Jindasuwan, "Sol–gel processed iron oxide–silica nanocomposite films as room-temperature humidity sensors," *Sensors and Actuators B: Chemical*, vol. 106, no. 2, pp. 523–528, 2005.

[226] H.-T. Sun, C. Cantalini, M. Faccio, and M. Pelino, "No2 gas sensitivity of sol-gel-derived α-fe2o3 thin films," *Thin Solid Films*, vol. 269, no. 1-2, pp. 97–101, 1995.

[227] M. Hjiri, M. S. Aida, and G. Neri, "No2 selective sensor based on α-fe2o3 nanoparticles synthesized via hydrothermal technique," *Sensors*, vol. 19, no. 1, p. 167, 2019.

[228] Y. Li, N. Guijarro, X. Zhang, M. S. Prevot, X. A. Jeanbourquin, K. Sivula, H. Chen, and Y. Li, "Templating sol–gel hematite films with sacrificial copper oxide: Enhancing photoanode performance with nanostructure and oxygen vacancies," *ACS applied materials & interfaces*, vol. 7, no. 31, pp. 16999–17007, 2015.

[229] X. Lian, X. Yang, S. Liu, Y. Xu, C. Jiang, J. Chen, and R. Wang, "Enhanced photoelectrochemical performance of ti-doped hematite thin films prepared by the sol–gel method," *Applied surface science*, vol. 258, no. 7, pp. 2307–2311, 2012.

[230] Y. Hida and H. Kozuka, "Photoanodic properties of sol–gel-derived iron oxide thin films with embedded gold nanoparticles: effects of polyvinylpyrrolidone in coating solutions," *Thin Solid Films*, vol. 476, no. 2, pp. 264–271, 2005.

[231] O. Akhavan, "Thickness dependent activity of nanostructured tio2/α-fe2o3 photocatalyst thin films," *Applied Surface Science*, vol. 257, no. 5, pp. 1724–1728, 2010.

[232] X.-M. Song, X. Zhou, C. Yuan, Y. Zhang, Q. Tong, Y. Li, L. Cui, D. Liu, and W. Zhang, "One-dimensional fe2o3/tio2 photoelectrode and investigation of its photoelectric properties in photoelectrochemical cell," *Applied Surface Science*, vol. 397, pp. 112–118, 2017.

[233] S. Somekawa, Y. Kusumoto, M. Abdulla-Al-Mamun, M. Muruganandham, and Y. Horie, "Wet-type fe2o3 solar cells based on fe2o3 films prepared by laser ablation: Drastic temperature effect," *Electrochemistry communications*, vol. 11, no. 11, pp. 2150–2152, 2009.

[234] Z. N. Kayani, E. S. Khan, F. Saleemi, S. Riaz, and S. Naseem, "Growth and characterization of iron oxide nanocrystalline thin films via sol-gel dip coating method," *IEEE Transactions on Magnetics*, vol. 50, no. 8, pp. 1–4, 2014.

[235] B. Wang, Y. Song, and H. Cui, "Sol–gel preparation of highly transparent α-fe 2 o 3 film for the application in red color filter," *Journal of sol-gel science and technology*, vol. 57, no. 1, pp. 20–23, 2011.

[236] S. Reda, "Synthesis of zno and fe2o3 nanoparticles by sol–gel method and their application in dye-sensitized solar cells," *Materials Science in Semiconductor Processing*, vol. 13, no. 5-6, pp. 417–425, 2010.

[237] H. Zhou, A. Mito, D. Kundu, and I. Honma, "Nonlinear optical susceptibility of fe2o3 thin film synthesized by a modified sol-gel method," *Journal of Sol-Gel Science and Technology*, vol. 19, no. 1, pp. 539–541, 2000.

[238] C. Aydın, S. A. Mansour, Z. Alahmed, and F. Yakuphanoglu, "Structural and optical characterization of sol–gel derived boron doped fe 2 o 3 nanostructured films," *Journal of sol-gel science and technology*, vol. 62, no. 3, pp. 397–403, 2012.

[239] S. Xia, L. Song, N. Hohn, K. Wang, S. Grott, M. Opel, M. Schwartzkopf, S. V. Roth, and P. Müller-Buschbaum, "Spray-coating magnetic thin hybrid films of ps-b-pnipam and magnetite nanoparticles," *Advanced functional materials*, vol. 29, no. 15, p. 1808427, 2019.

[240] S. Xia, E. Metwalli, M. Opel, P. A. Staniec, E. M. Herzig, and P. Muller-Buschbaum, "Printed thin magnetic films based on diblock copolymer and magnetic nanoparticles," *ACS applied materials & interfaces*, vol. 10, no. 3, pp. 2982–2991, 2018.

[241] J. Jang and J. Bae, "Fabrication of mesoporous polymer/silica hybrid using surfactant-mediated sol–gel method," *Journal of non-crystalline solids*, vol. 352, no. 38-39, pp. 3979–3984, 2006.

[242] H. T. Nguyen, T. T. T. Tran, and N. U. Nguyen-Thai, "Preparation of polydisperse polystyrene-block-poly (4-vinyl pyridine) synthesized by tempo-mediated radical polymerization and the facile nanostructure formation by self-assembly," *Journal of Nanostructure in Chemistry*, vol. 8, no. 1, pp. 61–69, 2018.

[243] J.-J. Kang, K. Shehu, C. Sachse, F. A. Jung, C.-H. Ko, L. C. Barnsley, R. Jordan, and C. M. Papadakis, "A molecular brush with thermoresponsive poly (2-ethyl-2-oxazoline) side chains: a structural investigation," *Colloid and Polymer Science*, vol. 299, no. 2, pp. 193–203, 2021.

[244] I. Kudose, K. Arai, and T. Kotaka, "Morphology and viscoelastic properties of quarternized poly (styrene-b-butadiene-b-4-vinylpyridine) three-block polymers," *Polymer journal*, vol. 16, no. 3, pp. 241–247, 1984.

[245] E. B. Gowd, M. Böhme, and M. Stamm, "In situ gisaxs study on solvent vapour induced orientation switching in ps-b-p4vp block copolymer thin films," in *IOP Conference Series: Materials Science and Engineering*, vol. 14, p. 012015, IOP Publishing, 2010.

[246] S. Yin, L. Song, S. Xia, Y. Cheng, N. Hohn, W. Chen, K. Wang, W. Cao, S. Hou, and P. Müller-Buschbaum, "Key factors for template-oriented porous titania synthesis: Solvents and catalysts," *Small Methods*, vol. 4, no. 3, p. 1900689, 2020.

[247] V. Luthra, K. F. Pratt, I. P. Parkin, D. E. Williams, and R. Tandon, "Fabrication and characterization of fe1. 90ti0. 10o3 gas sensitive resistors for carbon monoxide," *Sensors and Actuators B: Chemical*, vol. 135, no. 2, pp. 430–435, 2009.

[248] W. Voit, W. Zapka, L. Belova, and K. Rao, "Application of inkjet technology for the deposition of magnetic nanoparticles to form micron-scale structures," *IEE Proceedings-Science, Measurement and Technology*, vol. 150, no. 5, pp. 252–256, 2003.

[249] D. Yang, S. Grott, X. Jiang, K. S. Wienhold, M. Schwartzkopf, S. V. Roth, and P. Müller-Buschbaum, "In situ studies of solvent additive effects on the morphology development during printing of bulk heterojunction films for organic solar cells," *Small methods*, vol. 4, no. 9, p. 2000418, 2020.

[250] G. Renaud, R. Lazzari, and F. Leroy, "Probing surface and interface morphology with grazing incidence small angle x-ray scattering," *Surface Science Reports*, vol. 64, no. 8, pp. 255–380, 2009.

[251] A. Gibaud, A. Baptiste, D. Doshi, C. Brinker, L. Yang, and B. Ocko, "Wall thickness and core radius determination in surfactant templated silica thin films using gisaxs and x-ray reflectivity," *EPL (Europhysics Letters)*, vol. 63, no. 6, p. 833, 2003.

[252] N. Li, L. Song, L. Bießmann, S. Xia, W. Ohm, C. J. Brett, E. Hadjixenophontos, G. Schmitz, S. V. Roth, and P. Müller-Buschbaum, "Morphology phase diagram of slot-die printed tio2 films based on sol–gel synthesis," *Advanced materials interfaces*, vol. 6, no. 12, p. 1900558, 2019.

[253] K. S. Wienhold, C. L. Weindl, S. Yin, T. Tian, M. Schwartzkopf, A. Rothkirch, S. V. Roth, and P. Muller-Buschbaum, "Following in situ the evolution of morphology and optical properties during printing of thin films for application in non-fullerene acceptor based organic solar cells," *ACS applied materials & interfaces*, vol. 12, no. 36, pp. 40381–40392, 2020.

[254] J. Jakeš, "Regularized positive exponential sum (repes) program-a way of inverting laplace transform data obtained by dynamic light scattering," *Collection of Czechoslovak chemical communications*, vol. 60, no. 11, pp. 1781–1797, 1995.

[255] Z. Wu, M. Cai, J. Cao, J. Zhang, and X. Luo, "Effects of copolymer component on the properties of phosphorylcholine micelles," *International journal of nanomedicine*, vol. 12, p. 487, 2017.

[256] X. Ye, H. Niroomand, S. Hu, and B. Khomami, "Block copolymer micelle formation in a solvent good for all the blocks," *Colloid and Polymer Science*, vol. 293, no. 10, pp. 2799–2805, 2015.

[257] B. Sohn and B. Seo, "Fabrication of the multilayered nanostructure of alternating polymers and gold nanoparticles with thin films of self-assembling diblock copolymers," *Chemistry of materials*, vol. 13, no. 5, pp. 1752–1757, 2001.

[258] A. Buffet, M. M. Abul Kashem, J. Perlich, G. Herzog, M. Schwartzkopf, R. Gehrke, and S. V. Roth, "Stripe-like pattern formation in airbrush-spray deposition of colloidal polymer film," *Advanced Engineering Materials*, vol. 12, no. 12, pp. 1235–1239, 2010.

[259] E. B. Gowd, T. Koga, M. K. Endoh, K. Kumar, and M. Stamm, "Pathways of cylindrical orientations in ps-b-p4vp diblock copolymer thin films upon solvent vapor annealing," *Soft Matter*, vol. 10, no. 39, pp. 7753–7761, 2014.

[260] G. Freychet, M. Maret, M. Fernandez-Regulez, R. Tiron, A. Gharbi, C. Nicolet, and P. Gergaud, "Morphology of poly (lactide)-block-poly (dimethylsiloxane)-block-polylactide high-χ triblock copolymer film studied by grazing incidence small-angle x-ray scattering," *Journal of Polymer Science*, vol. 58, no. 15, pp. 2041–2050, 2020.

[261] H. Ogawa, M. Takenaka, T. Miyazaki, A. Fujiwara, B. Lee, K. Shimokita, E. Nishibori, and M. Takata, "Direct observation on spin-coating process of ps-b-p2vp thin films," *Macromolecules*, vol. 49, no. 9, pp. 3471–3477, 2016.

[262] B. Du, X. Chen, B. Zhao, A. Mei, Q. Wang, J. Xu, and Z. Fan, "Interfacial entrapment of noble metal nanoparticles and nanorods capped with amphiphilic multiblock copolymer at a selective liquid–liquid interface," *Nanoscale*, vol. 2, no. 9, pp. 1684–1689, 2010.

[263] M. Hildebrandt, E.-y. Shin, S. Yang, W. Ali, S. Altinpinar, and J. S. Gutmann, "Investigation of roughness correlation in polymer brushes via x-ray scattering," *Polymers*, vol. 12, no. 9, p. 2101, 2020.

[264] M. Schwartzkopf, S.-J. Wöhnert, V. Waclawek, N. Carstens, A. Rothkirch, J. Rubeck, M. Gensch, J. Drewes, O. Polonskyi, T. Strunskus, *et al.*, "Real-time insight into nanostructure evolution during the rapid formation of ultra-thin gold layers on polymers," *Nanoscale horizons*, vol. 6, no. 2, pp. 132–138, 2021.

[265] J. Wang, J. Su, and L. Guo, "Controlled aqueous growth of hematite nanoplate arrays directly on transparent conductive substrates and their photoelectrochemical properties," *Chemistry–An Asian Journal*, vol. 11, no. 16, pp. 2328–2334, 2016.

[266] J. Pena, J. M. González-Calbet, and M. Vallet-Regí, "Fe2o3 thin films by the spray pyrolysis technique," in *Materials science forum*, vol. 269, pp. 313–318, Trans Tech Publ, 1998.

[267] M. Sharmin and J. Podder, "Influence of al doping on the structure and properties of fe2o3 thin films: high transparency, wide band gap, ferromagnetic behavior," *Semiconductor Science and Technology*, vol. 34, no. 7, p. 075033, 2019.

[268] H. Tai, Y. Jiang, C. Duan, W. Dan, and X. Li, "Development of a novel formaldehyde otft sensor based on p3ht/fe2o3 nanocomposite thin film," *Integrated Ferroelectrics*, vol. 144, no. 1, pp. 15–21, 2013.

[269] Y. Tembhurkar, "Structural and optical properties of spray pyrolytically prepared fe 2 o 3 thin films," *Bulletin of Materials Science*, vol. 19, no. 1, pp. 155–159, 1996.

[270] V. Balouria, A. Singh, N. S. Ramgir, A. Debnath, A. Mahajan, R. Bedi, D. Aswal, and S. Gupta, "Enhanced h 2 s response of au modified fe 2 o 3 thin films," in *AIP Conference Proceedings*, vol. 1512, pp. 782–783, American Institute of Physics, 2013.

[271] V. Balouria, N. S. Ramgir, A. Singh, A. Debnath, A. Mahajan, R. Bedi, D. Aswal, and S. Gupta, "Enhanced h2s sensing characteristics of au modified fe2o3 thin films," *Sensors and Actuators B: Chemical*, vol. 219, pp. 125–132, 2015.

[272] C. Chai, J. Peng, and B. Yan, "Preparation and gas-sensing properties of α-fe 2 o 3 thin films," *Journal of electronic materials*, vol. 24, no. 7, pp. 799–804, 1995.

[273] A. A. Tahir, M. Mat-Teridi, and K. U. Wijayantha, "Photoelectrochemical properties of texture-controlled nanostructured α-fe2o3 thin films prepared by aacvd," *physica status solidi (RRL)–Rapid Research Letters*, vol. 8, no. 12, pp. 976–981, 2014.

[274] H. Zhang, D. M. Marincel, S. Trolier-McKinstry, W. M. Rainforth, and I. M. Reaney, "Coherent growth of α-fe2o3 in ti and nd co-doped bifeo3 thin films," *Materials Research Letters*, vol. 4, no. 3, pp. 168–173, 2016.

[275] M. T. Johnson and C. B. Carter, "Thin-film reaction between α-fe2o3 and (001) mgo," *Microscopy and Microanalysis*, vol. 4, no. 2, pp. 141–145, 1998.

[276] Z. Jiao, S. Wang, L. Bian, and J. Liu, "Stability of sno2/fe2o3 multilayer thin film gas sensor," *Materials research bulletin*, vol. 35, no. 5, pp. 741–745, 2000.

[277] U. Khan, A. Akbar, H. Yousaf, S. Riaz, and S. Naseem, "Ferromagnetic properties of al-doped fe2o3 thin films by sol-gel," *Materials Today: Proceedings*, vol. 2, no. 10, pp. 5415–5420, 2015.

[278] R. K. Sonker and B. Yadav, "Low temperature study of nanostructured fe2o3 thin films as no2 sensor," *Materials Today: Proceedings*, vol. 3, no. 6, pp. 2315–2320, 2016.

[279] S. N. Khatavkar and S. D. Sartale, "α-fe2o3 thin film on stainless steel mesh: A flexible electrode for supercapacitor," *Materials Chemistry and Physics*, vol. 225, pp. 284–291, 2019.

[280] G. Neri, A. Bonavita, G. Rizzo, S. Galvagno, S. Capone, and P. Siciliano, "Methanol gas-sensing properties of ceo2–fe2o3 thin films," *Sensors and Actuators B: Chemical*, vol. 114, no. 2, pp. 687–695, 2006.

[281] Y. Liu, Y.-X. Yu, and W.-D. Zhang, "Photoelectrochemical properties of ni-doped fe2o3 thin films prepared by electrodeposition," *Electrochimica acta*, vol. 59, pp. 121–127, 2012.

[282] B. Lokhande, R. Ambare, and S. Bharadwaj, "Thermal optimization and super-capacitive application of electrodeposited fe2o3 thin films," *Measurement*, vol. 47, pp. 427–432, 2014.

[283] M. Gomi and H. Toyoshima, "Heteroepitaxial growth of α-fe 2o 3 thin films on (111) ggg," *Japanese journal of applied physics*, vol. 35, no. 5A, p. L544, 1996.

[284] J. Sarradin, M. Ribes, A. Guessous, and K. Elkacemi, "Study of fe2o3-based thin film electrodes for lithium-ion batteries," *Solid State Ionics*, vol. 112, no. 1-2, pp. 35–40, 1998.

[285] T. S. Cho, M. S. Yi, D. Y. Noh, S. J. Doh, and J. H. Je, "Thickness dependence of the crystallization of α-fe2o3/α-al2o3 (0001) thin films grown by sputtering," in *Solid State Phenomena*, vol. 124, pp. 1213–1216, Trans Tech Publ, 2007.

[286] K. Sarkar, M. Rawolle, E. M. Herzig, W. Wang, A. Buffet, S. V. Roth, and P. Müller-Buschbaum, "Custom-made morphologies of zno nanostructured films templated by a poly (styrene-block-ethylene oxide) diblock copolymer obtained by a sol–gel technique," *ChemSusChem*, vol. 6, no. 8, pp. 1414–1424, 2013.

[287] P. F. Green and R. Limary, "Block copolymer thin films: pattern formation and phase behavior," *Advances in Colloid and interface Science*, vol. 94, no. 1-3, pp. 53–81, 2001.

[288] P. Zhang, Z. Wang, H. Huang, and T. He, "Direct observation of the relief structure formation in the nearly symmetric poly (styrene)-block-poly (ε-caprolactone) diblock copolymer thin film," *Macromolecules*, vol. 45, no. 22, pp. 9139–9146, 2012.

[289] S.-J. Park, S.-W. Lee, K.-J. Lee, J.-H. Lee, K.-D. Kim, J.-H. Jeong, and J.-H. Choi, "An antireflective nanostructure array fabricated by nanosilver colloidal lithography on a silicon substrate," *Nanoscale research letters*, vol. 5, no. 10, pp. 1570–1577, 2010.

[290] D. L. Wertz and M. L. Steele, "Coordination of iron (3+) ion in concentrated aqueous solutions with chloride ligands," *Inorganic Chemistry*, vol. 19, no. 6, pp. 1652–1656, 1980.

[291] K. Murata and D. E. Irish, "Raman studies of the hydrated melt of fecl36h2o," *Spectrochimica Acta Part A: Molecular Spectroscopy*, vol. 44, no. 7, pp. 739–743, 1988.

[292] S. Saleem, S. Rangou, C. Abetz, B. Lademann, V. Filiz, and V. Abetz, "Block copolymer membranes from polystyrene-b-poly (solketal methacrylate)(ps-b-psma) and amphiphilic polystyrene-b-poly (glyceryl methacrylate)(ps-b-pgma)," *Polymers*, vol. 9, no. 6, p. 216, 2017.

[293] M. M. Crowley, A. Fredersdorf, B. Schroeder, S. Kucera, S. Prodduturi, M. A. Repka, and J. W. McGinity, "The influence of guaifenesin and ketoprofen on the properties of hot-melt extruded polyethylene oxide films," *European journal of pharmaceutical sciences*, vol. 22, no. 5, pp. 409–418, 2004.

[294] H. Wu and X. Huang, "Structural evolution of low-molecular-weight poly (ethylene oxide)-block-polystyrene diblock copolymer thin film," *The Scientific World Journal*, vol. 2013, 2013.

[295] C. Neto, M. James, and A. M. Telford, "On the composition of the top layer of microphase separated thin ps-peo films," *Macromolecules*, vol. 42, no. 13, pp. 4801–4808, 2009.

[296] G. Reiter and L. Vidal, "Crystal growth rates of diblock copolymers in thin films: Influence of film thickness," *The European Physical Journal E*, vol. 12, no. 3, pp. 497–505, 2003.

[297] J. R. Schneider, J. G. Baker, and S. F. Bent, "The influence of ozone: Superstoichiometric oxygen in atomic layer deposition of fe2o3 using tert-butylferrocene and o3," *Advanced Materials Interfaces*, vol. 7, no. 11, p. 2000318, 2020.

[298] D.-M. Smilgies, "Scherrer grain-size analysis adapted to grazing-incidence scattering with area detectors," *Journal of applied crystallography*, vol. 42, no. 6, pp. 1030–1034, 2009.

[299] D. Yang, F. C. Löhrer, V. Körstgens, A. Schreiber, B. Cao, S. Bernstorff, and P. Müller-Buschbaum, "In operando gisaxs and giwaxs stability study of organic solar cells based on pffbt4t-2od: Pc71bm with and without solvent additive," *Advanced Science*, vol. 7, no. 16, p. 2001117, 2020.

[300] W. Wang, C. J. Schaffer, L. Song, V. Körstgens, S. Pröller, E. D. Indari, T. Wang, A. Abdelsamie, S. Bernstorff, and P. Müller-Buschbaum, "In operando morphology investigation of inverted bulk heterojunction organic solar cells by gisaxs," *Journal of Materials Chemistry A*, vol. 3, no. 16, pp. 8324–8331, 2015.

[301] S. Xia, L. Song, V. Körstgens, M. Opel, M. Schwartzkopf, S. V. Roth, and P. Müller-Buschbaum, "Magnetic nanoparticle-containing soft–hard diblock copolymer films with high order," *Nanoscale*, vol. 10, no. 25, pp. 11930–11941, 2018.

[302] D. Babonneau, S. Camelio, D. Lantiat, L. Simonot, and A. Michel, "Waveguiding and correlated roughness effects in layered nanocomposite thin films studied by grazing-incidence small-angle x-ray scattering," *Physical Review B*, vol. 80, no. 15, p. 155446, 2009.

[303] T. H. Epps, D. M. DeLongchamp, M. J. Fasolka, D. A. Fischer, and E. L. Jablonski, "Substrate surface energy dependent morphology and dewetting in an abc triblock copolymer film," *Langmuir*, vol. 23, no. 6, pp. 3355–3362, 2007.

[304] E. W. Edwards, M. P. Stoykovich, M. Müller, H. H. Solak, J. J. De Pablo, and P. F. Nealey, "Mechanism and kinetics of ordering in diblock copolymer thin films on chemically nanopatterned substrates," *Journal of Polymer Science Part B: Polymer Physics*, vol. 43, no. 23, pp. 3444–3459, 2005.

[305] S. Ji, C.-C. Liu, W. Liao, A. L. Fenske, G. S. Craig, and P. F. Nealey, "Domain orientation and grain coarsening in cylinder-forming poly (styrene-b-methyl methacrylate) films," *Macromolecules*, vol. 44, no. 11, pp. 4291–4300, 2011.

[306] U. Nagpal, M. Muller, P. F. Nealey, and J. J. De Pablo, "Free energy of defects in ordered assemblies of block copolymer domains," *ACS Macro Letters*, vol. 1, no. 3, pp. 418–422, 2012.

List of publications

Publications related to the dissertation

- S. Yin, L. Song, S. Xia, Y. Cheng, N. Hohn, W. Chen, K. Wang, W. Cao, S. Hou, P. Müller-Buschbaum,"Key Factors for Template-Oriented Porous Titania Synthesis: Solvents and Catalysts", *Small Methods*, vol. 4, pp. 1900689, 2020.
- S. Yin, T. Tian, K. S. Wienhold, C. L. Weindl, R. Guo, M. Schwartzkopf, S. V. Roth, P. Müller-Buschbaum, "Key Factor Study for Amphiphilic Block Copolymer-Templated Mesoporous SnO_2 Thin Film Synthesis: Influence of Solvent and Catalyst", *Adv. Mater. Interfaces*, vol. 7, pp.2001002, 2020.
- S. Yin, W. Cao, Q. Ji, Y. Cheng, L. Song, N. Li, C. L. Weindl, M. Schwartzkopf, S. V. Roth, P. Müller-Buschbaum,"Multidimensional Morphology Control for PS-b-P4VP Templated Mesoporous Iron (III) Oxide Thin Films", *Adv. Mater. Interfaces*, vol. 14, pp.2100141, 2021.
- S. Yin, T. Tian, C. L. Weindl, Q. Ji, Y. Cheng, Y. Li, C. M. Papadakis, M. Schwartzkopf, S. V. Roth, P. Müller-Buschbaum, üller-Buschbaum,"In-situ GISAXS Observation and Large Area Homogeneity Study of Slot-Die Printed PS-b-P4VP and PS-b-P4VP/$FeCl_3$ Thin Films", *ACS Appl. Mater. Interfaces*, vol. 14, pp.31433155, 2022.
- S. Yin, Y. Zou, M. A. Reus, X. Jiang, S. Tu, T. Tian, R. Qi, Z. Xu, S. Liang, Y. Cheng, J. E. Heger, M. Schwartzkopf, S. V. Roth, P. Müller-Buschbaum,"Tailored Fabrication of Quasi-Isoporous and Double Layered α-Fe_2O_3 Thin Films and Their Application in Photovoltaic Devices", *Chem. Eng.*, pp.140135, 2022.

Further publications

- W. Cao, S. Yin, M. Bitsch, S. Liang, M. Plank, M. Opel, M. A. Scheel, M. Gallei, O. Janka, M. Schwartzkopf, S. V. Roth, P. Müller-Buschbaum"In Situ Study of

FePt Nanoparticles-Induced Morphology Development during Printing of Magnetic Hybrid Diblock Copolymer Films."*Adv. Funct. Mater.*, vol. 32, pp.2107667, 2021.

- W. Cao, S. Xia, X. Jiang, M. Appold, M. Opel, M. Plank, R. Schaffrinna, L. P. Kreuzer, S. Yin, M. Gallei, M. Schwartzkopf, S. V. Roth, P. Müller-Buschbaum,"Self-Assembly of Large Magnetic Nanoparticles in Ultrahigh Molecular Weight Linear Diblock Copolymer Films" *ACS Appl. Mater. Interfaces*, vol. 12, pp. 7557–7564, 2020.
- K. S. Wienhold, W. Chen, S. Yin, R. Guo, M. Schwartzkopf, S. V. Roth, P. Müller-Buschbaum,"Following in Operando the Structure Evolution-Induced Degradation in Printed Organic Solar Cells with Nonfullerene Small Molecule Acceptor", *Sol. RRL*, vol.4, pp. 2000251, 2020.
- K. S. Wienhold, C. L. Weindl, S. Yin, T. Tian, M. Schwartzkopf, A. Rothkirch,S. V. Roth, P. Müller-Buschbaum,"Following in situ the evolution of morphology and optical properties during printing of thin films for application in non-fullerene acceptor based organic solar cells."*ACS Appl. Mater. Interfaces*, vol.12, pp. 40381-40392.
- N. Hohn, X. Wang, M. A. Giebel,S. Yin, D. Müller, A. E. Hetzenecker, L. Bießmann, L. P. Kreuzer, G. E. Möhl, H. Yu, J. G. C. Veinot, T. F. Fässler,Y. J. Cheng, P. Muller-Buschbaum, "Mesoporous GeO_x/Ge/C as a Highly Reversible Anode Material with High Specific Capacity for Lithium-Ion Batteries."*ACS Appl. Mater. Interfaces*, vol.12, pp. 47002–47009.
- X. Jiang, H. Kim, P. S. Deimel, W. Chen, W. Cao, D. Yang, S. Yin, R. Schaffrinna, F. Allegretti, J. V. Barth, M. Schwager, H.Tang, K. Wang, M. Schwartzkopf, S. V. Roth, P. Müller-Buschbaum,"Internal nanoscale architecture and charge carrier dynamics of wide bandgap non-fullerene bulk heterojunction active layers in organic solar cells."*J. Mater. Chem. A* ., vol.8, pp. 23628–23636.
- Y. Zou, R. Guo, A. Buyruk, W. Chen, T. Xiao, S. Yin, X. Jiang, L. P. Kreuzer,C. Mu, T. Ameri, M. Schwartzkopf,S. V. Roth, P. Müller-Buschbaum, "Sodium Dodecylbenzene Sulfonate Interface Modification of Methylammonium Lead Iodide for Surface Passivation of Perovskite Solar Cells."*ACS Appl. Mater. Interfaces*, vol.12, pp. 52643–52651.
- W. Cao, S. Yin, M. Plank, A. Chumakov, M. Opel, W. Chen, L. P. Kreuzer, J. E. Heger, M. Gallei, C. J. Brett, M. Schwartzkopf, A. A. Eliseev, E. O. Anokhin, L. A. Trusov, S. V. Roth, P. Müller-Buschbaum,"Spray-Deposited Anisotropic Ferromagnetic Hybrid Polymer Films of PS-b-PMMA and Strontium Hexaferrite Magnetic Nanoplatelets."*ACS Appl. Mater. Interfaces*, vol.13, pp. 1592–1602.

- S. Liang, W. Chen, S. Yin, S. J. Schaper, R. Guo, J. Drewes, N. Carstens, M. Gensch, M. Schwartzkopf, F. Faupel, V. R. Stephan, Y. J. Cheng, P. Müller-Buschbaum,"Tailoring the Optical Properties of Sputter-Deposited Gold Nanostructures on Nanostructured Titanium Dioxide Templates Based on In Situ Grazing-Incidence Small-Angle X-ray Scattering Determined Growth Laws"*ACS Appl. Mater. Interfaces*, vol. 13, pp. 14728–14740, 2021.
- S. Hou, W. Li, S. Watzele, R. M. Kluge, S. Xue,S. Yin, X. Jiang, M. Döblinger, A. Welle, B. Garlyyev, M. Koch, P. Müller-Buschbaum, C. Wöll, A. S. Bandarenka, R. A. Fischer,"Metamorphosis of Heterostructured Surface-Mounted Metal–Organic Frameworks Yielding Record Oxygen Evolution Mass Activities"*Adv. Mater.*, vol. 33, pp.2103218, 2021.
- T. Tian, S. Yin, S. Tu, C. L. Weindl, K. S. Wienhold, S. Liang, M. Schwartzkopf, S. V. Roth, P. Müller-Buschbaum "Morphology Transformation Pathway of Block Copolymer-Directed Cooperative Self-Assembly of ZnO Hybrid Films Monitored In Situ during Slot-Die Coating"*Adv. Funct. Mater.*, pp.2105644, 2021.
- S. Tu, T. Tian, A. L. Oechsle, S. Yin, X. Jiang, W. Cao, N. Li, M. A. Scheel, L. K.Reb, S. Hou, A.S.Bandarenka, M. Schwartzkopf, S. V. Roth, P. Müller-Buschbaum, "Improvement of the thermoelectric properties of PEDOT:PSS films via DMSO addition and DMSO/salt post-treatment resolved from a fundamental view"*Chem. Eng. J.*,vol. 429, pp.132295, 2022.
- A. L. Oechsle, J. E. Heger, N. Li, S. Yin, S. Bernstorff, P. Müller-Buschbaum "Correlation of Thermoelectric Performance, Domain Morphology and Doping Level in PEDOT:PSS Thin Films Post-Treated with Ionic Liquids"*Macromol. Rapid Commun.*,vol. 429, pp.2100397, 2021.
- R. Guo, D. Han, W. Chen, L. Dai, K. Ji, Q. Xiong, S. Li, L. K. Reb, M. A. Scheel, S. Pratap, N. Li, S. Yin, T. Xiao, S. Liang, A. L. Oechsle, C. L. Weindl, M. Schwartzkopf, H. Ebert, P. Gao, K. Wang, M. Yuan, N. C. Greenham, S. D. Stranks, S. V. Roth, R. H. Friend, P. Müller-Buschbaum "Degradation mechanisms of perovskite solar cells under vacuum and one atmosphere of nitrogen"*Nat. Energy*, vol. 6, pp.977-986, 2021.
- Y. Zou, S. Yuan, A. Buyruk, J. Eichhorn, S. Yin, M. A. Reus, T. Xiao, S. Pratap, S. Liang, C. L. Weindl, W. Chen, C. Mu, I. D. Sharp, T. Ameri, M. Schwartzkopf, S. V. Roth, P. Müller-Buschbaum " The Influence of CsBr on Crystal Orientation and Optoelectronic Properties of MAPbI3-Based Solar Cells" *ACS Appl. Mater. Interfaces*, vol. 14, pp.2958-2967, 2022.

- S. Grott, A. Kotobi, L. K. Reb, C. L. Weindl, R. Guo, S. Yin, K. S. Wienhold, W. Chen, T. Ameri, M. Schwartzkopf, S.V. Roth, P. Müller-Buschbaum"Solvent tuning of the active layer morphology of non-fullerene based organic solar cells" *Solar RRL*, pp.2101084, 2022.
- J. E. Heger, W. Chen, S. Yin, N. Li, V. Körstgens, C. J. Brett, W. Ohm, S. V. Roth, P. Müller-Buschbaum," Low-Temperature and Water-Based Biotemplating of Nanostructured Foam-Like Titania Films Using ß-Lactoglobulin. Advanced Functional Materials" *Adv. Funct. Mater.*, pp.2113080, 2022.

Scientific reports

- S. Yin, L. Song, S. Xia, P. Müller-Buschbaum "Nanostructured TiO_2 Lithium-Ion Battery Anode Templated by Electron Conductive Amphiphilic Block Copolymer", *Lehrstuhl für Funktionelle Materialien, Annual Report*, 2017.
- S. Yin, P. Müller-Buschbaum, "Preparation of various intriguing TiO2 structures via amphiphilic diblock copolymer assisted sol-gel chemistry", *Lehrstuhl für Funktionelle Materialien, Annual Report*, 2018.
- S. Yin, T. Tian, M. Schwartzkopf, S. V. Roth, P. Müller-Buschbaum, "Key factors study in amphiphilic block copolymer-oriented porous SnO_2 synthesis process", *Lehrstuhl für Funktionelle Materialien, Annual Report*, 2019.
- L. Song, M. A. Niedermeier, P. Müller-Buschbaum, "Morphology control of PS-b-P4VP templated monolayer mesoporous α-Fe_2O_3 thin films", *Lehrstuhl für Funktionelle Materialien, Annual Report*, 2020.

Conference talks

- S. Yin "Sol-gel derived nanostructured metal oxide films for LIB anodes",*Seminar Talk*, Chair for Functional Materials, Physics-Department, TU München, Germany, 2018.
- S. Yin "White light interferometry (WLI)and Elipsometry", Polymer Physics Summer School, Obertauern, Austria, 2018.
- S. Yin "Preparation of porous SnO_2 thin films by tuning the precursor category, precursor content and HCl content", Polymer Physics Summer School, Obertauern, Austria, 2019.

- S. Yin "In-situ GISAXS observation and large-area homogeneity study of slot-die printed PS-b-P4VP and PS-b-P4VP/FeCl3 thin films", DPG meeting, Regensburg, 2022.

Conference poster presentations

- S. Yin, P. Müller-Buschbaum, "TiO_2 and SnO_2 anode material for lithium ion battery", DPGFrühjahrstagung, Berlin, Germany, 2018.
- S. Yin, P. Müller-Buschbaum, "TiO_2 and SnO_2 anode material for lithium ion battery", 9th Energy Colloquium of the Munich School of Engineering, Garching, Germany, 2018.
- S. Yin, P. Müller-Buschbaum, "TiO_2 and SnO_2 anode material for lithium ion battery", MLZ User Meeting, Garching, Germany, 2019.
- S. Yin, P. Müller-Buschbaum, "Key factor study for amphiphilic block copolymer-templated mesoporous SnO_2 thin film synthesis: Influence of solvent and catalyst", MRS Spring meeting, Phoenix, Arizona, 2020.
- S. Yin, P. Müller-Buschbaum,"Multi-Dimensional Morphology Control for PS-b-P4VP Templated Mesoporous Iron (III) Oxide Thin Films", 10th Energy Colloquium of the Munich School of Engineering, Garching, Germany, 2020.
- S. Yin, W. Cao, M. Schwartzkopf, S. V. Roth, P. Müller Buschbaum, "Morphology control of PS-b-P4VP templated monolayer mesoporous Fe_2O_3 thin films", Virtual DPG Spring Meeting 2021, 22-24 March, 2021
- S. Yin, W. Cao, M. Schwartzkopf, S. V. Roth, P. Müller Buschbaum, "Morphology control of PS-b-P4VP templated monolayer mesoporous Fe_2O_3 thin films" 11th MSE Colloquium 2021, 28 – 29 July, 2021
- S. Yin, W. Cao, M. Schwartzkopf, S. V. Roth, P. Müller Buschbaum, "Morphology control of PS-b-P4VP templated monolayer mesoporous Fe_2O_3 thin films" DPG Meeting "SKM 2021", 27 September – 01 October, 2021
- S. Yin, W. Cao, M. Schwartzkopf, S. V. Roth, P. Müller Buschbaum, "Morphology control of PS-b-P4VP templated monolayer mesoporous Fe_2O_3 thin films" MLZ User Meeting 2021, 07 – 08 December, 2021

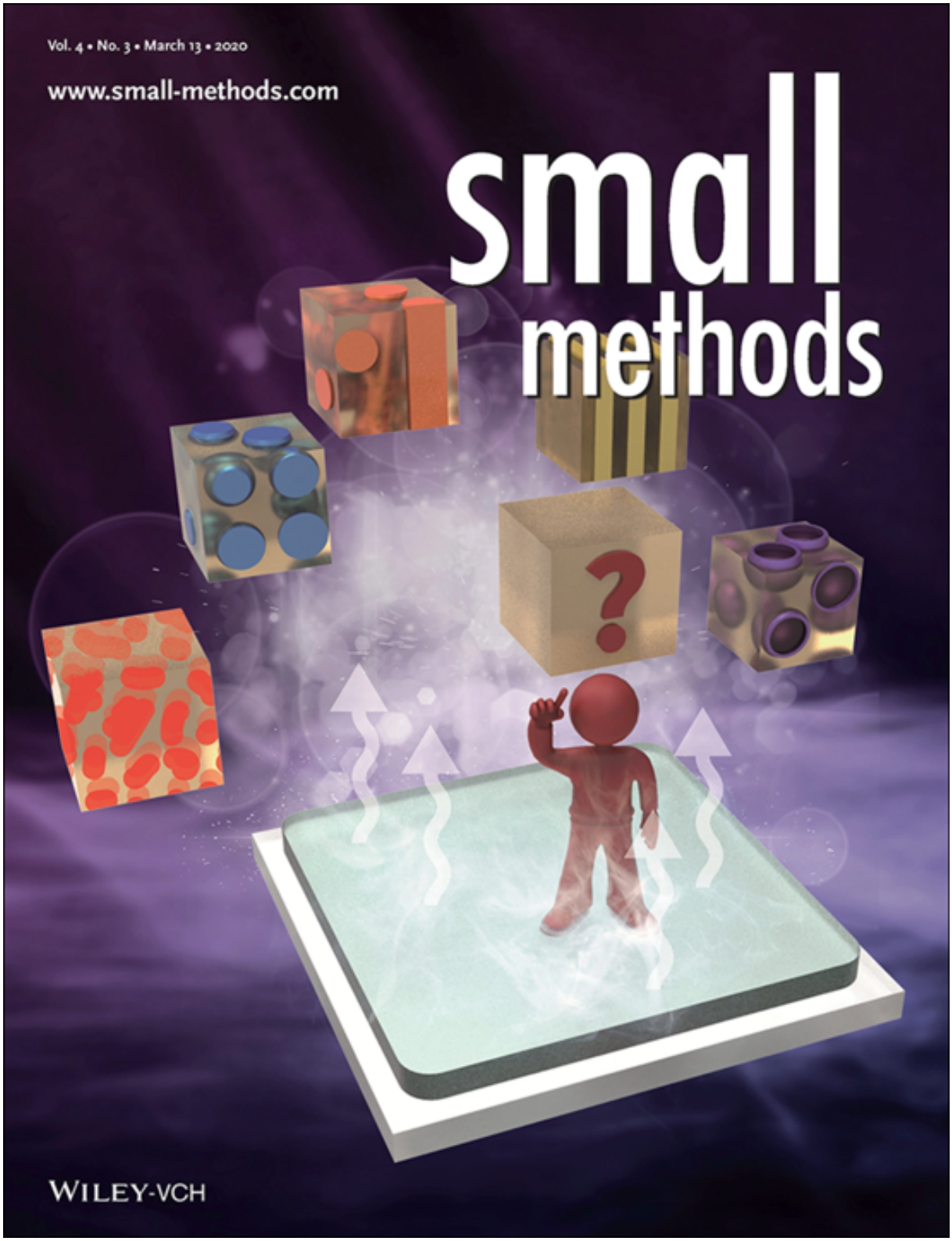

Figure 10.1: *Cover Image featured on Small Methods, vol. 4, pp. 1900689, 2020.*

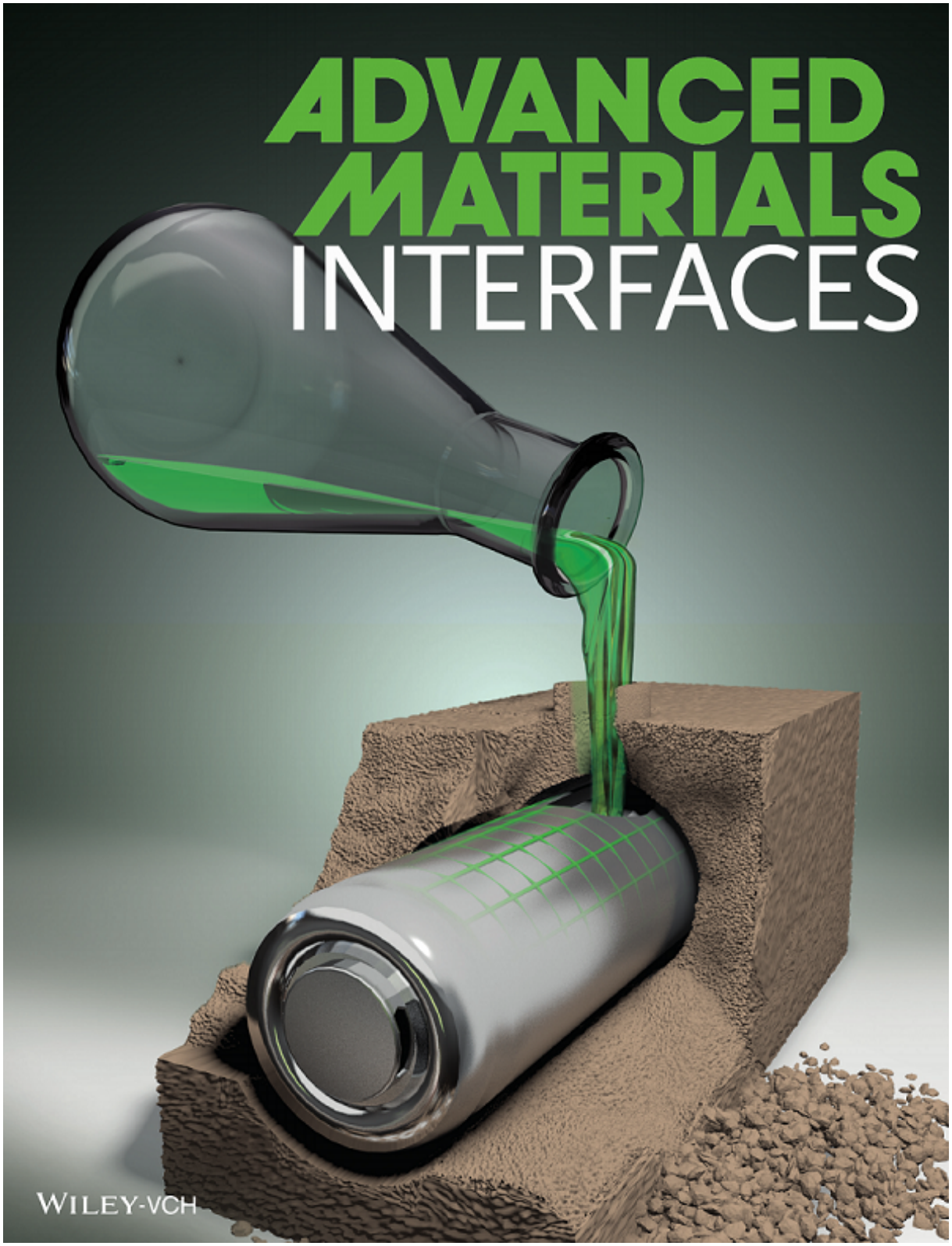

Figure 10.2: *Cover Image featured on Adv. Mater. Interfaces, vol. 14, pp.2100141, 2021.*

Acknowledgments

Firstly, I would like to thank my supervisor Prof. Dr. Peter Müller-Buschbaum for proving me the opportunity to join the Chair of Functional Materials at the Physics Department and to work on the interesting topic of nanostructured thin films. I really like the free and open research environment in our chair, which gives me lighthearted and fulfilling research and life experience. I highly appreciate his guiding advice on my research and his encouragement to have lunch and coffee break together in order to make the time at our chair as pleasant as possible. Moreover, his encouragement to attend the international conferences also greatly broadened my knowledge in my field of study. Apart from research, I,m also grateful to the colorful amateur life, which takes us to feel the liveliness of the Oktoberfest, and appreciates the tranquility and beauty of the town during the summer school. Moreover, the gift exchange activities and well-arranged activities during Christmas also made me feel the warmth of our chair. In addition, the experience of working with the rare synchrotron radiation source in our chair will become the most unforgettable and precious memories in my life.

Furthermore, I would like to thank my mentor Prof. Dr. Christine M. Papadakis. Sincere thanks to her for providing me the opportunity to do the DLS measurement in her lab. Her rigorous attitude towards scientific research deeply touched me. I would like to thank her and Dr. Volker Körstgens for giving me the precious chance for finishing my teaching points during the last year of my phD study.

This research could not have been accomplished without the constructive discussions with my dear colleagues. For this, I especially want to thank Prof. Dr. Lin Song, Dr. Senlin Xia, Dr. Wei Cao, Julian Heger, Dr. Nuri Hohn, Dr. Nian Li, Dr. Wei Chen, Dr. Kun Wang, Dr. Dan Yang, Dr. Florian Jung, Dr. Kerstin S. Wienhold, Dr. Lucas Kreuzer, Tobias Widmann, Sebastian Grott, Julian Heger, Simon Jakob Schaper, Dr. Shambhavi Pratap, Anna-Lena Oechsle, Roy Schaffrinna, Dominik Schwaiger, Lennart Reb, Christina Geiger, Manuel Scheel, Christian Weindl, Nian Li, Xinyu Jiang, Renjun Guo, Suzhe Liang, Tianxiao Xiao, Peixi Wang, Ting Tian, Suo Tu, Yanan Li, Tianfu Guan, Guangjiu Pan, Zerui Li, Zhuijun Xu. Especially, I would like to thank Prof. Dr. Lin Song for his valuable suggestions and discussions on my experiments. Also, he personally

demonstrated to me how to prepare mesoporous TiO_2 thin films via the traditional sol-gel method and informed me about the details that need to be paid attention to in the experiment. Thanks to him again. I also would like to thank Dr. Senlin Xia, he helped me a lot for doing the SEM measurement at the early stage of my research. In addition, I would like to thank Dr. Wei Chen for teaching me how to analyze GISAXS data. During the last section of my reasearch, Yuqin Zou spent a lot of time and effort to teach me the fabrication and measurement of the perovskite solar cells. Without their help and guidance, I will absolutely not be able to make progress so fast on my research. I would like to thank the beamline scientists for their careful explanation and discussion, which is critical for the precise data acquisition during the whole beamtime. Many thanks to Dr. Sigrid Bernstorff (Elettra), Prof. Dr. Stephan V. Roth (DESY), Dr. Matthias Schwartzkopf (DESY). I am also very grateful to my team members during the beamtime, the smooth progress of the measurements will not be possible without their support and cooperation. Within this frame, I would like to thank Lennart Reb, Sebastian Grott, Dr. Wei Chen, Renjun Guo, Dr. Kerstin S. Wienhold, Dr. Wei Cao, Dr. Nian Li, Anna-Lena Oechsle, Manuel Scheel, Christian Weindl, Xinyu Jiang, Ting Tian, Suo Tu.

Regarding the characterization aspect, I would like to thank Simon Jakob Schaper for his detailed and patient instruction for the XRD measurement and Dr. Lucas Kreuzer for the instruction on the FTIR measurement. In addition, Finally, I am highly appreciated that Prof. Alexander Holleitner and Peter Weiser provided me the chance for operating the SEM device. They helped me a lot to solve the technical problems during the long operation period. Moreover, I would like to thank Prof. Yajun Cheng and Ruoxuan Qi for doing the XPS measurements. I am very grateful to the China Scholarship Council (CSC) for providing me the financial support during my phD study, which saved me from financial hardship during my PhD studies.

I am sincerely grateful to Dr. Volker Kürstgens, Dr. Florian Jung, Dr. Lucas Kreuzer, Christopher Everett, Julian Heger, Julija Reitenbach, Tianxiao Xiao, Suzhe Liang and Yanan Li for proof reading of the present thesis. All corrections are valuable for the improvement of my thesis.

A big thank to our secretaries Marion Waletzki and Carola Kappauf, who made plenty of transactional work in our chair. They helped me a lot on the enrollment, reimbursements, visa extension, and job contract issues, and so on. Also, most of the non-scientific activities in our chair were organized by them. In addition, thanks to Julian Heger,help on the translation issues. Thanks to Dominik Schwaiger and Jia-Jhen Kang for their support on IT issues in our chair. Thanks to Dr. Florian Jung, Dr. Chia-Hsin Ko, Dr. Jia-Jhen Kang, Yanan Li and Bahar Yazdanshenas for their help in ordering experimental reagents for us.

In the end, I am appreciative to the time I spent with my first landlord's family, which gave me a lot of happiness during the first 3 years of my phD study. They always treat me as their own child, and do the laundry and cook for me, take care of me when I'm sick, always prepare me a gift and celebrate with a lot of delicious food on my birthday, thank them again. I also want to thank my family. My parents and sister have always provided unconditional support to me whenever I need. They always give me enormous endorsement and encouragement unconditionally on the road of my life.